LEABHARLANN CHOLÁISTE NA TRÍONÓIDE, BAILE ÁTHA CLIATH
Ollscoil Átha Cliath

TRINITY COLLEGE LIBRARY DUBLIN
The University of Dublin

Terms and Conditions of Use of Digitised Theses from Trinity College Library Dublin

Copyright statement

All material supplied by Trinity College Library is protected by copyright (under the Copyright and Related Rights Act, 2000 as amended) and other relevant Intellectual Property Rights. By accessing and using a Digitised Thesis from Trinity College Library you acknowledge that all Intellectual Property Rights in any Works supplied are the sole and exclusive property of the copyright and/or other IPR holder. Specific copyright holders may not be explicitly identified. Use of materials from other sources within a thesis should not be construed as a claim over them.

A non-exclusive, non-transferable licence is hereby granted to those using or reproducing, in whole or in part, the material for valid purposes, providing the copyright owners are acknowledged using the normal conventions. Where specific permission to use material is required, this is identified and such permission must be sought from the copyright holder or agency cited.

Liability statement

By using a Digitised Thesis, I accept that Trinity College Dublin bears no legal responsibility for the accuracy, legality or comprehensiveness of materials contained within the thesis, and that Trinity College Dublin accepts no liability for indirect, consequential, or incidental, damages or losses arising from use of the thesis for whatever reason. Information located in a thesis may be subject to specific use constraints, details of which may not be explicitly described. It is the responsibility of potential and actual users to be aware of such constraints and to abide by them. By making use of material from a digitised thesis, you accept these copyright and disclaimer provisions. Where it is brought to the attention of Trinity College Library that there may be a breach of copyright or other restraint, it is the policy to withdraw or take down access to a thesis while the issue is being resolved.

Access Agreement

By using a Digitised Thesis from Trinity College Library you are bound by the following Terms & Conditions. Please read them carefully.

I have read and I understand the following statement: All material supplied via a Digitised Thesis from Trinity College Library is protected by copyright and other intellectual property rights, and duplication or sale of all or part of any of a thesis is not permitted, except that material may be duplicated by you for your research use or for educational purposes in electronic or print form providing the copyright owners are acknowledged using the normal conventions. You must obtain permission for any other use. Electronic or print copies may not be offered, whether for sale or otherwise to anyone. This copy has been supplied on the understanding that it is copyright material and that no quotation from the thesis may be published without proper acknowledgement.

Investigation into semiconductor microcavity light emitting structures, and the assessment of InAs/GaAs quantum dots as sources for etched microstructures.

by

Alan J. Shaw

a thesis submitted for the degree of
Doctor of Philosophy
in the University of Dublin

under the supervision of

Prof. John Hegarty
Department of Physics
Trinity College Dublin

October 2001

TRINITY COLLEGE
13 FEB 2002
LIBRARY DUBLIN
THESIS 6558

Declaration

This thesis has not been submitted as an exercise for a degree at any other university. The work described is entirely my own, except for the assistance mentioned in the acknowledgements and the collaborative work mentioned in the list of publications. I agree that Trinity College Library may lend or copy this thesis upon request.

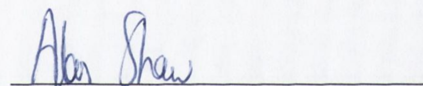

Alan J. Shaw

Summary

The spectral, spatial, and temporal characteristics of the spontaneous light emission process are dependent on the optical environment with which the emitter interacts. Cavity structures with dimensions of the order of the emission wavelength produce strong modifications of this optical environment and hence the spontaneous emission process of an internal emitter. Such microcavity structures possess the potential for the realisation light emitting diodes with increased efficiency, spectral purity, directionality and speed.

In this thesis the emission properties of a planar microcavity LED emitting in the red region of the spectrum, and of a novel higher dimensional microcavity structure emitting in the infra-red are presented, together with an investigation into the ability of InAs/GaAs quantum dot emitters to reduce the impact of edge recombination effects in etched microcavity structures.

We investigate the design and performance of planar microcavity LEDs whose emission wavelength is matched to the plastic optical fibre transmission window at 650nm. The measured electrical and optical characteristics of a fabricated device are presented, showing strong microcavity effects in the spatial and spectral emission properties. Carrier leakage, device heating, and non-optimised cavity design are all shown to play a role in determining the low efficiency (<1.5%) and low maximum output power (<1mW) of the device. We present simulation results showing the impact of cavity resonance wavelength position, source emission linewidth, and mirror properties on device efficiency. Optimised optical designs of microcavities emitting at 650nm for maximum emission efficiency into air and into a fibre with a numerical aperture of 0.5 are presented.

The emission properties of a novel microcavity structure offering full three-dimensional optical confinement are discussed. The structure known as a 'microleek' consists of a circular Bragg reflector etched in a slab waveguide. A distinct threshold is measured in the light-light characteristics of a microleek containing quantum well active layers. This observation combined with the sudden changes in both the emission spectrum and nearfield at the threshold pump intensity confirm the onset of lasing. The wavelengths of cavity modes of known azimuthal component are uniquely identified from the lasing spectra and nearfields. These cavity mode properties are successfully modelled for

different sized microleeks using a simple model based on the modes of a disk resonator. Despite the high cavity quality factor of ≈ 600 (measured from below threshold emission spectra) and small modal volume (microleek diameter $\approx 3\mu m$) of the microleek, time-resolved photoluminescence measurements performed on microleek structures containing quantum dot emitters at 77K show no cavity-induced modification of the spontaneous emission lifetime. This failure to observe any enhancement of the emission rate is seen to be consistent with theoretical predictions based on the cavity Purcell factor, when the spatial distribution of emitters in the cavity is taken into account. The combination of cavity dimensions and cavity quality factor required to produce an enhanced emission rate from a microleek is estimated.

The use of lateral mirror structures deeply etched through the active layer in multi-dimensional microcavity structures introduces non-radiative carrier recombination effects at the etched interfaces. Quantum dot active layers possess the potential to eliminate this effect through the trapping of carriers in discrete dots and thereby preventing their diffusion towards the non-radiative centres at the etched interfaces. We investigate the emission properties of InAs/GaAs self-assembled quantum dots and in particular their ability to reduce carrier spreading in the active layer. The roles of thermally activated carrier escape from dots, and the redistribution of carriers between different sized dots in the active layer are identified from photoluminescence spectra in bulk material in the 30K to 297K temperature range. The carrier diffusion length in both the InAs/GaAs quantum dot layer and an InGaAs/GaAs quantum well layer in the 77K to 297K temperature range are measured. A complete suppression of carrier spreading is observed in the quantum dot layer at temperatures <150K. At room temperature carrier spreading in the quantum dot layer matches that expected for an ambipolar diffusion length of $\approx 6.5\mu m$, while a diffusion length of $\approx 10\mu m$ is measured for the quantum well layer. The variation in emission intensity from the centre of an etched microcavity containing either quantum dot or quantum well active layers with temperature is shown to be consistent with the measured diffusion lengths. The measured loss at room temperature of 87% of carriers that recombine radiatively in InAs/GaAs quantum dots in bulk material to non-radiative edge recombination in a $\approx 3\mu m$ diameter cavity shows the failure of InAs/GaAs quantum dots to eliminate edge effects in etched microstructures.

Acknowledgements

I wish to thank my supervisor Prof. John Hegarty for providing me with the opportunity of carrying out this research, as well as ensuring the availability of sufficient financial and physical resources for its successful completion. Together with his SMILED lieutenant Dr. Brendan Roycroft, he provided guidance in establishing the framework of this work, for this I am extremely grateful to them both.

I also wish to thank the rest of the SMILED crew in Trinity – Tara, Pascal, and Hervé, for their support and help.

This research would not have been possible without the support and samples provided by SMILED collaborators across Europe. I particularly want to thank TUT for providing the 650nm microcavity samples, and EPFL and GU for the growth and processing of the microleek structures. Special mention must also go the Dr. Henri Benisty and his colleagues at EPP for their help in understanding the emission properties of the microleek structures, and to Dr. Ross Stanley for the sharing of his microcavity modelling expertise.

My time in the TCD optoelectronics group has coincided with a time of change and restructuring for the group and consequently there has been a large number of people both leaving and joining in the past four years as evidenced by the long list below, however in the midst of all this change certain people have remained steadfast sources of support – particular thanks must go to Dr. Vincent Weldon for his eternal patience, helpfulness, and expertise in the face often fraught requests, and to Mick Lynch for his knowledge, optimism and 'can-do' spirit that not even I could dampen.

This research would not have been completed without the support of my fellow members of the optronics PhD class of 2001, namely - John P for his constant willingness to go to the pub to watch matches (even if he supports the wrong team), Andrea for her attempts to introduce me to the delights of dinner parties, and Cian for being a true friend through thick and thin. All our shared disappointments, frustrations and occasional successes have provided essential comfort and hope in the darker moments of the last four years.

To all the other inhabitants of the lab old and new – Tom Aherne, Dave Fewer, Christophe, Fred, Fergal, Louise, Paul, Stephen, Declan, Gary, Adrian Donohoe, Karl,

Canice, Hervé, Richard, Tom McCormack, Dave McDonald, Dave Martin, Adrian Lavin, Shane, James, the many visiting students and to anyone else I've forgotten, it was a pleasure to meet you all.

Special thanks to Dr. John Donegan, Hervé and Mick for proof reading this thesis.

I would like to acknowledge Enterprise Ireland, Optronics and the European Union, via the ESPRIT program, for financial support.

Finally and most importantly, to my Family, for whose love and support I am eternally grateful, and without whom I would never have got to this point in my life. This thesis is dedicated to them.

Publications and Presentations

"Development of 650nm Microcavity LEDs", A. Shaw, B. Roycroft, J. Hegarty, P. Landais, T. Kavanagh, J. Kongas, M. Pessa, and M. Jalonen presented at Confined Photon Systems: Fundamentals and Applications, Cargése, August 1998.

"Microcavity LEDs for Plastic Optical Fiber applications", A.Shaw, B. Roycroft, J. Hegarty, P. Landais, T. Kavanagh, J. Kongas, M. Pessa, and M. Jalonen, presented at Institute of Physics conference, Newcastle, Northern Ireland, March 1999.

"Lasing properties of disk microcavity based on a circular Bragg reflector", A. Shaw, B. Roycroft, J. Hegarty, D. Labilloy, H. Benisty, C. Weisbuch, T. F. Krauss, C. J. M. Smith, R. Stanley, R. Houdré, and U. Oesterle, Appl. Phys. Lett. **75** (20) pp. 3051-3053 (1999)

"Lasing properties of disk microcavity based on a circular Bragg reflector", A. Shaw, B. Roycroft, J. Hegarty, D. Labilloy, H. Benisty, C. Weisbuch, T. F. Krauss, C. J. M. Smith, R. Stanley, R. Houdré, and U. Oesterle, presented at QE-14 Quantum Electronics & Photonics Conference, Manchester, September 1999.

"Lasing modes of a cylindrical microcavity containing quantum wells at room temperature" B. Roycroft, A. Shaw, J. Hegarty, D. Labilloy, H. Benisty, C. Weisbuch, T. F. Krauss, C. J. M. Smith, R. Stanley, R. Houdré and U. Oesterle presented at European Semiconductor Laser Workshop, Paris, September 1999.

"Lasers the size of a photon", A. Shaw, B. Roycroft, J. Hegarty, The Irish Scientist Yearbook, 1999.

"Small-Signal Analysis of 1.3μm Microcavity Light-Emitting Diodes", P. Landais, B. Roycroft, A. Shaw, B. Depreter, I. Moerman, and J. Hegarty, IEEE Photonics Technology Letters, **11** (11) pp.1342-1344 (1999)

"Programmable array microscope with a ferroelectric liquid-crystal spatial light modulator" P. J. Smith, C. M. Taylor, A. J. Shaw, and E. McCabe, Applied Optics **39** (16) pp. 2664-2669 (2000)

"Carrier diffusion in InAs/GaAs quantum dot layers and its impact on light emission from etched microstructures" A. Shaw, H. Folliot, J. F. Donegan, and J. Hegarty, *to be submitted.*

Table of Contents

1. Introduction *1*

1.1 Background 1

1.2 Thesis Overview 4

1.3 References 5

2. Background Information and Theory *8*

2.1 Introduction 8

2.2 Limitations on LED performance 8

2.2.1 Extraction efficiency *8*

2.2.2 Emission profile *9*

2.2.3 Spectral width *10*

2.2.4 Modulation Bandwidth *11*

2.3 Current LED technology 11

2.4 Introduction to microcavity concept 16

2.4.1 Modification of spontaneous emission pattern *17*

2.4.2 Modification of spontaneous emission rate *24*

2.5 Mirrors 27

2.6 Microcavity Structures 30

2.6.1 One-dimensional microcavities *30*

2.6.2 Higher dimensional microcavities *31*

2.7 Photon recycling 33

2.8 References 34

3. Red Planar Microcavity LEDs *38*

3.1 Introduction 38

3.2 Design considerations for a MCLED source for POF applications. 40

3.3 MCLED device structure. 42

3.4 MCLED Characterisation 43

3.4.1 Current-Voltage Characteristics *44*

3.4.2 Power-Current & Quantum Efficiency Characteristics *45*

3.4.3 Spectral Characteristics *48*

3.4.4 Nearfield Pattern *49*

3.4.5 Farfield Pattern *51*

3.4.6 Discussion of Characterisation Results *52*

3.5 MCLED device modelling 56

3.5.1 Modelling of characterised device *56*

3.5.2 Optimised cavity design for 650nm MCLED *64*

3.6 Subsequent developments in 650nm MCLEDs 69

3.7 Limitations on the extraction efficiency of planar MCLEDs 70

3.8 Conclusions 73

3.9 References 74

4. Higher Dimensional Microcavity Structure (Microleek) 78
4.1 Introduction 78
4.2 Cavity structure 80
4.2.1 Design principle 80
4.2.2 Samples 81
4.3 Modelling of cavity modes. 82
4.4 Experimental Set-up 87
4.5 Emission processes in Microleek structure. 89
4.6 Microleeks containing Quantum Wells. 90
4.6.1 Lasing Results 90
4.6.2 Summary 99
4.7 Microleeks containing Quantum Dots 99
4.7.1 Photoluminescence spectra 100
4.7.2 Photoluminescence Lifetimes 103
4.7.3 Summary 110
4.8 Conclusion 111
4.9 References 112

5. PL spectral characterisation of InAs/GaAs quantum dots. 116
5.1 Introduction 116
5.2 Quantum Dots – Background 116
5.3 QD fabrication processes. 119
5.4 Stranski-Krastanow growth mode. 121
5.5 Samples 123
5.6 Electronic structure of self-assembled InAs/GaAs QDs. 124
5.7 Experimental Set-up 125
5.8 Results and discussion 127
5.8.1 Temperature dependence of QD and QW PL spectra 127
5.8.2 Excitation Intensity dependence of QD PL spectrum. 137
5.9 Conclusions 141
5.10 References 142

6. Carrier diffusion in InAs/GaAs QD and InGaAs/GaAs QW layers and its impact on the performance of etched microcavity structures. 147
6.1 Introduction 147
6.2.Non-radiative surface recombination. 147
6.3 Experimental setup 149
6.4 Diffusion measurements 151
6.4.1 Introduction 151
6.4.2 Theory - The Diffusion Equation 154

6.4.3 Results _155_
6.4.4 Simulation _160_
6.4.5 Discussion _163_
6.5 Cavity measurements 167
6.5.1 Introduction _167_
6.5.2 Cavity structure _169_
6.5.3 Results and Discussion _169_
6.6 Discussion 172
6.7 Conclusion 175
6.8 References 176

7. Conclusions _181_

Appendices

A2. Derivation of Purcell Factor from Fermi's Golden Rule. 186

A2. Model for dipole emission in multilayer structure. 189

Chapter 1

Introduction

1.1 Background

Radiative transitions involving the transfer of an electron between an initial and final quantum state with the simultaneous emission of a photon represent both one of the most fundamental and most important processes in optoelectronic devices. Photon emission can occur by two distinct mechanisms, namely spontaneous and stimulated emission, as first postulated by Einstein [1]. In the spontaneous emission process, the radiative transition occurs spontaneously without the intervention of any external stimulus. In the stimulated emission process, radiative transitions are induced by photons, with the stimulating and emitted photons having the same propagation direction and phase.

In semiconductors, transitions occur between two groups of electronic levels known as the conduction band and valence band. Electrons excited from the valence band into the conduction band leave vacancies in the valence band known as holes. In direct bandgap semiconductors there is a high probability of the recombination of an electron and hole resulting in the emission of a photon, while in indirect bandgap semiconductors most electron and hole recombination is non-radiative, generating heat rather than light.

The potential for harnessing stimulated emission processes to develop laser devices was first realised by Schawlow and Townes in 1958 [2]. By 1960 Maiman had demonstrated an operational Ruby laser [3] and by 1962 several groups had reported lasing action in semiconductors [4,5,6,7]. In 1970 the first room temperature semiconductor laser was realised [8]. The intrinsic properties of the stimulated emission process have been exploited to produce high bandwidth, spectrally pure, and highly directional emission from laser devices. This combination of properties has enabled the semiconductor laser to play a key role in the explosive growth of optical communications.

Spontaneous emission processes are employed in light emitting diodes (LEDs). The LED is one of the simplest optoelectronic devices, which in its most basic form consists of a forward biased p-n junction of a direct bandgap material. The injected minority charge recombines with the majority charge in the depletion region leading to the generation of light, a phenomenon known as electroluminescence. The first observation of electroluminescence was from a silicon carbide Schottky diode in 1907 [9]. While LEDs cannot match laser diodes for emission bandwidth, directionality or efficiency due to their reliance on spontaneous emission processes, their relatively simple structure results in low fabrication costs. The combined annual market for visible and infra-red LEDs is worth several billion dollars and is growing at 10-15% per year. LEDs have found applications in short haul fibre optic data links, free space links, visible displays and indicators. They are also considered superior to incandescent sources for several applications including vehicular lighting (e.g. tail lights, indicators) and traffic lights [10]. White-light LEDs are expected to ultimately replace incandescent bulbs as the standard interior lighting source.

Considerable developments in semiconductor LED technology have occurred since their first introduction in 1962 [6]. The evolution in the electronic structure of LEDs has mirrored that of semiconductor laser diodes; beginning with simple homojunctions, through single- and double-heterostructures, to quantum well structures. Further improvements have been achieved through advances in material growth, processing and packaging technologies, such as reduced non-radiative recombination, improved carrier and optical confinement, access to new emission wavelengths, and improved light extraction schemes. The currently favoured material systems are GaInN/GaN for blue and green emission, AlGaInP/GaAs or AlGaInP/GaP for red and orange emission, and GaAs/AlGaAs or InGaAs/InP for infrared emission.

Despite the huge market for LEDs, comparatively little research into improving fundamental recombination processes in LEDs has been performed in the last 30 years relative to laser diodes. One of the reasons for this may have been the widely held view of spontaneous emission as an intrinsic unalterable atomic property. However despite the implication of the name, spontaneous emission is not an uncontrollable process, but rather can be modified by tailoring the optical environment in which the process occurs [11]. This was first realised by Purcell in 1946 [12], who noted that the spontaneous

emission rate could be enhanced for an atom placed inside a wavelength sized cavity (microcavity), and by Kleppner [13], who discussed the opposite case of inhibited spontaneous emission. This field of research known as cavity quantum electrodynamics (CQED) was initially confined to atomic physics and microwave frequencies. In the microwave regime wavelength sized cavities are of the order of millimetres and thus relatively easy to fabricate. In the past fifteen years investigations into CQED effects have been extended to optical frequencies. The drive towards miniaturisation and reduced threshold current, principally in the field of vertical cavity surface emitting lasers (VCSELs), has played a key role in the realisation of wavelength sized cavities in the optical region of the spectrum. Microcavity structures with a wide range of optically active media including organic dyes [14,15], semiconductors [16,17], rare-earth-doped silica [18] and organic polymers [19,20] have been realised. In these publications clear changes in the spectral, spatial, and temporal emission characteristics of spontaneous emission processes were demonstrated.

Current injected microcavity LEDs (MCLEDs) were first demonstrated in the GaAs material system in 1992 [21], and subsequently in organic light-emitting materials in 1993 [19]. In both cases a narrowing of the emission linewidth due to the cavity was observed. Blondelle et al. demonstrated enhanced efficiencies for MCLEDs in 1995 [22]. The ability of microcavities to modify the spontaneous emission process has resulted in the realisation of MCLEDs with higher brightness, increased spectral purity and higher efficiency compared to conventional LEDs.

While enhanced spontaneous emission rates have been demonstrated for semiconductor microcavities at optical frequencies [23], these results remain in the realm of low temperature, optically pumped experiments. A semiconductor MCLED with an enhanced emission rate has yet to be realised.

As the above discussion shows, the 1990s saw an explosive growth in research on optical microcavity structures. Two multi-institutional European projects played a central role in the development of an understanding of the potential and limitations of semiconductor microcavities. The first project, ‘Semiconductor Microcavity Light Emitters’ (SMILES), which ran from 1993 to 1997, investigated both fundamental and applied concepts relating to all areas of microcavity physics and technology. The second project, ‘Semiconductor Microcavity Light Emitting Diodes’ (SMILED), which operated between

1997 and 2000 focussed on the transfer of MCLED technology to commercial devices, and the development of higher dimensional microcavity structures. The research contained in this thesis was performed primarily within the framework of, and in collaboration with partners of, the SMILED project.

1.2 Thesis Overview

The layout of the thesis is as follows:

Chapter 2 provides a general introduction to both commercial LED technology and the operating principles of MCLEDs. The limitations on LED performance due to their reliance on spontaneous emission processes, together with the approaches adopted by commercial LEDs to circumvent these limitations are discussed. The ability of a cavity to modify the spontaneous emission process is discussed in terms of Fermi's Golden Rule and the Purcell factor. A simple model for the emission from an ideal one-dimensional cavity is used to demonstrate the ability of the microcavity to produce enhanced efficiency, directionality and spectral purity of emission. The final part of the chapter contains a discussion of the properties of different mirror structures, and different one- and three-dimensional cavity types.

Chapter 3 contains our investigations into planar MCLEDs. The results presented relate to the development of a planar MCLED emitting at 650nm for plastic optical fibre applications. The design considerations for a MCLED emitting at this wavelength are discussed, and results of electrical and optical characterisation measurements on an early red MCLED are presented. The emission properties of the characterised device together with the expected improvement in performance for an optimised device structure are modelled in the second half of the chapter. Both the measured and modelled results are discussed in terms of general planar microcavity effects. Finally the ultimate limitations on the efficiency of planar MCLED structures are discussed using the model. This chapter serves as an introduction to practical microcavity structures, and as a starting point for our investigations into more complex microcavity designs.

Chapter 4 contains the results of our studies on a novel three-dimensional cavity, known as a microleek. The design principle of the microleek structure is introduced, together with the specific details on the composition and dimensions of the structures investigated.

A basic model is used to derive expressions for the wavelengths of the cavity modes and to highlight different classes of confined modes. Experimental results on the lasing properties of the microleek, in particular the emission spectra and nearfields, are used to probe the cavity mode structure. Time-resolved photoluminescence measurements on the microleek structure are presented in the final section of the chapter, together with a calculation of the cavity properties required to observe a modified emission lifetime.

Chapter 5 contains a discussion of the bulk emission properties of the InAs/GaAs quantum dot (QD) and InGaAs/GaAs quantum well (QW) active layers in our microleek. The chapter begins with a general introduction to quantum dots. Different fabrication methods for QDs are discussed, with particular emphasis on strain-induced self-assembly processes. Photoluminescence spectra from the QD and QW layers as functions of sample temperature and excitation intensity are presented. The temperature dependence of the emission lineshape, linewidth, integrated intensity, and peak wavelength are explained in terms of thermally activated carrier escape processes. The excitation intensity at which saturation of the ground state transition of the QDs occurs is identified from the excitation dependent PL studies.

Chapter 6 is dedicated to our investigations of carrier diffusion in QD and QW active layers, and its impact on non-radiative edge recombination processes in etched microcavities. Carrier diffusion in both QD and QW layers in the temperature range 77K to 297K is quantified in terms of ambipolar diffusion lengths. An estimation of the trapping efficiency of the QDs as a function of temperature is obtained from a comparison of the results for the QD and QW layers. The impact of non-radiative edge recombination processes on the photoluminescence emission intensity from 3.2μm diameter etched microcavities containing either QDs or QWs is investigated. The temperature dependence of edge recombination effects and carrier diffusion lengths are compared. Finally the results of our carrier diffusion measurements are discussed in terms of the thermally activated carrier escape processes identified from bulk PL measurements in chapter 5.

Chapter 7 presents our conclusions.

1.3 References

1 “Zur quantentheorie der strahlung”, A. Z. Einstein, Zeitschrift fur Physik, **18** p.121 (1917)

2 “Infrared and optical masers”, A. L. Schawlow and C. H. Townes, Phys. Rev. **112** (6) p. 1940 (1958)

3 “Stimulated optical radiation in ruby lasers”, T. H. Maiman, Nature **187** p.493 (1960)

4 “Coherent light emission from GaAs junctions”, R. N. Hall, G. E. Fenner, J. D. Kingsley, T. J. Soltys, and R. O. Carlson, Phys. Rev. Lett. **9** (9) p.366 (1962)

5 “Stimulated emission of radiation from GaAs p-n junction”, M. I. Nathan, W. P. Dumke, G. Burns, F. H. Dill Jr., and G. J. Lasher, Appl. Phys. Lett. **1** (3) p.62 (1962)

6 “Coherent (visible) light emission from Ga($As_{1-x}P_x$) junctions”, N. Holonyak, and S. Bevacqua, Appl. Phys. Lett. **1** (4)p.82 (1962)

7 “Semiconductor maser of GaAs”, T. M. Quist, R. H. Rediker, R. J. Keyes, W. E. Krag, B. Lax, A. L. McWorther and H. J. Zeigler, Appl. Phys. Lett. **1** p.91 (1962)

8 “Junction lasers which operate continuously at room temperature”, I. Hayashi, M. B. Panish, P. W. Foy, and S. Sumski, Appl. Phys. Lett. **17** (3) p.109 (1970)

9 “A note on Carborundum”, H. J. Round, Electrical World, **49** p.309 (1907)

10 “LEDs challenge the incandescents”, M. G. Crawford, IEEE Circuits and Devices, **8** (5) p.24 (1992)

11 “Cavity quantum electrodynamics”, S. Haroche and D. Kleppner, Physics Today **42** (1) p. 24 (1989)

12 “Spontaneous emission probabilities at radio frequencies”, E. M. Purcell, Phys. Rev. **69** p.681 (1946)

13 “Inhibited Spontaneous Emission”, D. Kleppner, Phys. Rev. Lett. **47** (4) p. 233 (1981)

14 “Anomalous spontaneous emission time in a microscopic optical cavity”, F. De Martini, G. Innocenti, G. R. Jacobovitz, and P. Mataloni, Phys. Rev. Lett. **59** (26) p.2955 (1987)

15 “Observation of spontaneous emission lifetime change of dye-containing Langmuir-Blodgett films in optical microcavities”, M. Suzuki, H. Yokoyama, S. D. Brorson, and E. P. Ippen, Appl. Phys. Lett. **58** (10) p. 998 (1991).

16 "Inhibited and enhanced spontaneous emission from optically thin AlGaAs/GaAs double heterostructures", E. Yablonovitch, T. J. Gmitter, and R. Bhat, Phys. Rev. Lett. **61** (22) p. 2546 (1988)

17 "Enhanced spontaneous emission from GaAs quantum wells in monolithic microcavities", H. Yokoyama, K. Nishi, T. Anan, H. Yamada, S. D. Brorson, E. P. Ippen, Appl. Phys. Lett. **57** (26) p.2814 (1990)

18 "Giant enhancement of luminescence intensity in Er-doped Si/SiO_2 resonant cavities", E. F. Schubert, A. M. Vredenberg, N. E. J. Hunt, Y. H. Wong, P. C. Becker, J. M. Poate, D. C. Jacobson, L. C. Feldman, and G. J. Zydzik, Appl. Phys. Lett. **61** (12) p.1381 (1992)

19 "Organic photo- and electroluminescent devices with double mirrors", T. Nakayama, Y. Itoh, and A. Kakuta, Appl. Phys. Lett. **63** (5) p. 594 (1993)

20 "Color variation with electroluminescent organic semiconductors in multimode resonant cavities", A. Dodabalapur, L. J. Rothberg, and T. M. Miller, Appl. Phys. Lett. **65** (18) p.2308 (1994)

21 "Resonant cavity light emitting diode", E. F. Schubert, Y.-H. Wang, A. Y. Cho, L.-W. Tu and G. J. Zydzik, Appl. Phys. Lett. **60** (8) p. 921 (1992)

22 "6% external quantum efficiency from InGaAs/(Al)GaAs single quantum well planar microcavity LEDs", J. Blondelle, H. De Neve, P. Demeester, P. Van Daele, G. Borghs, and R. Baets, Electron. Lett. **30** (21) p. 1787 (1995)

23 "Enhanced Spontaneous Emission by Quantum Boxes in a Monolithic Optical Microcavity", J. M. Gérard, B. Sermage, B. Gayral, B. Legrand, E. Costard, and V. Thierry-Mieg, Phys. Rev. Lett. **81** (5) p.1110 (1998)

Chapter 2

Background Information and Theory

2.1 Introduction

The reliance of light emitting diodes (LEDs) on spontaneous emission processes for the generation of light introduces a number of limitations on device performance. The first half of this chapter contains a discussion of these limitations, and briefly outlines the approach of current LED technology to overcoming these limitations. The second half of the chapter contains an introduction to the concepts of photon confinement and microcavity structures. The ability of microcavities to modify the spontaneous emission process and the potential improvements to LED performance offered by microcavity structures are discussed. Finally practical realisations of microcavity structures offering photon confinement in one or more dimensions are introduced.

2.2 Limitations on LED performance

2.2.1 Extraction efficiency

The extraction efficiency of a device is defined as the fraction of photons generated internally in the device that are emitted from the device. The relatively high refractive indices (n=2.8→3.5) of most semiconductor materials result in small critical angles, θ_c, for the semiconductor-air interface. For light to escape into air it must be emitted internally in the semiconductor material at angles less than the critical angle. Light emitted at all other angles suffers total internal reflection at the interface. The internal solid angle from which emission can couple to air, $\Omega_c = 2\pi(1-\cos(\theta_c))$, represents only a few percents of the 4π steradian total space solid angle. A simple approximation ($\cos(\theta_c) \approx 1-(\theta_c)^2/2=1-1/2n^2$), leads to the fraction $\Omega_c/4\pi=1/4n^2$, which is thus the extraction

efficiency at a single planar face for an isotropic emitter in a semiconductor of refractive index *n*, typically 2-3%. The assumption of isotropic internal emission is valid for the bulk active regions of double heterostructure LEDs, with emission from quantum well active regions somewhat better coupled to extracted angles [1]. However in either case the extraction efficiency is very low resulting in poor external quantum efficiency* and power conversion efficiency. The industrial solutions to this issue and their limitations are discussed in section 2.3.

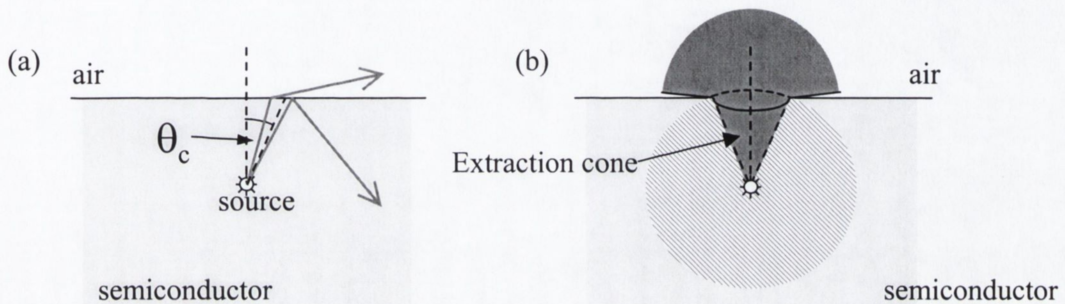

Figure 2.1 *(a) Ray diagram showing critical angle for semiconductor-air interface, (b) Schematic diagram of extraction cone, and the coupling of emission to angles in air.*

2.2.2 Emission profile

A consequence of the near isotropic internal emission in LED devices, is an external angular distribution of emitted power which is well approximated by

$$I(\theta) = I_0 \cos(\theta) \qquad (2.1)$$

where θ is the angle from the normal. A source exhibiting such a cosine dependence of emitted power on angle is known as a Lambertian source. The broad angular distribution of the emission (full width at half maximum of 120 degrees) means that it is very difficult to couple light from an LED into an optical fibre without the use of intermediate lenses. In such a coupling configuration, known as butt coupling, the coupling efficiency η_{fibre} from a Lambertian source is approximately given by [2]

* External quantum efficiency η_{extern}, defined as $\eta_{extern} = \dfrac{\text{number of photons emitted from device}}{\text{number of electrons flowing in external circuit}}$

$$\eta_{fibre} = (NA)^2 \quad (2.2)$$

where NA is the numerical aperture of the fibre. Since typical ranges for the numerical apertures of silica and plastic optical fibres are 0.1-0.3 and 0.4-0.5 respectively, only a small percentage of the emitted power is coupled into the fibre.

2.2.3 Spectral width

The spectral purity or the linewidth of the emitted radiation is an important characteristic of optical devices. The spectral linewidth of standard LEDs is determined by the spontaneous emission spectrum of the active layer, which depends on the electron and hole occupation probabilities and the density of states. The distribution of electron and hole energies results in an emission linewidth in energy, ΔE, roughly equal to $1.8k_BT$, where k_B is Boltzmann's constant and T is the absolute temperature [2]. This can be expressed as an emission linewidth in wavelength $\Delta\lambda$ of $1.8k_BT\lambda^2/hc$, where λ is the peak emission wavelength, h is Planck's constant and c is the speed of light. While this linewidth is dependent on emission wavelength, it represents a broad spectrum at all wavelengths. The importance of the emission linewidth is dependent on the application; for display applications it is not an issue but for fibre-optic data links it is of critical importance. The large spectral linewidth of LED transmitters results in considerable material dispersion in the fibre. The extent of the temporal broadening Δt, caused by the different spectral components propagating at different velocities in the fibre is given by [3]

$$\Delta t = \mathrm{M}l\Delta\lambda \quad (2.4)$$

where l is the fibre length, and M is the material dispersion parameter of the fibre. Excessive temporal broadening of the pulse will result in an increased bit error rate. For this reason the use of LED transmitters in fibre networks is limited to low bit rate, short distance optical fibre data links.

2.2.4 Modulation Bandwidth

Modulation of the optical output of an LED is achieved through the modulation of the injected carriers. Ignoring electrical parasitics and assuming that the charge is injected instantaneously, the switching speed of the LED is determined by the time taken to remove the injected carriers. This time is determined by the carrier recombination time or carrier lifetime, τ_c. The frequency response function of an LED can be written simply as [4]

$$H(\omega) = \frac{1}{\sqrt{1+\omega^2 \tau_c^{\ 2}}} \tag{2.5}$$

where ω is the angular modulation frequency. This expression shows that at higher frequencies the LED response decreases, with the carrier lifetime determining the bandwidth. The 3dB bandwidth, f_{3dB} is defined as the frequency at which the output power has dropped by 3dB from the low frequency value, and can be determined from (2.5) as

$$f_{3dB} = \frac{1}{2\pi\tau_c} \tag{2.6}$$

The carrier recombination rate is equal to the sum of the radiative and non-radiative recombination rates, giving

$$\frac{1}{\tau_c} = \frac{1}{\tau_r} + \frac{1}{\tau_{nr}} \tag{2.7}$$

where τ_r and τ_{nr} are the radiative and non-radiative recombination times. For high quality materials $\tau_c \approx \tau_r$. Clearly for a large modulation bandwidth the carrier lifetime should be as short as possible. Several methods of achieving a reduced lifetime are mentioned in section 2.3.

Ultimately, the modulation bandwidth is limited by the electron-hole recombination time, which is typically of the order of 1ns for an LED under normal operating conditions [2]. Thus, the modulation bandwidth of LEDs can approach 1GHz.

2.3 Current LED technology

In the above discussion on the limitations on LED performance we focussed on the emission properties of a planar LED utilising emission through a single surface directly

into air. Current commercial LED technology utilises various packaging schemes to improve overall performance.

The poor extraction efficiency is improved through the use of emission from the sides of the sawn LED chip as well as the top. Figure 2.2 shows schematic representations of two such designs. The redirection of emission from the sides of the chip towards the normal is achieved by placing the chip in a cup reflector. The extraction cone through each surface can also be increased through the encapsulation of the LED chip in a transparent epoxy, with a typical refractive index of ≈1.5. The increased refractive index of the epoxy relative to air results in an increased critical angle for the semiconductor-epoxy interface, while the dome shape of the epoxy results in a reduced angle of incidence for light at the epoxy-air interface. The use of epoxy can increase the extraction efficiency per facet by a factor of 2 [5], resulting in an overall improvement for emission from 6 sides using epoxy over single sided emission directly into air of a factor of 12. The extraction efficiency can be further increased by cutting the chip into a truncated inverted pyramid as opposed to the traditional cuboid shape. Extraction efficiencies as high as 55% have been demonstrated using the truncated inverted pyramid shape [6]. However in order to access emission from all sides of the chip the substrate must be removed, a costly process, in the frequent case in which it is absorbing. The incorporation of the cup reflector and epoxy also introduce additional packaging costs.

Despite the very high extraction efficiencies of these devices, they are not "brighter" at the chip level than a device utilising emission through a single side. This is because the increase in optical power P is accompanied by an equivalent increase in source area S so

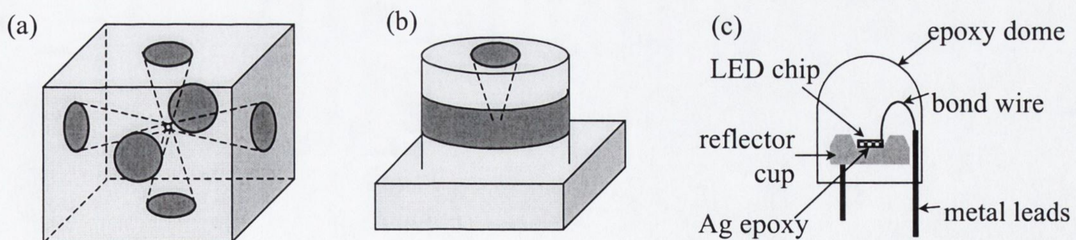

Figure 2.2 *(a) and (b) Schematic diagrams of different geometric shaped LEDs. (a) cuboid LED dice with six escape cones, (b) cylindrical LED with top escape cone and side escape ring. (c) A typical hemispherical epoxy dome LED package.*

that the radiance dP/dSdΩ remains basically unchanged [1]. The limitation on LED radiance introduces major limitations on the fibre coupling efficiency achievable.

While the epoxy dome is shaped to reduce the angular divergence of the emitted light from the device for some applications, more dedicated collecting optics are usually employed to improve fibre coupling efficiency. Figure 2.3 shows three possible coupling configurations for surface emitting LEDs. Emission from only one side of the LED chip is used in devices designed as fibre sources, since the increased emitting area resulting from the use of emission from all sides of the chip is considerably greater than the fibre core.

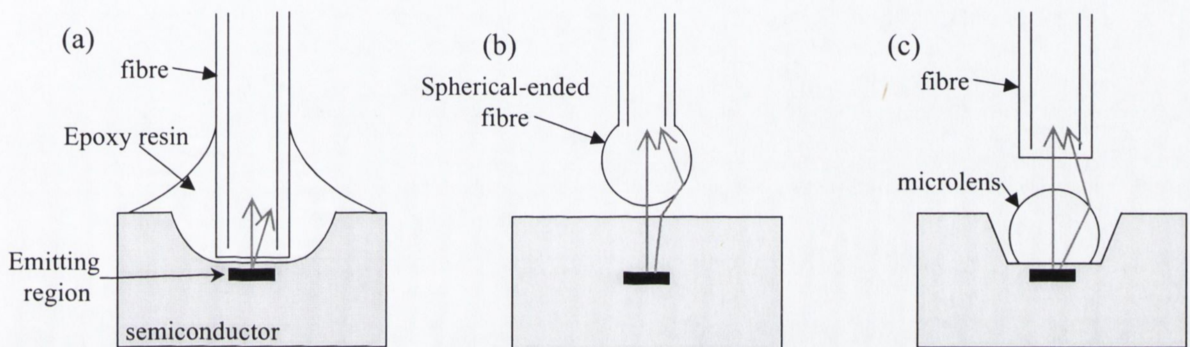

Figure 2.3 *Schematic diagrams of different fibre coupling configurations for a surface emitting LED. (a) A 'Burrus type' LED, with the fibre end directly positioned over the emitting region and encapsulated with epoxy resin, (b) use of a lens-ended fibre and (c) use of a truncated spherical microlens.*

A second generic class of LEDs known as edge emitting LEDs also exist. The schematic diagram of an edge emitting LED shown in Figure 2.4 shows the similarities to an edge emitting laser diode, and similar technology is employed in both their fabrications. An important feature of the edge emitting LED is the wide bandgap (lower refractive index) cladding layers that confine not only the electrons and holes to the active layer, but also cause the emitted photons to travel along the LED axis and emerge from the edge of the device. This waveguiding narrows the divergence of the emitted beam to a full width at half maximum of around 30 degrees in the plane perpendicular to the junction. However the divergence in the plane of the junction remains similar to that expected for a Lambertian source ($\approx$120 degress). The improved directionality of the emission from an

edge emitting LED results in improved butt coupling efficiencies to fibre, which can be further increased using lenses in similar configurations to those shown for the surface emitting LED in Figure 2.3.

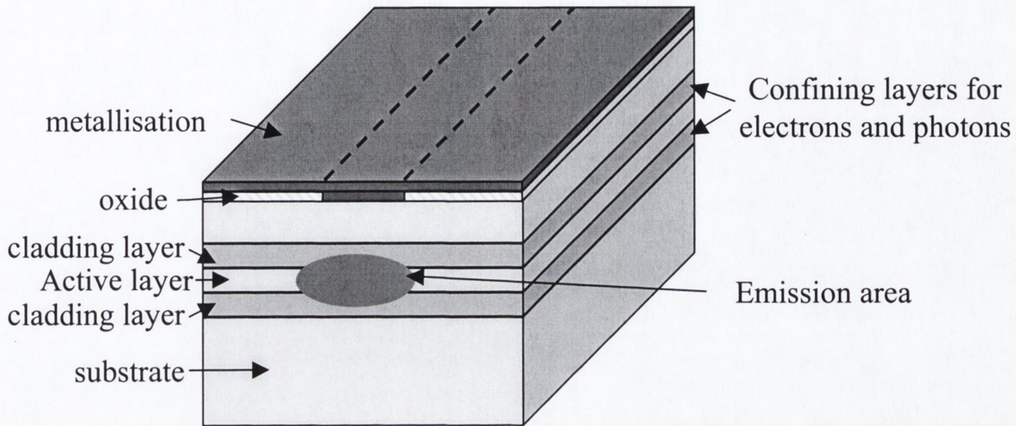

Figure 2.4 *Schematic diagram of generic edge emitting LED.*

The final limitation on LED performance described in section 2.2 concerned the modulation bandwidth of the device. We saw the bandwidth was determined by the carrier recombination lifetime. The carrier lifetime is dependent on the doping concentration, the number of injected carriers into the active region, the surface recombination velocity, and the thickness of the active layer. The two main approaches to reducing the carrier lifetime involve increasing the doping of the active layer, thereby reducing the non-radiative recombination lifetime, and increasing the carrier concentration in the active layer. Modulation bandwidths in excess of 1.5GHz have been demonstrated for LEDs with doped active layers [7]. However the reduced non-radiative lifetime also results in a reduction of the external quantum efficiency and consequently the output power.

Alternatively the carrier density in the active layer can be increased by either reducing its thickness or increasing the bias current. For high current densities the carrier lifetime depends on the current density, J, in the following manner [8]

$$\tau_c = \sqrt{\frac{ed}{B_r J}} \tag{2.8}$$

where e is the electronic charge, d is the thickness of the active layer and B_r is the bimolecular radiative recombination coefficient. This relationship has been confirmed for a variety of device structures and materials [8]. LEDs incorporating thin active layers have demonstrated data rates of up to 1 Gbit/s while maintaining high external quantum efficiencies of 29% [9].

Despite the improvements in the emission properties of LEDs achieved through the various approaches outlined above, LED emission properties still suffer in comparison to the high efficiency, high power and highly directional emission offered by laser diodes. LEDs do however enjoy a number of significant advantages over laser diodes:

- *Simpler fabrication.*
- *Cost.* The simpler fabrication of LEDs leads to much reduced costs.
- *Reliability.* LEDs do not exhibit catastrophic degradation and have proved far less sensitive to gradual degradation.
- *Less temperature dependent performance.* The light output against current characteristic is less affected by temperature. Also since the LED is not a threshold device, there is no possibility of a temperature rise increasing the threshold current above the operating point.
- *Simpler drive circuitry.* LEDs generally require lower drive currents, and do not require temperature stabilisation circuits.

These advantages make LEDs very attractive sources for many applications. However if LEDs could close the gap in terms of bandwidth and directionality to laser diodes then this range of applications would increase considerably. It appears unlikely that developments in packaging or the exploitation of fast non-radiative recombination processes will yield the required improvements in device performance; rather an ability to fundamentally alter the spontaneous emission process is required. Such a modification to both the spontaneous emission pattern and rate has been demonstrated for an emitter in an optical cavity, whose dimensions are of the order of the wavelength of the emitted radiation, a so-called microcavity [10,11]. The following section provides an introduction to the microcavity concept and its application to LEDs.

2.4 Introduction to microcavity concept

In 1946 Purcell predicted that the spontaneous emission rate of an excited atom would be altered if the atom was placed in a cavity with dimensions comparable to the transition wavelength, a structure now known as a microcavity. This ability to modify the spontaneous emission process by controlling the optical environment of the excited atom can be understood in terms of spontaneous emission being a specific case of stimulated emission, where stimulation is provided by vacuum-field fluctuations of the electromagnetic field. Cavity Quantum Electrodynamics (CQED) has provided a solid theoretical basis as well as impressive experimental support for this concept [12,13,14].

Two coupling regimes between the radiating dipole in a cavity and the cavity mode can be identified in CQED. The "weak coupling regime" is where the escape time of emitted photons out of the cavity is much less than the radiative lifetime and reabsorption is negligible. In this regime, the light matter interaction can be treated in a perturbative manner, with the excited state decaying in an irreversible manner at a rate given by Fermi's Golden rule. Another regime also exists where the light matter interaction is so strong that it cannot be treated in a perturbative fashion. This regime is known as the "strong coupling regime", and is characterised by the periodic exchange of excitation between the dipole and field; a phenomenon known as Rabi oscillation [15]. Very high reflectivity cavities are usually required to observe strong coupling behaviour. All the devices and cavities investigated in this thesis operate in the weak coupling regime, therefore we will confine our discussion of cavity-induced modifications of spontaneous emission to this situation.

In the weak coupling regime the spontaneous emission rate of a radiating dipole γ_{sp} is given by Fermi's golden rule as [16]

$$\gamma_{sp} = \frac{1}{\tau_{sp}} = \frac{2\pi}{\hbar} \rho(\omega_e) \left\langle \left| \vec{d} \cdot \vec{\varepsilon}(\vec{r}) \right|^2 \right\rangle \qquad (2.9)$$

where τ_{sp} is the spontaneous emission lifetime, $\vec{\varepsilon}(\vec{r})$ is the vacuum electric-field at the location $\vec{r}$ of the emitter, $\vec{d}$ is the electric dipole and $\rho(\omega_e)$ is the density of photon modes at the emitters angular frequency ω_e. The averaging of the squared dipolar matrix element is performed over the various modes seen by the emitter. It is clear from (2.9) that the

spontaneous emission rate can be modified by either modifying the mode density, or by modifying the vacuum electric field at the location of the radiating dipole. In a microcavity both the mode density and the vacuum field intensity will be different from those in free space or in a bulk sample.

The microcavity can be used to produce two potentially beneficial modifications of the spontaneous emission process, a modification of the spatial distribution of emission and a modification of the emission rate. The modification of the spatial distribution of emission need not be accompanied by any modification of the emission rate; this is because the emission at certain angles can be enhanced/suppressed through an increase/decrease of the electric field intensity at the dipole of the modes propagating at that angle without any modification of average electric field of modes propagating over all angles or the overall $\rho(\omega_e)$. This redistribution of emission can be used to improve the directionality of emission and extraction efficiency of microcavity structures as described below. In order to observe a change in the spontaneous emission rate a modification of the total $\rho(\omega_e)$ or the average vacuum electrical field intensity at the dipole over all angles is required. While the potential benefits of an enhanced spontaneous emission rate in the fabrication of LEDs with high modulation bandwidths are obvious, a greater modification and control of the optical environment by the cavity is required.

2.4.1 Modification of spontaneous emission pattern

In order to demonstrate the ability of a microcavity to modify the angular distribution of emission and its potential application in improving the efficiency of LEDs, the emission from a source in a planar cavity (Fabry-Perot cavity) is calculated using a classical multiple beam interference approach.

A source emitting at vacuum wavelength λ, positioned in a cavity of thickness L and refractive index n, at a distance z_1 from the bottom mirror (see Figure 2.5) is considered. The top (bottom) mirror reflectivity and transmission are denoted $R_1=r_1^2$ ($R_2=r_2^2$) and $T_1=t_1^2$ ($T_2=t_2^2$) respectively, where r_1 and r_2 (t_1 and t_2) are electric field amplitude reflection (transmission) coefficients. The source emits rays that interfere before being collected in the farfield above the cavity. The summation of two series of waves one

emitted at θ and the other emitted at π-θ, gives the following expression for the farfield intensity E^2 corresponding to an internal angle θ

$$|E|^2 = |E_0|^2 \times \frac{T_1}{|1 - r_1 r_2 e^{2i\phi}|^2} \times |1 + r_2 e^{2i\phi'}|^2 \tag{2.10}$$

where $\phi' = kz_1\cos\theta$, $\phi = kL\cos\theta$, with $k=2\pi n/\lambda$, and E_0 is the radiated far-field from the source at an angle θ in the absence of any mirror.

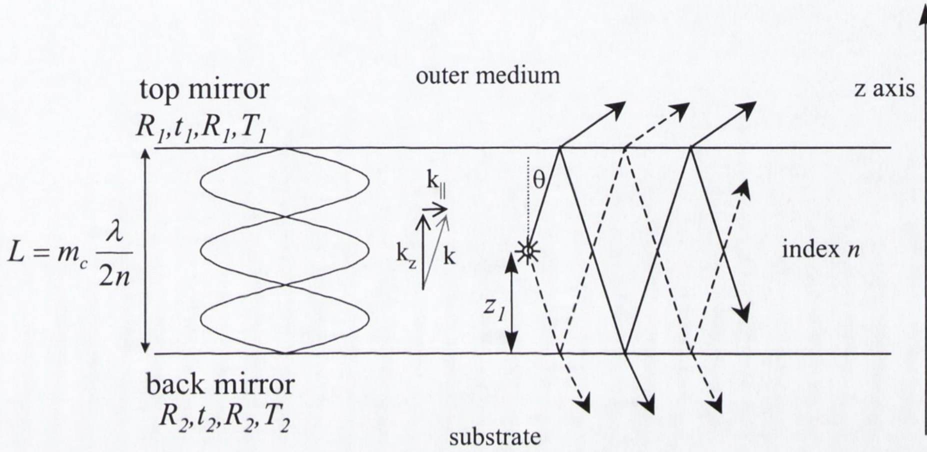

Figure 2.5 *Schematic representation of planar cavity of index n and length L, with a source inside emitting two series of waves.*

The final term $|1 + r_2 e^{2i\phi'}|^2$ in (2.10) is called the antinode factor ζ, and corresponds to the enhancement of the upward radiated farfield in the presence of a single bottom mirror. The periodic variation of ζ with ϕ', shown in Figure 2.6, corresponds to constructive and destructive interference between the rays emitted from the source at θ and those emitted at π-θ, in the presence of a single bottom mirror. To maximise the farfield intensity at the angle θ, for the source wavelength λ, we require $2\phi'(=2kz_1\cos\theta)=2m\pi$ where m is a (half) integer for (-) $+r_2$. To satisfy this condition at $\theta=0$, we require $kz_1=m\pi$ or $z_1=m\pi/k=m(\lambda/2n)$. Since the only dependence of the farfield intensity from the cavity, given by (2.10), on the source position z_1, is contained in ζ, the source should be positioned at an integer number of half wavelengths from the bottom mirror for

maximum on axis (θ=0) emission (for $+r_2$). This corresponds to the positioning of the source at an antinode of the cavity mode.

The second term in (2.10), $\frac{T_1}{\left|1-r_1r_2e^{2i\phi}\right|^2}$ is known as the Airy factor and accounts for the cavity mode structure. It reproduces the intrinsic enhancement/inhibition of each mode (i.e. each wavelength, angle pair) by the cavity. The Airy function is a maximum for $\phi(=kL\cos\theta)=m\pi$, with the width of the resonance around the maximum value determined by the mirror reflectivities. This resonance condition determines the wavelength-angle pairs that represent cavity modes.

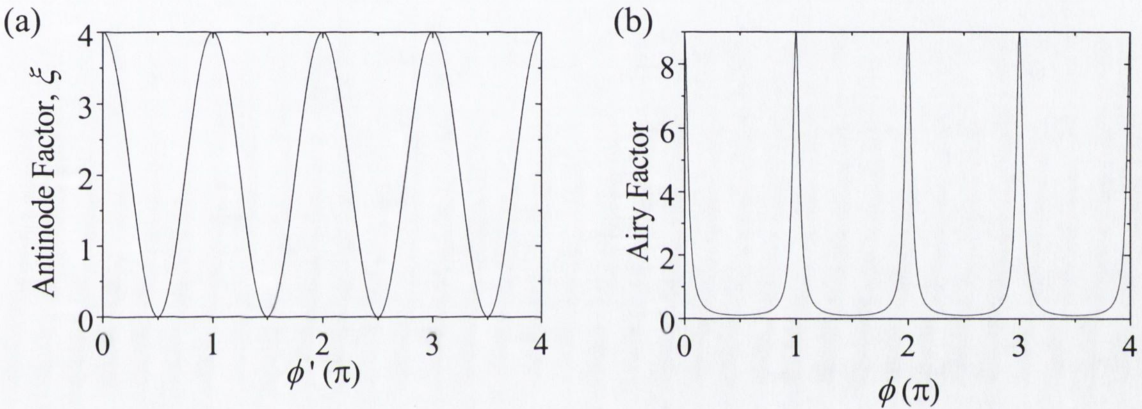

Figure 2.6 *(a) Antinode factor ζ as a function of ϕ' for r_2=+1 (b) Airy factor as a function of ϕ for r_2=+1, r_1=+0.8, and T_1=0.36.*

For a fixed emission wavelength, k is constant and ϕ can vary from 0 at $\theta=\pi/2$ to kL at θ=0, satisfying the resonance condition of the cavity at angles θ such that $k\cos\theta=m\pi/L$. Therefore the cavity order m_c, defined as the number of cavity resonances, is given by m_c=integer[kL/π] (where integer[x] means the value of x rounded down to the nearest interger). While the cavity length for a cavity with a resonant mode at θ=0, is given by $L=m_c\lambda/2n$.

The farfield emission for a source positioned at the centre of a m_c=6 cavity, together with the Airy and antinode functions are shown in Figure 2.7. The six modes of the cavity are clearly visible in the Airy function, while the antinode factor shows that the positioning

of the emitter at the centre of the cavity results in emission only coupling to every second cavity mode. Depending on the emitter position in the cavity emission into the even or odd cavity modes can be equally or unequally favoured. Figure 2.7 shows the capability of the cavity to radically alter the emission pattern of an isotropic source placed in a cavity. This effect can obviously be used to alter the emission profile from microcavity LED structures, however the angular redistribution of emission inside the cavity can also be used to improve the extraction efficiency of LEDs.

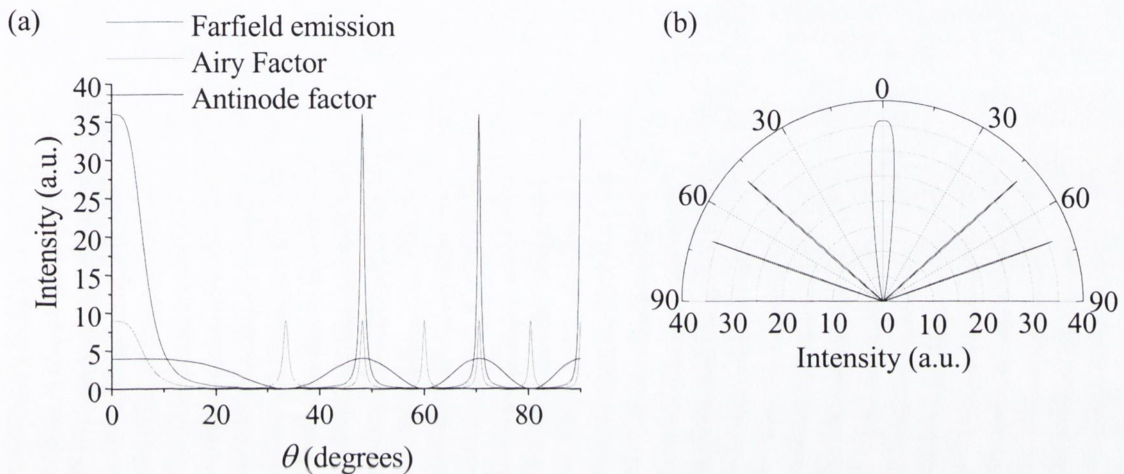

Figure 2.7 *(a) Emission profile of an isotropic source (monochromatic emission at wavelength λ) positioned at the centre of an m_c=6 ($L=3\lambda/n$), for r_2=+1,r_1=+0.8, and T_1=0.36, (b) same emission profile on a polar plot.*

The ability of a microcavity to enhance the extraction efficiency is best demonstrated using a *k*-space plot of the cavity modes and Airy function, a scheme developed by Benisty et al. [17]. The case of a monochromatic source is again considered, but in order to simplify the discussion we initially assume that ζ is the same for all modes in the cavity (this corresponds to a situation where the source is distributed throughout the cavity). In this situation the angular distribution of emission is determined solely by the Airy function, whose resonances are periodic in $k_z=k\cos\theta$. The intersection of the quarter circle of radius k, with the horizontal lines for each resonant $k_z=m\pi/L$ determines the angles of the resonant cavity modes. It can be shown that the total emission in a cone between two angles θ_1 and θ_2, accounting for the variation in solid angle with θ, is given

to within a constant factor by the integration of the Airy function on the left of Figure 2.8 between k_z=$k\cos\theta_1$ and k_z=$k\cos\theta_2$ [17]. Since all resonances of the Airy function have equal area (in the limit $R_1R_2\rightarrow 1$), equal fractions of emission couple to each of the cavity modes. Therefore in the case of sharp, well-separated resonances the extraction efficiency η_{extra} becomes

$$\eta_{\text{extra}} = \frac{\text{number of modes with } \theta < \theta_c}{\text{total number of modes}} \tag{2.10}$$

In the large cavity limit illustrated in Figure 2.8(a), because the $\cos\theta$'s of the large number of cavity modes are equally spaced from 1 to 0, this ratio tends towards the ratio of solid angles $\Omega_c/2\pi = 1-\cos\theta_c \approx 1/2n^2$. This is the same extraction efficiency expected for a single bottom mirror far from the source. However if we consider the microcavity regime as illustrated in Figure 2.8(b), when there are only a few cavity modes and specifically only one at $\theta<\theta_c$, then

$$\eta_{\text{extra}} = \frac{1}{m_c} \tag{2.11}$$

giving η_{extra} =0.25 for the situation illustrated in Figure 2.8(b). Ultimately we could

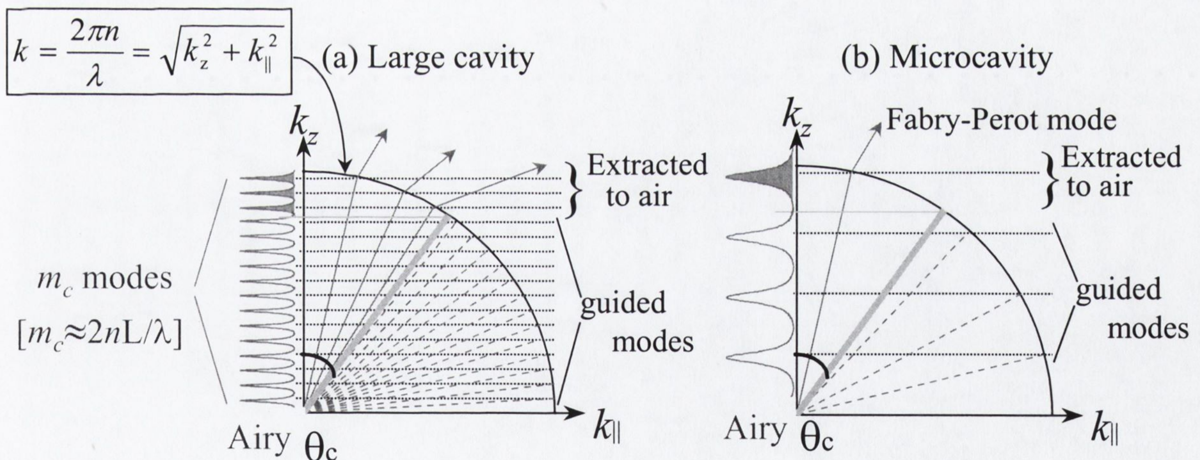

Figure 2.8 *Plot in k-space depicting cavity modes, airy function and critical angle. The green shaded area under the Airy function at $\theta<\theta_c$ is proportional to the extracted emission. (a) large cavity limit – many modes extracted (b) microcavity regime – one of a small number of modes extracted.*

imagine a η_{extra} =1 value for a cavity with only a single mode whose Airy resonance was confined to angles $\theta<\theta_c$, however as discussed later such a cavity is beyond the limits of current technology.

At this stage we can re-introduce the antinode factor ζ, to allow the possibility of different coupling between the source and the different cavity modes due to the source location or orientation. If we label each cavity mode i=1,2,...m_c, then we can assign each mode an antinode factor ζ_i (assuming sharply defined resonances allow the identification of a single ζ_i for each mode). Then we can rewrite a corrected form of the generalised expression (2.10) as

$$\eta = \frac{\sum_{\text{extracted modes}} \zeta_i}{\sum_{\text{all modes}} \zeta_i} \tag{2.12}$$

which becomes

$$\eta = \frac{\zeta}{\sum_{\text{all modes}} \zeta_i} \tag{2.13}$$

for the microcavity case with a single extracted mode of antinode factor ζ.

One final issue with regard to the optimisation of the extraction efficiency of a planar microcavity structure is the positioning of the extracted mode resonance within the escape window. Since the Airy peak of the extracted resonance has some width, it should be centred in the escape window in terms of k_z: denoting θ_0 the internal angle of the resonant extracted mode, $\cos\theta_0$ should lie halfway between 1 and $\cos\theta_c$. This means

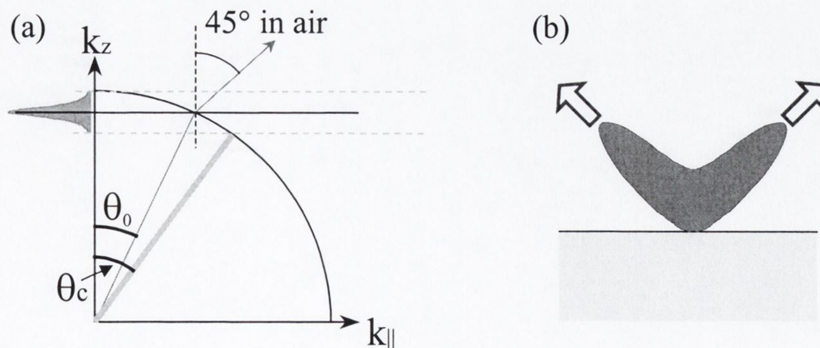

Figure 2.9 *(a) Optimal position of cavity mode in escape window (b) corresponding emission pattern showing maximum emission off axis at $\theta\approx45°$.*

$\cos\theta_0 = 1 - 1/4n^2$, and hence $\theta_0 \approx \theta_c/\sqrt{2}$. Translated to air by Snell's law, this gives the maximum emission occurring at 45° from the normal. Therefore a planar microcavity optimised for maximum extraction efficiency will exhibit a two-lobed emission pattern as shown schematically in Figure 2.9(b). Since the cavity mode shifts to shorter wavelengths with increasing angle, the cavity mode wavelength at $\theta=0$ must be located at a longer wavelength than the source emission wavelength for the internal emission wavelength to be resonant off-axis. This difference between the cavity mode wavelength at $\theta=0$ and the source emission wavelength is commonly referred to as the cavity detuning.

This treatment of the ability of a planar microcavity structure to alter the emission pattern and extraction efficiency of an isotropic emitter has not extended to include important factors in practical structures such as the source emission linewidth, the angular dependence of mirror reflectivities, and the distributed nature of reflections from certain mirrors. However it does highlight some important generic design considerations/operating principles of microcavity structures:

- The positioning of the source at the antinode (node) of a cavity mode to enhance (inhibit) emission into that mode.
- The influence of the ratio of extracted modes to total number of modes on the extraction efficiency of the structure.
- The dependence the external emission angle on the cavity resonance condition.

The progression from planar cavities offering photon confinement in one dimension to cavities offering photon confinement in two and three dimensions results in the quantisation of the k component in each of the confined directions. Therefore in the case of full three dimensional (3D) confinement in a cavity of dimensions L_x, L_y and L_z in the x, y and z directions respectively, all three components of the wavevector k of the resonant cavity modes are quantised, with the resonant k values given by

$$k^2 = k_x^2 + k_y^2 + k_z^2 = \left(\frac{m_x \pi}{L_x}\right)^2 + \left(\frac{m_y \pi}{L_y}\right)^2 + \left(\frac{m_z \pi}{L_z}\right)^2 \qquad (2.14)$$

where m_x, m_y and m_z take integer values. As discussed for the planar cavity the impact of this quantisation becomes particularly significant when the scale to which the photon is confined is comparable to its wavelength, so called microcavity structures. The ability of higher dimensional microcavity structures to modify the emission profile and extraction efficiency for an internal source is illustrated in Figure 2.10(b). The emission profile is determined by the existence of cavity modes defined in all three dimensions compared to the rings of allowed modes for the planar cavity. The extraction efficiency is still determined by the ratio of cavity modes in the extraction cone to the total number of cavity modes, however the number of angles at which modes satisfy the more stringent resonance condition is reduced compared to the planar cavity case.

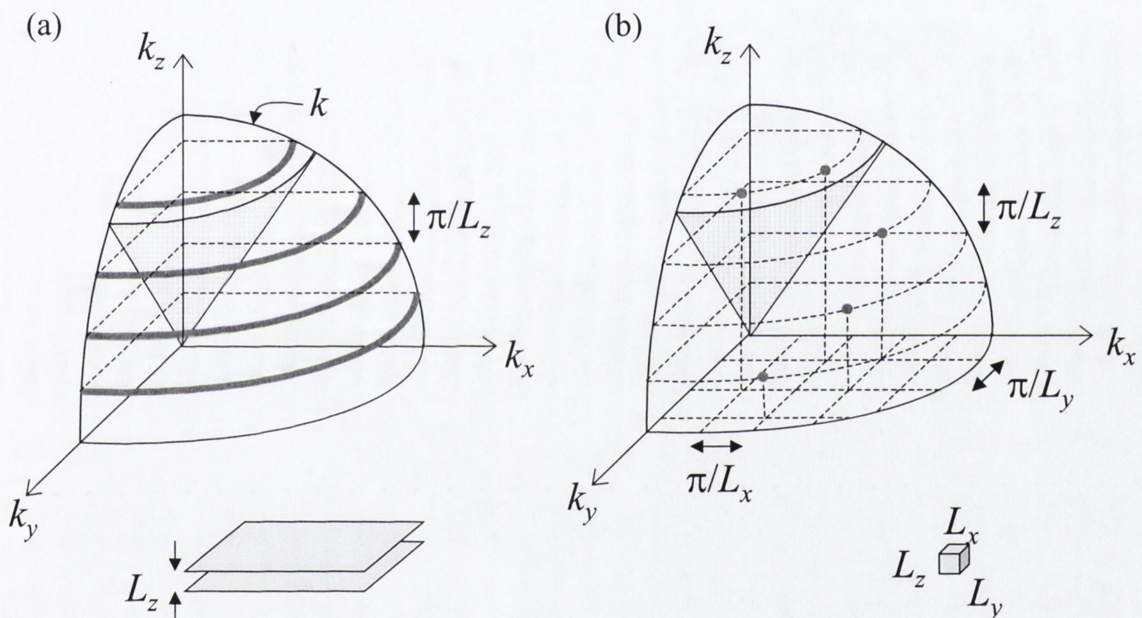

Figure 2.10 *Diagrams showing quantisation of cavity modes in k-space for (a) a planar cavity – only k_z quantised (b) a 3-dimensional cavity – k_x, k_y and k_z all quantised. The escape cone defined by the critical angle is shaded in both cases.*

2.4.2 Modification of spontaneous emission rate

As already discussed in the context of Fermi's Golden Rule (equation (2.9)), a modification of the spontaneous emission rate requires a modification of the total density

of states at the emitter frequency, $\rho(\omega_e)$, or a modification of the average vacuum electrical field intensity at the source, of modes propagating at all angles.

Such modifications of the optical environment can be achieved with low order planar microcavity structures. Figure 2.11 shows the modified spontaneous emission rate γ_{cav}, for a horizontal dipole positioned at the centre of a planar cavity with ideal mirrors (reflectivity coefficients, $r_1 = r_2 = \pm 1$) relative to the free-space spontaneous emission rate, γ_0, as derived in reference [18]. For mirror reflectivities $r_{1,2}=+1$, a factor of nearly two enhancement in the spontaneous emission rate is predicted for an $L=\lambda/n$ cavity, while even greater enhancement is predicted for very thin cavities $L<<\lambda/2n$. A factor of three enhancement in the spontaneous emission rate is predicted for a $L=\lambda/2n$ cavity with mirror reflectivities $r_{1,2}= -1$ (corresponding to a π phase shift in the reflected wave). Figure 2.11 also shows that for $L>3\lambda/2n$ the maximum enhancement factor is less than 1.5.

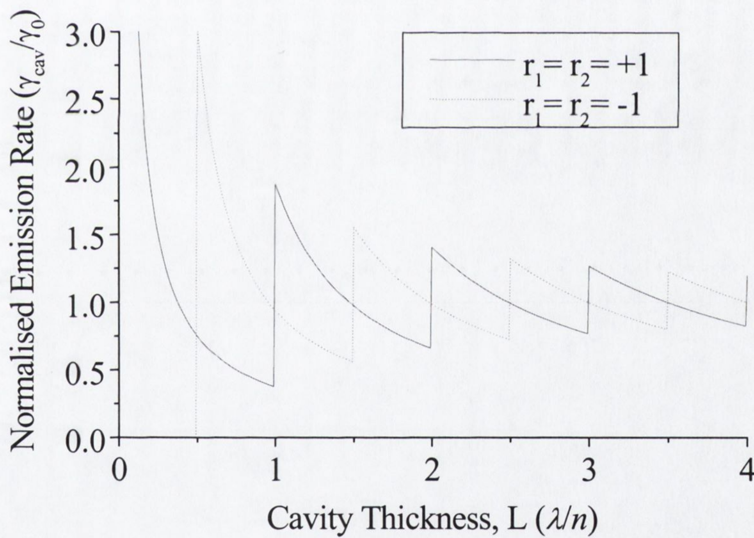

Figure 2.11 *γ_{cav}/γ_0 for a horizontal dipole placed in the centre of a planar microcavity with ideal mirrors ($r_1 = r_2 = \pm 1$) as a function of the cavity thickness L.*

The most successful realisations of very thin ($L<\lambda/2n$) planar microcavity structures, as required to observe enhanced emission rates, have consisted of Eu^{3+}or Er^{3+} doped emitting layers embedded between two metal mirrors. Such structures have demonstrated enhancement factors of ≈2.3 [19]. However the significant absorption in metals makes it

difficult to extract light efficiently through a metal mirror, while the fabrication of metal-clad microcavities is extremely difficult especially for semiconductor active layers. Therefore at least one mirror in most practical semiconductor microcavities is a distributed Bragg reflector (DBR), the properties of which are described below. These properties prevent the realisation of very low order cavities, and hence the maximum predicted enhancement of the emission rate for a planar microcavity structure defined by two DBR mirrors in the GaAs/AlAs material system is <1.3 [18].

In order to obtain greater modifications of the spontaneous emission rate in solid state microcavities, the increased modification of $\rho(\omega)$ produced by two and three dimensional photon confinement, as illustrated in Figure 2.12, is required. In the case of a three dimensional microcavity, the enhancement factor of the spontaneous emission rate, derived from Fermi's Golden Rule (see Appendix A1), is given by the Purcell factor F_p [10] as

$$F_p = \frac{\gamma_{cav}}{\gamma_0} = \frac{3Q(\lambda_c / n)^3}{4\pi^2 V_{eff}} \tag{2.15}$$

where λ_c is the cavity mode wavelength, Q (= $\lambda_c/\Delta\lambda_c$, $\Delta\lambda_c$ = cavity mode linewidth) is the quality factor of the cavity, and V_{eff} is the effective cavity mode volume. A detailed discussion these cavity parameters and the applicability of (2.15) is contained in section 4.7.2.

Impressive enhancement of the spontaneous emission rate from indium arsenide (InAs) quantum dots embedded in three dimensional microcavity structures have been observed,

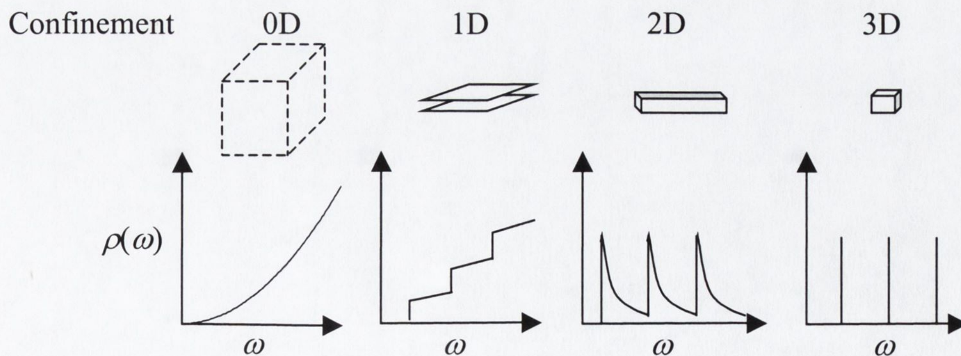

Figure 2.12 *Schematic representation of the photonic density of states of optically confined systems of different dimensionality, adapted from [15]*

in agreement with (2.15). Reductions in the emission lifetime of quantum dots in micropillars and microdisks by factors of up to 5 and 12 respectively have been measured [16,20].

2.5 Mirrors

There are several different types of mirror structures that can be used to confine light in cavities. Some of these reflector types are shown in Figure 2.13, including metallic reflectors, distributed Bragg reflectors, and reflectors based on total internal reflection. Hybrid metal-DBR reflectors are also commonly used [21].

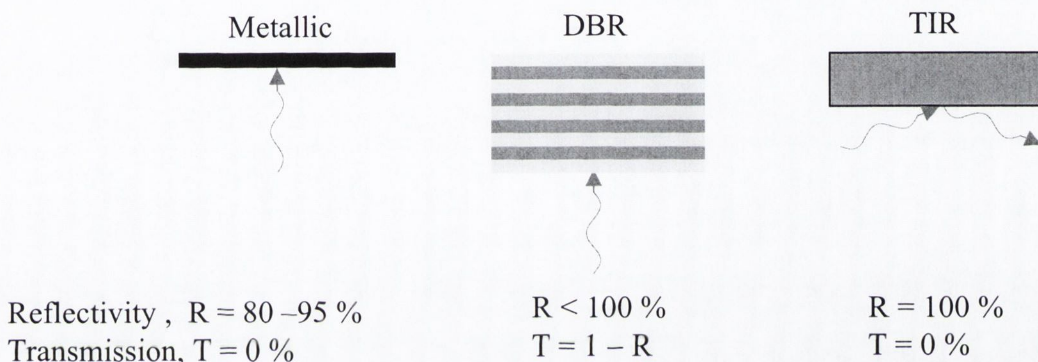

Figure 2.13 *Illustration of different types of reflectors.*

Metallic mirrors offer high reflectivity (>90%) over a very wide spectral range from the visible to the infra-red. However the absorption in metals results in near zero transmission for metallic mirrors, unless the thickness of the metal layer is very thin [22]. For this reason light cannot be coupled out of a cavity through a standard metal mirror.

DBR mirrors consist of alternate low index (n_{lo}) and high index (n_{hi}) layers. High reflectivity is achieved through the constructive interference between reflections from successive dielectric interfaces. Since the amplitude of the Fresnel reflection at each interface is dependent on the refractive index difference $\Delta n = n_{hi} - n_{lo}$, as well as the angle of incidence, the number of DBR pairs required to produce high reflectivities can be large. Each layer should have an optical thickness of a quarter wavelength in order to satisfy the condition for constructive interference as shown in Figure 2.14(a). Clearly this condition can only be satisfied for one wavelength denoted λ_b, however the calculated

reflectivity spectrum at normal incidence for a 25 period DBR with alternate layers of refractive index n_{hi} (n_{lo}) and thickness $L_{hi}=\lambda_b/4n_{hi}$ ($L_{lo}=\lambda_b/4n_{lo}$) shown in Figure 2.14(b) displays high reflectivity for a range of wavelengths centred on λ_b. This high reflectivity band denoted $\Delta\lambda_{DBR}$ is known as the stopband and is given by

$$\Delta\lambda_{DBR} = \frac{2\lambda_b \Delta n}{\pi n_{eff}} \tag{2.16}$$

where n_{eff} is the effective index of the mirror. For small refractive index differences n_{eff} can be replaced with the average of n_{hi} and n_{lo}. The width of the DBR stopband is independent of the number of DBR pairs, but a flat stopband is only achieved for a sufficiently large number of periods.

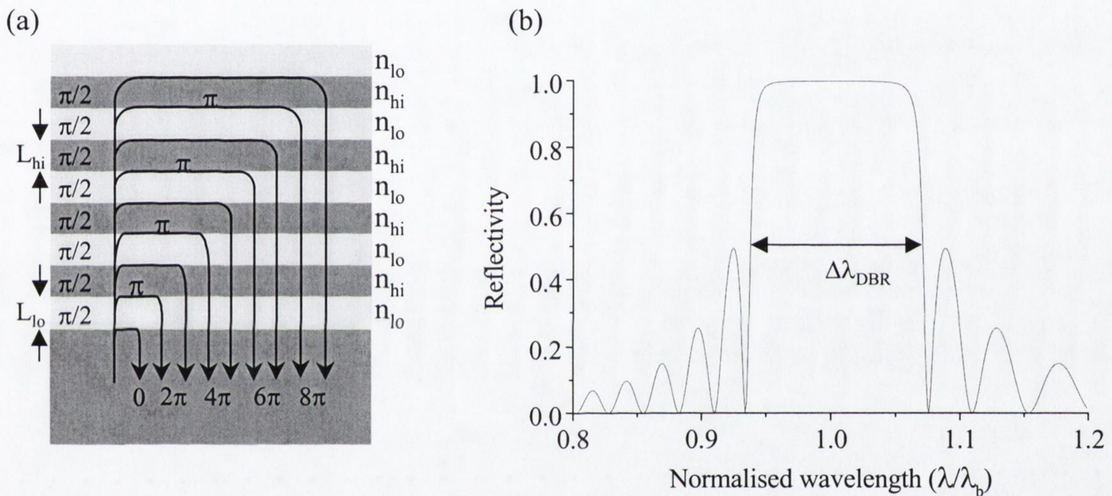

Figure 2.14 *(a) Schematic diagram of DBR showing phase differences between reflections from each interface in the structure. (b) Calculated reflectivity spectrum at normal incidence ($\theta=0$) of 25 period DBR with $n_{hi}=3.6$ and $n_{lo}=3.0$, showing the DBR spectral stopband $\Delta\lambda_{DBR}$.*

A DBR also only displays high reflectivity over a limited range of angles, known as the angular stopband denoted $\Delta\theta_{DBR}$, and approximately given by [23]

$$\Delta\theta_{DBR} = \pm 2\sqrt{\frac{\Delta n}{\pi n_{eff}}} \tag{2.17}$$

The calculated angular dependent reflectivity at $\lambda=\lambda_b$ of a 25 period DBR structure with $n_{hi}=3.6$ and $n_{lo}=3.0$, surrounded by a medium with $n=3.6$ is shown in Figure 2.15. At off

axis angles the reflectivities of transverse electric TE, and transverse magnetic TM, polarisations are different. For these refractive index values, which are similar to those of a GaAs/AlAs DBR, the high reflectivity stopband only extends as far as $\theta \approx \pm 20$ degrees for both polarisations. The increase in solid angle with θ, means that only a small fraction around the normal (θ=0) of all possible incidence angles are strongly reflected by the DBR.

While reflections in an ideal mirror take place at a well-defined plane, reflections in a DBR mirror are distributed over a number of interfaces, resulting in a penetration of the incident radiation into the mirror structure. This penetration of the incident field can be modelled by an ideal mirror positioned at a distance known as the penetration distance inside the DBR [17]. Both the limited angular reflectivity stopband and the penetration of the field have implications for the design of microcavities using DBRs.

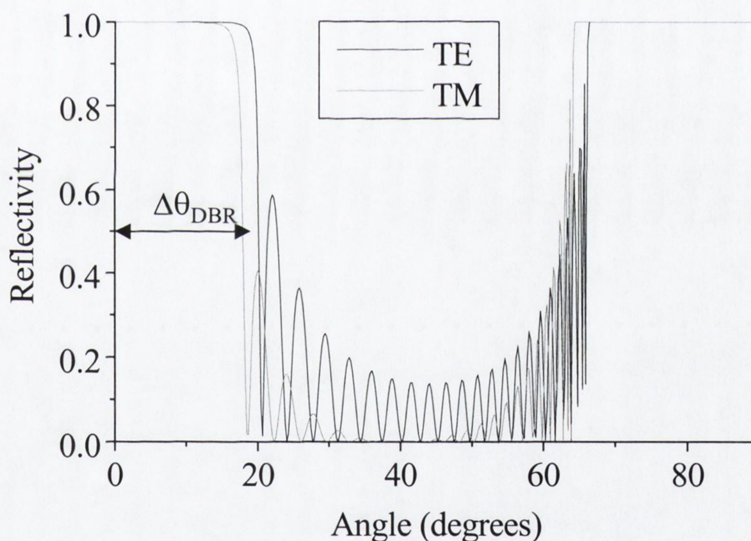

Figure 2.15 *Calculated reflectivity ($\lambda=\lambda_b$) as a function of incident angle (n of incident medium =3.6) for a 25 period DBR with n_{hi}=3.6 and n_{lo}=3.0. Both TE and TM polarisations are shown.*

Mirrors based on total internal reflection provide 100% reflectivity at a single interface between media of different refractive indices for angles of incidence greater than the critical angle. For a critical angle to exist the light must be incident from the high index

side of the interface, with the critical angle value determined by the ratio of refractive indices across the interface. At angles less than the critical angle, the reflectivity is just the Fresnel reflection for a single interface.

2.6 Microcavity Structures

2.6.1 One-dimensional microcavities

Three main classes of planar microcavity structures can be identified on the basis of their mirrors, (i) metal clad microcavities with two metal mirrors (ii) asymmetric metal-DBR microcavities with one metal and one DBR mirror and (iii) symmetric DBR microcavities, with two DBR mirrors.

The difficulties in extracting light from metal clad microcavities due to absorption in the mirrors, limits the efficiency of such structures, while the difficulty and cost of fabricating semiconductor microcavities bounded by two metal mirrors using current technology limits their potential as commercial devices. However the properties of metal mirrors allow the strong modification of the optical environment inside metal clad microcavities as required to produce modified emission rates, as previously discussed.

Asymmetric metal-DBR microcavities do not suffer from the same difficulties with light extraction and fabrication as metal clad cavities. Light can be extracted through a non-absorbing DBR, whose reflectivity can be adjusted by varying the number of DBR pairs. The fabrication of a bottom DBR and central cavity region can be achieved with existing semiconductor epitaxial growth techniques, allowing the subsequent deposition of the top metal mirror. However the limited angular reflectivity stopband of the DBR as discussed above results in the transmission of light through the DBR at angles greater than $\Delta\lambda_{DBR}$ and less than the critical angle for the interface between successive DBR layers (between $\theta \approx 20°$ and $\theta \approx 65°$ in Figure 2.15). The unconfined modes that exist at these angles are known as leaky modes. The penetration of the optical field into the DBR structure increases the effective cavity length, and prevents the realisation of very low order cavities (short cavity lengths). The lower limit on the cavity order achievable, and the inability to control emission into leaky modes limit the ability of asymmetric cavities to

modify the optical environment experienced by an emitter in the cavity. Despite these limitations, extraction efficiencies as high as 20% have been achieved from such structures [24], however only slight modifications (factors of <1.3) of the spontaneous emission rate have been reported [25].

Symmetric DBR cavities suffer from the presence of leaky modes, and the penetration of cavity modes into the mirrors, on both sides of the cavity, further reducing their ability to modify the spontaneous emission from an internal source. However as we will see in Chapter 3, this type of structure has to be employed in certain situations were light cannot be extracted through the substrate, and still offers improved extraction efficiency over non-cavity structures.

2.6.2 Higher dimensional microcavities

Many approaches to obtaining three dimensional photon confinement in solid state microcavity structures have been investigated since 1990, including pillar microresonators, photonic disks and wires, and photonic bandgap microcavities. All these structures display a discrete set of resonant modes and possess the potential to produce modified spontaneous emission rates.

Considerable research has been performed on micropillars structures since the fabrication of the first vertical cavity surface emitter lasers [26,27]. A schematic diagram of a micropillar is shown in Figure 2.16(a), the three dimensional optical confinement is achieved through a combination of the waveguiding along the pillar (due to the high refractive index contrast at the semiconductor/air interface) and of vertical confinement

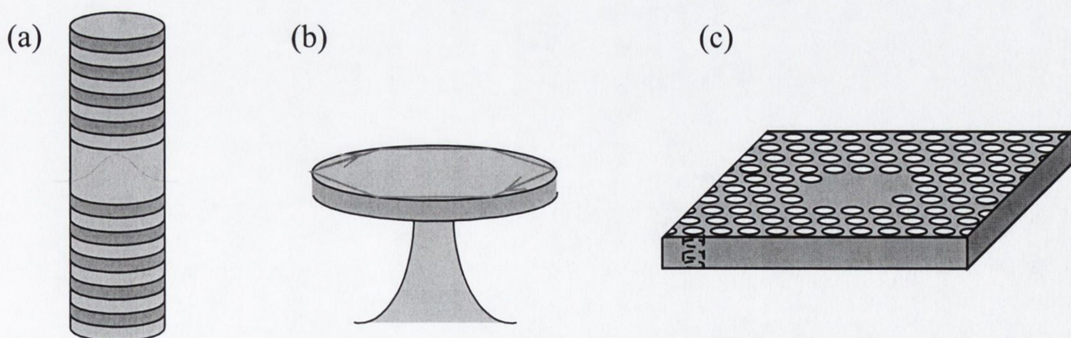

Figure 2.16 *Schematic diagrams of 3 types of higher dimensional microcavities offering photon confinement in all three dimensions (a) micropillar (b) microdisk and (c) Photonic bandgap defined cavity.*

by the DBRs. The potential of such structures for controlling spontaneous emission was first highlighted as early as 1991 [28].

The microdisk structure, as shown in Figure 2.16(b), was first investigated by S. L. McCall et al in 1992 [29]. Semiconductor microdisk structures consist of a thin disk supported by a pedestal at the centre, and are usually fabricated through a combination of reactive ion etching and selective wet chemical etching [30]. The microdisk structure supports a series of whispering gallery modes, which propagate around the edge of the disk confined by total internal reflection. These modes occupy a small fraction of the disk volume around the lateral edge, while the thin semiconductor disk acts as a slab waveguide in the vertical direction. This combination of confinement allows the realisation of effective mode volumes for whispering gallery modes as small as $6(\lambda_c/n)^3$. This small mode volume combined with the high Q values of whispering gallery modes (Q>10000, for 1.8μm diameter microdisk [30]) has resulted in the observation of strongly modified spontaneous emission lifetimes in microdisk structures [20].

Figure 2.16(c) shows a third possible cavity design, using a photonic crystal structure to confine light in the two lateral dimensions and a waveguide to provide vertical confinement, thereby producing a full three dimensional cavity. The two-dimensional periodic refractive index variation produced by the array of etched air cylinders in the semiconductor (known as a photonic crystal) can be designed to prohibit the propagation of photons of a certain energy range [31,32]. The cavity is created by leaving a certain number of the cylinders at the centre of the array unetched. Hexagonal shaped cavities defined by two dimensional photonic bandgap boundaries have been realised with mode volumes as small as $\approx 20(\lambda_c/n)^3$ and with Q's as large as ≈1000 [33]. Three dimensional photonic crystals (require a three dimensional periodic variation of the refractive index) represent the ultimate approach to obtaining small cavities, with mode volumes as small as $0.3(\lambda_c/n)^3$ predicted due to the small penetration of the cavity mode into the photonic crystal [30].

2.7 Photon recycling

One mechanism for improving the efficiency of all LEDs is known as photon recycling. This term refers to the reabsorption of light emitted by the active layer resulting in the generation of a new electron-hole pair, which subsequently recombine to produce a secondary photon. Any photons that are initially emitted from the active layer of an LED at angles less than the critical (escape) angle will only spend a short time inside the device before being emitted from the structure and therefore are unlikely to be reabsorbed. However light emitted at angles greater than the critical angle for escape from the device will propagate laterally inside, with a certain fraction being reabsorbed by the active layer. The secondary photon resulting from this reabsorption process has the same probability of being emitted at angles inside the escape cone as any other photon emitted by the active layer; therefore photon recycling provides a mechanism for converting photons initially emitted at angles outside the escape cone into extracted photons.

This process has been exploited to produce a very high external quantum efficiency of 72% from an optically pumped structure [34], however an estimated 25 recycling events were required to produce this efficiency. Such a high number of recycling events requires an extremely high internal quantum efficiency (estimated at 99.7% for the above structure), and a large lateral structure size (>300μm diameter for the above structure).

The increase in the extraction efficiency accrued from each recycling event is dependent on the probability of the secondary photon escaping the device, which we have seen is increased in microcavity structures. Therefore less recycling events, and hence lower internal quantum efficiencies and device sizes are required in planar microcavity LED structures compared to conventional LED structures in order to benefit from photon recycling processes [35]. However measurements on planar MCLED structures of different diameters show that device diameters >100μm are still required in order to fully exploit the benefits of photon recycling [36]. Such large device diameters, which are incompatible with certain fibre coupling applications (butt coupling to silica fibre), can be avoided while still maintaining strong recycling effects by using side mirrors to confine light propagating laterally inside the device to a central region. The size of the central region is determined by the limits on device size and need not approach the wavelength

scale dimensions required for modification of the spontaneous emission process in three-dimensional microcavities.

Photon recycling slows the light emission process from the structure due to the recreation of carriers subsequent to the initial recombination. The response time of the structure is increased by a factor of $1/(1-A_{pr})$, where A_{pr} is the fraction of emitted protons that are reabsorbed [37].

2.8 References

1 "Physics of Light Extraction Efficiency in Planar Microcavity Light-Emitting Diodes", H. Benisty, in *Confined Photon Systems, Fundamentals and Applications*, H. Benisty, J.-M. Gérard, R. Houdré, J. Rarity, and C. Weisbuch (Eds.) (Springer, Verlag, 1999)

2 *Semiconductor Optoelectronics, Physics and Technology*, J. Singh (McGraw-Hill Inc.,Singapore, 1995)

3 *Optical Fiber Communications, Principles and Practice 2nd edition,* J. M. Senior (Prentice Hall, New York, 1992)

4 *Optoelectronics an introduction, 3rd edition*, J Wilson and J. Hawkes (Prentice Hall, London 1998)

5 "Commercial light emitting diode technology: status, trends, and possible future performance", M. G. Craford, in *Microcavities and Photonic Bandgaps: Physics and Applications*, J. Rarity and C. Weisbuch (Eds.) (NATO ASI Series, Kluwer Academic Publishers, Dordrecht, 1996)

6 "High-Power truncated-inverted-pyramid $(Al_xGa_{1-x})_{0.5}In_{0.5}P/GaP$ light-emitting diodes exhibiting >50% external quantum efficiency", M. R. Krames, M. Ochiai-Holcomb, G. E. Hofler, C. Carter-Coman, E. I. Chen, I. H. Tan, P. Grillot, N. F. Gardner, H. C. Chui, J. W. Huang, S. A. Stockman, F. A. Kish, M. G. Craford, T. S. Tan, C. P. Kocot, M. Hueschen, J. Posselt, B. Loh, G. Sasser and D. Collins et. al., Appl. Phys. Lett. **75** (16) p. 2365 (1999).

7 "GHz bandwidth GaAs light-emitting diodes", C. H. Chen, M. Hargis, J. M. Woodall, M. R. Melloch, J. S. Reynolds, E. Yablonovitch, and W. Wang, Appl. Phys. Lett. 74 (21) p. 3140 (1999)

8 "Light Emitting Diodes", M. H. Pilkuhn and W. Schairer in *Handbook on Semiconductors (Volume 4)*, T. S. Moss (Editor), (Elsevier SciencePublishers, 1993)

9 "Large-signal-modulation of high-efficiency light-emitting diodes for optical communication", R. Windisch, A. Knobloch, M. Kuijk, C. Rooman, B. Dutta, P. Kiesel, G. Borghs, G. H. Dohler, and P. Heremans, IEEE J. of Quant. Electron. **36** (12) p. 1445 (2000)

10 "Spontaneous emission probabilities at radio frequencies", E. M. Purcell, Phys. Rev. **69** p.681 (1946)

11 "Inhibited Spontaneous Emission", D. Kleppner, Phys. Rev. Lett. **47** (4) p. 233 (1981)

12 "Cavity Quantum Electrodynamics", S. Haroche and D. Kleppner, Phys. Today **42** p.24 (1989)

13 *Microcavities and Photonic Bandgaps: Physics and Applications*, J. Rarity and C. Weisbuch (Eds.), (NATO ASI Series, Kluwer Academic Publishers, Dordrecht, 1996)

14 *Confined Photon Systems, Fundamentals and Applications*, H. Benisty, J.-M. Gérard, R. Houdré, J. Rarity, and C. Weisbuch (Eds.) (Springer, Verlag, 1999)

15 "Microcavities and Semiconductors: The Strong-Coupling Regime", C. Weisbuch, R. Houdré, and R. Stanley, in *Spontaneous emission and Laser Oscillation in Microcavities*, H. Yokoyama and K. Ujihara (Eds.) (CRC Press, Boca Raton, 1995)

16 "Enhanced Spontaneous Emission by Quantum Boxes in a Monolithic Optical Microcavity", J. M. Gérard, B. Sermage, B. Gayral, B. Legrand, E. Costard, and V. Thierry-Mieg, Phys. Rev. Lett. **81** (5) p.1110 (1998)

17 "Impact of planar microcavity effects on light extraction - Part I: Basic concepts and analytical trends", H. Benisty, H. De Neve, C. Weisbuch, IEEE J Quant. Elect. **34** (9) p. 1612 (1998)

18 "Spontaneous Emission Control in Semiconductor Microcavities with Metallic or Bragg Mirrors", I. Abram, I. Robert, and R. Kuszelewicz, IEEE J. of Quant. Electron. **34** (1) p. 71 (1998)

19 "Rate and efficiency of spontaneous emission in metal-clad microcavities", P. T. Worthing, J. A. E. Wasey, and W. L. Barnes, J. of Appl. Phys. **89** (1) p.615 (2001)

20 "Time resolved probing of the Purcell effect for InAs quantum boxes in GaAs microdisks", B. Gayral, J. M. Gérard, B. Sermage, A. Lemaitre, and C. Dupuis, Appl. Phys. Lett. **78** (19) p. 2828 (2001)

21 *Vertical-Cavity Surface-Emitting Lasers - Design, Fabrication, Characterisation, and Applications*, C. W. Wilmsen, H. Temkin, and L. A. Coldren (Eds.) (Cambridge University Press, Cambridge, 1999)

22 "Vertical cavity surface emitting lasers with semitransparent metallic mirrors and high quantum efficiencies", L. W. Tu, E. F. Schubert, R. F. Kopf, G. J. Zydzik, M. Hong, S. N. G. Chu, J. P. Mannaerts, Appl. Phys. Lett. **57** (20) p. 2045 (1990)

23 "Spontaneous Emission in Dielectric Planar Microcavities", G. Bjork and Y. Yamamoto, in *Spontaneous emission and Laser Oscillation in Microcavities*, H. Yokoyama and K. Ujihara (Eds.) (CRC Press, Boca Raton, 1995)

24 "Recycling of guided mode light emission in planar microcavity light emitting diodes", H. De Neve, J. Blondelle, P. Van Daele, P. Demeester, R. Baets, and G. Borghs, Appl. Phys. Lett. **70** (7) p. 799 (1997)

25 "Controlled spontaneous emission lifetime in microcavity confined InGaAlAs/GaAs quantum dots", L. A. Graham, D. L. Duffaker, Q. Deng and D. G. Deppe, Appl. Phys. Lett. **72** (14) p. 1670 (1998)

26 "Surface Emitting Semiconductor Lasers", K. Iga, F. Koyama, and S. Kinoshita, IEEE J. of Quant. Electron. **24** (9) p. 1845 (1988)

27 "Transverse modes, waveguide dispersion, and 30 ps recovery in submicron GaAs/AlAs microresonators", J. L. Jewell, S. L. McCall, A. Scherer, H. H. Houh, N. A. Whitaker, A. C. Gossard, J. H. English, Appl. Phys. Lett. **55** (1) p. 22 (1989)

28 "Spontaneous Emission Factor of a Microcavity DBR Surface-Emitting Laser", T. BaBa, T. Hamamo, F. Koyama, and K. Iga, IEEE J. of Quant. Electron. **27**, p.1347 (1991)

29 "Whispering-gallery mode microdisk lasers", S. L. McCall, A. F. J. Levi, R. E. Slusher, S. J. Pearton, and R. A. Logan, Appl. Phys. Lett. **60** (3) p. 289 (1992)

30 "Semiconductor Microcavities, Quantum Boxes and the Purcell Effect", J. M. Gérard and B. Gayral in *Confined Photon Systems, Fundamentals and Applications*, H. Benisty, J. M. Gérard, R. Houdré, J. Rarity, and C. Weisbuch (Eds.) (Springer, Verlag, 1999)

31 *Photonic Crystals: Molding the Flow of Light,* J. D. Joannopoulos, R. D. Meade, and J. N. Winn (Princeton University Press, Princeton NJ, 1995)

32 "Optical and Confinement Properties of Two-Dimensional Photonic Crystals", H. Benisty, C. Weisbuch, D. Labilloy, M. Rattier, C. J. M. Smith, T. F. Krauss, R. De La Rue, R. Houdré, U. Oesterle, C. Jouanin, and D. Cassagne, J. of Lightwave Technol. **17** (11) p.2063 (1999)

33 "Near-infrared microcavities confined by two-dimensional photonic bandgap crystals", C. J. M. Smith, H. Benisty, D. Labilloy, U. Oesterle, R. Houdré, T. F. Krauss, R. M. De La Rue, and C. Weisbuch, Electron. Lett. **35** (3) p.228 (1998)

34 "Ultrahigh spontaneous emission quantum efficiency, 99.7% internally and 72% externally, from AlGaAs/GaAs/AlGaAs double heterostructures", I. Schnitzer, E. Yablonovitch, C. Caneau, and T. J. Gmitter, Appl. Phys. Lett. **62** (2) p. 131 (1992)

35 "Impact of planar microcavity effects on light extraction - Part II: Selected Exact Simulations and Role of Photon Recycling", H. Benisty, H. De Neve, C. Weisbuch, IEEE J Quant. Elect. **34** (9) p. 1632 (1998)

36 "High Efficiency Planar Microcavity LEDs", H. De Neve, J. Blondelle, P. Demeester, P. Van Daele, R. Baets and G. Borghs, Proc. of 23rd International Conference on the Physics of Semiconductors vol. **4** p.3079 (World Scientific, Singapore,1996)

37 "Dynamics of microcavity light emitters", B. J. Roycroft, T. P. Aherne, J. Hegarty, I. Moerman, P. Van Daele, and R. Baets, SPIE Proc. Vol. **3611** p. 182 (1999)

Chapter 3

Red Planar Microcavity LEDs

3.1 Introduction

Fred Schubert and co-workers at AT&T Bell Laboratories first applied the microcavity concept to light emitting diodes in 1992 [1]; by placing the active region in a short cavity they demonstrated a narrow linewidth, high brightness LED emitting at 860nm. MCLEDs emitting at 660nm [2,3], 940nm [4], 1.3μm [5], and 3.2μm [6] were subsequently demonstrated by different research groups. All these results focused on the ability of microcavities to produce narrower emission linewidths and less divergent farfield emission patterns compared to conventional LEDs. However no attempt was made to optimise the cavity design for maximum extraction efficiency, a fundamental limitation of LED technology, and consequently the spectrally integrated emitted power from these MCLEDs was low. The potential of MCLEDs to produce high extraction efficiencies through a single surface was first realised Blondelle et al. [7]. The development of a comprehensive model allowing the calculation of the dipole emission into the various modes of an arbitrary planar structure [8] enabled a systematic study of the impact of cavity-source detuning, mirror reflectivities, and source linewidth on the extraction efficiency and farfield of MCLEDs [9]. A MCLED emitting at 980nm, designed for maximum extraction efficiency, produced a record efficiency at that time of 20% for single-side emission into air [10]. By the end of the SMILES project in 1997, a thorough investigation into the MCLED concept had been carried out on the InGaAs/GaAs material system, and a basic set of design rules for MCLED structures had been established [11,9]. However no enhancement of LED extraction efficiency or brightness* had been demonstrated using the microcavity concept at wavelengths other than 980nm.

* Brightness is defined as the optical power per unit emitting area per unit solid angle

Investigations into MCLEDs emitting at 980nm had shown that the advantage of MCLEDs over commercial LEDs was not in overall efficiency, where the high extraction efficiency of MCLEDs is surpassed by commercial LEDs utilising cup reflectors to collect light from all sides of a sawn chip, but in brightness. The MCLEDs use of light emitted through only one facet results in a considerably reduced emitting area relative to the large spatial extent of a cup reflector. This small emitting area combined with the ability to tailor the farfield emission pattern offered the potential of high coupling efficiencies from MCLEDs into optical fibres. One of the main goals of the SMILED collaboration was to transfer the MCLED technology to wavelengths compatible with fibre coupling applications; specifically the transmission windows at 640-660nm for plastic optical fibre (POF) and 1300nm for silica fibre.

The results of the first red (660nm) MCLEDs fabricated in the SMILED collaboration are presented in the first half of this chapter. Prior to this work the maximum reported output power for a MCLED emitting at 660nm was 20μw at 20mA [2], which corresponded to an external quantum efficiency of $<0.1\%$. The goal of this work was to investigate the difficulties faced in transferring the MCLED technology and simulation tools developed at 980nm to MCLEDs emitting at ≈650nm, and to determine the potential performance of optimised MCLEDs emitting at ≈650nm. Important design considerations for MCLEDs targeting POF applications are discussed in section 3.2, and the results of characterisation tests on the fabricated MCLED are presented in section 3.4. These results are compared with simulations of the grown structure, and the expected performance of a structure designed for maximum efficiency in section 3.5. While all the results presented relate to MCLEDs emitting at ≈650nm, many of the issues discussed relating to the performance, design, and modelling of these devices are generic to planar MCLEDs.

To demonstrate the need for higher dimensional microcavities, which are the focus of the research presented in the subsequent chapters in this thesis, the ultimate limitation of planar MCLEDs in terms of extraction efficiency is modelled and discussed in the final section of the chapter.

3.2 Design considerations for a MCLED source for POF applications.

The use of POF for local area networks is a powerful, low cost alternative to twisted-pair cables or silica fibres [12]. POF's large core diameters, rugged nature, and ability to be simply aligned and terminated results in low connectorisation costs [13]. Commercial POFs are based on polymethyl methacrylate (PMMA) and exhibit an attenuation minimum of ≈0.1dB/m in the 640-660nm wavelength range (see Figure 3.1). The realisation of low-cost emitters that operate in this transmission window and that are capable of sufficiently high transmission rates is essential to the implementation of POF based transmission systems. MCLEDs offer the potential for higher efficiency, narrower emission linewidths and enhanced directionality over conventional LEDs, and lower fabrication costs, less temperature sensitive performance, and threshold-less power-current characteristics compared to edge emitting lasers. Therefore, in the absence of a reliable and temperature insensitive vertical cavity surface emitting laser (VCSEL) emitting at these wavelengths, MCLEDs possess the potential to dominate the market for POF network sources. However the direct implementation of the MCLED design successful at 980nm, which consisted of an asymmetric cavity with a metal top mirror and a DBR bottom mirror with the light extracted through the substrate, is not possible at 650nm for structures grown on GaAs

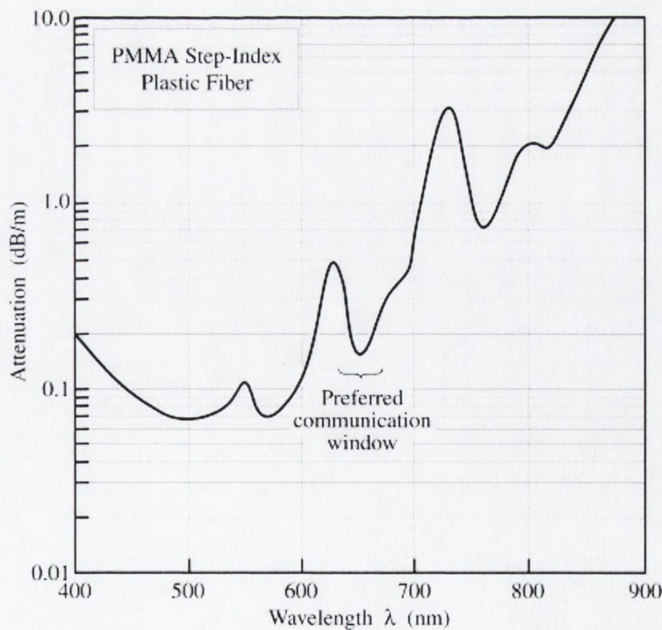

Figure 3.1 *Attenuation of PMMA POF. At 650nm, the preferred communication wavelength, the attenuation is ≈0.15dB/km (after data sheet of Toray Industries Ltd.).*

substrates due to the absorption in GaAs. Therefore the light has to be extracted through the top mirror requiring a non-absorbing top mirror of lower reflectivity than the bottom mirror. This is achieved by using DBRs as both top and bottom mirrors in the cavity, with the bottom DBR mirror containing more periods. The need to avoid absorption of emitted light in the DBRs limits the aluminium concentration in the $Al_xGa_{1-x}As$ DBR layers to x>0.5. The reduced refractive index contrast in $Al_{0.5}Ga_{0.5}As$/AlAs DBRs relative to GaAs/AlAs DBRs results in a reduced DBR stopband and increased penetration of the optical field into the mirrors. The reduced DBR angular stopband results in increased coupling of emission into leaky modes, while the increased penetration of the optical field results in an increased effective cavity length. Both these consequences of the need to eliminate absorption in the structure reduce the ability of the cavity to modify the optical environment with which the emitter interacts.

Quantum well active regions consisting of GaInP wells and AlGaInP barriers were employed to obtain emission in the 650-670nm wavelength range. The greater bandgap of AlGaInP compared to AlGaAs is necessary to access these shorter wavelengths, however

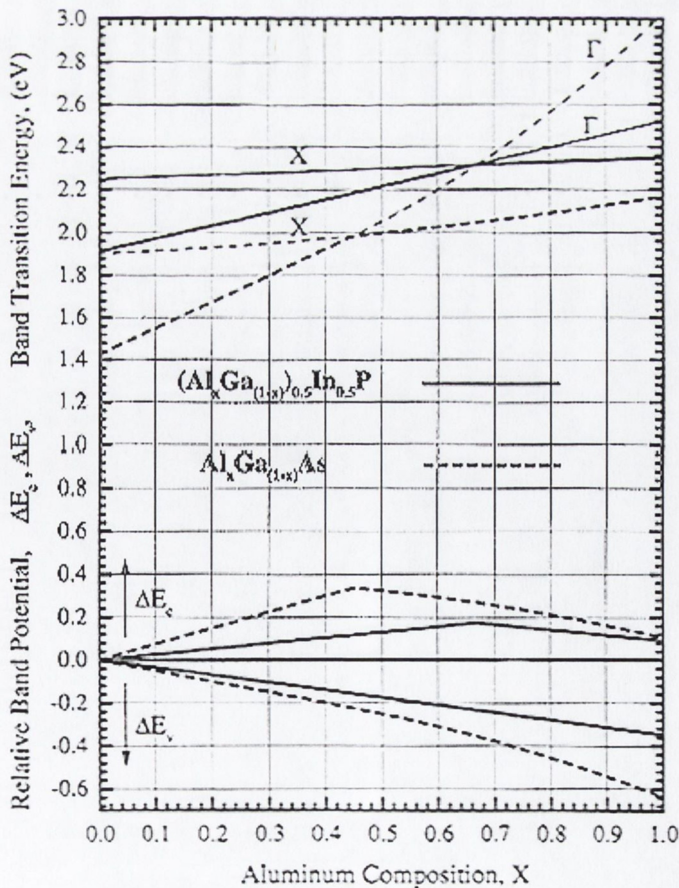

Figure 3.2 *Bandgaps and band offsets for the AlGaAs and AlGaInP (lattice matched to GaAs) material systems as a function of Al composition. ΔE_c and ΔE_v are the conduction and valence band offsets, respectively, and E_Γ and E_X are the gaps relative to the Γ direct and X indirect conduction band minima, respectively.(reproduced from ref [14])*

the conduction and valence band offsets in the AlGaInP material system are considerably reduced relative to the AlGaAs system (see Figure 3.2), resulting in reduced carrier confinement in GaInP/AlGaInP QWs [14].

When designing a MCLED for fibre coupling applications as well as matching the emission wavelength to the transmission window of the fibre, the coupling of the emitted light into the fibre has to be considered. Only light incident on the fibre core at angles less than the acceptance angle of the fibre is guided in the fibre. For a butt-coupling configuration (i.e. when the fibre core is position directly on top of the source without any intermediate lens) the emitting area should be less than the fibre core diameter and the power emitted at angles less than the acceptance angle of the fibre should be maximised. The large core of POFs (typically diameter >250μm) makes it easy to produce MCLEDs with smaller emitting areas. However the peak off axis emission of a MCLED designed for maximum extraction efficiency into air may not be optimised for butt-coupling applications, and a MCLED designed to produce a less divergent farfield pattern even at the expense of overall efficiency may result in greater launched power into the fibre when butt-coupling to POF.

These were the design issues that were being considered at the time of this research. The impact of the different DBR and active layer materials required for 660nm MCLEDs is explored in our measurements, while the issue of optimal device design is explored in our modelling.

3.3 MCLED device structure.

The MCLED devices investigated were grown by solid source molecular beam epitaxy in Tampere University of Technology. The structures were grown on (100) Si-doped GaAs wafers. A schematic diagram of the layer structure of the MCLED is shown in Figure 3.3. Three $Ga_{0.42}In_{0.58}P$(6nm)/$(Al_{0.3}Ga_{0.7})_{0.51}In_{0.49}P$(6nm) quantum wells were positioned in the centre of a 1λ-thick Fabry-Perot cavity. The Quantum well region was surrounded by $(Al_{0.3}Ga_{0.7})_{0.51}In_{0.49}P$ (40nm) spacer layers and $(Al_{0.7}Ga_{0.3})_{0.51}In_{0.49}P$ cladding layers, doped with Si on the *n*-side and Be on the *p*-side. The top p-doped DBR consisted of 8 pairs of alternating $Al_{0.5}Ga_{0.5}As$ and $Al_{0.9}Ga_{0.1}As$ (or $Al_{0.97}Ga_{0.03}As$ for bottom pair) λ/4 layers. The bottom DBR consisted of 32.5 pairs of alternating n-doped $Al_{0.5}Ga_{0.5}As$ and AlAs λ/4 layers, with 10nm $Al_{0.75}Ga_{0.25}As$ barrier reduction layers at each interface.

MCLEDs with ring top contacts and emitting windows of 10, 20, 40 and 80μm diameter were processed. Current apertures equalling the emitting areas were formed by lateral wet oxidation of the $Al_{0.97}Ga_{0.03}As$ bottom layer of the top DBR. An ohmic metal contact was deposited on the back surface. Full details of the growth and processing of these devices is contained in reference [15]. The processed wafer was diced into single devices which were bonded onto TO headers with conducting epoxy. The header was left uncapped in order to allow access to the device surface.

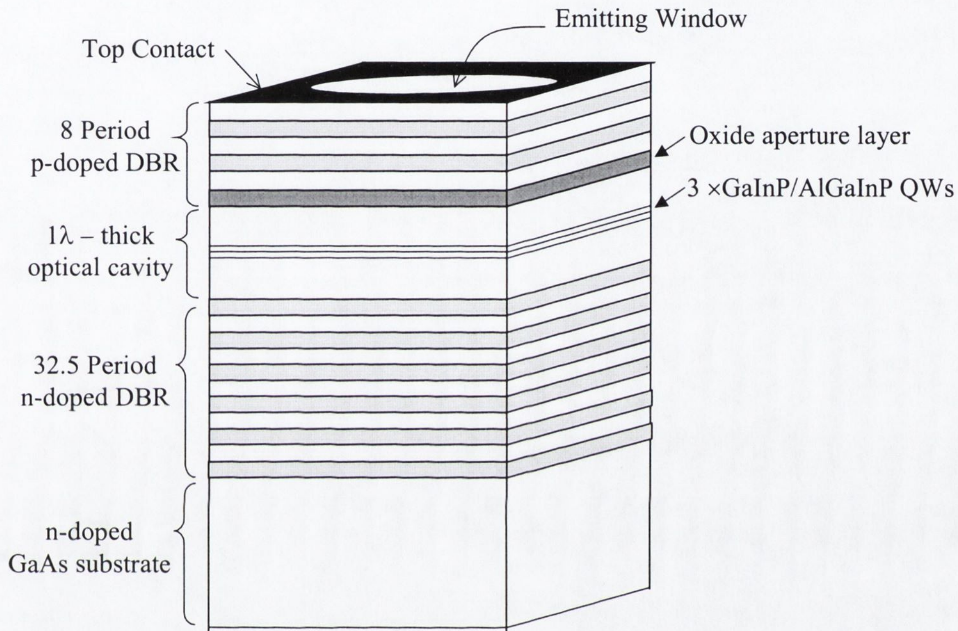

Figure 3.3 *Schematic diagram of MCLED structure.*

3.4 MCLED Characterisation

The emission characteristics of an 80μm diameter MCLED are presented in this section. The emission properties of 10, 20, and 40μm diameter MCLEDs were also measured, and similar behaviour was observed from all devices, allowing for the increased current densities in the smaller devices.

The device header was attached to a copper block whose temperature was set using Peltier devices. Electrical connections were made to the MCLED device via the pins of the header package. The ground pin of the header was in electrical contact with the bottom n-

metallisation of the MCLED, while a through pin, electrically isolated from the header surface, was connected to the top ring contact of the MCLED via a bond pad.

3.4.1 Current-Voltage Characteristics

The measured current-voltage (*I-V*) characteristics of the 80μm diameter MCLED for temperatures between 20°C and 70°C are shown in Figure 2.4. The device exhibits a turn-on voltage of approximately 1.7V, with only a small decrease in the turn-on voltage observed with increasing temperature. This value is slightly less than the expected turn-on voltage of ≈1.8V for emission at ≈660nm ($V_{turn-on} \approx hc/e\lambda$, h=Planck's constant, c=speed of light, e=electron charge, λ=emission wavelength), and may indicate the existence of a small leakage current. The diode equation, modified to account for series resistance, was fitted to the 10-30 mA region of the *I-V* curve to obtain an estimate of the MCLED series resistance. The lower current region of the curve was not fitted due to the possible influence of any carrier leakage around turn-on, which is not accounted for by a shunt resistance in our diode equation. A good fit to the high current region of the *I-V* curves

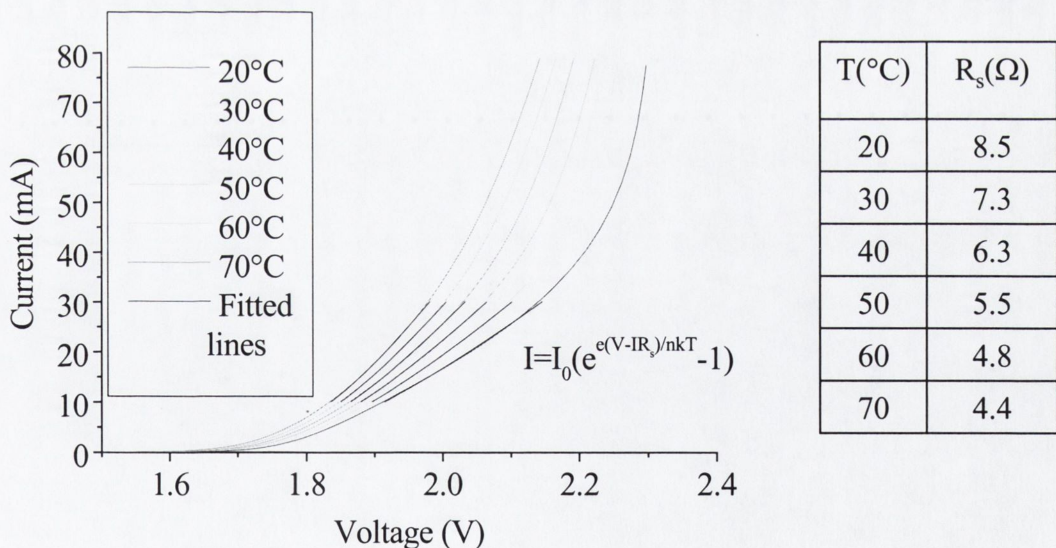

T(°C)	$R_s(\Omega)$
20	8.5
30	7.3
40	6.3
50	5.5
60	4.8
70	4.4

Figure 3.4 (a) *Measured current-voltage characteristics for the 80mm diameter MCLED as a function of temperature. (b) Table showing fitted values for series resistance R_s of MCLED.*

could not be obtained using (3.1), possibly due to increased carrier leakage from the QWs at higher carrier densities, an effect not accounted for by (3.1). The modified diode equation used was

$$I = I_0 \exp(e(V - IR_s) / nkT - 1) \tag{3.1}$$

where I_0 is a constant, e is the electron charge, R_s is the series resistance, n is the ideality factor, k is Boltzmann's constant, and T is the temperature.

The fitted values for the device series resistance decrease from 8.5Ω at 20°C to 4.4Ω at 70°C. The large series resistance of this device at room temperature would result in poor power conversion efficiency even if the device possessed high external quantum efficiency. The development of a commercial device would require a reduction in this series resistance. Optimised doping profiles and concentrations in the DBRs may yield such a reduction.

3.4.2 Power-Current & Quantum Efficiency Characteristics

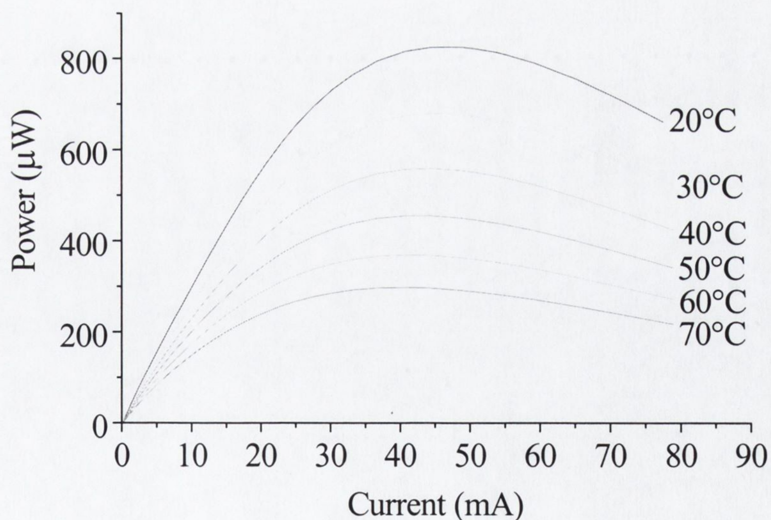

Figure 3.5 *Power-current characteristics of 80μm diameter MCLED device.*

The output power of the MCLED was measured using a calibrated power meter (Photodyne Model 550 (Silicon) Integrating Head). The device was positioned inside the integrating head of the detector to ensure collection of all the emitted light. The measured output power as a function of current in the 20°C to 70°C temperature range is shown in Figure 3.5. At low bias (<5mA) the device displays a linear dependence of output power on current at all temperatures. No threshold current for the turn-on of power is evident on this scale. Such threshold like turn-on has been observed by some workers and has been attributed to current leakage and/or saturation of non-radiative centres [16].

At all temperatures the output power saturates at currents between 40 and 50 mA (decreasing slightly with increasing temperature within this range) and decreases at higher currents. This phenomenon, termed radiance saturation, which produces a very non-linear power-current characteristic has implications when using the device as a modulated source, as well as limiting the maximum light power obtainable from the device. The maximum power from the 80μm diameter MCLED was 820μW at 20°C and 300μW at 70°C.

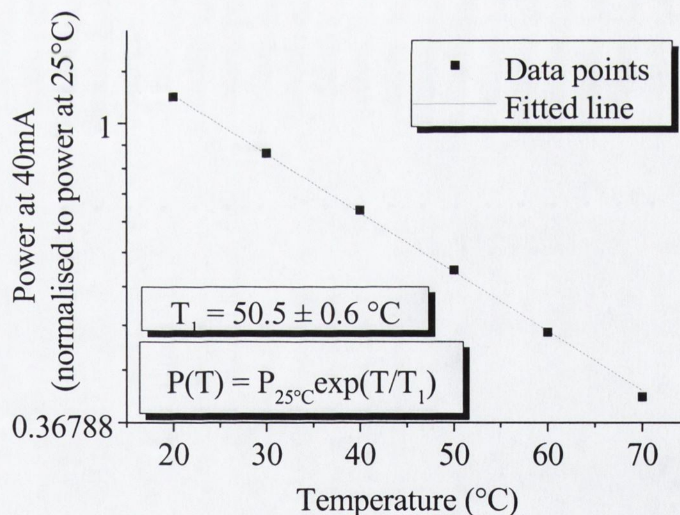

Figure 3.6 *Semilog plot of output power at 40mA as a function of temperature, normalised to the output power at 25°C.*

The standard equation describing the temperature dependence of an LED's output power takes the form [17]

$$P(T) = P_0 \exp(-T/T_1) \tag{3.2}$$

where P_0 is the output power at a reference temperature (25°C), and T_l is the characteristic temperature of the device. The T_l value of the LED should be as large as possible to ensure the least temperature dependent performance. A T_l value of 50.5 ± 0.6°C was obtained for the MCLED device from the fit of (3.2) to the temperature dependence of the output power at a current of 40mA. This T_l value would have to improve considerably to match the expected T_l values for commercial red LEDs of >100°C.

The external quantum efficiency η_{extern}, which represents the ratio of photons emitted from the device to electrons flowing through the device, was calculated for the MCLED in the 20°C to 70°C temperature range from the measured current-voltage and power-current characteristics using the expression

$$\eta_{extern} = \frac{P}{I}\frac{\lambda e}{hc} \tag{3.3}$$

where P is the total emitted optical power and I is the current (λ, e, h, and c have their usual meaning as defined in section 3.4.1). The maximum external quantum efficiency, varying from 1.7% at 20°C to 0.9% at 70°C, occurred at a bias current of 3mA at all temperatures. The external quantum efficiency decreased steadily with increasing current above 3mA, with external quantum efficiencies at the peak emission power bias current (≈ 40mA) of only 0.9% at 20°C and 0.4% at 70°C.

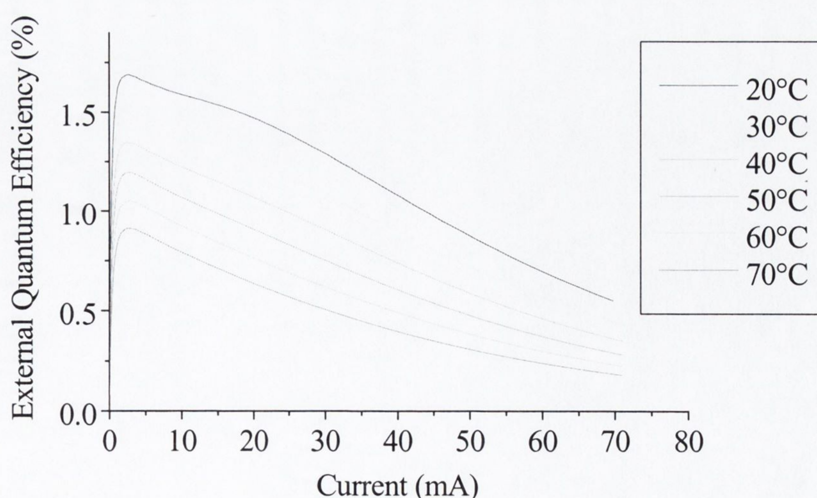

Figure 3.7 *The external quantum efficiency of the 80μm diameter MCLED device.*

3.4.3 Spectral Characteristics

The MCLED emission, collimated using a ×10, 0.25NA microscope objective, was coupled into a 62.5μm core fibre using a second ×10 microscope objective. The fibre output was connected to a HP 70951A Optical Spectrum Analyser (OSA), which was set to a spectral resolution of 0.5nm.

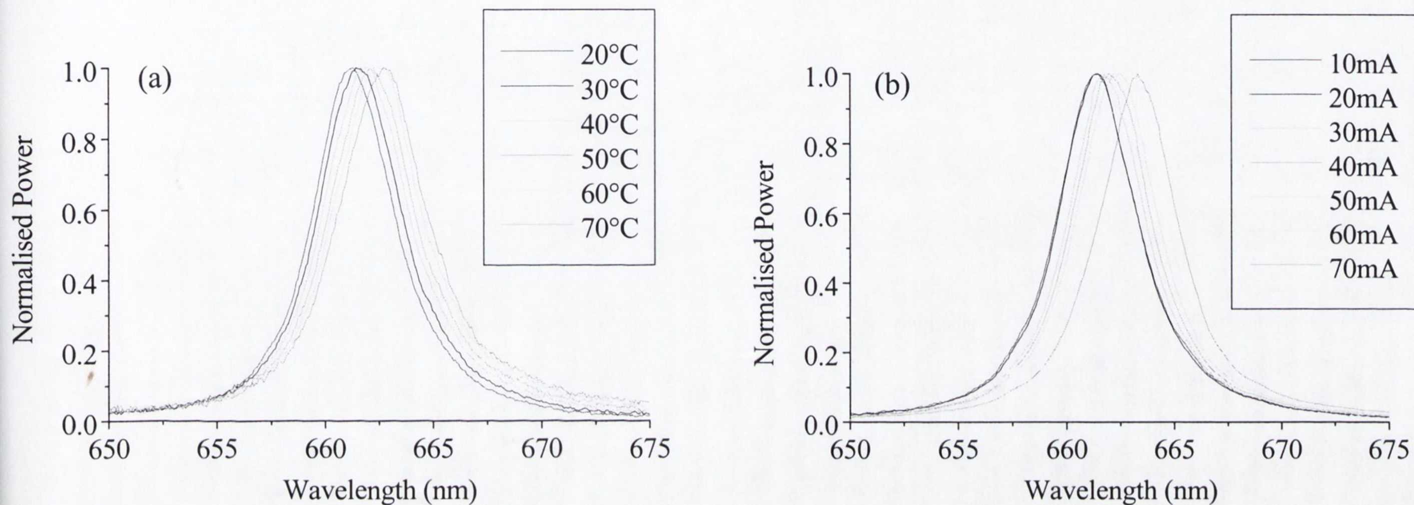

Figure 3.8 *Normalised emission spectra of 80μm diameter MCLED, (a) at a bias current of 5mA and ambient temperatures between 20°C and 70°C (b) at ambient room temperature (no temperature controlling) and bias currents between 10mA and 70mA.*

The spectra shown in Figure 3.8 are of the integrated MCLED emission at angles less than 15° from the normal to the device surface due to the limited collection angle of the microscope objective used to collimate the MCLED emission. Because of the angular dispersion in the microcavity emission (cavity mode shifts with angle see Figure 3.11), the spectral linewidth of the total MCLED emission is expected to be greater than the 5nm full width at half maximum (FWHM) of the spectra in Figure 3.8, and was estimated at 16nm at room temperature and medium bias current (20mA) from integration of the angular resolved spectra shown in Figure 3.13(a). The spectral linewidth for the integrated emission at angles less than 30° (corresponding to the typical acceptance angle of POF) was estimated as 9nm. In comparison the emission linewidth of standard AlGaInP LEDs emitting at these wavelengths is ≈17nm [2] and is independent of angular considerations.

Figure 3.8 shows that the peak emission wavelength of the MCLED is relatively insensitive to either temperature or bias current – exhibiting an approximately linear dependence on temperature of 0.03nm°C^{-1}, and shifting from 661.4nm at a bias current of 10mA to 663.3nm at 70mA. These shifts are considerably less than observed in conventional LEDs where the shift in peak emission wavelength is determined by the shift in the recombination energy in the material. The peak emission wavelength of the MCLED is determined by the wavelength of the cavity mode, which is determined by the refractive index and thickness of the cavity, properties that in comparison to the recombination energy are only weakly dependent on temperature and carrier density.

The narrow emission linewidths for restricted emission angles, and reduced sensitivity to operating temperature and current shown for the MCLED structure in Figure 3.8 confirm that the spectral characteristics of the MCLED's emission are determined by the optical properties of the cavity.

3.4.4 Nearfield Pattern

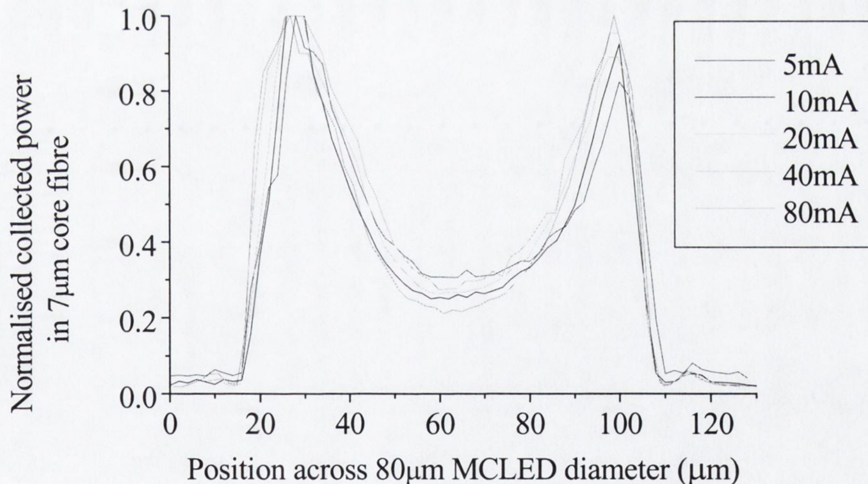

Figure 3.9 *Pseudo-nearfield measurement, showing power collected by 7μm core fibre positioned 10μm above the MCLED surface versus position of the fibre across the diameter of the device.*

A uniform carrier distribution in the active layer of the MCLED is essential to minimise carrier leakage and contact shadowing (blocking of emitted light by contact). The ring top contact employed in these 80μm diameter MCLED devices requires considerable lateral carrier spreading in order to achieve such a uniform distribution. The spatial distribution of carriers in the QWs of the device was investigated by measuring the nearfield emission pattern. The profile of emitted power across the surface of the device indicates the profile of carrier recombination in the underlying quantum well.

Since high resolution imaging of the nearfield was not required, a simple pseudo nearfield measurement technique was employed. A single mode fibre (7μm core) was scanned across the device surface at a height of 10μm, and the spectrally integrated power coupled to the fibre as a function of position was recorded. The advantage of this technique is that no dedicated imaging lenses or cameras are required.

The results in Figure 3.9 show the emitted power per unit area at the centre of the device was only 30% of the emitted power per unit area at the edge of the device. This indicates considerable current crowding around the edge of the device, which results in increased contact shadowing due the presence of the non-transparent top contact around the device edge, and in increased carrier leakage from the active layer due to the increased carrier density in the QWs at the edge of the device.

Possible approaches to improving the spatial uniformity of the carrier distribution in the active layer of the device include increasing the doping of the top DBR, incorporating a current spreading layer between the top DBR and top contact, and using an alternative top contact geometry to allow carrier injection across the device. However the top current spreading layer and alternative contact geometries result in reduced cavity effectiveness and increased contact shadowing respectively. Therefore the optimal device design requires a balance between light extraction and uniform carrier injection.

The use of a honeycomb mesh shaped top contact, allowing injection of carriers within ≈10μm of all points on the device surface, combined with a top current spreading layer of ≈10nm thickness was shown to produce good carrier uniformity with limited impact on light extraction efficiency in subsequent 650nm MCLED devices [18].

3.4.5 Farfield Pattern

The MCLED device was mounted at the centre of a rotation stage, and a microscope objective lens was positioned in the plane of rotation of the device at a distance of 60cm. The microscope objective lens was orientated such that its optical axis was directed towards the device. Emission from the MCLED device incident on the aperture of the lens was focussed onto a power meter (Photodyne Model 550) positioned behind the lens. The farfield emission pattern was measured by rotating the device and recording the power collected by the stationary objective lens. The 1cm aperture of the lens provided an angular resolution of ≈1 degree.

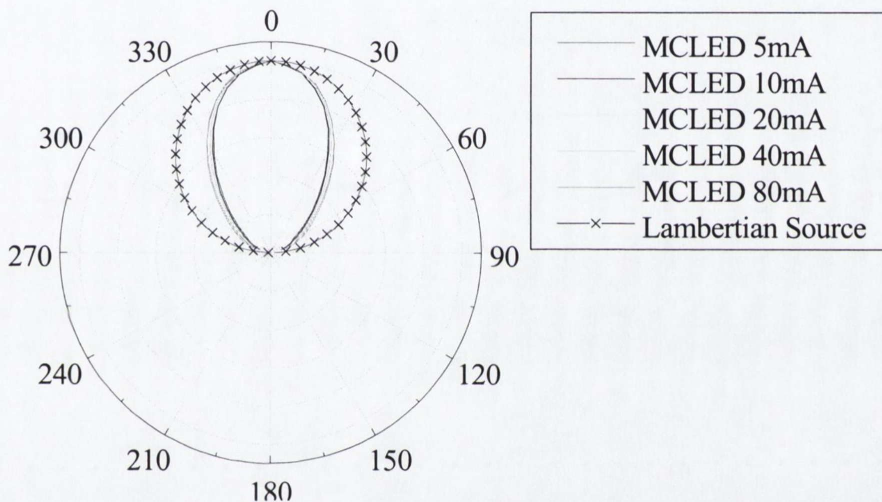

Figure 3.10 *Normalised farfield emission patterns of the 80μm diameter MCLED at a range of bias currents. The simulated farfield of a Lambertian source is shown for comparison.*

The farfield patterns of the 80μm diameter MCLED at room temperature and bias currents between 5mA and 80mA are compared to a Lambertian emission pattern (emitted power proportional to cosine of emission angle) in Figure 3.10. The angular FWHM of the MCLED farfield increases with current from 66° at 5mA to 72° at 80mA, but is considerably less than the 120° angular FWHM of the Lambertian farfield emission pattern observed for most conventional surface emitting LEDs [19].

This significant deviation of the MCLED farfield pattern from that of a Lambertian source is due to the enhancement by the cavity of emission at certain angles, however the two

lobed farfield pattern observed from MCLEDs optimised for maximum efficiency was not seen from our device.

3.4.6 Discussion of Characterisation Results

The encouraging aspect of these results in the context of developing a commercial MCLED emitting at 650nm was the clear microcavity effect visible in the narrow spectral emission linewidth, the reduced farfield angle, and the reduced temperature sensitivity of the spectral characteristics of this device compared to a conventional non-cavity LED. These results demonstrated the ability to produce strong microcavity effects at 660nm using a cavity defined by two DBRs even with the limited refractive index contrast available in this material system at this wavelength.

The disappointing aspects of these results were the low maximum power output, the highly non-linear power-current characteristics and the high temperature sensitivity of the power output of the MCLED device. The maximum output power, which despite being a factor of ten greater than previously reported results for red MCLEDs [2], was poor compared to either MCLEDs emitting at 980nm or conventional LEDs emitting at 650nm. The power-current characteristics exhibited a saturation of the output power at a bias current of only 40mA, while the T_l value of the MCLED device was considerably less than that expected for commercial devices.

For the future development of MCLEDs at this wavelength it was important to establish the origins of this poor performance and to identify the path towards future improvements. At this point in the discussion it is convenient to define three further efficiencies whose product determines the external quantum efficiency, η_{extern}, of a device. The carrier injection efficiency, η_{inj} defined as

$$\eta_{inj} = \frac{\textit{number of electrons in the active region per unit time}}{\textit{number of electrons flowing in the external circuit per unit time}} \qquad (3.4)$$

is equal to the fraction of injected carriers that end up in the active region, and is less than unity when there is carrier leakage. The radiative efficiency, η_{rad} defined as

$$\eta_{rad} = \frac{radiative\ recombination\ rate}{total\ recombination\ rate} = \frac{1}{1 + \tau_r / \tau_{nr}} \tag{3.5}$$

where τ_r and τ_{nr} are the radiative and non-radiative recombination lifetimes, is essentially determined by the material quality of the active layer. The extraction efficiency η_{extra} is defined as

$$\eta_{extra} = \frac{number\ of\ photons\ emitted\ from\ device\ per\ unit\ time}{number\ of\ photons\ emitted\ internally\ from\ active\ layer\ per\ unit\ time} \tag{3.6}$$

and accounts for absorption losses and transmittance of the semiconductor-air interface. The ability of the microcavity to redirect internal emission into angles less than the critical angle for the semiconductor-air interface is reflected in an increased η_{extra} value. Combining these three efficiencies we can write

$$\eta_{extern} = \eta_{inj} \times \eta_{rad} \times \eta_{extra} \tag{3.7}$$

Before discussing the specific causes of the poor temperature sensitivity and low output power of our device in terms of these efficiencies, two alterations to the MCLED design that would offer improved η_{extern}, evident from our characterisation results are mentioned. Firstly, the correct positioning of the cavity resonance relative to the QW emission should result in the peak QW emission being resonant with the cavity mode off-axis and an improved η_{extra}. The exact improvements in η_{extra} that could be expected from optimisation of the cavity design are shown in section 3.5. Secondly, an improvement in the spatial distribution of carriers in the active layer of the device as already discussed in section 3.4.4 should reduce carrier leakage and contact shadowing effects, improving η_{inj} and η_{extra} respectively.

To understand the temperature dependence of the performance of our MCLED device the impact of temperature on all three efficiencies has to be considered. An increase in temperature results in a reduction in the η_{rad} of an active layer due to an increased non-radiative recombination rate. η_{inj} also reduces with increasing temperature due to the

increased probability of carrier leakage from the QW. Finally η_{extra} can either increase or decrease with increasing temperature depending on the cavity design. This is because the QW emission wavelength is expected to exhibit greater temperature sensitivity than the cavity resonant wavelength resulting in the relative positioning of the cavity and QW emission wavelengths changing with temperature. The structure can be designed such that the separation of the cavity and QW wavelengths is non-optimal at room temperature, but improves with increasing temperature, thereby producing an increase in η_{extra} with increasing temperature.

It is difficult to accurately determine the temperature dependencies of the different efficiencies of our device, however the widely reported problem of increased carrier leakage from GaInP/AlGaInP QWs at higher temperatures due to the small barrier offsets [20,21] suggests that a reduced η_{inj} at higher temperatures may have been the cause of the poor temperature characteristics of our MCLED device. This problem is universal to devices based on this material system and emitting at these wavelengths, and not inherently due to the microcavity structure. Through optimisation of the core, cladding, barrier and QW compositions in the cavity, the temperature dependency of the MCLED device should match LEDs based on the same material system and emitting at the same wavelength. Indeed the microcavity structure allows the possibility of a η_{extra} temperature dependence to compensate the η_{inj} temperature dependence as outlined above, thereby producing an overall less temperature dependent output than a non-cavity LED structure.

In order to determine the cause of the highly non-linear power-current characteristics of our device, the role of current induced device heating due to the series resistance of our MCLED structure was examined. The magnitude of this effect was estimated from comparison of the spectral shifts induced by changes in the ambient device temperature at low bias currents and by changes in the bias current at constant ambient room temperature as shown in Figure 3.8. The estimated device temperature as a function of bias current is shown in Figure 3.11. It suggests significant device heating occurring at bias currents greater than 20 mA. However the fact that the shift in the bias current at which radiance saturation occurs with ambient device temperature (Figure 3.5) is only small, indicates that device heating is not the only process responsible for this effect.

Both η_{inj} and η_{extra} are also expected to decrease with increasing current due to the increased probability of carrier leakage and the increased spectral linewidth of the internal QW emission (see Figure 3.14) respectively. It is again difficult to determine the exact roles played by these effects in determining the power-current characteristics of this device. However the drop in the external quantum efficiency at low currents (< 20 mA), where carrier leakage due to heating or high carrier densities is likely to be small, is probably due to a decreasing η_{extra}, an effect previously reported in MCLEDs emitting at 980nm [10,22]. At higher currents the drop in η_{inj} caused by heating and higher carrier densities is expected to have played a significant role in the saturation of the output power.

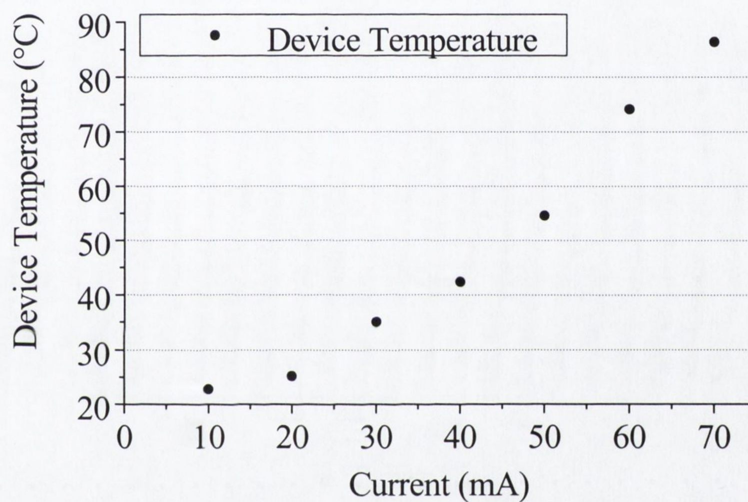

Figure 3.10 *Device heating due to bias current estimated from spectral measurements.*

To summarise, improvements in the series resistance, uniformity of carrier injection, carrier confinement in active region and cavity design are all required for the realisation of a MCLED of optimum performance. Such a device should offer considerably improved temperature dependency and power output characteristics over this device. Of the required improvements, only the optimisation of the cavity design is unique to the MCLED technology and is the focus of section 3.5.

3.5 MCLED device modelling

In order to gain a further insight into the performance of our MCLED device and explore the improvements that could be expected from optimisation of the cavity design, a numerical simulation tool capable of the exact calculation of dipole emission modifications in an arbitrary multilayer structure was implemented. The modelling tool was initially developed to simulate the performance of MCLEDs emitting at 980nm [23] and is capable of calculating the enhancement or inhibition of emission from the active layer of a microcavity, due to the modified optical environment, as a function of angle and wavelength given the refractive index (real and imaginary) and thickness of each layer in the structure. If the intrinsic spontaneous emission spectrum of the active layer in the cavity is also known the extraction efficiency of the microcavity can be calculated through careful integration over emission angles and wavelengths.

The details of the model are contained in reference [8], and also in Appendix A2. It is based on the transfer matrix technique for propagating electromagnetic waves of a given TE or TM polarisation through a multilayered structure, with source terms introduced as an additive discontinuity to the electromagnetic field at the dipole (active) layer. The source terms are dependent on the polarisation of the wave and the orientation of the emitting dipole with respect to the layer interfaces.

The model deals purely with the optical properties of the cavity and takes no account of electrical issues such as carrier transport and leakage, and therefore provides no information about η_{inj} or η_{rad}. The emission properties of the MCLED device characterised above are modelled in Section 3.5.1, while the extraction efficiencies and emission patterns for MCLED structures optimised for maximum extraction efficiency into air and into the acceptance cone of a fibre of NA=0.5 are calculated in Section 3.5.2.

3.5.1 Modelling of characterised device

As mentioned above, the input parameters required by the model to simulate the emission properties of a MCLED are the refractive indices and thicknesses of each layer in the structure and the intrinsic emission spectrum of the active layer. Values for the refractive indices of the layers of our MCLED as functions of wavelength were taken from references [24,25], and the target growth thicknesses of the layers in the structure were also known.

The intrinsic emission spectrum of the QWs in our device was determined from angular resolved measurements, using a deconvolution technique developed by P. Royo et al. [26,27,28], and briefly outlined below.

The power emitted per unit solid angle and area outside the MCLED can be expressed as [11]

$$\Pi_{ext}(\theta,\lambda) = \zeta(\theta,\lambda) A(\theta,\lambda) R_{sp}(\theta,\lambda) \qquad (3.8)$$

where $\zeta(\theta,\lambda)$, and $A(\theta,\lambda)$ are the antinode factor and cavity Airy function as described before in section 2.4.1. R_{sp} is the spontaneous emission spectrum of the active layer in an unbounded semiconductor and can be expressed as [28]

$$R_{sp}(\theta,\lambda) = r_{spont}(\lambda) \left|\langle M_t(\theta,\lambda)\rangle\right|^2 \qquad (3.9)$$

where $r_{spont}(\lambda)$ is the intrinsic spectrum, and is equal to the product of the joint density of states, their occupation probabilities, and a function describing line shape broadening effects. This function is independent of emission angle. The transition matrix element $\left|\langle M_t(\theta,\lambda)\rangle\right|^2$ contains the polarisation dependence of the light-matter interaction.

Using the dipole approximation and representing the active region as a collection of non-correlated oscillating electric dipoles*, the model can numerically calculate the quantity $\Pi_{sim}(\theta,\lambda)$ defined as

$$\Pi_{sim}(\theta,\lambda) = \zeta(\theta,\lambda) A(\theta,\lambda) \left|\langle M_t(\theta,\lambda)\rangle\right|^2 \qquad (3.10)$$

therefore in theory, $r_{spont}(\lambda)$ can be obtained by dividing the measured $\Pi_{ext}(\theta,\lambda)$ by the modelled $\Pi_{sim}(\theta,\lambda)$ at any given angle. The difficulty in doing this is that any error in the thicknesses or refractive indices of the layers, introduces significant errors into $\Pi_{sim}(\theta,\lambda)$ and hence the calculated $r_{spont}(\lambda)$, especially at wavelengths away from the resonant mode

* A QW active layer is represented by an isotropic distribution of horizontal (orientated parallel to the layer interfaces) dipoles in the model. This approach is justified by the predominant role played by heavy-holes in the recombination processes of many III-V QW materials [9].

wavelength, where $\Pi_{sim}(\theta,\lambda)$ is small [26]. This difficulty is overcome by comparing $\Pi_{ext}(\theta,\lambda)$ and $\Pi_{sim}(\theta,\lambda)$ at a range of angles: the shift in resonant wavelength to shorter wavelengths with increasing angle allows the accurate determination of $r_{spont}(\lambda)$ over a wide range of the spectrum, while the error in $r_{spont}(\lambda)$ at wavelengths not matched to the cavity mode at any angle is reduced by averaging results from different angles.

The angle resolved spectra were recorded using the same experimental setup as employed for the farfield measurements, with the collecting lens used to focus light into a fibre in place of the power meter. The output of the fibre was connected to the OSA that spectrally

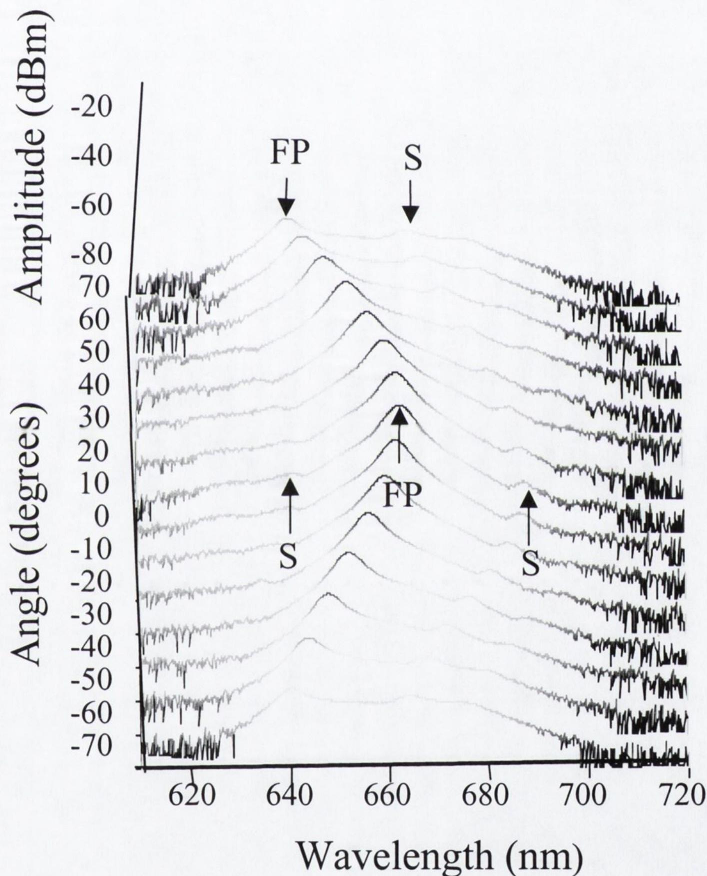

Figure 3.11 *MCLED emission spectra from our 80μm diameter MCLED device as a function of emission angle. The main emission peak due to the Fabry-Perot cavity mode, FP, and the smaller side peaks, S, due to the minimum in the DBR mirror reflectivity at the edge of the stopband are labelled. The amplitude is on a logarithmic scale.*

resolved the emission with a resolution of 0.5nm. The results obtained from our device at a bias current of 20mA are shown in Figure 3.11.

The expected shift in the peak emission wavelength to shorter wavelengths with increasing angle was observed, while two smaller peaks either side of the cavity mode displayed a similar angular dependence. The separation of these two smaller peaks matched the calculated top DBR spectral reflectivity stopband, which shifts similarly with angle, and hence the peaks were identified with the top DBR reflectivity minima located at the edge of the DBR stopband.

Due to slight differences between the target and grown layer thicknesses in our structure it was necessary to adjust the nominal thicknesses of the cavity spacer layers and the top DBR layers to match the spectral positions of the measured and simulated cavity mode and DBR stopband at normal incidence. The required adjustments to the layer thicknesses were less than 3% of the target values.

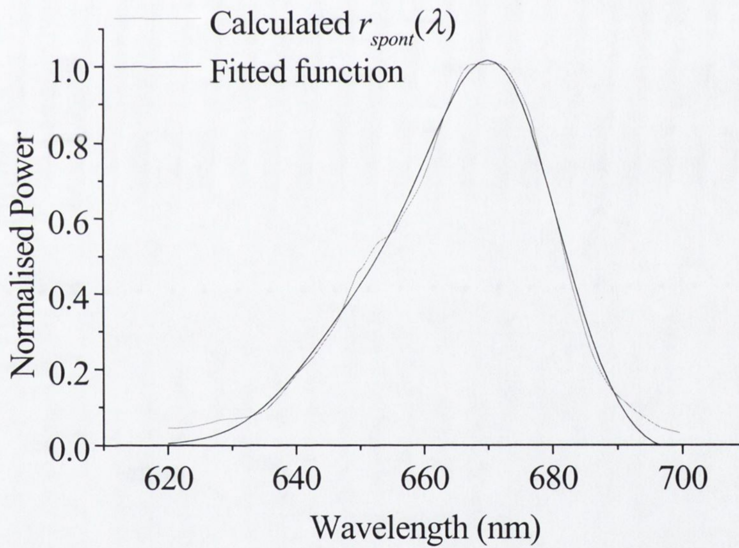

Figure 3.12 *Calculated $r_{spont}(\lambda)$ using equation (3.11). The fitted line used to provide an analytic expression for the $r_{spont}(\lambda)$ in subsequent simulations was obtained using a Gram-Charlier peak function (this function allows an asymmetric peak shape, which can occur in the QW emission spectrum due to band filling effects)*

Using the adjusted layer structure, $\Pi_{sim}(\theta,\lambda)$ was simulated at the measurement angles (0° to 70° in 10° steps), and $r_{spont}(\lambda)$ was calculated as follows

$$r_{spont}(\lambda) = \frac{\sum_{\theta=0}^{70} \Pi_{ext}(\lambda,\theta)}{\sum_{\theta=0}^{70} \Pi_{sim}(\lambda,\theta)} \tag{3.11}$$

The resulting r_{spont} spectrum following smoothing by adjacent averaging over 4nm intervals is shown in Figure 3.12. The peak emission wavelength λ_{QW}, and the spectral FWHM of the intrinsic QW emission $\Delta\lambda_{QW}$, of our device at the bias current of 20mA (current density $\approx$ 400 Acm^{-2}) were determined as 670nm and 30nm respectively.

Using the fitted function in Figure 3.12 for $r_{spont}(\lambda)$ the match between the measured and simulated emission spectra at different angles are shown in Figure 3.13(a). The model reproduces the measured variation in both the amplitude and wavelength of the cavity mode emission with angle. The agreement between the measured and modelled wavelength of the smaller peak (labelled *S* in Figure 3.11) can be seen at large angles (> 50°) in Figure 3.13(a). The reduced amplitude of this side peak in the simulated spectrum is attributed to uncertainties in the precise thickness and refractive indices of the grown structure. The wavelength integration of the modelled emission spectra at each angle produces a farfield emission pattern, which is compared to the measured farfield pattern in Figure 3.13(b).

The good agreement between the measured and simulated angular resolved spectra and farfield patterns suggests that $r_{spont}(\lambda)$, and the refractive indices and adjusted layer thicknesses used in the model provide a good representation of the intrinsic QW emission and layer structure of our MCLED device respectively. Taking the same input parameters the extraction efficiency of our MCLED device can now be calculated. To determine the extraction efficiency of a structure the total extracted power through the chosen side of the structure is calculated as [8]

$$P_{ext} = 2\pi \int_{-\infty}^{+\infty}\int_{0}^{\pi} \Pi_{ext}(\theta,\lambda)\sin\theta d\theta d\lambda = 2\pi \int_{-\infty}^{+\infty}\int_{0}^{\pi} \Pi_{sim}(\theta,\lambda) r_{spont}(\lambda)\sin\theta d\theta d\lambda \tag{3.12}$$

and divided by the total power emitted by the active layer integrated over all internal angles in the device and all wavelengths. The simulated extraction efficiency of our MCLED

device at 20mA was 4.8%. Comparing this to the measured η_{extern} value of 1.4%, we conclude that the internal efficiency of the device defined as the product of the injection and radiative efficiencies is 29% at a bias current of 20mA. The probable origins of this poor internal efficiency were discussed above.

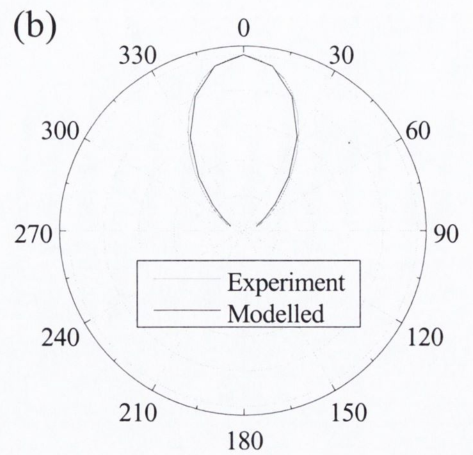

Figure 3.13 *(a) Measured and modelled angular resolved spectra (modelled spectrum =* $r_{spont}(\lambda)\times\Pi_{sim}(\theta,\lambda)$*). (b) Polar plots of measured and modelled farfield emission patterns.*

The dependence of the extraction efficiency on $\Delta\lambda_{QW}$ and the detuning of the cavity and intrinsic emission wavelengths δ (=λ_{QW}-λ_{FP}, λ_{FP} is defined as the cavity FP mode wavelength at normal incidence), is shown in Figure 3.14. $\Delta\lambda_{QW}$ was varied between 5 and 50nm (maintaining the same line shape as determined for the measured device), while λ_{QW} remained fixed at 670nm. λ_{FP} was varied between 650nm and 710nm by multiplying all layers in the structure by a constant factor; thereby ensuring the Fabry-Perot mode remained centred on the DBR stopband throughout the simulation.

Figure 3.14 confirms that the 7.5nm detuning of our MCLED device was not optimal for maximum extraction efficiency into air. This had already been indicated by the single lobed farfield of the device in contrast to the two-lobed farfield characteristic of MCLEDs optimised for maximum extraction efficiency into air. The simulation results in Figure 3.14

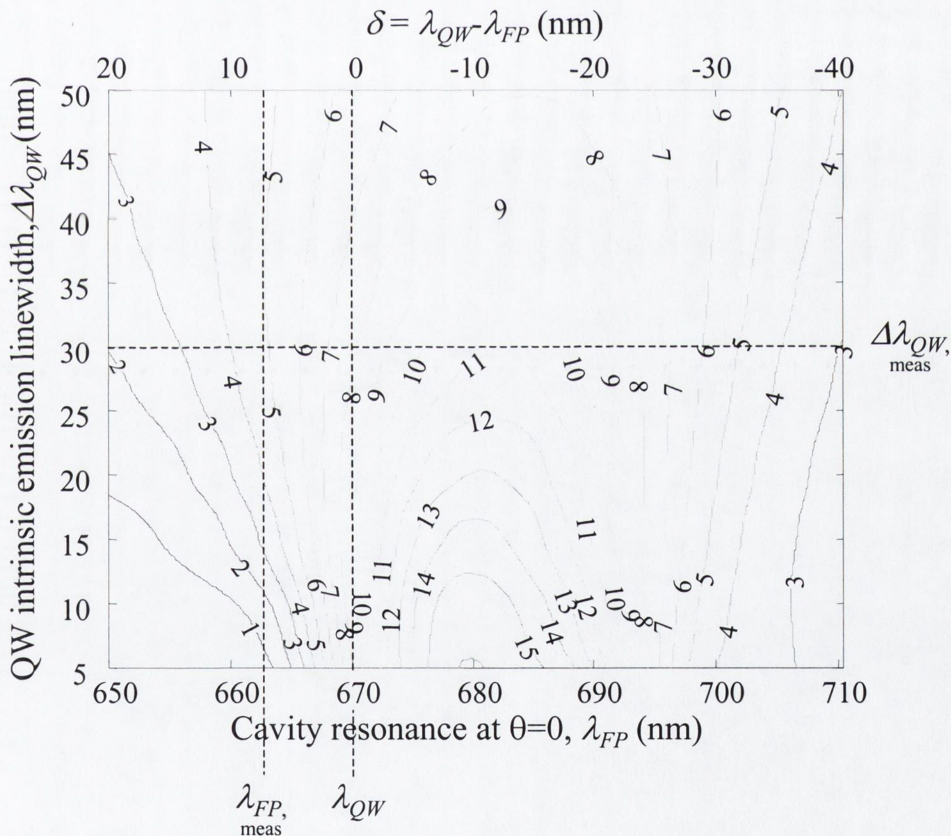

Figure 3.14 *Contour plot of η_{extra} (%) into air as function of $\Delta\lambda_{QW}$ and δ, for λ_{QW} fixed at 670nm. The λ_{FP} and $\Delta\lambda_{QW}$ of the measured MCLED device are shown as dashed lines, the intersection of which locate the calculated extraction efficiency of the device.*

show the optimal detuning for a MCLED with the same active layer and mirrors is –12nm, and the expected extraction efficiency from such a device is 10.8%. Therefore by simply adjusting the thickness of the layers of our structure to achieve the optimal position of the cavity mode and DBR stopbands, a factor of more than two improvement in the extraction efficiency and hence the external quantum efficiency of our MCLED device could be achieved.

The dependence of η_{extra} on the source emission linewidth is clearly visible in Figure 3.14. Since there exists an optimal value for the detuning between the internal source emission wavelength and the cavity wavelength for maximum η_{extra}, as the internal emission linewidth increases less of the emission can be optimally matched to the cavity mode resulting in a reduced η_{extra}.

3.5.2 Optimised cavity design for 650nm MCLED

In the previous section the dependence of η_{extra} on the intrinsic emission linewidth of the source and the detuning of the cavity for a MCLED structure with the same λ_{QW} and mirror structures as the fabricated device was calculated (see Figure 3.14). The optimised detuning δ and the importance of the intrinsic QW emission linewidth for such a structure were noted. However the λ_{QW} value of 670nm, taken from the measured device, used in these simulations resulted in emission spectra unmatched to the POF absorption minimum at 650nm, while no attempt was made to optimise the front and back mirror reflectivities.

In this section MCLED structures emitting at 650nm designed for maximum extraction efficiency into all angles (η_{extra}) and into angles guided by a fibre with NA=0.5 (η_{fibre}) are discussed. The full optimisation of a generic cavity design allowing for variation in $\Delta\lambda_{QW}$, δ, and the refractive indices and the number of pairs in both DBR mirrors is a complex and involved process. The interplay between and optimisation of these various parameters with respect to η_{extra} for a generalised microcavity structure has been extensively discussed elsewhere both using the same numerical model implemented here [9] and by a more analytic approach [29]. In order to simplify the design process we fixed some of the device parameters using our measured results and the limitations on refractive index contrast available in this material system at 650nm (see section 3.2). Firstly we set λ_{QW} = 650nm in

order to satisfy our requirement for emission at this wavelength, while $\Delta\lambda_{QW}$ was set equal to the estimated value for the QWs in our measured structure at 20mA of 30nm (the same intrinsic emission lineshape was also used, see Figure 3.12). Finally the composition of the top and bottom DBRs in our grown structure provided near the maximum refractive index contrast available, subject to the need to avoid absorption and allow carrier transport through the structure, and therefore the same material composition was used for the DBR pairs in the simulation.

Having fixed these parameters there are three design variables that have to be optimised namely the thickness of the cavity spacer layers, the thickness of the DBR layers and the number of DBR pairs, which determine λ_{FP}, the DBR stopband position, and the mirror reflectivities respectively. In order to further simplify the optimisation process the ratio of the cavity and DBR layer thicknesses was fixed so that λ_{FP} would be centred on the DBR stopband at all times. This resulted in three variable parameters – the number of front DBR pairs, the number of back DBR pairs and the cavity mode/DBR wavelength. The number of front and back DBR pairs was adjusted between 0 and 10, and 5 and 30 respectively. For each combination of mirror pairs λ_{FP} was adjusted by varying the layer thicknesses to maximise η_{extra}. The resulting maximum η_{extra} as a function of the number of back mirror pairs for different numbers of front mirror pairs is plotted in Figure 3.15.

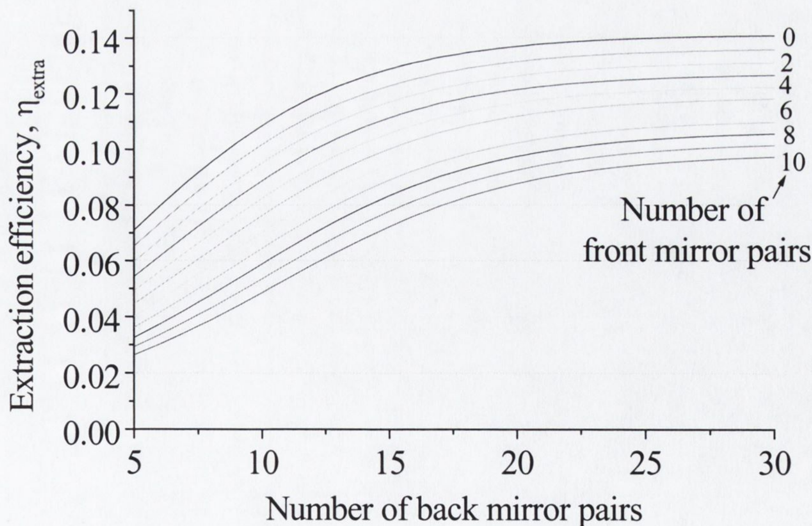

Figure 3.15 *Maximum η_{extra} as a function of number of mirror pairs ($\Delta\lambda_{QW}$=30nm)*

The consistent increase in η_{extra} with the number of back DBR pairs is due to the increased bottom mirror reflectivity reducing the loss of emitted light towards the absorbing substrate. η_{extra} will always increase with increasing numbers of back DBR pairs, however a diminishing increase from each additional pair is predicted, and beyond a certain number the benefit from adding another pair doesn't justify the increase in series resistance. Figure 3.15 shows that increasing the number of back DBR pairs beyond 25 yields only a very small improvement in η_{extra}.

The dependence of η_{extra} on the number of front DBR pairs is slightly more surprising; η_{extra} decreases with increasing number of front DBR pairs, with a maximum η_{extra} occurring for no front mirror pairs. Despite the absence of any front DBR in this optimised structure, a cavity still exists with the semiconductor-air interface acting as the front mirror with a reflectivity of ≈30%. The importance of the cavity effect is shown by a sensitivity of η_{extra} to the thickness of the cavity spacer layers. To understand the reason no improvement in η_{extra} is observed for an increased number of front DBR pairs, we first have to consider the influence of the internal source linewidth on η_{extra}. For a monochromatic source increasing the front mirror reflectivity reduces the cavity mode linewidth, allowing a better confinement of the Airy peak of the FP mode in the extraction window (see Figure 2.8(b)) and hence an increase in η_{extra}. When the internal source has a finite spectral linewidth, the peak of the FP mode for each wavelength is located at a different angle, angles that are independent of the front mirror reflectivity. Therefore if the intrinsic emission linewidth of the source is considerably broader than the FP linewidth, the integrated Airy mode linewidth over the internal spectrum is determined by the internal source linewidth rather than the cavity FP mode linewidth. In this case increasing the front mirror reflectivity does not result in better confinement of the integrated Airy mode within the escape cone, and hence does not lead to an increased η_{extra}. The FWHM of the FP mode linewidth for the simulated structure with no front DBR pairs was ≈15nm, which is considerably less than $\Delta\lambda_{QW}$, therefore the linewidth of the spectrally integrated Airy mode for the simulated structure is limited by the internal emission linewidth, and any increase in the front mirror reflectivity does not result in increased confinement of the integrated Airy mode within the escape cone. Increasing the number of front DBR periods does however increase the effective cavity order of the structure [29], and the fraction of emission directed towards

the substrate, both of which result in a reduced η_{extra}. Therefore the maximum η_{extra} occurs for no front DBR pairs. This same trend has been observed in simulations on other microcavity structures defined by DBR mirrors with limited refractive index contrast and broad internal emission linewidth [29].

Figure 3.16 shows η_{fibre} as a function of number of front and back DBR pairs. For each combination of mirrors the position of λ_{FP} was adjusted to maximise η_{fibre}. η_{fibre} shows a similar dependence on number of front and back mirror pairs as η_{extra}, but the maximum extraction efficiency into angles defined by the fibre NA of 0.5 ($\theta<\sin^{-1}(0.5)=30°$) is only 0.04 compared to the maximum η_{extra} value of 0.14.

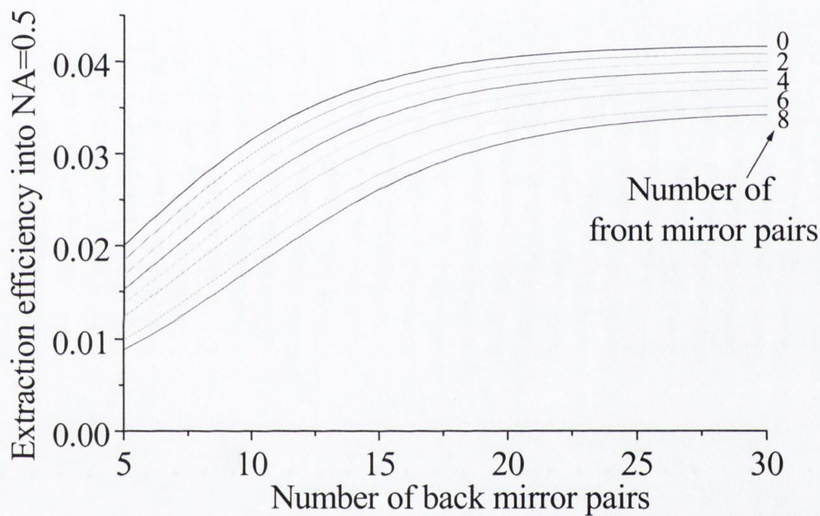

Figure 3.15 *Maximum η_{fibre} as function of number of mirror pairs ($\Delta\lambda_{QW}$=30nm)*

While the maximum values for η_{extra} and η_{fibre} were obtained for the same mirror structures, the thickness of the cavity spacer layers and hence the value of λ_{FP} was different for the optimised structures in both cases. This is not surprising since the detuning of the cavity FP mode to longer wavelengths than λ_{QW} to maximise η_{extra} results in a two lobed farfield (λ_{QW} resonant off-axis, $\theta\neq 0$), which will be unfavourable for butt coupling the emission into a fibre. The simulated farfield emission patterns of the microcavities with no front mirror pairs and 30 back mirror pairs optimised for maximum η_{extra} and η_{fibre} are shown in Figure 3.16. The structure designed for maximum η_{extra}, which has a detuning $\delta = -10$nm shows

the expected heart-shaped farfield pattern, however the maximum emission occurs at θ=28°, rather than at θ=45° as expected for a monochromatic source [11]. This difference is due to the asymmetric nature of the source emission spectrum used in the simulations. The greater intrinsic emission at $\lambda<\lambda_{QW}$ compared with $\lambda>\lambda_{QW}$ results in a reduced optimal detuning and hence the maximum in the farfield pattern occurs at a reduced angle compared to a cavity with a symmetric intrinsic emission spectrum. In comparison the smaller absolute δ value of –5nm for the structure optimised for maximum η_{fibre} results in maximum emission occurring at θ =12°, slightly less than middle of the 30° acceptance cone defined by the fibre NA.

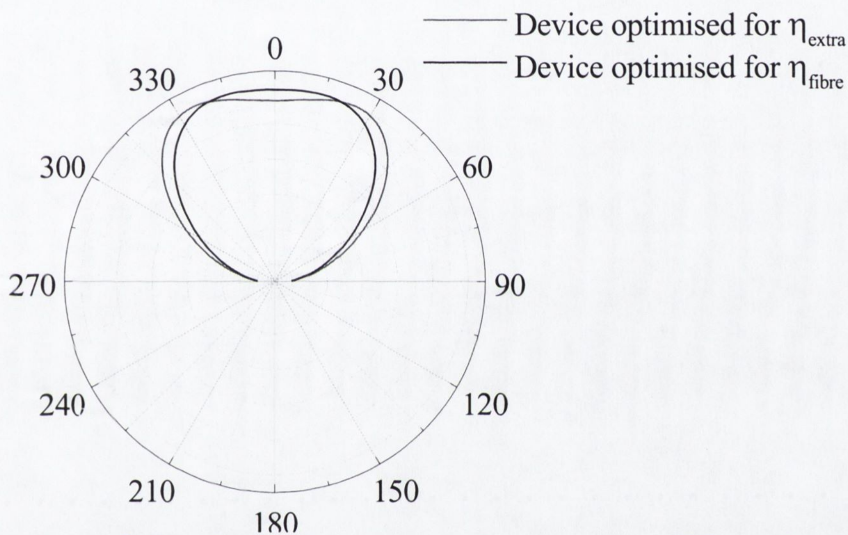

Figure 3.16 *Simulated Farfield emission patterns for structures with no front mirror pairs and 30 back mirror pairs, optimised for either maximum η_{extra} or maximum η_{fibre}.*

The simulation results presented in this section are designed to underline the importance of the intrinsic emission linewidth and lineshape, and the role of mirror reflectivities in determining the optimised cavity design. However both the QW emission linewidth and lineshape change with current density in the device, while λ_{QW} and λ_{FP} also shift with both temperature and current. Therefore the optimisation of a practical device design for operation at a range of currents and temperatures and allowing for electrical design considerations is a far more complex task than described here. References [9,29] provide information on general trends and considerations involved, while specific details of the

optimisation of a MCLED emitting at 650nm for POF applications are contained in reference [18].

3.6 Subsequent developments in 650nm MCLEDs

The MCLED device, whose emission properties have been presented in this chapter, was the first MCLED device emitting at these wavelengths fabricated under the SMILED collaboration. Considerable improvements in device performance were subsequently achieved under the SMILED program, through addressing the problems highlighted by the measurements in this chapter and by measurements on subsequent devices, as well as through extensive simulations. At this point a very brief summary of this progress is given. Specific details of the various device designs and performances can be found in the referenced documents.

An 84μm diameter MCLED structure emitting at 660nm with near-optimal detuning for maximum extraction efficiency, and with a grid top contact, produced a maximum external quantum efficiency of 4.8% at 4mA and a maximum emitted power of 2.6mW at 80mA [30]. This structure contained 7 top DBR pairs as it was found that reducing the number of pairs below this number resulted in reduced current spreading in the top DBR and increased series resistance. A data transmission rate of 350Mbit/s was demonstrated with this device [31].

The most recent results report external quantum efficiencies of 10% for an 80μm diameter MCLED emitting at 650nm [32], with the improvement in performance attributed to improved internal quantum efficiency. The temperature dependence of the power is still an issue; however narrowing of the farfield at higher temperatures offsets this effect in fibre coupling applications [33].

Even prior to this latest improvement in device performance, SMILED industrial partners Mitel were marketing a commercial 650nm MCLED device targeting POF applications. Therefore the future of red MCLEDs appears promising, subject to the absence of improved VCSEL performance at these wavelengths.

3.7 Limitations on the extraction efficiency of planar MCLEDs

The purpose of this section is to demonstrate using our model the limitations on the extraction efficiency of practically realisable planar MCLED structures. As before we do not present an exhaustive analysis of the role played by different cavity and source parameters in determining this limit as this as been done elsewhere [9], instead the emission properties of a generic microcavity structure with near optimal mirror properties subject to practical considerations are calculated and discussed by way of an illustrative example.

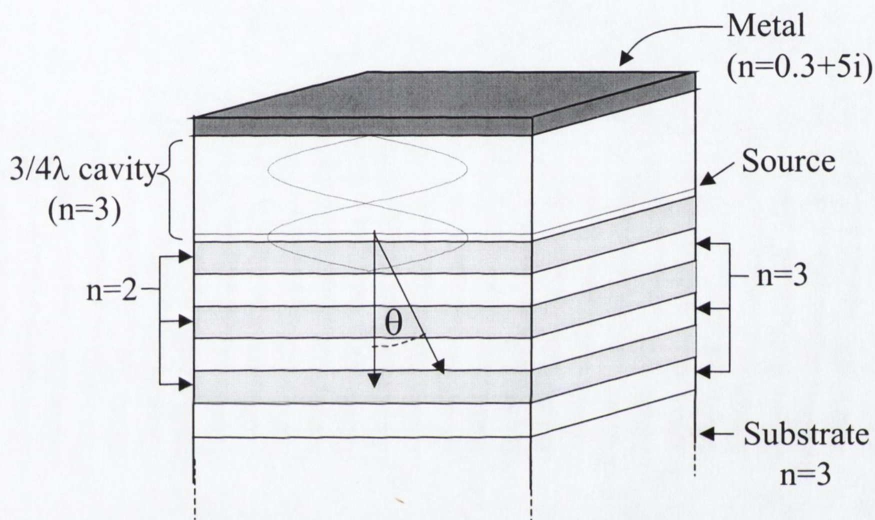

Figure 3.17 *Asymmetric microcavity structure used in simulations, showing extracted mode profile in blue.*

The chosen structure is designed to emit through the substrate thereby allowing the use of a metal top mirror, which provides high reflectivity and minimises the cavity length. There is no absorption in any layer of the structure other than the metal, whose refractive index is taken as 0.3+5i. The source layer (consisting of a horizontal dipole as before) is positioned at an antinode of the 3λ/4 cavity, while the bottom DBR consists of 3 pairs of alternate n=2 and n=3 layers. The refractive index difference between the DBR layers was chosen as an upper bound for that available in most material systems, while the number of DBR pairs was chosen to provide the maximum η_{extra}. In our simulations we consider a monochromatic source, again providing an upper bound on the η_{extra} that could be expected for a real source.

In order to understand the emission processes in the structure, the power emitted per unit solid angle at the source layer was calculated. The integration of this quantity over all angles equals the total emitted power by the source. The plot of power emitted per unit solid angle, as a function of internal angle in Figure 3.18 illustrates the distribution of power between different modes in the structure. Emission at internal angles between 0° and the critical angle for an n=3 to air interface either couples to external angles in air between 0° and 90° or is absorbed in the metal mirror. The fraction that couples to air represents the extracted emission from the structure. At internal angles greater than the critical angle for an n=3 to an n=2 interface, emitted light undergoes total internal reflection at the cavity DBR boundary, and hence is confined to the central cavity region. Modes that exist at these angles are known as guided modes and propagate laterally, only damped by their overlap with absorbing layers, in this case the top metal mirror. These guided modes exist at sharp angular resonances whose width is only limited by absorption in the structure. At internal angles between these two critical angles, emitted light undergoes total internal reflection at the air interface, but can still penetrate into the DBR, and couples to modes known as leaky modes. The balance between emission into extracted, leaky and guided modes together with absorption determines the performance of any microcavity structure.

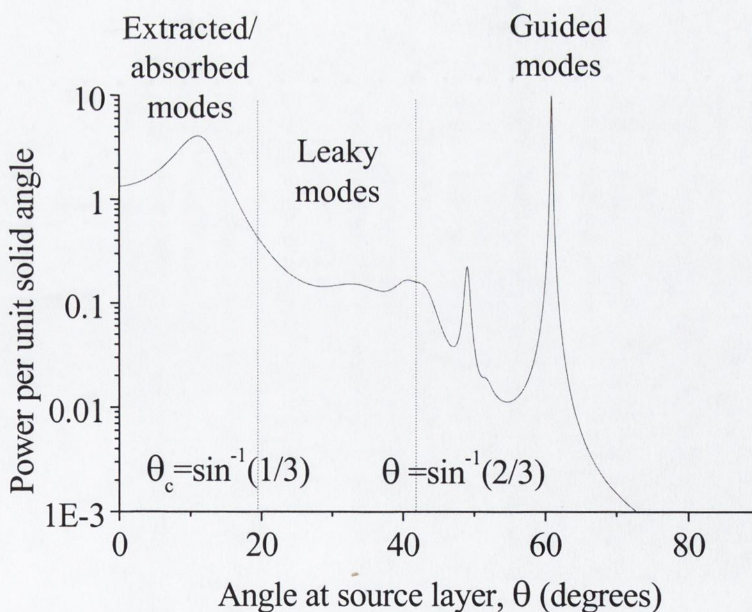

Figure 3.18 *Emitted power per unit solid angle as a function of angle at source layer.*

The fractions of the total emitted power that couple to each of these classes of modes, as well as the fraction absorbed in the metal mirror, as functions of the normalised source wavelength are shown in Figure 3.19. A full explanation of the trends shown in Figure 3.19 is given in reference [9], however in the context of the limitations on η_{extra} for planar microcavities the following two observations are relevant. Firstly, the fraction of total emission extracted, η_{extra}, never exceeds 0.42, and secondly, at wavelengths where η_{extra} is maximised, emission into guided modes dominates the non-extracted light. The choice of DBR refractive index contrast, the use of a monochromatic source and the absence of absorption in the semiconductor layers in our simulation means that the maximum calculated η_{extra} is unlikely to be exceeded by any presently realisable planar microcavity structure incorporating one or two DBRs. However the large fraction of emission coupled to the guided mode of the structure suggests that photon-recycling processes, as described in section 2.7, but not accounted for in our model, may provide a mechanism for surpassing this limit. As previously discussed, the exploitation of photon recycling effects while avoiding extremely large device sizes that are undesirable for many applications requires the development of higher dimensional cavities with lateral mirrors to confine light emitted

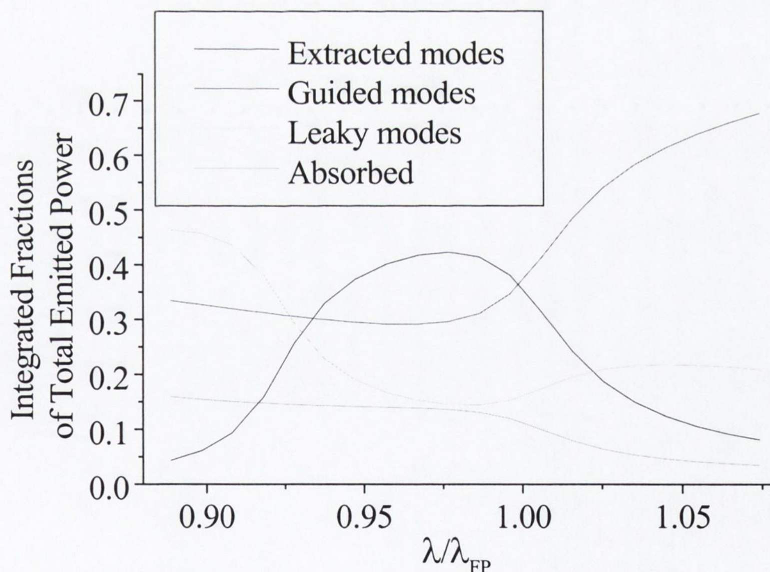

Figure 3.19 *Integrated fractions of total emitted power coupled to various classes of modes and lost to absorption in the metal layer as a function of source wavelength normalised to the cavity FP mode wavelength.*

into the guided modes. Higher dimensional microcavities also possess the potential for increased extraction efficiency in the absence of recycling, and increased recombination rates as discussed in the previous chapter. Whatever the mechanism, it appears the development of multidimensional structures will be required to extend η_{ext} for microcavities substantially beyond the limits outlined above without resorting to extremely large devices.

3.8 Conclusions

The emission properties of a planar MCLED emitting at 660nm have been presented and discussed. Despite evidence of a strong microcavity effect in the emission spectrum and farfield pattern, the maximum external quantum efficiency of the device was less than 2%, and a maximum output power of only 0.8mW was measured. This poor performance was attributed to both a non-optimised cavity design and problems with carrier leakage from the QWs in the device.

The optical design of the cavity, an issue intrinsic to the microcavity concept, was further investigated using a numerical model. The model successfully reproduced the measured angular resolved spectra and farfield patterns and predicted a factor of 2 increase in the extraction efficiency through the correct positioning of the cavity resonance wavelength. The influence of mirror reflectivities, source emission linewidth, and positioning of cavity resonance on the extraction efficiency of MCLED structures emitting at this wavelength was further investigated using the model. Optimised cavity designs for maximum extraction efficiency into air and into an NA of 0.5, assuming a fixed source emission linewidth and ignoring electrical design considerations were presented, with calculated efficiencies of 0.14 and 0.04 respectively.

These measurements and simulations played an important role in the initial development of MCLED technology at 650nm; a development process that has resulted in greatly improved device performance and the realisation of a commercial MCLED device at 650nm. The results also highlight some of the important design considerations common to all microcavity light emitting structures, such as mirror reflectivities and relative positioning of cavity and source emission wavelengths, and therefore serve as a valuable starting point for our investigations into more complex microcavity structures offering higher dimensional photon confinement.

One of the motivations for investigating higher dimensional microcavities is highlighted in the final section of the chapter where the ultimate limitation on the extraction efficiency achievable with planar microcavity structures incorporating DBR mirrors, in the absence of photon recycling effects, was investigated using the model. Simulations of the angular distribution of emitted power at the source inside such a planar microcavity show the significant coupling of emission to guided modes. These results show the need to redistribute light from guided to extracted modes through photon recycling or some other mechanism if extraction efficiencies in excess of 40% are to be realised by microcavity structures. The remainder of the thesis is concerned with exploring aspects of higher dimensional microcavities, structures that possess the potential for achieving such a redistribution.

3.9 References

1 "Resonant cavity light emitting diode", E. F. Schubert, Y.-H. Wang, A. Y. Cho, L.-W. Tu and G. J. Zydzik, Appl. Phys. Lett. **60** (8) p. 921 (1992)

2 "Visible (660nm) resonant cavity light emitting diodes", J. A. Lott, R. P. Schneider Jnr., G. A. Vawter,J. C. Zopler and K. J. Malloy, Elec. Lett., **29** (4), p. 328 (1993)

3 "AlGaInP Visible Resonant Cavity Light-Emitting diodes", J. A. Lott, R. P. Schneider, Jr., J. C. Zolper, and K. J. Malloy, IEEE Photon. Technol. Lett. **5** (6) p. 631 (1993)

4 "Increased fiber communications bandwidth from a resonant cavity light emitting diode emitting at λ=940nm", N. E. J. Hunt, E. F. Schubert, R. F. Kopf, D. L. Sivco, A. Y. Cho, and G. L. Zydzik, Appl. Phys. Lett. **63** (19) p. 2600 (1993)

5 "Enhanced spectral power density and reduced linewidth at 1.3μm in an InGaAsP quantum well resonant cavity light emitting diode", N. E. J. Hunt, E. F. Schubert, R. A. Logan and G. J. Zydzik, Appl. Phys. Lett., **61** (19) p. 2287 (1992)

6 "3.2μm resonant cavity light emitting diode", E. Hadji, J. Bleuse, N. Magnea and J. L. Pautrat, Appl. Phys. Lett. **67** (18) p. 2591 (1995)

7 "6% external quantum efficiency from InGaAs/(Al)GaAs single quantum well planar microcavity LEDs", J. Blondelle, H. De Neve, P. Demeester, P. Van Daele, G. Borghs, and R. Baets, Electron. Lett. **30** (21) p. 1787 (1995)

8 "Method of source terms for dipole emission modification in modes of arbitrary planar structures", H. Benisty, R. Stanley, and M. Mayer, J. Opt. Soc. Am. A **15** (5) p. 1192 (1998)

9 "Impact of planar microcavity effects on light extraction - Part II: Selected exact simulations and role of photon recycling", H. Benisty, H. De Neve, C. Weisbuch, IEEE J Quant. Elect. **34** (9) p. 1632 (1998)

10 "Recycling of guided mode light emission in planar microcavity light emitting diodes", H. De Neve, J. Blondelle, P. Van Daele, P. Demeester, R. Baets, and G. Borghs, Appl. Phys. Lett. **70** (7) p. 799 (1997)

11 "Impact of planar microcavity effects on light extraction - Part I: Basic concepts and analytical trends", H. Benisty, H. De Neve, C. Weisbuch, IEEE J Quant. Elect. **34** (9) p. 1612 (1998)

12 "Graded-index polymer optical fiber for high-speed data communication", T. Ishigure, E. Nihei, and Y. Koike Appl. Optics **33**, p. 4261 (1994)

13 "Large-core, high-bandwidth polymer optical fiber for near infra-red use", T. Ishigure, E. Nihei, Y. Koike, C. E. Forbes, L. LaNieve, R. Straff, and H. A. Deckers, IEEE Photon. Technol. Lett. **7** (4) p. 403 (1995)

14 *Vertical-Cavity Surface-Emitting Lasers – design, fabrication, characterization, and applications,* edited by C. Wilmsen, H. Temkin, and L. Coldren (Cambridge University Press, New York, 1999)

15 "Oxide-confined resonant cavity red light-emitting diode grown by solid source molecular beam epitaxy", M. Jalonen, M. Toivonen, J. Köngäs, A. Salokatve, and M. Pessa, Elec. Lett. **33** (23) p. 1989 (1997)

16 "Power and efficiency limits in single mirror light emitting diodes", N. E. J. Hunt, E. F. Schibert, D. L. Sivco, A. Y. Cho, and G. J. Zydzik, Elec. Lett. **28** (23) p. 2169 (1992).

17 *Semiconductor Optoelectronics, Physics and Technology*, J Singh, (McGraw-Hill, Inc. New York, 1995)

18 Reports of EC ESPRIT #24997, Semiconductor Microcavity Light Emitting Diodes (SMILED) project, 1997-2000.

19 *Principles of Optics* 6th Ed., M. Born and E. Wolf, (Cambridge University Press, Cambridge, 1997)

20 "Influence of leakage and gain-cavity alignment on the performance of Al(GaInP) visible vertical-cavity surface emitting lasers", G. Knowles, S. J. Sweeney, and T. Sale, IEE Proc.-Optoelectron. **148** (1) p.55 (2001)

21 "Drift Leakage current in AlGaInP Quantum-Well Lasers", D. P. Bour, D. W. Treat, R. L. Thornton, R. S. Geels, and D. F. Welch, IEEE J Quantum Electron. **29** (5) p. 1337 (1993)

22 Tom Aherne, Ph.D. Thesis, Trinity College Dublin (1998).

23 Reports of EC ESPRIT #8447, Semiconductor Microcavity Light Emitters (SMILES) project, 1993-1997.

24 *Properties of Aluminium Gallium Arsenide,* edited by S. Adachi (INSPEC, London, 1993)

25 *Quantum Well Lasers*, edited by P. S. Zory (Academic Press, 1993)

26 "Device simultaneous determination of source and cavity parameters of a microcavity light-emitting diode" D. Ochoa, R. Houdré, R. P. Stanley, C. Dill, U. Oesterle and M. Ilegems, J. of Appl. Phys. **85** (5) p. 2994 (1999)

27 "On-wafer determination of intrinsic spontaneous spectrum of vertical cavity surface-emitting devices", P. Royo, R. P. Stanley, M. Illegems, K. Streubel, and K. H. Gulden, Electron. Lett. **36** (25) p.2106 (2000).

28 "Deconvolution of the intrinsic spontaneous emission spectrum of vertical-cavity surface emitting devices", P. Royo, R. P. Stanley, M. Illegems, K. Streubel, and K. H. Gulden, Appl. Phys. Lett. **77** (24) p. 3899 (2000)

29 "Planar dielectric microcavity light-emitting diodes: Analytic analysis of the extraction efficiency" P. Royo, R. P. Stanley, and M. Ilegems, J. of Appl. Phys. **90** (1) p. 283. (2001)

30 "High Brightness Visible (660nm) Resonant-Cavity Light-Emitting Diode" K. Streubel, U. Helin, V. Oskarsson, E. Backlin, and A. Johansson, Photon. Technol. Lett. **10** (12) p. 1685 (1998)

31 "250 Mbit/s fibre transmission using 660nm resonant cavity light emitting diode", K. Streubel and R. Stevens, Electron. Lett. **34** (19) p.1862 (1998)

32 "High-Efficiency Resonant-Cavity LEDs Emitting at 650nm", R. Wirth, C. Karnutsch, S. Kugler, and K. Streubel, IEEE Photon. Technol. Lett. **13** (5) p. 421 (2001)

33 "Temperature behaviour of resonant cavity light-emitting diodes at 650nm" P. Sipila, M. Saarinen, M. Guina, V. Vilokkinen, M. Toivonen, and M. Pessa, Semicond. Sci. Technol. **15** p.418 (2000)

Chapter 4

Higher Dimensional Microcavity Structure (Microleek)

4.1 Introduction

In Chapter 3 the use of effective lateral mirrors to confine light in the plane of the device was proposed as a mechanism for surpassing the limits on the extraction efficiency of planar microcavities. 3D photon confinement to wavelength scale lengths also offers the potential for strong modification of the spontaneous emission process, and specifically the spontaneous emission rate (see section 2.4.2). However, the realisation of lateral mirrors in structures that confine light to wavelength scales in two dimensions is a major challenge. Various structures that offer 3D confinement of light including micropillars [1], microdisks [2], and hexagonal photonic bandgap microcavities [3] have been demonstrated. Micropillars and microdisks use a single semiconductor/air interface in the lateral direction to produce a cylindrical waveguide or confinement by total internal reflection (TIR) respectively. However neither structure offers full lateral confinement due to the limited range of angles for which light is guided or reflected respectively. 2D photonic crystal structures, which can possess omnidirectional reflection properties have been used to produce strong lateral confinement of light in hexagonal shaped cavities [3], however the emission properties of these structures remain extremely complex. In this chapter the emission properties of a novel structure offering 3D confinement of light are investigated.

The structure consists of circular concentric deeply etched trenches defined in a planar waveguide that act as a circular Bragg reflector around a central cavity. The structure is referred to as a "microleek" [4] due to its layered cylindrical structure and small dimensions. The lateral mirror structure is designed to confine light incident at the central cavity pillar edge at small angles near normal, thereby expanding the range of confined

angles beyond the large incidence confinement offered by TIR in microdisk structures. While the microleek structure falls short of the omnidirectional confinement promised by cavities bounded by photonic bandgap structures, the simpler design of the microleek provides an interesting intermediate structure with less complex mirror properties and cavity mode structure.

Concentric etched lateral structures similar to the microleek, termed “fingerprint” structures were implemented in circularly symmetric distributed feedback lasers (DFBs) [5,6]. However the shallow etch depth in such “fingerprint” structures results in modest light confinement and large modal volumes, manifested in broad area surface emission (diameters $\phi \approx 100\mu m$) [5]. In contrast, the comparatively large etch depth of the air trenches of the microleek results in stronger confinement of the light to much smaller volumes ($\phi \approx 3\mu m$). Therefore the microleek structure offers increased lateral light confinement over conventional 3D optical resonators such as microdisks and micropillars, while maintaining a small modal volume, making it a potentially interesting structure for studying enhanced 3D microcavity effects.

Our study of the photoluminescence (PL) properties of the microleek structure is divided into two broad sections. The first consists of measurements performed at high excitation densities on structures containing quantum well active layers. The high reflectivity of the microleek mirror is confirmed by the observation of lasing, with the detailed lasing properties of the structure presented in section 4.6. The above threshold spectral and near-field emission properties are explained using a model based on the modes of a disk resonator.

The second part of our studies focused on time resolved PL measurements on quantum dot emitters in a microleek structure. The PL lifetime of quantum dots coupled to a mode of the microleek structure is compared to the PL lifetime of quantum dots coupled to unconfined modes, and the PL lifetime of quantum dots outside the cavity. Finally the cavity properties required to produce a modified spontaneous emission rate for an emitter in a microleek structure are discussed.

4.2 Cavity structure

4.2.1 Design principle

The novel concept of the microleek structure is the use of concentric deeply etched air trenches to act as a circular DBR. Along a radius the successive trenches are designed to operate at the fourth Bragg order in reflection. The use of fourth-order Bragg periods and thin trenches minimizes scattering losses [7], while still giving high reflectivities within a limited number of periods. Due to the 8π phase difference of a round trip between successive trenches, light diffracted towards the vertical direction at successive trenches interfere constructively (4π phase difference), resulting in the coherent outcoupling of light from the cavity towards the substrate and air.

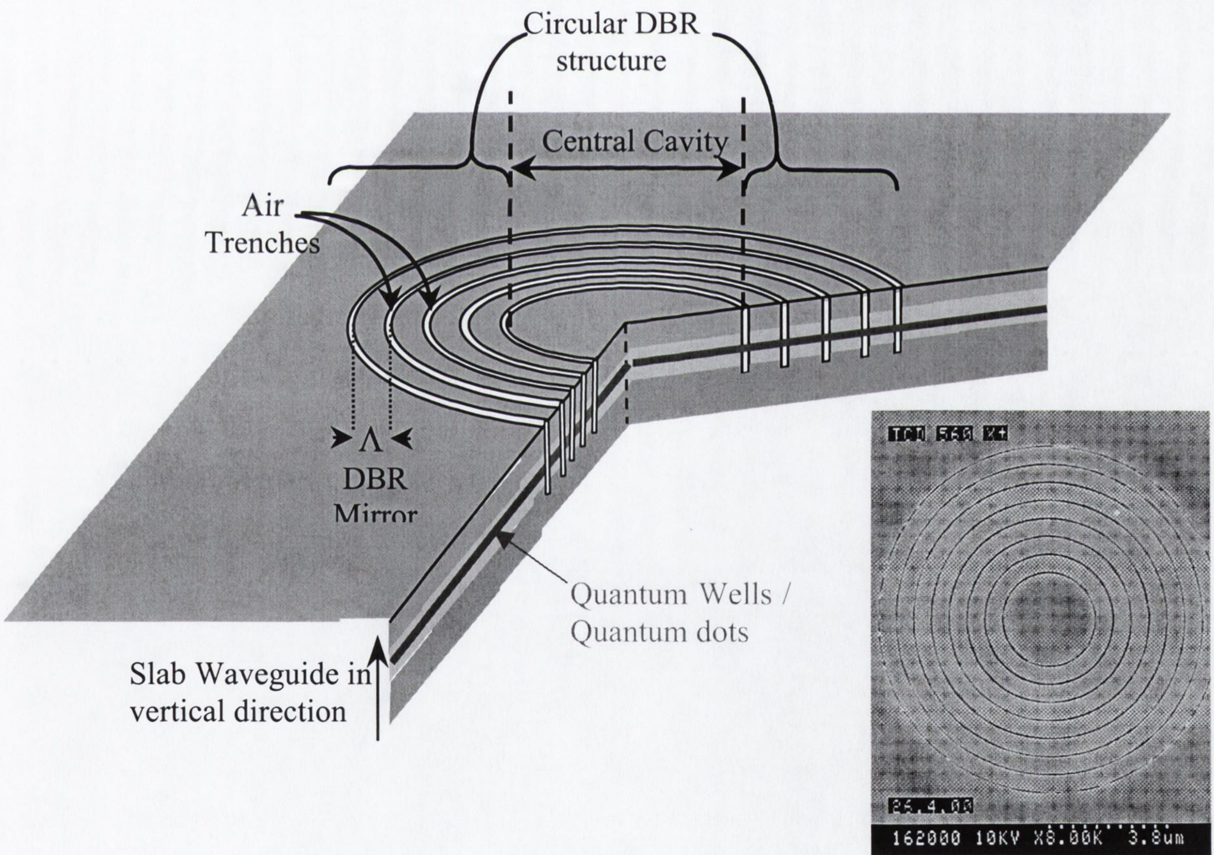

Figure 4.1 *Diagram of the microleek structure, showing the deeply etched air trenches that are designed to act as a fourth-order circular Bragg reflector. A scanning electron micrograph of an 8 period microleek is also shown.*

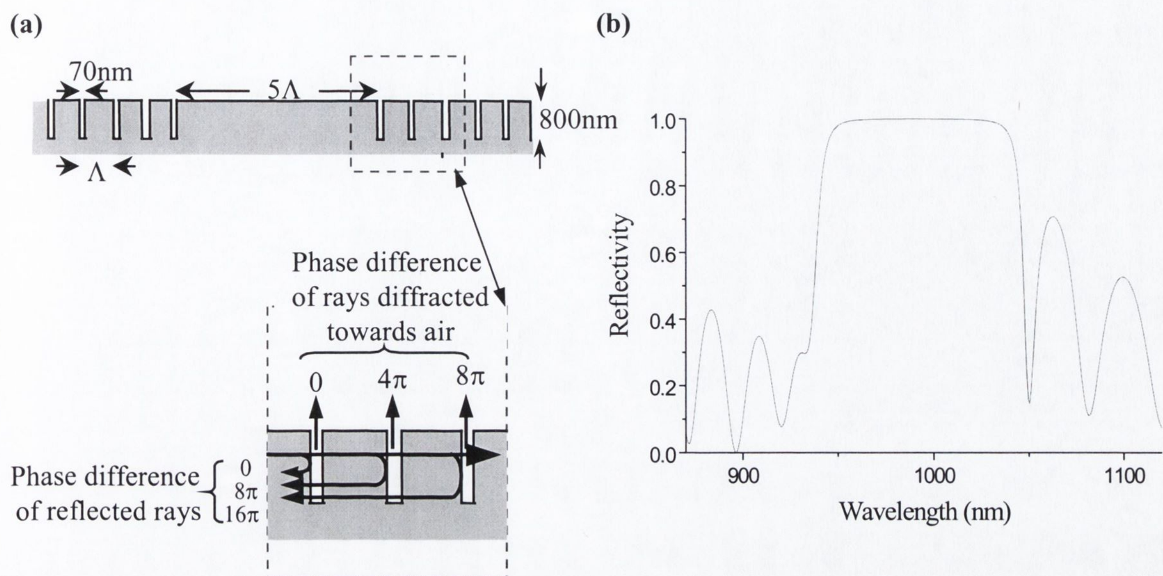

Figure 4.2 (a) *Cross section of microleek structure showing phase differences between light reflected and diffracted vertically at successive trenches.* **(b)** *Calculated reflectivity spectrum of a 5 period circular Bragg mirror with Λ =620nm for light incident in the radial direction (normal to the mirror).*

The limited etch depth achievable for such fine features prohibits the incorporation of a top DBR mirror. However three-dimensional confinement of the light, over the range of angles reflected by the CDBR, is achieved using a slab waveguide to confine the light in the vertical direction.

4.2.2 Samples

Two wafers were grown by molecular beam epitaxy (MBE) on gallium arsenide (GaAs) substrates at École Polytechnique Federale Lausanne (EPFL). Both wafers consisted of a planar AlGaAs/GaAs waveguide (see Fig 4.3 for details), with three $In_{0.17}Ga_{0.83}As$ quantum wells (QWs) positioned in the center of the waveguide in one wafer and three layers of InAs self-assembled quantum dots (QDs) similarly positioned in the second wafer. Nanometer-scale e-beam lithography and reactive ion etching processes were used to define the ≈800 nm-deep and 70 nm-wide trenches [8]. Structures with different Bragg periods (defined as the difference in radius between successive trenches) Λ= 580, 600, 620 and 640nm and between 1 and 8 periods were etched in both wafers. The central

cavity (defined by the inner diameter of the first trench) was equal to $5\times\Lambda$ in all structures.

The different emission properties of QDs and QWs are a source of significant interest in both fundamental and applied research [9], and are discussed in more depth in chapters 5 and 6. The relevant properties of the active layers in the structures in the context of this chapter are listed below.

- Carrier trapping in QDs at low temperature produces localized emitters.
- Individual QDs have very narrow emission linewidths.
- Variation in the emission wavelength between individual QDs results in a broad integrated PL spectrum from an ensemble of dots.
- This large inhomogeneous broadening results in a reduced peak optical gain for the QD layer, relative to the QW layer.

4.3 Modelling of cavity modes.

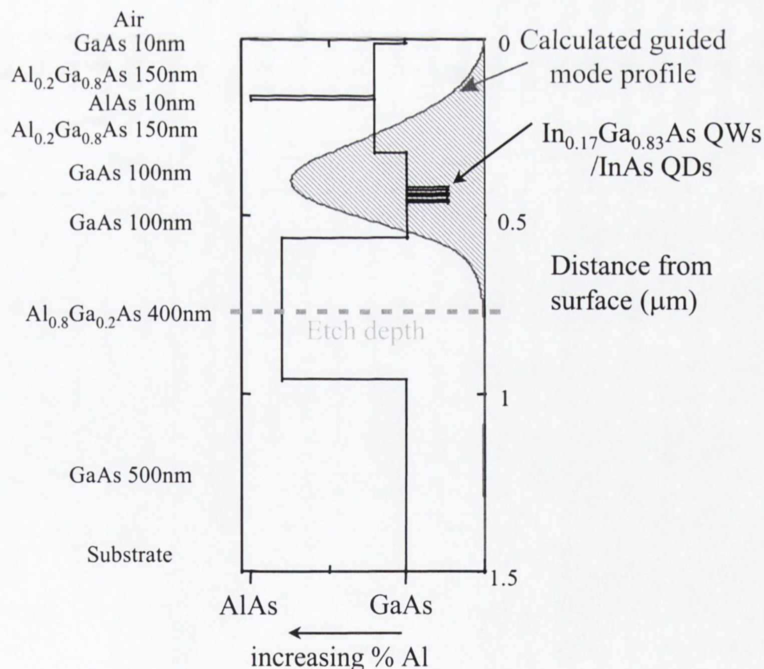

Figure 4.3 *Layer structure of GaAs/AlGaAs waveguide, with calculated guided mode profile at λ=1000nm superimposed.*

The modelling of the optical modes of the microleek structure can be reduced from a 3D to a 2D problem by considering the 3D guided light propagation in the GaAs/AlGaAs waveguide as 2D planar propagation in a medium of effective refractive index n_{eff} of the guided mode. The guided mode profile of the heterostructure planar waveguide is calculated numerically using a series expansion method [10] and standard refractive indices for the $Al_xGa_{1-x}As$ material system [11]. The calculated mode profile is shown in figure 4.3 and confirms the strong confinement of the mode to the section of the waveguide above the etch depth. This ensures a strong interaction of the guided light with the etched circular Bragg reflector. The variation in n_{eff} of the waveguide mode with λ was calculated and found to be well approximated over the range 800-1010nm by the expression $n_{eff}(\lambda)=3.39-4.0\times10^{-4}[\lambda(\text{nm})-1000]$.

The problem is thus reduced to solving for the optical field $\psi(r,\theta)$ in the 2D transverse direction. To simplify the problem further an ideal optically transparent disk of radius R is considered [Note: this is a change in notation from Chapters 2 and 3 where R represented reflectivity]. In this case, we require solutions to the Helmholtz equation

$$\nabla^2\psi + k^2\psi = 0 \tag{4.1}$$

where $k=n_{eff}\omega/c$. The two dimensional Laplacian ∇^2 is expressed in terms of polar coordinates r and θ as

$$\nabla^2\psi(r,\theta) = \frac{\partial^2\psi}{\partial r^2} + \frac{1}{r}\frac{\partial\psi}{\partial r} + \frac{1}{r^2}\frac{\partial^2\psi}{\partial\theta^2} \tag{4.2}$$

We then write $\psi(r,\theta)$ as a product of functions of r and θ:

$$\psi(r,\theta) = P(r)\Theta(\theta) \tag{4.3}$$

substituting (4.3) and (4.2) into (4.1), we obtain

$$\frac{r^2}{P}\frac{\partial^2 P}{\partial r^2} + \frac{r}{P}\frac{\partial P}{\partial r} + \frac{1}{\Theta}\frac{\partial^2\Theta}{\partial\theta^2} + k^2r^2 = 0 \tag{4.4}$$

where each term in (4.4) has also been multiplied by $r^2/P\Theta$. Since $\frac{1}{\Theta}\frac{\partial^2\Theta}{\partial\theta^2}$ is only a function of θ and $\frac{r^2}{P}\frac{\partial^2 P}{\partial r^2}+\frac{r}{P}\frac{\partial P}{\partial r}+k^2r^2$ is only a function of r, each of these two functions must be equal to a constant so that (4.4) may remain valid for all values of r and θ. Therefore,

$$r^2\left[\frac{1}{P}\frac{d^2P}{dr^2}+\frac{1}{rP}\frac{dP}{dr}+k^2\right]=M^2 \tag{4.5}$$

$$\frac{1}{\Theta}\frac{d^2\Theta}{d\theta^2}=-M^2 \tag{4.6}$$

where M^2 is called the separation constant.

The solution to (4.6), the θ dependent equation, is simply

$$\Theta(\theta)=Ae^{iM\theta} \tag{4.7}$$

where M=0, ±1, ±2,….to guarantee that $\Theta(\theta)$ is single-valued (i.e. $\Theta(\theta)=\Theta(\theta+2\pi n)$ for n=1,2,3….) and A is a constant.

To solve (4.5), we first rearrange the terms to get

$$\frac{d^2P}{dr^2}+\frac{1}{r}\frac{dP}{dr}+\left(k^2-\frac{M^2}{r^2}\right)P=0 \tag{4.8}$$

The general solution to the differential equation (4.8) is

$$P(r)=BJ_M(kr)+CN_M(kr) \tag{4.9}$$

where B and C are constants, $J_M(kr)$ is a Bessel function of the first kind of order M, and $N_M(kr)$ is a Bessel function of the second kind (Neumann function) of order M [12]. The singularity in the Neumann function at $r = 0$ means C must be zero for the field to remain finite at r = 0. Therefore, the optical field $\psi(r,\theta)$ for r<R is given by

$$\psi(r,\theta) = ABJ_M(kr)e^{iM\theta} \tag{4.10}$$

We now enforce a zero field boundary condition at the edge of the disk, $\psi(R,\theta)=0$. To satisfy this boundary condition kR must equal a root of the Bessel function of order M. The solutions for k satisfying this resonance condition ($J_M(kR)=0$) are labeled $k_{M,N}$, such that $k_{M,N}R = X_{M,N}$, the Nth zero of the Mth order Bessel function.

Therefore the resonant modes of an ideal transparent dielectric disk, assuming a zero field boundary condition are uniquely labeled by M and N the azimuthal and radial quantum numbers, respectively. The optical field of any such resonant mode for $r \leq R$ is given by

$$\psi(r,\theta) = A_{M,N}J_M(k_{M,N}r)e^{iM\theta} \tag{4.11}$$

where $A_{M,N}$ is a normalization constant. The optical field of the mode has M nodal diameters and N nodal circles. The resonant angular frequencies ($\omega_{M,N}$) and wavelengths ($\lambda_{M,N}$) of the disk are given by

$$\omega_{M,N} = \frac{X_{M,N}c}{n_{eff}R} \tag{4.12}$$

$$\lambda_{M,N} = \frac{2\pi n_{eff}R}{X_{M,N}} \tag{4.13}$$

Having derived expressions for the field, and frequency of the resonant modes of an ideal dielectric disk, we can identify the two extreme cases of modes. Modes with $M>>N$ which propagate about the edge of the disk and are known as whispering gallery modes (WGMs), and modes with $M<<N$ which are incident at the disk edge close to normal incidence, with only a small tangential component to their wavevector, and are known as quasi-radial modes (QRMs). WGMs are confined by TIR at a single semiconductor/air interface, and are the lasing modes in microdisk lasers. These modes are confined close to the disk boundary and have small modal volumes (Figure 4.4 (b)). Conversely, due to the large radial component of their wave vector, QRMs sample the entire disk (Figure 4.4(a)). Therefore the interaction of emitters evenly distributed across the disk is much greater with the QRMs than the WGMs [13], making the control of the QRMs essential to

controlling spontaneous emission from the entire structure. QRMs are not confined by TIR but should be confined by the circular Bragg leek structure.

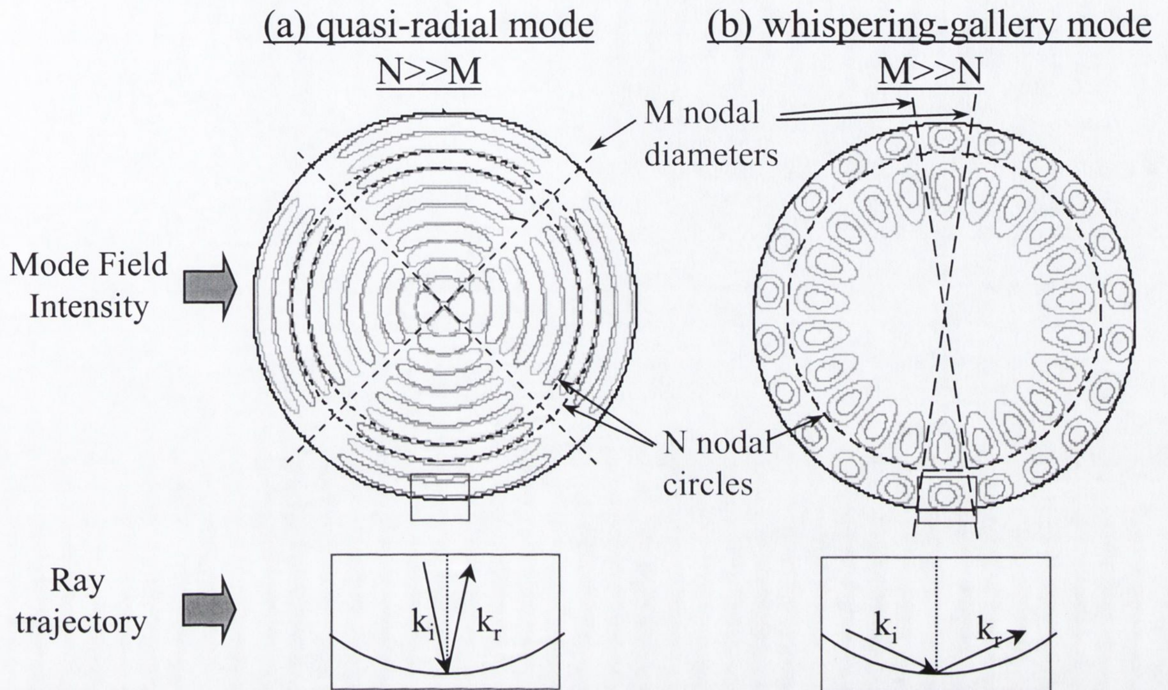

Figure 4.4 *Top - Mode structure of (a) a QRM with M=2, N=10 and (b) a WGM with M=11, N=2, of an ideal disk resonator. Bottom – Corresponding schematic ray trajectory for both modes, showing the incident (k_i) and reflected (k_r) wavevectors.*

Having reduced the problem of modelling the modes of our structures from a 3D to a 2D problem by using the effective refractive index of the guided mode of the slab waveguide, we have derived expressions for the fields and wavelengths of the modes of an ideal dielectric disk. However, the zero field boundary condition at the disk edge assumed in the derivation is only true for WGMs [14] in the microleek structure. Since the circular Bragg reflector used to confine the QRMs in the microleek structure relies on the constructive interference of reflections from successive interfaces to confine the light, the optical field penetrates beyond the central cavity edge into the mirror structure, resulting in a non-zero optical field at the cavity edge. In order to model the QRMs of the microleek structure of central cavity radius R, we calculate the QRMs of an ideal dielectric disk of refractive index n_{eff} and radius $R'=R+d$, where the additional term d accounts for the penetration of the field beyond the cavity edge. This approach fails to properly account for the multiple reflections utilized in the circular Bragg structure, and

the role played by the air trenches in the mode structure of the microleek. However it provides us with a simple model, with only one fitting parameter *d*, with which we can attempt to simulate and interpret our experimental results.

4.4 Experimental Setup

In order to investigate the emission properties of the microleek we have to selectively excite carriers in the central cavity of the structure. To do this using photoluminescence techniques requires an excitation spot smaller than the central cavity diameter, and an ability to image the surface of the sample.

The experimental setup used to perform photoluminescence measurements is shown in Figure 4.5. A mode locked Ti:sapphire laser, pumped using a 12watt Ar^+ laser, producing 2ps full width at half maximum (FWHM) pulses at a repetition rate of 83MHz and a wavelength of 830nm was used to excite carriers in the sample. The laser light was delivered to the system using a single mode fibre with a core diameter of 5.5μm. The use of this fibre ensured that the incident light originated from a well-characterized point source. The output from the fibre was collimated using a ×10, 0.25 NA microscope objective (MO1). The collimated beam was directed using a beamsplitter (BS1) onto a ×40, 0.65 NA microscope objective (MO2) positioned in front of the sample. The sample was positioned in the focal plane of the microscope objective resulting in an excitation spot of approximately 1.5μm diameter on the sample surface. The luminescence and reflected laser were collected by MO2, and the reflected laser light was removed using a GaAs filter to absorb light with $\lambda <$ 890nm. Approximately half of the collimated luminescence beam was directed toward the spectrometer using a beamsplitter (BS2), and focused onto the entrance slit of the spectrometer using a 10cm focal length lens. The spectrometer consisting of a monochromator (JobinYvon HR320) with a Hamamatsu microchannel plate (MCP) photomultiplier tube (PMT) positioned at the exit slit, had a resolution of ≈0.5nm. The portion of the collimated luminescence beam transmitted by the beamsplitter (BS2) is focused using a 20 cm focal length lens (L2) onto a 1317×1035 pixel air-cooled CCD array. The choice of a 20 cm focal length for L2 provides an overall

system magnification of ×40 between the object (sample surface) and detector (CCD array) planes. Therefore one pixel (pixel width = 6.8μm) on the CCD camera corresponds to 170nm on the sample surface, enabling the accurate positioning of the excitation spot on the microleek cavity centre.

When performing the low temperature measurements on the microleek structures containing QDs, the sample was mounted in an open cycle liquid nitrogen cryostat, which allowed temperature tuning between 77K-297K. A ×40, 0.5NA microscope objective with a long working distance of ≈8mm was used as lens MO2 when the sample was in the cryostat. Since the magnification of the microscope objective is unchanged from that used for room temperature measurements the overall magnification of the imaging system was unchanged. However the lower NA of the microscope objective used to perform low temperature measurements resulted in a slightly larger excitation spot of FWHM ≈2.0μm on the sample.

The MCP-PMT positioned at the output slit of the monochromator also formed part of a time correlated single photon counting (TCSPC) system used to perform time-resolved PL measurements. In order to achieve single photon detection the MCP-PMT was biased to 3000Volts. In a TCSPC system the time difference between a reference signal synchronized with the laser excitation pulses and a detected luminescence photon collected from the sample is measured [15]. A histogram of the time differences between the laser pulse and luminescence photon produces a plot of light intensity as a function of time. The time resolution of the system was ≈80ps.

This setup enabled the simultaneous measurement of high resolution near field emission patterns, PL emission spectra and PL emission lifetimes from the microleek structure. The setup was adapted to perform the same measurements in the temperature range (T=77K to 297K) using a liquid nitrogen cryostat.

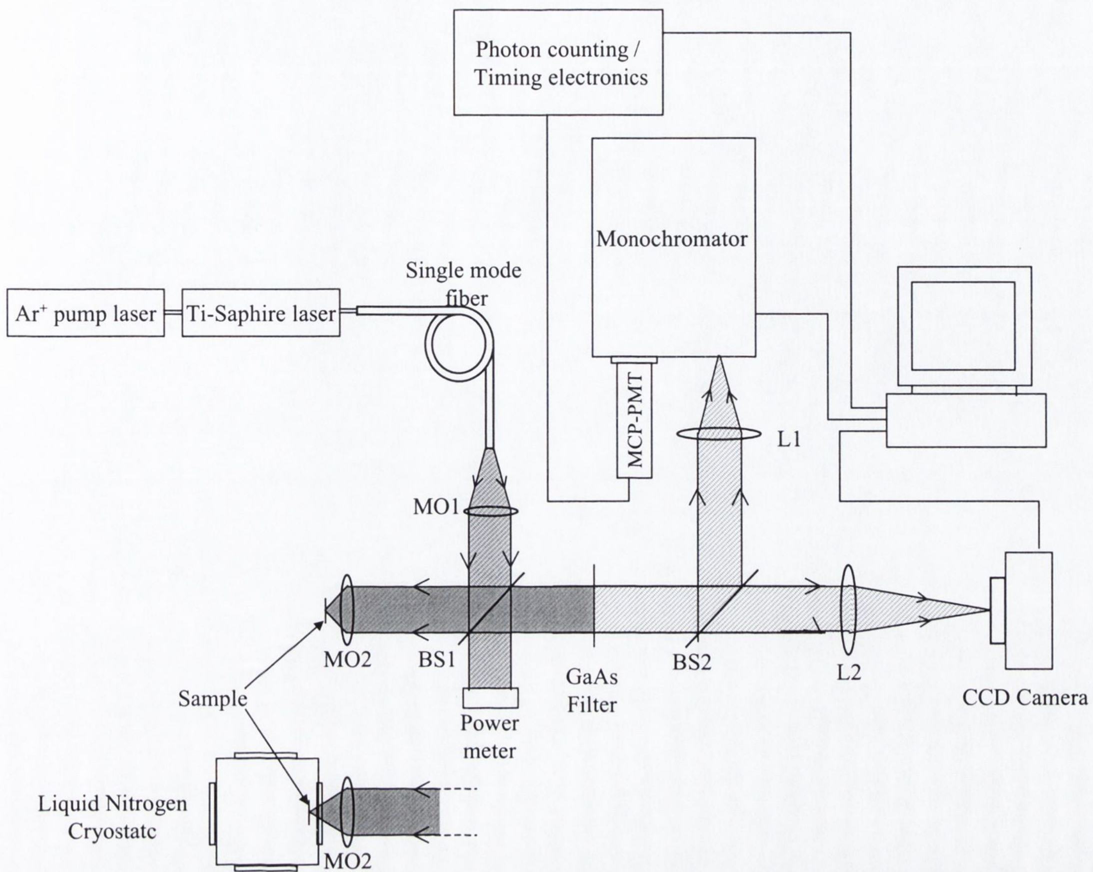

Figure 4.5 *Diagram of experimental setup used to perform photoluminescence measurements on the microleek structure. MO1= ×10, 0.25 NA microscope objective, MO2= ×40, 0.65 NA microscope objective (MO2= ×40, 0.5 NA when using cryostat), L1 = 10 cm focal length spherical lens, L2 = 20 cm focal length spherical lens, and BS = beamsplitter.*

4.5 Emission processes in Microleek structure.

Using the setup described in section 4.4 to perform PL measurements we can selectively excite carriers in the central cavity of the microleek structure. These carriers can recombine either radiatively or non-radiatively. The role of non-radiative recombination at defects in bulk semiconductor material and at the etched interfaces of the air trenches is discussed in Chapters 5 and 6 respectively. In this chapter we focus on the radiative recombination processes in the microleek to determine the mode structure of the cavity and the effect this modified mode structure has on light-matter interaction in the cavity.

Light produced by the radiative recombination of carriers in the cavity centre can couple to either guided or unguided modes of the vertical waveguide. Light that is emitted into unguided modes escapes into air or the substrate. Since these unguided modes do not impinge on the lateral mirror structures, emission into these modes does not experience any lateral confinement. Therefore any cavity effects will only be experienced by the in-plane guided emission. This in-plane guided emission couples to the modes of the 2D cavity and is out coupled into air through diffraction at the circular Bragg reflector as shown in Figure 4.2.

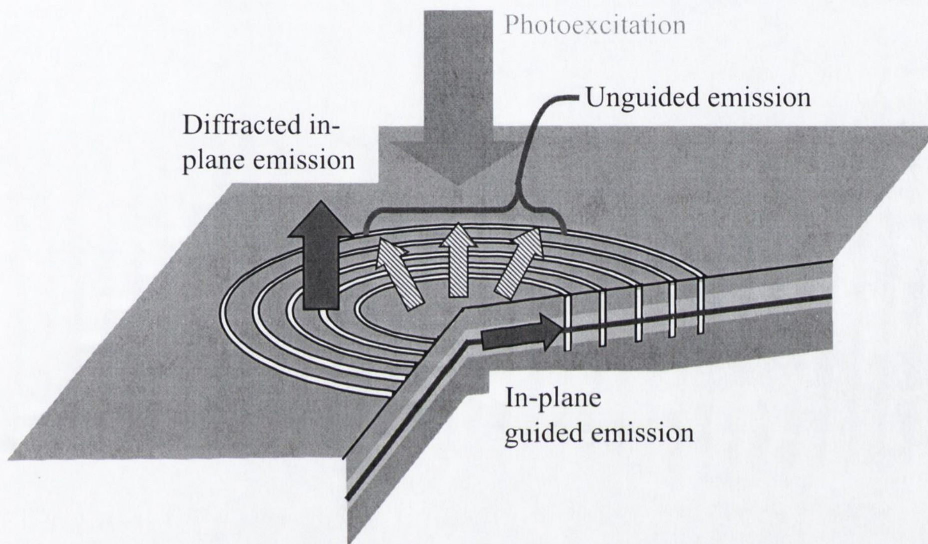

Figure 4.6 *Schematic diagram of radiative emission processes in microleek structure.*

4.6 Microleeks containing Quantum Wells.

4.6.1 Lasing Results

When performing PL measurements at room temperature a sudden and simultaneous change in both the nearfield emission pattern and emission spectrum was observed, when the excitation power was increased above a certain threshold. The nearfield changed from a featureless disk to a distinct lobed pattern (Figure 4.7). This shows that below the

threshold, collected luminescence consisted of a mixture of unguided emission from the centre of the microleek, and light diffracted upwards out of the confined modes of the structure by the circular Bragg mirror, while above the threshold, very little unguided emission occurs from centre of the structure, with the collected luminescence being dominated by light diffracted from the circular Bragg mirror. This indicated that the emission changed from being roughly isotropic to being highly directional in the plane of the waveguide. The spectrum of collected luminescence changed at the same threshold pump excitation intensity from consisting of several small, broad peaks superimposed on a background emission, to a spectrum dominated by one or two narrow peaks with FWHM < 1nm.

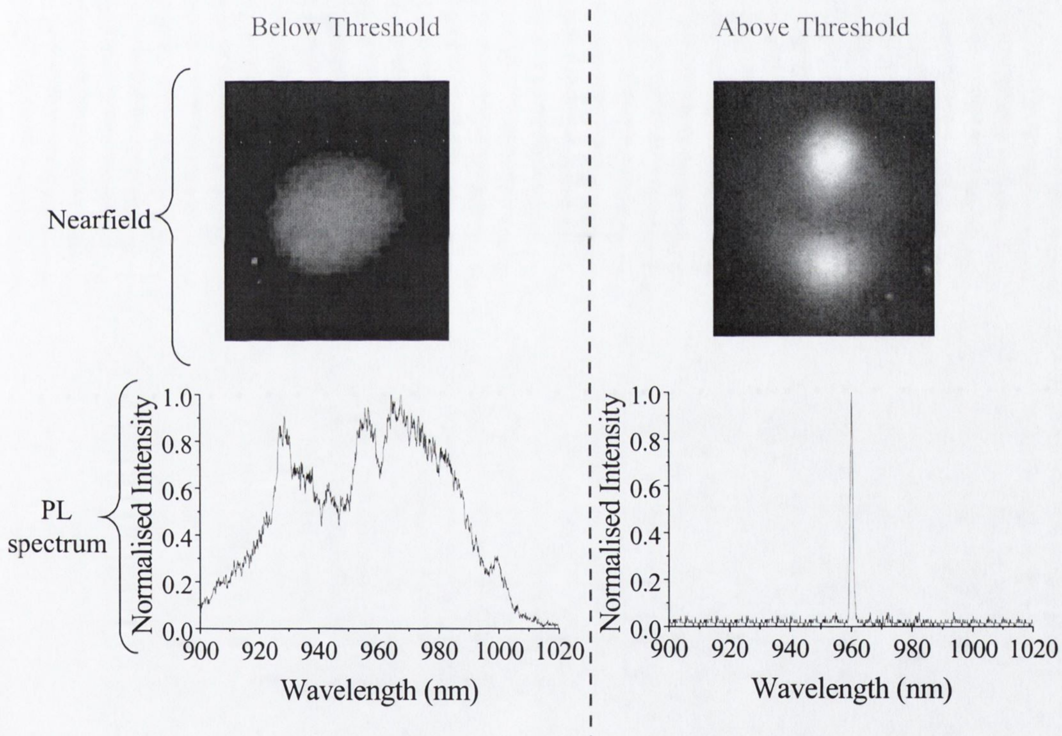

Figure 4.7 *Typical Measured nearfield and PL spectra below and above threshold.*

To confirm that the threshold behaviour observed was due to the occurrence of lasing, a light-light curve was measured which showed a clear threshold at the same pump power of 0.45mW, corresponding to an average pump intensity of 14.2kWcm^{-2}. Given the excitation wavelength of 830nm, the pump beam is not absorbed in the two AlGaAs cladding layers, but only in the central GaAs cavity and QWs, whose total thickness, L_{GaAs}, is 220nm. A typical value for the absorption coefficient of GaAs at the pump wavelength is α_{pump} = 6000cm^{-1}[16], hence $\alpha_{pump} \cdot L_{GaAs}$ = 0.132. Combined with the ≈ 30% reflection of the incident laser at the air/GaAs interface, this gives an absorbed pump power at threshold of 1.3 kWcm^{-2}. As our excitation laser produced mode-locked pulses at a repetition rate of 83MHz, with incident photon energy of 1.5eV, the peak carrier density per quantum well at threshold is calculated at approximately 2.2×10^{13}cm^{-2}. This carrier density can be converted to an equivalent average current density per quantum well, J, of 3.9 kAcm^{-2} using the expression $J=nq/\tau$, where n is the carrier density per unit area, q is the electronic charge, and τ is the carrier lifetime, measured as 0.9ns.

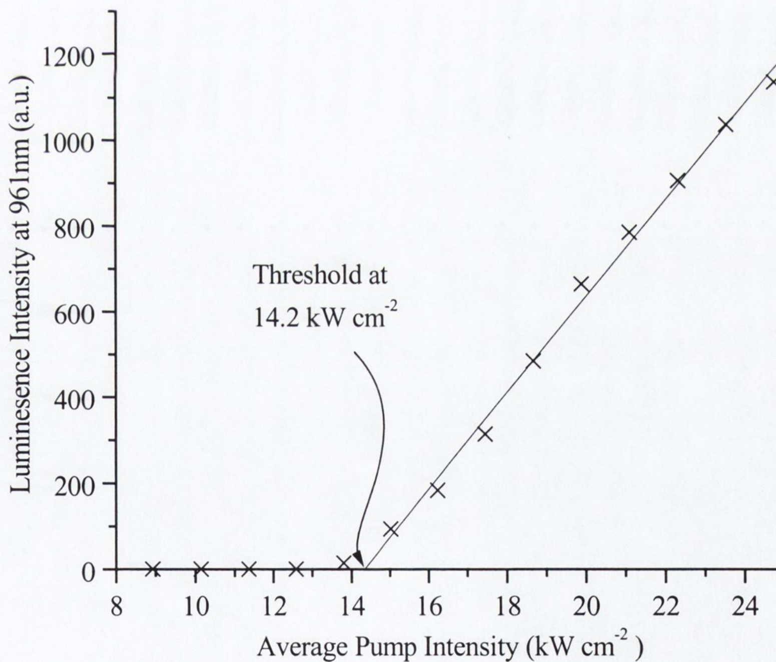

Figure 4.8 *Luminescence intensity vs. Pump Intensity for microleek structure, central cavity diameter = 3.2μm, surrounded by a 6 period circular Bragg reflector with Λ=640nm. The threshold pump intensity is extrapolated from a straight line fitted to the data points with pump intensities greater than 16 kWcm^{-2}.*

By treating the quasi-radial modes of the microleek structure as modes of a 1D cavity of length equal to the diameter of the central cavity, we can calculate a value for the theoretical threshold gain, g_{th}, using the equation [17]

$$\Gamma g_{th} = \frac{1}{2R} \ln\left(\frac{1}{R_{CBR}} \right) \qquad (4.14)$$

where Γ is the confinement factor, $2R$ is the cavity diameter, and R_{CBR} is the lateral circular Bragg mirror reflectivity near normal incidence. From the calculated guided mode profile we estimate $\Gamma = 0.1$. The reflectivity of the circular Bragg structure is estimated at ≈90% from cavity mode linewidth measurements for similar structures as shown in section 4.7.1, and from previously reported values [4]. Using these values, we obtain a theoretical estimate for the threshold gain required to observe lasing in the quasi-radial modes of the microleek structure of g_{th} = 3200cm^{-1} or a gain of approximately 1100cm^{-1} per quantum well. Such a material gain should be observed at the peak gain of InGaAs/GaAs quantum wells at a radiative current density of 110Acm^{-2} per quantum well [18]. The large discrepancy between the calculated threshold radiative current density of 110Acm^{-2} and the measured threshold current density of 3900Acm^{-2} can be attributed to the loss of carriers through non-radiative recombination at the etched trench surrounding the central cavity and the spectral mismatch between the peak in the QW gain and the lasing mode.

Since the primary focus of this project is on the use of microcavities to control spontaneous emission processes in semiconductors, we are more concerned with what the lasing properties of this structure can tell us about the confinement and mode structure of the microleek, than in the development of the structure as a practical laser device. From this perspective, the real benefit of the above threshold measurements is the unique identification of the nearfield emission profile and associated wavelength of individual modes of the microleek cavity. The nearfield emission profiles show the number of nodal diameter in the field of the lasing mode, (i.e. 2 lobed emission profile corresponds to 1 nodal diameter in the field, and a 4 lobed profile to 2 nodal diameters). Since the number of nodal diameters in the mode field equals the azimuthal quantum number (M) of the mode, we can unambiguously identify the existence of a mode of a known M value at a

given wavelength. From Figure 4.9(a) we identify an M = 1 (two lobed) mode at λ=996nm, and from Figure 4.9(c) we identify an M = 2 (four lobed) mode at λ = 960nm, in both cases for a microleek structure with a central pillar radius of 1.6μm. Taking a value of d = 55nm to account for the penetration of the QRM modes into the mirror structure, the mode wavelengths of a disk of radius R'(=R+d) of 1.655nm were calculated using (4.13) and are shown in Figure 4.9(b). This value of d predicts the existence of N=11 modes with the correct M values and approximately correct wavelengths to agree with experimental results.

The occurrence of lasing in the M=1 mode in only one direction indicates a lack of

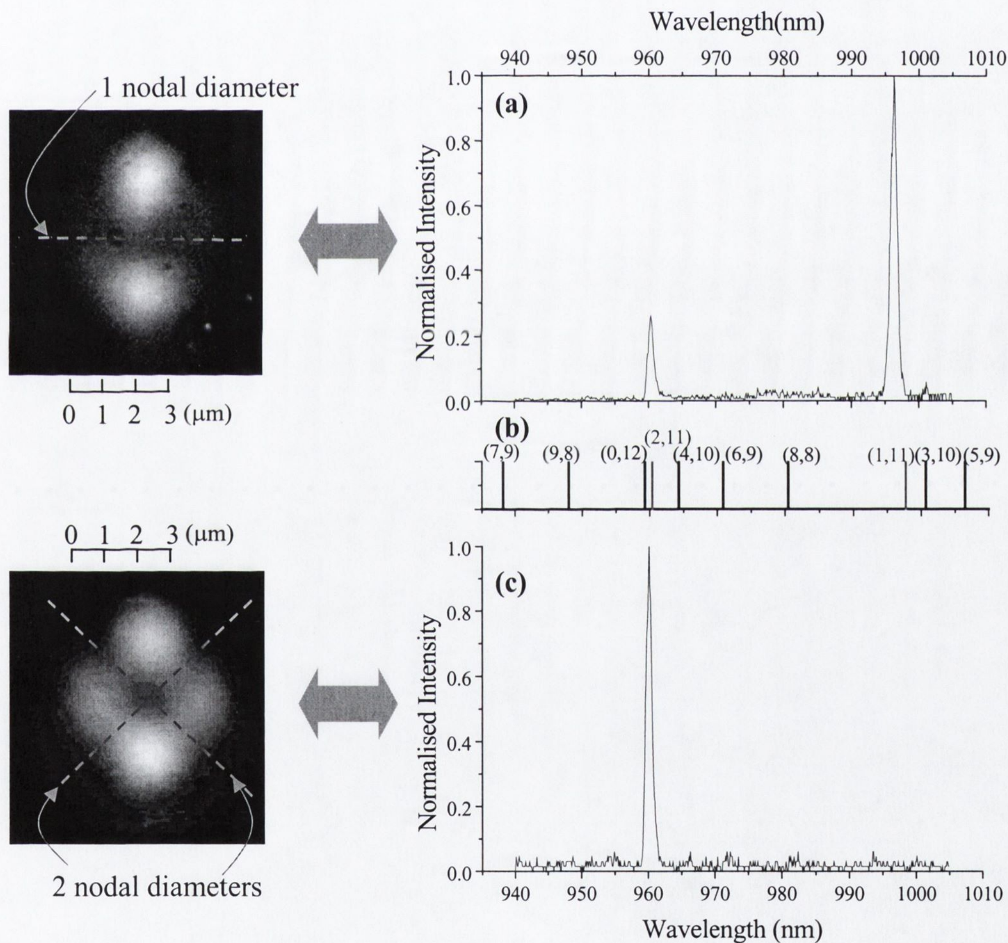

Figure 4.9 *Above threshold spectra and associated nearfield emission profiles of Λ=640nm structures with (a) 5 reflector periods and (c) 7 reflector periods. In (b) the calculated mode wavelengths of a disk of radius R'=1655nm, labeled (M,N) are shown.*

azimuthal symmetry in the microleek structure. This asymmetry may be due to slight variations in etched trench width in the x and y directions, as reported for the "fingerprint" structures [5], or a slight ellipticity of the central post. Variations in etch trench width would result in azimuthal variations in mirror reflectivity and scattering losses. Any ellipticity of the central pillar would also remove the azimuthal symmetry of the structure [19]. An asymmetry in the nearfield of the $M = 2$ mode in Figure 4.9(c) is also observed, with the top and bottom lobes brighter than the left and right lobes as shown. This can again be explained by a variation in the trench width in the x and y directions resulting in a higher diffraction efficiency of the lasing mode into the collection cone of our microscope objective at the top and bottom of the structure.

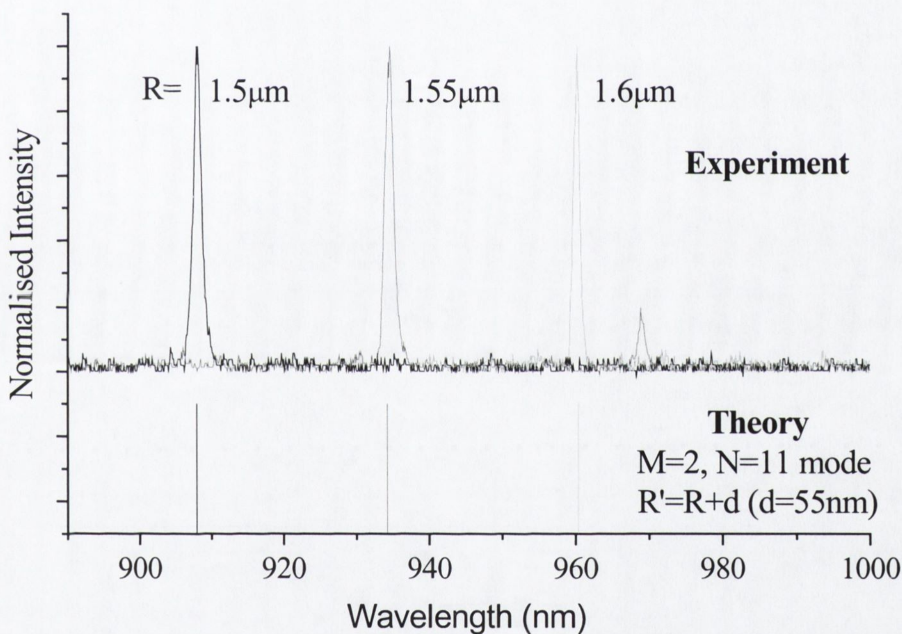

Figure 4.10 *Lasing spectra of 6 period Λ = 600, 620 and 640 nm microleeks, compared to the calculated wavelengths of the M=2, N=11 mode.*

Lasing was also observed in microleek structures with Λ = 600, 620 and 640 nm. The lasing spectra of modes, identified as $M = 2$ modes from nearfield images, for the three different sized devices are shown in Figure 4.10. Also shown are the calculated mode wavelengths of the M=2, N=11 modes, using the same value of d = 55nm. The results of our measurements on the lasing properties of microleeks are summarized in Table 4.1.

Radius of central pillar, (=5×Λ) R (nm)	M number of lasing mode, (from nearfield) M	Measured wavelength of lasing mode. λ_{meas} (nm)	Calculated wavelength of mode of correct M number and N=11 for disk of radius $R'=R+d$, d=55nm. λ_{calc} (nm)
1600	1	996.3 ± 0.5	997.7
1600	2	960.2 ± 0.5	960.4
1550	2	934.5 ± 0.5	934.2
1500	2	908.0 ± 0.5	907.9

Table 4.1 *Summary of measurements of lasing properties of microleeks.*

The final two columns of Table 4.1 show the excellent agreement between the measured and calculated mode wavelengths using a value of d = 55nm in the model. To check whether other values of d, which might give as good or better agreement with measurements, exist, the difference between the measured mode wavelength and the nearest modelled mode wavelength with the correct M quantum number was calculated for a range of d values. The results in Figure 4.11 show how values of d around 195nm and 330nm can produce good agreement between theory (N=12 and N= 13 modes respectively) and experiment for individual modes, however the values of d required for agreement differ for different modes. Figure 4.12 shows how d = 55nm produces the best overall agreement between the modelled and measured wavelengths for the four modes, with the average difference equaling 0.5nm, which is equal to the resolution of our spectrometer. The best fit of the experimental modes to modelled N=12 (N=13) modes occurs for d = 195 nm (336nm) giving an average difference between modelled and measured wavelengths of 1.8nm (3.8nm).

While any error in n_{eff} would translate itself into an error in d if results from only one sized device were considered, a single value of d cannot correct for any error in n_{eff} when microleeks of different diameter are considered. Therefore the success of our model in reproducing the mode wavelengths for different sized devices suggests that the error in our value of n_{eff} is small and that our fitted value for d is well defined.

As previously mentioned the fitting parameter d accounts for the penetration of the optical field of the quasi-radial modes into the lateral CDBR mirror structure. The penetration of the optical field is a consequence of the distributed nature of reflections from a Bragg mirror and can be accounted for by an equivalent model of an ideal mirror positioned at a distance known as the penetration depth inside the Bragg mirror structure. An estimate for the penetration depth can be obtained from the calculated variation in the phase of the reflection across the DBR stopband [20], with typical values of 1.5λ obtained for $\lambda/4$ GaAs/AlAs DBRs [21]. The variation in the phase of the reflected light from our CDBR across the spectral stopband at normal incidence was calculated using the transfer matrix method outlined in Appendix A2, from which a penetration depth of 150nm was estimated. While this is less than the period of our CDBR, the high reflectivity at each interface of the first air trench of the structure makes such a small penetration depth possible. This estimate for the penetration depth is considerably larger than the fitted d value of 50nm used to model our measured results, however both our model for the modes of the microleek structure and our calculated estimate for the penetration depth are simplified approximations of the optical properties of the physical structures. Despite this it should also be considered that different modes might penetrate different depths into the CDBR, so that different d values may be appropriate for different modes, which would allow the matching of N=12 modes with slightly different d values of $\approx$195nm to the measured lasing modes as shown in Figure 4.11. Therefore while a single fitted d value of 55nm reproduces the observed lasing properties, it appears small in the context of its interpretation as a penetration depth, with calculated estimates suggesting a larger value would provide a more physically meaningful value.

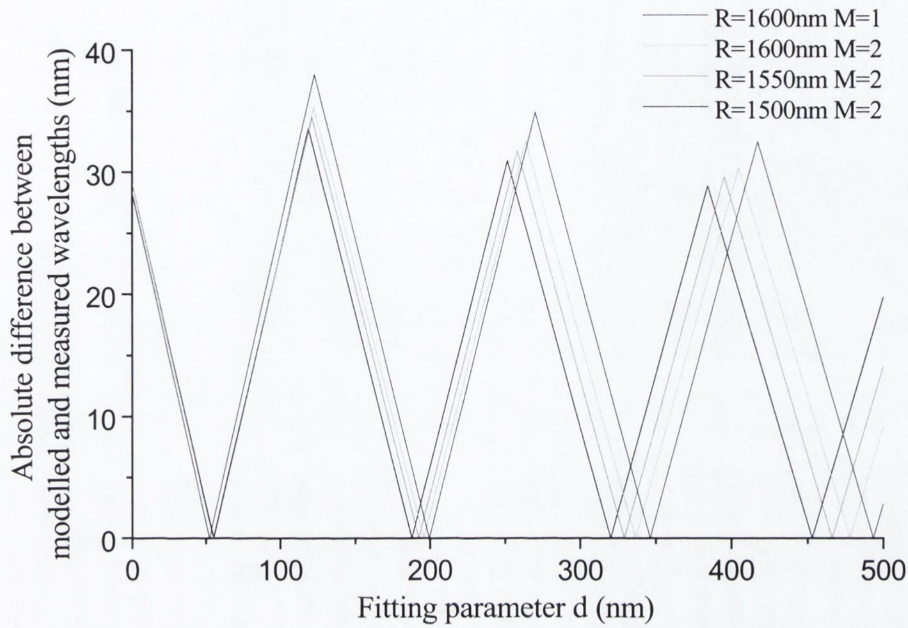

Figure 4.11 *Difference between measured and nearest modelled wavelength of correct M number, for 4 modes listed in Table 4.1 as a function of fitting parameter d.*

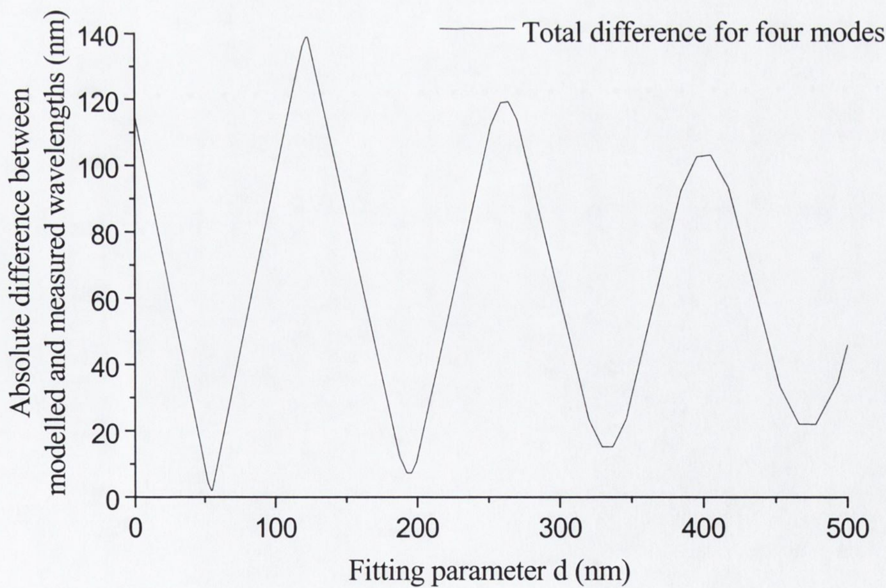

Figure 4.12 *Overall difference between measured and nearest modelled wavelength of correct M number for 4 modes listed in Table 4.1 as a function of fitting parameter d.*

4.6.2 Summary

Lasing has been observed in a microleek structure containing quantum well emitters. The measurement of nearfield emission patterns has enabled the identification of the azimuthal component (M number) of the lasing mode. The measured wavelengths of modes with different M numbers (1 and 2) and from different diameter devices have been successfully modelled using the modes of an ideal disk resonator. The model contained a single fitting parameter to account for the penetration of the QRM fields into the lateral mirror structure. The radial quantum number of the lasing modes were determined from the model as N=11, and hence the lasing modes were clearly identified as QRMs ($M<<N$), which are not confined in standard microdisk structures. The observation of lasing in the QRMs of the microleek structures, albeit at high carrier densities, confirms the high reflectivity of the etched circular Bragg reflector used to confine these modes. The small value of d, which accounts for the penetration of the mode into the mirror, used to successfully model the mode wavelengths, highlights the strong confinement of the QRMs to the central cavity of the microleek structure.

4.7 Microleeks containing Quantum Dots

The reasons for incorporating QDs as emitters in microleek structures were threefold:

- they provide a broad band PL spectrum without any sharp features which enables the clear identification of the cavity modes over a wide range of wavelengths [22].
- carrier trapping in the QDs should reduce the effect of non-radiative recombination at the etched walls.
- the discrete electron energy levels in a single quantum dot ensure an electronic transition spectrally narrower than the cavity mode, thereby enabling it to experience the full enhancement of the cavity mode [23].

Having established the strong 3D confinement of light in the microleek structure, our primary motivation for studying similar structures containing QDs was to establish whether the microcavity effect was sufficient to produce an enhanced spontaneous emission rate. However as a first step the modes of these structures had to be identified

since only emission into a cavity mode experiences any cavity effect. The PL spectral measurements used to establish the cavity mode wavelengths are presented in section 4.7.1. The time resolved PL measurements on the structures are presented in section 4.7.2.

4.7.1 Photoluminescence spectra

Photoluminescence spectra and nearfields were measured for a range of microleek structures (Λ=600nm, 620nm, and 640nm) containing QDs, however lasing was not observed even at high carrier densities. This can be explained by the lower peak optical gain of the QDs relative to QWs due to the large inhomogeneous broadening in the QD layer (see Chapter 5). Since lasing was not observed no insight into the mode structure could be obtained from the nearfield patterns, however the spontaneous emission PL spectra from the microleek structures displayed clear peaks, not present in the PL spectrum from QDs outside the cavity.

Similar spontaneous emission PL spectra of microleek structures containing QDs were first measured at room temperature and explained in terms of QRMs by Labilloy et al. [4], using the model outlined in section 4.3. However, since cryogenic temperatures were required when investigating PL lifetime effects, the mode structure of the devices had to be mapped as a function of temperature. The spectra were modelled following the approach of [4], with the modes in the simulated spectra weighted by an *ad hoc* visibility factor $g(M)=\mathrm{sinc}^2[(M+1)/12]$, to account for the impaired collection efficiency with increasing M. This is due to the greater azimuthal component of a mode's wavevector as M increases, resulting in light diffracting out of the mode at increased angles from the vertical, reducing the probability of collection within the limited NA of the microscope objective. The modelled mode linewidths are a result of an assumed cavity finesse F = 50. ($F=FSR/\Delta\lambda$ where $\Delta\lambda$ is the FWHM of cavity mode and FSR is the free spectral range between two modes of the same parity (same value of M, N values differ by 1) [34]).

The additional temperature dependence of the cavity mode structure is modelled using literature values for the temperature coefficient of the refractive index *dn/dT* of GaAs as 3×10^{-4} K^{-1}[24] and $Al_xGa_{1-x}As$ (e.g. AlAs value of 1.25×10^{-4} K^{-1}) [25], and assuming a linear thermal expansion coefficient of 6×10^{-6}m K^{-1}[26].

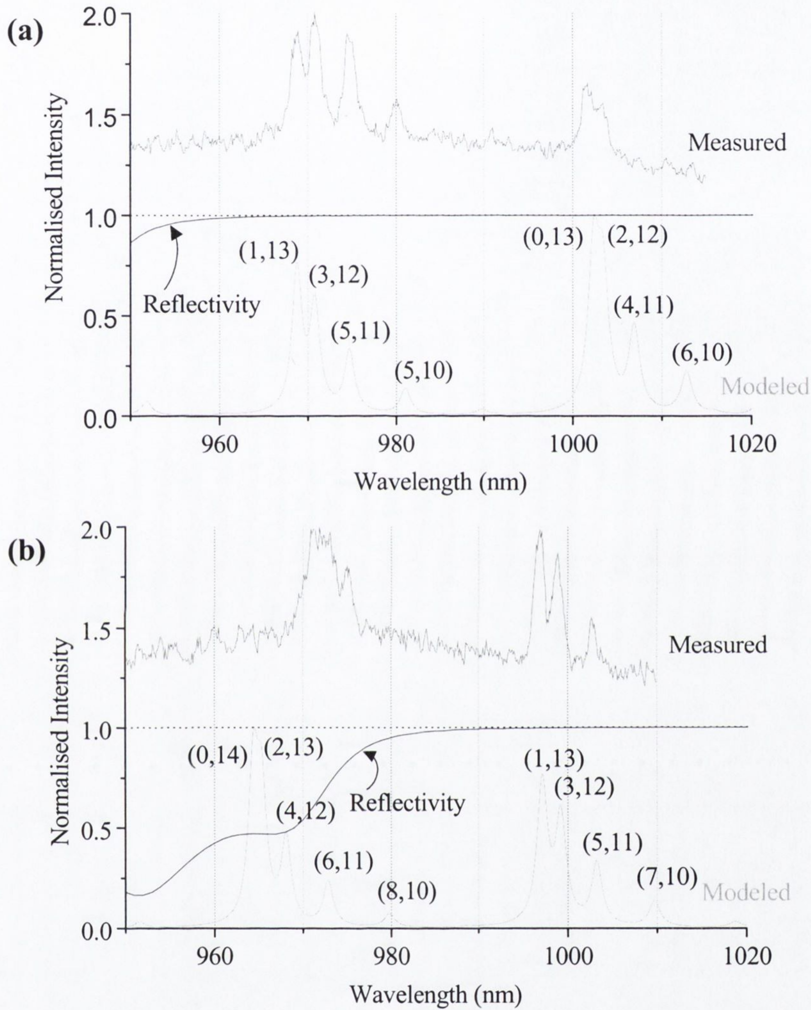

Figure 4.12 *Measured and simulated PL spectra from 8 period microleek structures with (a) Λ=620nm and (b) Λ=640nm at T=125K. The modelled spectra assume a cavity finesse of 50 and the mode amplitudes are weighted to account for the light collection efficiency dependence on mode M number. The numbers in parentheses are the mode quantum numbers (M,N). The modelled reflectivity of the circular Bragg reflector of the structures for normally incident light (i.e. light propagating along the radius of the structure) is also shown. The measured spectra are offset by 1 for clarity.*

Good agreement between the measured and modelled PL spectra for two microleek structures at an intermediate temperature of T=125K are shown in Figure 4.12, for a value of d = 360 nm. Both the mode positions and linewidths are reproduced by the model, while the general trend of decreasing intensity with increasing M number is observed in the measured spectra.

The success of our simple linear approximations in reproducing the temperature dependence of the (M,N)=(1,13) mode wavelength is shown in Figure 4.13, while similar agreement was observed for other modes.

The larger value of d=360nm required to reproduce the experimental spectra for the microleek structures containing QDs compared to d=55nm for the microleek structures containing QWs, indicates greater penetration of the mode fields into the Bragg reflector in the structures containing QDs. This is probably due to a slightly greater trench etch depth in the structures containing QWs, which results in a greater interaction between light in the guided mode and the etched mirror structure. The reflectivity, R_{CBR} of the circular Bragg reflector can be estimated from the value of F used to model the spectra. The approximation $F \approx \pi / (1-R_{CBR})$ for a planar Fabry-Perot mode in the limit $R_{CBR} \approx 1$ [27] is still valid for the microleek structures since $R >> \lambda/(2\pi n_{eff})$ (where R is the microleek central cavity radius), giving $R_{CBR} \approx 1 - \pi/F \approx 94\%$.

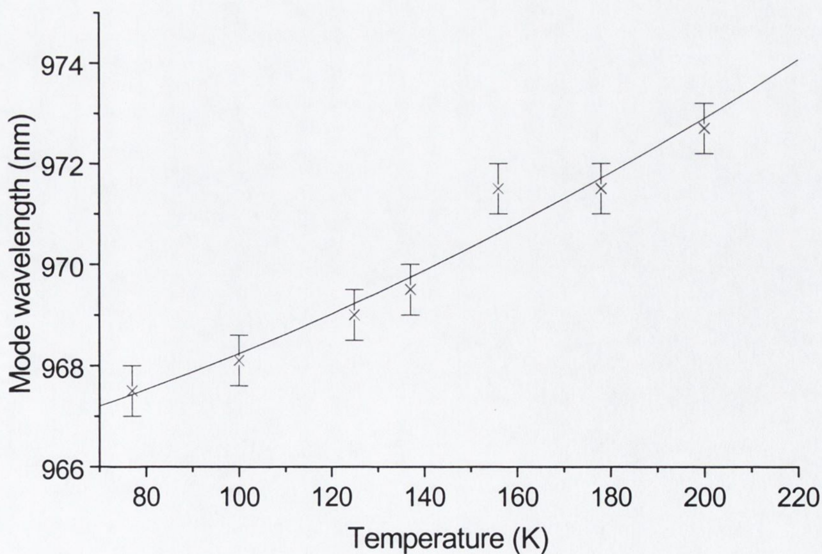

Figure 4.13 *Measured (data points) and modelled (solid line) wavelengths of (1,13) mode of Λ=620 nm microleek structure as a function of sample temperature.*

We have measured the spontaneous emission PL spectra from microleek structures in the temperature range T=77K to 297K, and shown that our model can be adapted to reproduce the observed cavity mode structure. The measurements confirm the high reflectivity of the circular Bragg reflector and the strong confinement of the cavity modes to the central pillar of the microleek.

4.7.2 Photoluminescence Lifetimes

The ability of a cavity to modify the spontaneous emission rate of a dipole by altering the dipole-field coupling and the density of available photon modes, a phenomenon known as the Purcell effect [28], was introduced in Chapter 2. We saw that the enhanced light-matter interaction due to the cavity is only sufficient to produce a significant modification of spontaneous emission rate when the cavity confines light to wavelength scale dimensions in all three directions, confirmed by measured enhancement factors for micropillar and microdisk structures [29]. Time resolved PL measurements were performed on the microleek structures to determine whether a cavity-induced enhancement of the spontaneous emission rate was present.

The correct choice of emitter in the cavity is essential if any effect is to be observed. Firstly, the spectral linewidth of the emitter must be narrower than the cavity mode linewidth, if the emitter is to experience the full effects of the cavity. Secondly, the emitters must be localised within the cavity to prevent non-radiative recombination at the microcavity sidewalls dominating the intrinsic cavity effects. InAs/GaAs QDs at low temperatures fulfill both these requirements, with individual dots possessing a narrow emission line with a FWHM < 0.15meV [30], and efficient carrier capture and trapping in the nanometer scale QDs resulting in localised emitters. However, at room temperature carriers have sufficient thermal energy to escape from the quantum dots, resulting in non-localised emitters in the cavity. Therefore, the PL lifetime measurements have to be performed at cryogenic temperatures.

An expression for the spontaneous emission rate of an emitter into the cavity mode, relative to the emission rate in a homogeneous surrounding medium can be derived from Fermi's Golden Rule (see Appendix A1), and is given by

$$\frac{\tau_0}{\tau_{cav}} = \frac{3Q(\lambda_c/n)^3}{4\pi^2 V_{eff}} \cdot \frac{\Delta\lambda_c^{\ 2}}{4(\lambda-\lambda_c)^2 + \Delta\lambda_c^{\ 2}} \cdot \xi^2 \left|\vec{f}(\vec{r}_e)\right|^2 \quad (4.15)$$

for an emitter of wavelength λ located at r_e, where τ_0 is the emission lifetime in a homogeneous medium of refractive index n, and τ_{cav} is the emission lifetime into the cavity mode. λ_c is the cavity mode wavelength; $\Delta\lambda_c$ is the FWHM of the cavity mode; n is the refractive index; Q $(=\lambda_c/\Delta\lambda_c)$ is the cavity quality factor; V_{eff} is the effective mode volume, defined as the spatial integral of the vacuum field intensity for the cavity mode, divided by its maximum value; $\vec{f}(\vec{r})$ is the normalised mode spatial function; and $\xi = \left|\vec{d}.\vec{f}(\vec{r}_e)\right| \Big/ \left|\vec{d}\right|\left|\vec{f}(\vec{r}_e)\right|$ describes the orientation matching of the electric dipole of the emitter, $\vec{d}$ and $\vec{f}(\vec{r}_e)$. The second term on the right hand side of (4.15) describes the spectral matching between the emitter and cavity mode wavelengths, while the third term in (4.15) describes the orientational and spatial matching between the emitter and the cavity mode. Both terms are equal to unity for a dipole emitting at λ_c, located at an antinode, and aligned with the electric field of the cavity mode. For such an emitter exactly matched both spectrally and spatially to the cavity mode, the enhancement factor is given by the Purcell factor, F_p.

$$F_p = \frac{\tau_0}{\tau_{cav}} = \frac{3Q(\lambda_c/n)^3}{4\pi^2 V_{eff}} \quad (4.16)$$

F_p corresponds to the largest enhancement the cavity can induce and hence acts as a figure of merit for the cavity. However when considering practical structures the spatially and orientation distribution of all emitting dipoles in the cavity contributing to the measured emission has to be taken into account.

A cavity induced modification of the spontaneous emission rate is unambiguously identified by comparing the measured PL lifetimes from emitters in the cavity at $\lambda=\lambda_c$ and at $\lambda\neq\lambda_c$. Only emitters with $\lambda=\lambda_c$ will couple to the cavity mode and experience any cavity-induced enhancement of the emission rate while emitters at $\lambda\neq\lambda_c$ can only couple to the leaky modes of the cavity. Since both lifetimes are measured for emitters in the

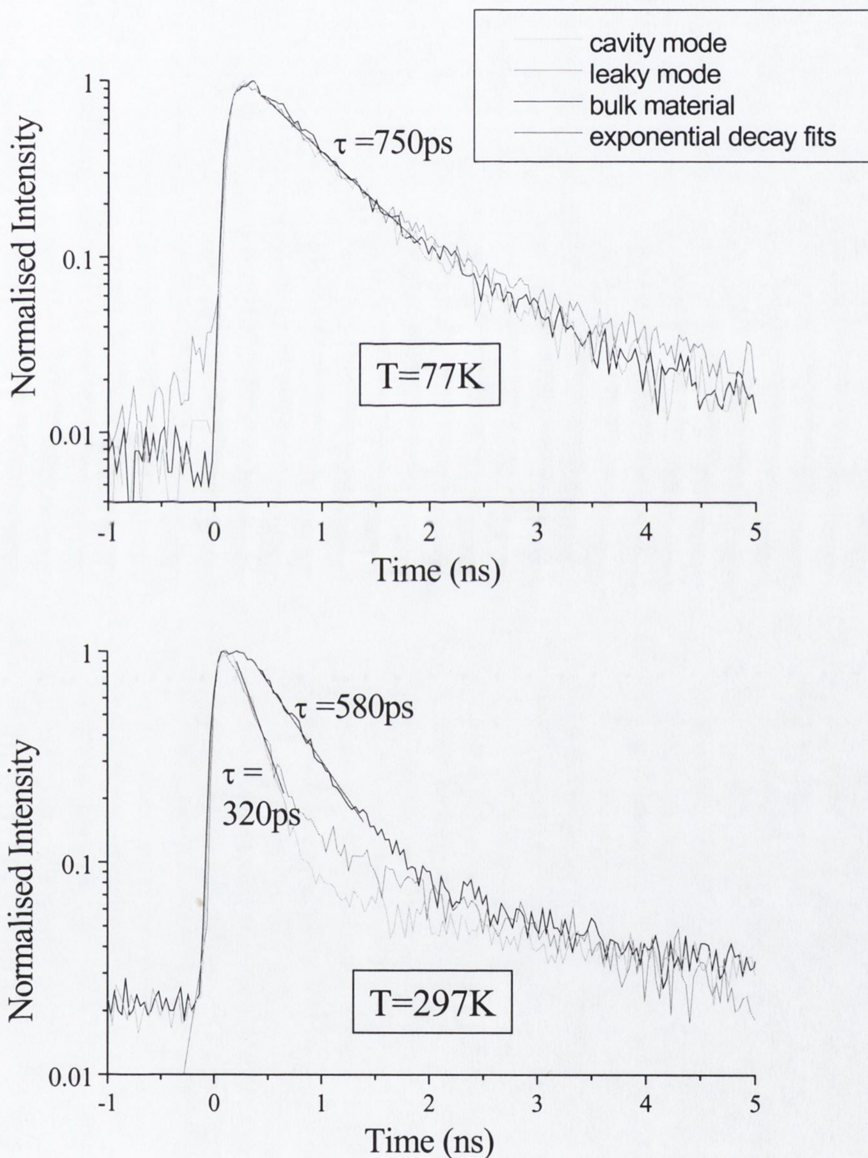

Figure 4.14 *Measured PL lifetimes at T=77K (top) and T=297K (bottom). Measurements were performed on an 8 period Λ= 620nm (R=1.55μm) structure, using the (3,12) mode as the cavity mode.*

cavity any effects due to the presence of the etched microcavity sidewalls such as increased non-radiative recombination, will be evident in both measurements. Therefore, a difference in these two measurements is taken as evidence of a cavity induced modification of the spontaneous emission lifetime.

While photon recycling effects can lead to an increase in the emission lifetime, the long absorption length for light in the guided mode by the QD layer (≈100μm [31]), combined with the small dimensions of the microleek, results in a prediction of the reabsorbed fraction of emission of < 0.08 [32], and hence an increase in the emission lifetime by a factor of < 0.09 (see section 2.7).

Figure 4.14 shows the measured PL decays for emission into (i) the (3,12) cavity mode of an R=1.55μm microleek structure, (ii) leaky modes at a slightly shorter wavelength of the same structure and (iii) modes of bulk material (away from any etched features). A single exponential of the form

$$I(t) = I_0 \exp(-t/\tau) \tag{4.17}$$

was fitted to the initial portion of each measured PL decay to determine the emission lifetime, τ. At T=77K the measured PL lifetimes for the three situations are the same (τ ≈750ps). Therefore, there is no Purcell effect in these microleek structures with $R \approx$ 1.5μm. At T=297K there is a significant difference between the emission lifetime from QDs coupled to the cavity mode (τ =320ps) and QDs in bulk material (τ =580ps), however a reduced lifetime is also observed for QDs in the structure coupled only to the leaky modes of the cavity due to their emission wavelength. Since any cavity induced

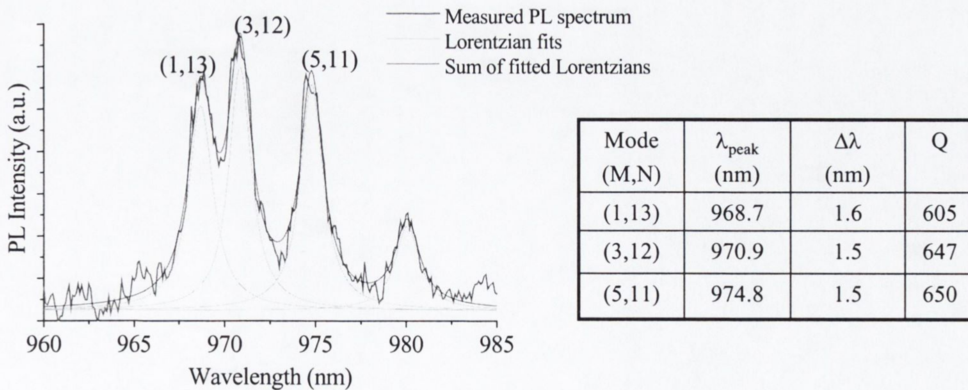

Mode (M,N)	λ_{peak} (nm)	$\Delta\lambda$ (nm)	Q
(1,13)	968.7	1.6	605
(3,12)	970.9	1.5	647
(5,11)	974.8	1.5	650

Figure 4.15 *Plot showing best-fit Lorentzian functions to measured PL spectra, and table of mode wavelength, mode linewidth and Q from fitted Lorentzians.*

enhancement of the emission rate is only experienced by emitters coupled to the cavity mode, the reduced emission lifetime at room temperature from QDs in the microleek structure is due to carriers reaching the fast non-radiative decay channel introduced by the defects in the etched cavity sidewalls.

To explain the absence of a Purcell effect in the microleek cavities, a direct measure of the cavity Q, is obtained from fitting a Lorentzian lineshape to the cavity mode. The best fit Lorentzian to the (3,12) mode of the measured spectra yields a cavity $Q \approx 650$, as shown in Figure 4.15. To calculate V_{eff} we need to integrate the spatial mode function $f(r,\theta,z)$ over all space, to do this $f(r,\theta,z)$ is first expressed as the product of two separate functions, $f(r,\theta,z)=g(r,\theta)h(z)$. Then we can write:

$$V_{eff} = \iiint |f(r,\theta,z)| dr d\theta dz = \left[\iint |g(r,\theta)| dr d\theta\right] \times \left[\int |h(z)| dz\right] \qquad (4.18)$$

$h(z)$ is just the normalised guided mode profile, the integral of which over all values of z equals 290nm and is called the effective mode height. The effective mode area which corresponds to the integral of $g(r,\theta)$ over all values of r and θ, is more difficult to calculate since our model does not predict the mode field in the lateral mirror structures. We estimate the effective mode area as the integral of (4.11) for a disk of radius $R'=R+d$, from $r=0$ to $r=R+d$, where R is the radius of the central cavity of the microleek and d is the fitting parameter to account for the penetration of the field into the mirrors. Using this approximation we obtain a value of $3.1\mu m^2$ for the effective mode area and hence $V_{eff}=(0.29\mu m \times 3.1\mu m^2)=0.9\mu m^3$, for the microleek structure measured ($R=1.55\mu m$, $d=320nm$). Taking $\lambda_{cav} = 971nm$, and $n_{eff} = 3.4$ we obtain a value of $F_p \approx 1.3$. Therefore, an emitter exactly matched both spectrally and spatially to the cavity mode would expect to experience an enhanced emission rate by a factor of 1.3 into the cavity mode, and with the twofold degeneracy of the cavity modes due to the $e^{i \pm M\theta}$ component of (4.11) [19], we would expect an overall enhanced emission rate from such an emitter into the cavity modes of 2.6.

However to simulate our experimental measurement we have to average the modified enhancement given by (4.15) over all QD's in the cavity whose emission wavelength lay

within our spectral resolution. Even if we assume that the spectral resolution of our experiment restricted our measured PL lifetime to QDs exactly spectrally matched to the cavity mode, setting the second term in (4.15) equal to unity for all QD emitters measured, we still have to consider the orientational and spatial distribution of emitters in the cavity. Since the dipole associated with the fundamental transition in the QDs is essentially randomly orientated [33], $\xi^2 \approx 1/3$ in (4.15). The average value of $|f(\vec{r}_e)|^2$ for QDs in the microleek cavity is estimated as the average value from $r=0$ to $r=R$ of $|\psi(r,\theta)|^2$ from (4.11) for a disk of radius $R'=R+d$ giving a value of ≈ 0.12. Finally, quantum dots spectrally matched to the cavity mode can still emit into leaky modes, corresponding to emission angles unguided by the vertical waveguide. From the measured PL lifetimes we know the spontaneous emission rate into unguided modes ($1/\tau_{leaky}$) is approximately equal to the emission rate in bulk material ($1/\tau_0$).

Combining these effects, we obtain a prediction for the average enhancement of the spontaneous emission rate into the microleek cavity mode ($1/\tau_{cav}$) of our structure of

$$\left(\frac{1}{\tau_{cav}}\right) \approx \left(F_p \times 2 \times \frac{1}{3} \times 0.12\right)\left(\frac{1}{\tau_{free}}\right) \approx (0.1)\left(\frac{1}{\tau_{free}}\right) \qquad (4.19)$$

and an estimate of the overall spontaneous emission rate of QD emitters coupled to the cavity mode ($1/\tau$) of

$$\left(\frac{1}{\tau}\right) = \left(\frac{1}{\tau_{cav}}\right) + \left(\frac{1}{\tau_{leaky}}\right) \approx (0.1)\left(\frac{1}{\tau_0}\right) + \left(\frac{1}{\tau_0}\right) \approx 1.1\left(\frac{1}{\tau_0}\right) \qquad (4.20)$$

Therefore when full account is taken of the spatial and orientational distribution of the QD emitters in the cavity, theory predicts approximately equal spontaneous emission rates from QDs coupled to the cavity mode of our microleek structure and QDs in bulk semiconductor, which agrees with our measurements.

To obtain an estimate of the combination of cavity dimensions and cavity Q required in a microleek structure to produce an enhanced emission rate, the overall enhancement of the spontaneous emission rate (τ_0/τ) into the (3,12) mode of microleek structures was calculated as functions of Q and R, assuming an unchanged emission wavelength and d value. The contour plot shown in Figure 4.16 highlights the very high value of Q/R required in order to observe an enhanced emission rate in microleek structures. A microleek structure with a central cavity radius of 0.6μm and a Q of 1200 would be required to observe a factor of 2 enhancement of the spontaneous emission rate, these are similar to the cavity parameters at which a factor of 2 enhancement of the emission rate was observed in micropillar structures [23].

The calculation takes account of emission coupling to both cavity and leaky modes. As previously discussed in section 4.5, only emission into the guided mode of the vertical waveguide couples to cavity modes and experiences the lateral confinement of the CDBR structure, while emission at angles unguided by the vertical waveguide couples to

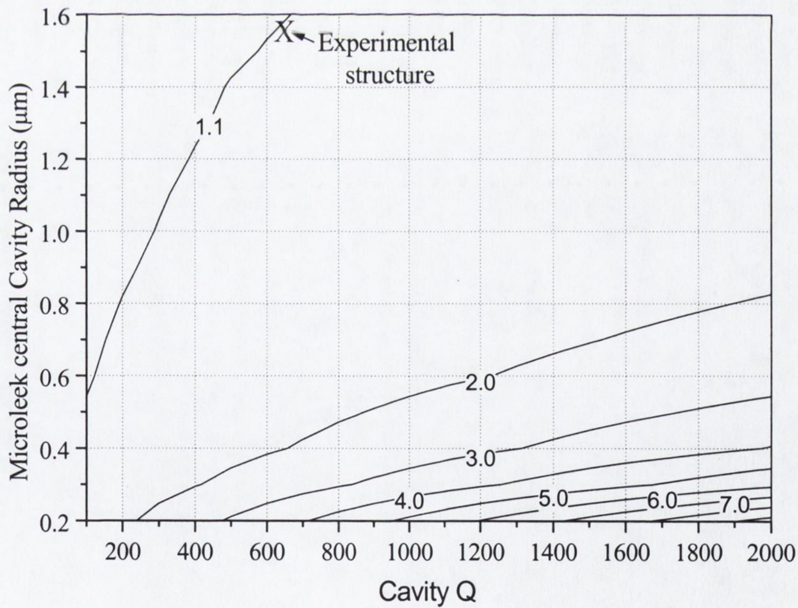

Figure 4.16 *Contour plot of overall enhancement of the spontaneous emission rate into a QRM of a microleek structure accounting for the spatial and orientational mismatch between QD emitters and cavity mode.*

unconfined modes and does not experience any cavity effects. The emission rate from a quantum dot in the microleek structure is the sum of the emission rates into cavity and leaky (unconfined) modes as expressed in (4.20). The enhancement factor of the emission rate into the cavity mode is calculated based on the Purcell factor as outlined above and is independent of angular considerations, while we estimate the emission rate into leaky modes as being approximately equal to the emission rate in bulk material from the measured PL lifetime from QDs at wavelengths where no cavity mode exists and hence the measured emission rate is the emission rate into leaky modes.

It should be noted that since our model does not account for the role of multiple reflections at the interfaces of the etched Bragg reflector, and hence doesn't properly model the penetration of the mode field into the lateral mirror, our expression for the mode field, $f(r, \theta)$ is only an approximation. Therefore, our calculated values of V_{eff} and $|f(\vec{r}_e)|^2$ used to calculate the emission rate are only approximations. The modes of these microleek structures have also been calculated using a 2D cylindrical model based on a transfer matrix method and Hankel functions [34], which accounts for the multiple reflections at the interfaces of the circular Bragg reflector. The results of these calculations [34] show good agreement with the mode wavelengths and mode volumes predicted by our simple model. This suggests that our model provides a good estimation of the cavity properties required to produce enhanced emission rates.

4.7.3 Summary

The PL spectra from microleek structures containing QD emitters showed a number of clear peaks that were explained in terms of the diffracted QRMs of the structure. The temperature dependence of the microleek mode structure was measured and successfully modelled using linear approximations for the temperature dependence of the refractive index and expansion coefficient.

The measured PL emission lifetime at 77K showed no cavity-induced enhancement of the spontaneous emission rate. This was shown to be consistent with calculations when averaged over the spatial distribution of QDs coupled to the cavity mode. The observed difference in PL lifetime from QDs in the microleek structure and from similar QDs in

bulk material at T=297K was attributed to the effect of increased non-radiative recombination caused by the presence of the etched cavity sidewalls.

4.8 Conclusion

The emission properties of a novel 2-dimensional microcavity incorporating a waveguide to confine light in the third dimension have been investigated. The design principle of the etched circular Bragg reflector and its advantages over the single semiconductor air interface of an isolated post structure were discussed.

Two sets of structures were investigated, incorporating either QD or QW emitters. The observation of lasing in the structures containing QWs enabled the identification of the azimuthal component (M number) and wavelength of individual modes from measured nearfields and spectra respectively. Modes with different M values and of different cavity sizes were successfully matched with the modes of an ideal disk resonator of slightly greater radius than the central cavity of the structure to account for the penetration of the mode fields into the Bragg reflector. The radial components of the lasing modes were determined from the model, resulting in their classification as QRMs, not confined in isolated post structures.

The spontaneous emission spectra from microleek structures containing QDs showed clear resonance peaks that were again identified with QRMs, with the reflectivity of the circular Bragg mirror estimated at > 90% from the fitted value for the cavity finesse. A value of 650 was obtained for the cavity Q from fitted mode linewidths. The temperature dependence of the cavity mode structure was also successfully reproduced by our model.

Despite the high reflectivity of the lateral mirrors and the strong confinement of the modes to the central cavity, evidenced by the size of the nearfield images above threshold, no cavity-induced modification of the emission lifetime was observed. Indeed calculations showed a considerable decrease in cavity radius and increase in cavity Q would be required to observe such an effect.

The negative impact of non-radiative recombination at the air interfaces of the deeply etched lateral mirror was highlighted by the high carrier density required for lasing and the shortened PL lifetime from the microleek structure at T=297K.

In summary, the lasing measurements have provided a unique and valuable insight into the mode structure of the microleek, and demonstrated the impressive performance and enhanced confinement of light by the etched Bragg reflector. However the failure to observe a Purcell effect highlighted the severe requirements on cavity properties required to produce enhanced spontaneous emission rates.

4.9 References

1 "Transverse modes, waveguide dispersion, and 30ps recovery in submicron GaAs/AlAs microresonators" J. L. Jewell, S. L. McCall, A. Scherer, H. H. Houh, N. A. Whitaker, A. C. Gossard, and J. H. English, Appl. Phys. Lett. **55** (1) p. 22 (1989).

2 "Whispering-gallery mode microdisk lasers" S. L. McCall, A. F. J. Levi, R. E. Slusher, S. J. Pearton, and R. A. Logan. Appl. Phys. Lett. **60** (3) p. 289 (1992)

3 "Near-Infrared microcavities confined by two-dimensional photonic bandgap crystals" C. J. M. Smith, H. Benisty, D. Labilloy, U. Oesterle, R. Houdré, T. F. Krauss, R. M. De La Rue and C. Weisbuch. Elec. Lett. **35** (3) p. 228 (1999).

4 "High-finesse disk microcavity based on a circular Bragg reflector" D. Labilloy, H. Benisty, C. Weisbuch, T. F. Krauss, C. J. M. Smith, R. Houdré, and U. Oesterle. Appl Phys. Lett. **73** (10) p.1314 (1998).

5 "Spatial modes of a concentric-circle-grating surface-emitting, AlGaAs/GaAs quantum well semiconductor laser" T. Erdogan, O. King, W. Wicks, D. G. Hall, C. L. Dennis, M. J. Rooks, Appl. Phys. Lett. **60** (15) p.1773 (1992).

6 "Circularly symmetric distributed feedback semiconductor laser: An analysis" T. Erdogan and D. G. Hall, J. Appl. Phys. **68** (4) p. 1435 (1990).

7 "Waveguide Microcavity Based on Photonic Microstructures" T. F. Krauss, B. Vogele, C. R. Stanley, and R. De La Rue, IEEE Photon. Technol. Lett. **9** (2) p. 176 (1997)

8 "Two-dimensional Photonic Bandgap structures operating at near-infrared wavelengths" T. F. Krauss, R. M. De La Rue, and S. Brand, Nature **383** p. 699(1996)

9 "Overview of fundamentals and applications of electrons, excitons, and photons in confined structures", C. Weisbuch, H. Benisty, and R. Houdré, J. of Lumines. **85** p. 271 (2000)

10 *Theory of Dielectric Optical Waveguides*, D. Marcuse (2nd Ed., Academic Press, 1991), chapter 8.

11 *Properties of Aluminium Gallium Arsenide*, edited by S. Adachi (Inspec, London, 1993)

12 *Electronmagnetic Waves*, D. H. Stalin, A. W. Morgenthaler, and J. A. Kong (Prentice-Hall, New Jersey, 1994)

13 "Optical and Confinement Properties of Two-Dimensional Photonic Crystals" H. Benisty, C. Weisbuch, D. Labilloy, M. Rattier, C. J. M. Smith, T. F. Krauss, R. M. De La Rue, R. Houdré, U. Oesterle, C. Jouanin, and D. Cassagne. Journal of Lightwave Technology, **17** (11), p. 2063, (1999).

14 "The spectrum of microdisk lasers" N. C. Frateschi and A. F. J. Levi. J. Appl. Phys. **80** (2) p. 644 (1996)

15 Brendan Roycroft, Ph.D. Thesis, Trinity College Dublin (1998).

16 *Semiconductor Optoelectronics* J. Singh (McGraw-Hill, New York, 1995) Appendix B.

17 *Optoelectronics : an introduction, 3rd ed.* , J. Wilson and J . Hawkes (Prentice Hall Europe, London, 1998)

18 "Theoretical gain in strained InGaAs/AlGaAs quantum wells including valence-band mixing effects" S. W. Corzine, R. H. Yan, and L. A. Coldren, Appl. Phys. Lett. **57**,(26) p. 2835 (1990).

19 "Optical study of GaAs/AlGaAs pillar microcavities with elliptical cross section" B. Gayral, J. M. Gérard, B. Legrand, E. Costard, and V. Thierry-Mieg. Appl. Phys. Lett. **72** (12) p.1421 (1998)

20 "Impact of planar microcavity effects on light extraction - Part I: Basic concepts and analytical trends", H. Benisty, H. De Neve, C. Weisbuch, IEEE J Quant. Elect. **34** (9) p. 1612 (1998)

21 "Spontaneous Emission in Dielectric Planar Microcavities", G. Bjork and Y. Yamamoto, in *Spontaneous emission and Laser Oscillation in Microcavities*, H. Yokoyama and K. Ujihara (Eds.) (CRC Press, Boca Raton, 1995)

22 "Finely resolved transmission spectra and band structure of two-dimensional photonic crystals using emission from InAs quantum dots" D. Labilloy, H. Benisty, C. Weisbuch,

C. J. M. Smith, T. F. Krauss, R. Houdré, and U. Oesterle, Phys. Rev. B **59** (3) p. 1649 (1999)

23 "Enhanced Spontaneous Emission by Quantum Boxes in a Monolithic Optical Microcavity" J. M. Gérard, B. Sermage, B. Gayral, B. Legrand, E. Costard, and V. Thierry-Mieg, Phys. Rev. Lett. **81** (5) p. 1110. (1998)

24 *Properties of Aluminium Gallium Arsenide,* edited by S. Adachi (INSPEC, London, 1993)

25 "The refractive index of $Al_xGa_{1-x}As$ below the band gap: Accurate determination and empirical modeling", S. Gehrsitz, F. K. Reinhart, C. Gourgon, N. Herres, A. Vonlanthen, and H. Sigg, J. Appl. Phys. **87** (11) p. 7825 (2000)

26 *Physical Properties of III-V Semiconductor Compounds – InP, InAs, GaAs, GaP, InGaAs, and InGaAsP*, S. Adachi (John Wiley and Sons, New York, 1992)

27 *Fundamentals of Photonics*, B. A. Saleh and M. C. Teich (John Wiley & Sons Inc., New York, 1991)

28 "Spontaneous Emission Probabilities at Radio Frequencies", E. M. Purcell Phys. Rev. **69**, p. 681 (1946)

29 "Semiconductor Microcavities, Quantum Boxes and the Purcell Effect", J. M. Gérard and B. Gayral in *Confined Photon Systems, Fundamentals and Applications*, H. Benisty, J. M. Gérard, R. Houdré, J. Rarirty, and C. Weisbuch (Eds.) (Springer, Verlag, 1999)

30 "Ultranarrow Luminescence Lines from Single Quantum Dots", M. Grundmann, J. Christen, N. N. Ledentsov, J. Bohrer, D. Bimberg, S. S. Ruvimov, P. Werner, U. Richter, U. Gosele, J. Heydenreich, V. M. Ustinov, A. Yu. Egorov, A. E. Zhukov, P. S. Kop'ev, and Zh. I. Alferov, Phys. Rev. Lett. **74** (20) p. 4043. (1995)

31 "Finely resolved transmission spectra and band structure of two-dimensional photonic crystals using emission from InAs quantum dots", D. Labilloy, H. Benisty, C. Weisbuch, C. J. M. Smith, T. F. Krauss, R. Houdré, U. Oesterle, Phys Rev. B **59** (3) p. 1649 (1999)

32 Only the ≈30% of emission that couples to the guided mode of the vertical waveguide remains confined in the cavity for long enough for it to have a significant probability of being reabsorbed. Assuming a mirror reflectivity of R=0.9, and a cavity length L=3.2μm (microleek diameter), we can estimate the mirror loss coefficient α_M as

$\alpha_{\mathrm{M}} = \frac{1}{2L}\ln\left(\frac{1}{R^2}\right) = 0.033\mu\mathrm{m}^{-1}$, while we can estimate the QD reabsorption coefficient α_R as α_R=1/(reabsorption length) $\approx 0.01\mu\mathrm{m}^{-1}$. The reabsorbed fraction of emission into the guided mode is given by $\alpha_R/(\alpha_R+\alpha_M) \approx 0.25$, and therefore the fraction of total emission reabsorbed by the QD layer is given by $0.3\times0.25=0.075$.

33 "Semiconductor Microcavities, Quantum Boxes, and the Purcell Effect" J-M. Gérard, and B. Gayral in *Confined Photon Systems, Fundamentals and Applications*, H. Benisty, J-M. Gérard, R. Houdré, J. Rarity and C. Weisbuch (Eds.) (Springer, Verlag, 1999)

34 "Diffraction of cylindrical Bragg reflectors surrounding an in-plane semiconductor microcavity" D. Ochoa, R. Houdré, M. Ilegems, H. Benisty, T. F. Krauss, and C. J. M. Smith, Phys. Rev. B **61** (7) p. 4806 (2000)

Chapter 5

PL spectral characterisation of InAs/GaAs quantum dots.

5.1 Introduction

This thesis is concerned with investigating the emission properties of microcavity light emitting structures, which are not only dependent on the effects of light confinement as explored in chapters 3 and 4, but also on the choice of active layer in the structure. In particular the role of the active layer in reducing the negative impact of non-radiative recombination at etched sidewalls is essential to the realisation of enhanced performance at room temperature of higher dimensional optical microcavities incorporating deeply etched lateral mirrors. Chapter 6 of this thesis focuses on the potential and limitations of quantum wells (QWs) and particularly quantum dots (QDs) as emitters in such microcavity structures.

However the range of reported behaviour of self-assembled quantum dots, of similar composition to those in our microleek structures, in photoluminescence measurements [1,2,3] reflects the sensitivity of the dot formation process to layer thicknesses and growth conditions [4], and necessitates the characterisation of the bulk emission properties of our QDs, before we can interpret their behaviour in etched cavity structures. Therefore in this chapter the PL spectrum of our self-assembled QD layer is measured as a function of temperature and pump intensity, to provide insights into the impact of thermally activated carrier escape and excited state transitions respectively. The measured temperature dependence of the PL spectrum of a QW is also presented for comparison.

5.2 Quantum Dots – Background

The effects of confining light to wavelength scale dimensions and the exploitation of the corresponding modification of the optical density of states have been the themes of chapters 3 and 4. Similarly the confinement of electrons to wavelength scale dimensions produces significant modifications of the electronic density of states [5], however the relevant wavelength for electrons is the de Broglie wavelength, which has a value of ≈10nm at 300K. The realisation of structures of such dimensions is clearly a huge technological challenge, however the benefits both demonstrated and predicted from the quantisation of the allowed electron energies are so significant that investigations into the properties of novel and refined structures offering quantum confinement of electrons remains one of the most active areas of both fundamental and applied research [5].

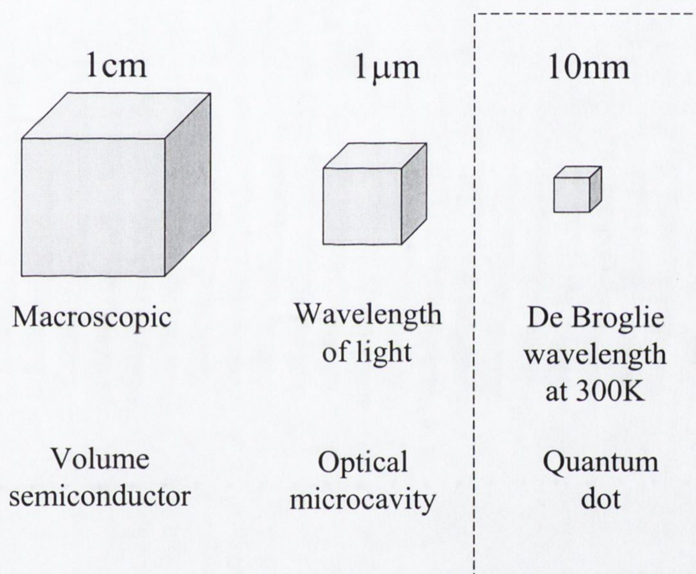

Figure 5.1 *Schematic comparison of typical dimensions required for observation of bulk, quantum optical confinement, and quantum electron confinement effects.*

The advent of novel epitaxial deposition techniques like molecular beam epitaxy (MBE) in the 1970's [6] enabled the growth of high quality semiconductor layers of uniform and controlled thickness, as thin as a few lattice constants. By inserting a layer of a semiconductor of a lower bandgap in a matrix with a larger bandgap, a so-called double heterojunction structure, an attractive squared potential for both electrons and holes is created. Reducing the thickness of the lower bandgap layer to the order of the de Broglie wavelength results in one dimensional electron quantum confinement, with carrier movement restricted to the two other dimensions. Such structures are called quantum

wells with the thickness of the lower bandgap layer determining the separation of the quantised electron levels of the attractive potential. The significant advantages of QWs in optoelectronic devices such as laser diodes [7], and modulators [8] have been clearly demonstrated, with QW's now essential to the performance of many commercial optoelectronic components.

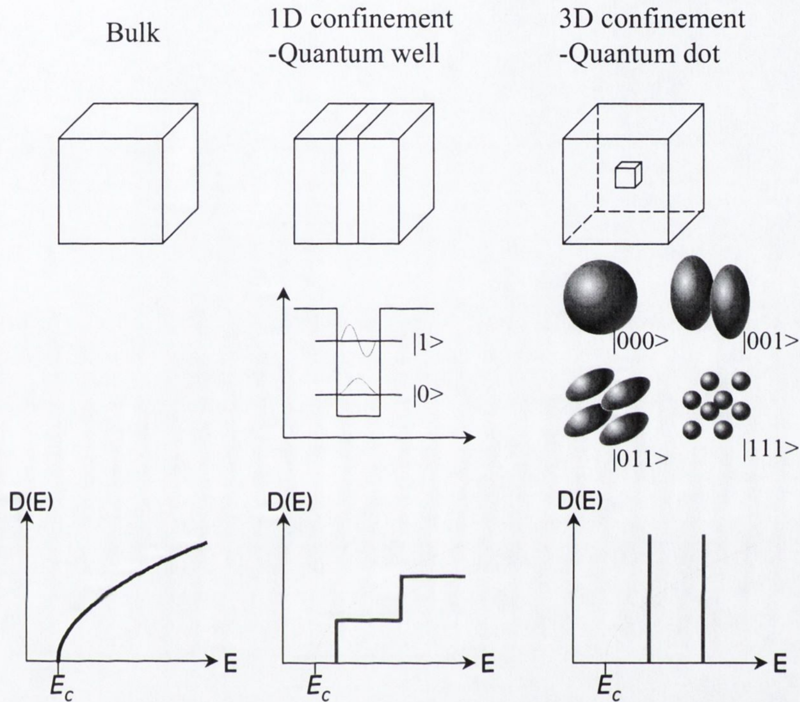

Figure 5.2 *Nature of electronic states in bulk material, quantum wells, and quantum dots. Top row: schematic of structure, centre row: quantised electronic states, bottom row: density of electronic states, D(E). Adapted from [21]*

By the end of the 1980's the main properties of QWs were well understood, and the interest of researchers shifted towards structures offering higher dimensional confinement, where the greater modification of the electronic density of states held the promise of further improvements in device performance [9]. With the ultimate goal of full three dimensional electron confinement in QDs resulting in a complete breakdown of the classical band structure model and the recovery of a discrete electron energy structure as observed for individual atoms (Figure 5.2). The comparison with the progression from planar to higher dimensional microcavities is striking, with the drive to realise extra confinement in the lateral directions the common goal. However the reduced scale to

which the confinement is required when shifting from photon to electron confinement makes the production of electronic QDs challenging for even the most advanced lithographic techniques. The most successful realisations of QD structures have involved the exploitation or adaptation of naturally occurring clustering processes. The last few years have seen considerable success in the production of nanometer scale QDs using self-organisation/self-assembly effects occurring naturally during the epitaxial growth of strained heterostructures [10]. Self-assembled QDs have been successfully incorporated as active layers into light emitting diodes [11], microcavity light emitting diodes [12] and laser diodes [13], while the emission properties of microleek structures incorporating self assembled QDs were presented in chapter 4.

The particular benefits of carrier trapping, in reducing non-radiative edge recombination, and narrow emission linewidth, in observing a Purcell effect, offered by QDs at cryogenic temperatures in microcavity structures were mentioned in chapter 4. However the room temperature emission properties of microleek structures containing QDs highlighted the failure of QDs to completely confine carriers at non-cryogenic temperatures. Since the advantages of QDs as emitters in microcavities incorporating etched sidewalls is dependent on their ability to trap carriers, these results raised the question of the suitability of our QDs as active layers in these structures at practical operating temperatures where the thermal energy of carriers is sufficient to introduce a significant probability of carrier escape.

5.3 QD fabrication processes.

While the QDs incorporated in our microleek structures and further investigated in this chapter were created by a self-assembly process, other methods of producing QDs exist and are briefly mentioned here for completeness.

The first realisations of QDs were nano-size II-VI microcrystals inserted in glass [14,15] (Figure 5.3(a)), however the non-conducting nature of the glass matrix prevents electrical injection and hence limits their usefulness in active optoelectronic devices. However II-VI nanocrystals remain the focus of considerable research [16].

QDs have also been successfully realised by patterning QW structures [17,18] (Figure 5.3(b)). Advanced lithographic techniques such as electron and focused ion beam

lithography are used to define the pattern while dry and wet etching processes are used to produce the QD. Lithographic based processes have the advantage of allowing the realisation of QDs of arbitrary lateral shape, size and arrangement, limited only by the resolution of the technique (≈10nm for e-beam [19]). Despite the demonstrated ability to fabricate free-standing etched quantum dots down to a size of ≈ 50nm [20], the etching processes produce a highly damaged layer of the order of 10nm thick at the surface [21], which severely degrades the luminescence efficiency of the material, thus limiting the present usefulness of such QDs.

The naturally occurring nanometer sized island formation observed during the growth of strained heterostructures has produced the most promising QD candidates for incorporation in practical devices. It is the combination of a high QD density, the lack of QD defects and the use of established epitaxial growth processes that makes the self-assembly process so attractive.

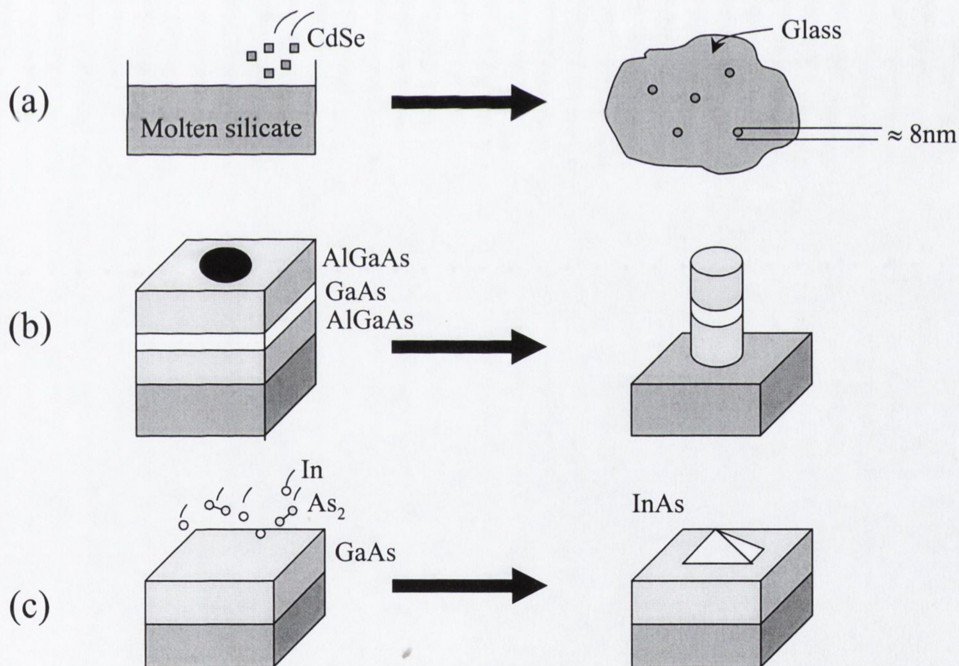

Figure 5.3 *Schematic representations of different approaches to fabrication of QDs: (a) nanocrystals in glass, (b) Etching of QW structures, (c) self-assembled growth. Adapted from [21].*

5.4 Stranski-Krastanow growth mode.

The self-assembly process responsible for the formation of the QDs investigated here is the result of the strain energy produced when successive layers with unmatched lattice constants are grown. Considerable expertise exists on the growth of strained quantum wells. Highly strained layers can be grown up to a critical layer thickness. Above the critical layer thickness the built-in strain energy releases by either the formation of defects and dislocations or by the formation of dislocation free islands (dots). When island formation occurs the layer is no longer of uniform thickness and hence the growth is referred to as 3D growth.

The particular QDs investigated in this work result from the growth of InAs on GaAs. The lattice constant of unstrained GaAs is 5.653Å compared to a 6.057Å for unstrained InAs, resulting in a lattice mismatch of $\approx$ 7% [22]. The significance of the magnitude of the mismatch is highlighted in the following qualitative discussion of 3D growth modes based on energy balance.

Two types of self-assembled growth modes can be distinguished, the Volmer-Weber mode and the Stranski-Krastanow mode [23]. The difference between the two modes is illustrated by considering, (i) the interfacial energy between the strained epitaxial layer and the substrate $E_{epi,sub}$, (ii) the bulk free energy of the (strained) epitaxial material, $E_{b,strain}$, and (iii) the interfacial energy between the (top) layer and the vacuum, $E_{epi,v}$. For an epitaxially grown layer the total energy can be written as [24]

$$E_{epi,total} = E_{b,strain} + E_{epi,v} + E_{epi,sub} \tag{5.1}$$

If clustering occurs, the bulk free energy may decrease by strain relaxation. However, the $E_{epi,v}$ increases since clustering increases the interfacial area with the vacuum. $E_{epi,sub}$ is assumed unchanged in both cases. The clustering is contingent on the balance between the $E_{epi,v}$ and $E_{b,strain}$. Thus, the critical layer thickness can also be defined as the thickness at which the decrease in $E_{b,strain}$ overrules the increase of $E_{epi,v}$.

When the lattice mismatch is very high (>8%) [24], the total energy decreases immediately by clustering since the energy gain from strain relief is large compared to the increased surface energy. This pure 3D growth is the so-called Volmer-Weber (VW)

mode. In this mode there is no critical layer thickness. The VW mode is typical for metals deposited on oxides or graphite [25].

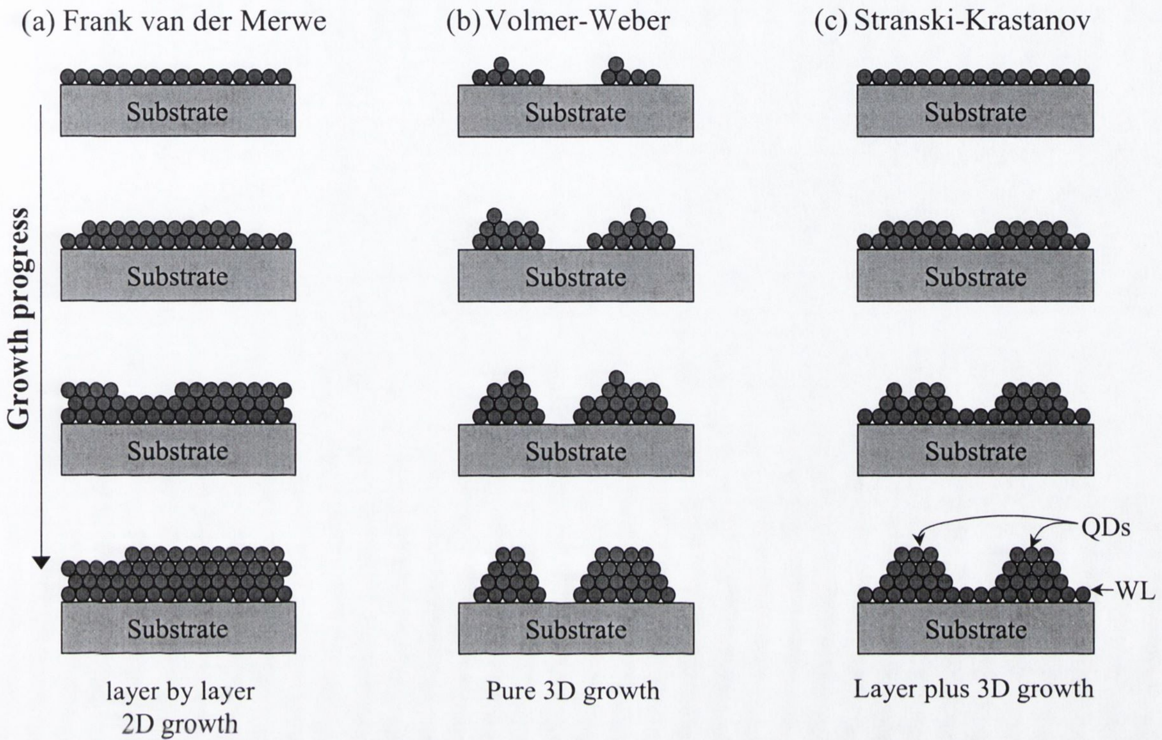

Figure 5.4 *Thin films can grow in three different modes, (a) Frank- van der Merwe or layer by layer growth, (b) Volmer-Weber or pure 3D growth, and (c) the Stranski-Krastanow growth, which is intermediate to (a) and (b).*

The Stranski-Krastanow (SK) mode is an intermediate case between the 2D layer by layer (Frank- van der Merwe) and pure 3D (VW) growth. First a highly strained layer is formed on the substrate. The total energy is not decreased by clustering, since the strain is less than in the VW-mode (<8%). However, the formation of islands becomes energetically more favourable as the epitaxial layer thickness increases. This results in dots forming on top of a continuous layer know as the wetting layer (WL). This growth mode is observed for the materials investigated here, i.e. InAs on GaAs. Due to the high strain value (7%), the critical layer thickness for this material combination is only ≈ 1.5 monolayers (MLs) [4]. Less strained systems (e.g. InGaAs/GaAs) have a greater critical layer thickness [26]. While this explanation oversimplifies the dynamics involved in the

growth of strained heterostrucutres, it provides an intuitive understanding of the origins of different growth modes.

5.5 Samples

Since the aim was to characterise the behaviour of QDs similar to those incorporated into our etched microcavities, an unprocessed section of the wafer in which the cavities investigated in chapters 4 and 6 were etched was examined. The section of the wafer used was close to the section in which the cavities were etched, thereby minimising any differences in the QD properties due to fluctuations across the wafer. The layer structure of the wafer is shown in Figure 4.3; the presence of the waveguide utilised in the etched cavities has no impact on our bulk QD measurements since we only collect emission through the top surface that results from emission at angles unguided by the waveguide.

Three identical QD layers are incorporated in the wafer that was grown by MBE on (001)–orientated GaAs substrates. Each QD layer consisted of 2.0MLs of InAs deposited on GaAs. After the deposition of the InAs there was a 5 second growth interruption before a capping layer of GaAs was grown. The growth temperatures were 520°C for the InAs layers and 620°C for all other layers in the structure. The 100Å GaAs spacing layers between the InAs layers is sufficiently large to eliminate electronic coupling between dots in different layers [27].

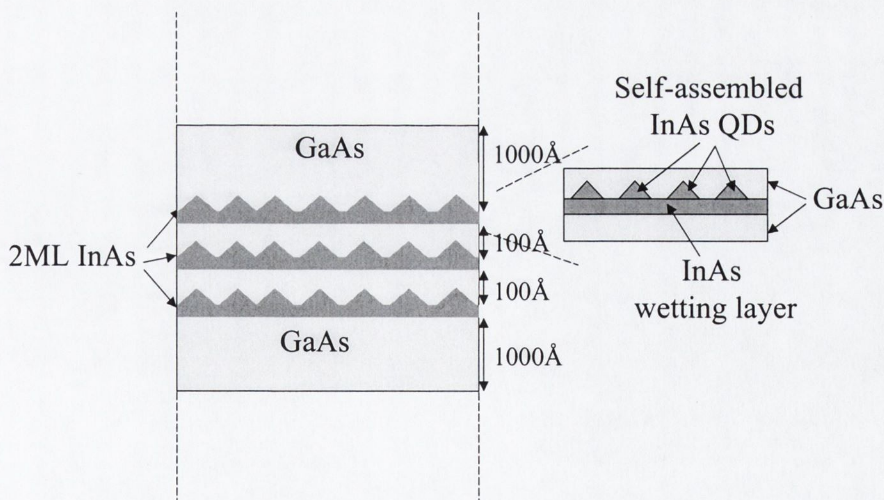

Figure 5.5 *Schematic diagram of 3 layers of self-assembled InAs/GaAs QDs, as incorporated into the investigated structure. The complete details of the other layers of the structure are contained in Figure 4.3.*

5.6 Electronic structure of self-assembled InAs/GaAs QDs.

The calculation of the electronic states of real QDs is a complex problem, with various reported approaches to account for the QD shape and the effect of strain and composition. The electronic structure of pyramidal shaped dots as observed for InAs/GaAs QD's [28], has been modelled using an effective mass approach incorporating, one, four and eight band **k·p** models [29,30,31,32], and pseudopotential models [33]. An atomistic pseudopotential method has also been reported [34]. A full treatment of these different

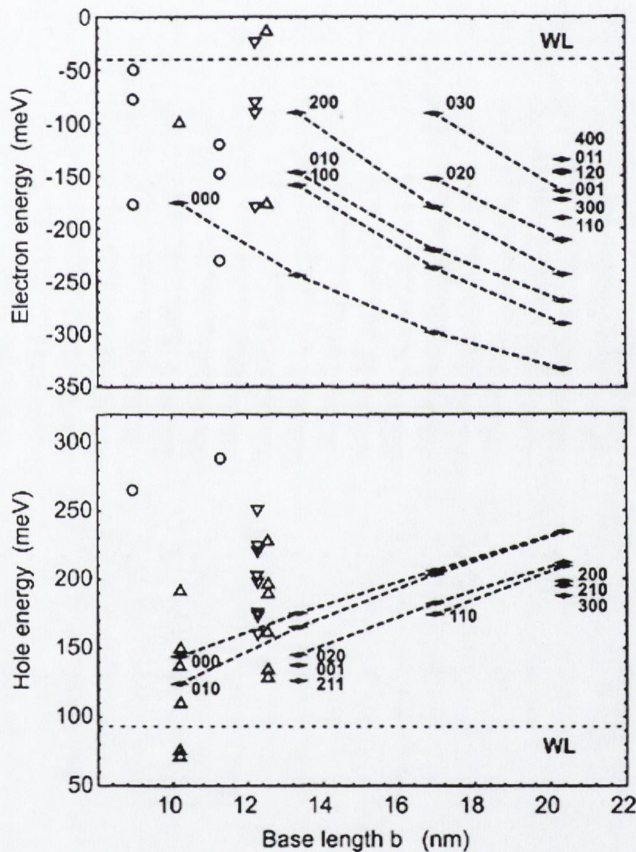

Figure 5.6 *Electron and hole levels for InAs/GaAs pyramids of different base lengths b, measured from the conduction and valence band edges of unstrained GaAs respectively, as predicted from eight band **k·p** theory ([32] solid diamonds), other **k·p** results(six band [30] open up triangles, eight band [31] open down triangles) and pseudo potential calculations ([33], open circles). (Reproduced from [21])*

approaches and the various strain models they use in predicting the electronic structure of self-assembled InAs QDs is beyond the scope of this thesis. However the variation in predicted confined electron and hole energies from even the sophisticated eight band **k·p** and pseudopotential approaches due to different strain models is highlighted by the assembled results shown in Figure 5.6.

Despite the lack of definitive literature values for confined electron and hole energies in InAs/GaAs QDs there are two consistent trends, (i) increasing confinement of both electrons and holes with increasing dot size, resulting in lower energy ground state transitions for larger dots, and (ii) the existence of excited electron and hole states in pyramidal shaped dots with base lengths as small as 10nm.

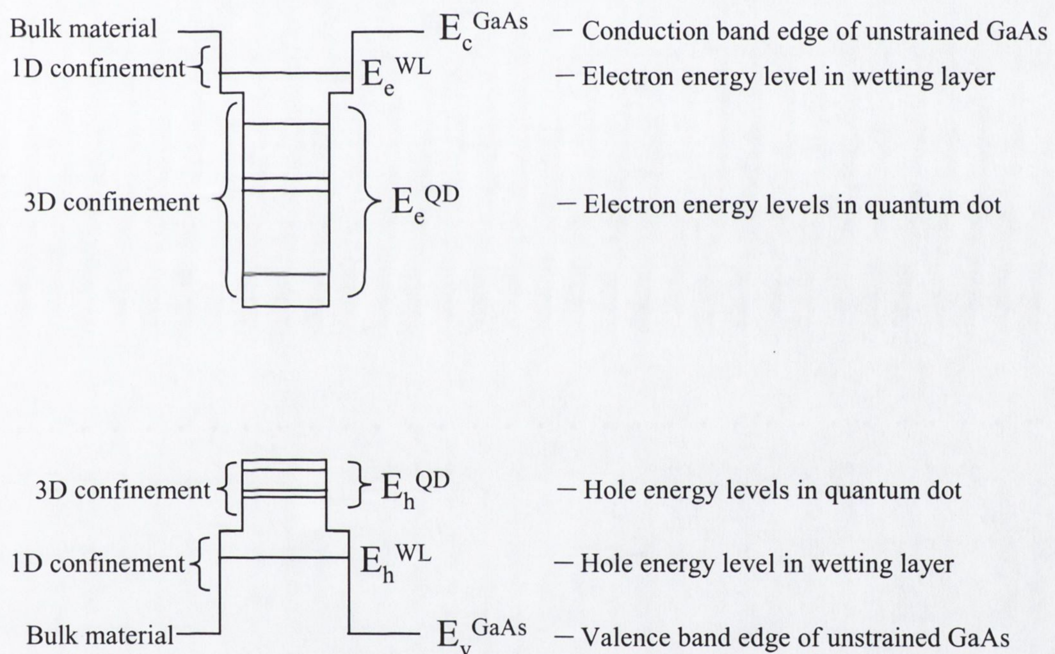

Figure 5.7 *Schematic diagram of Energy levels in InAs/GaAs self-assembled QD.*

5.7 Experimental Setup

The experimental set-up used to perform PL measurements on the InAs/GaAs quantum dots is shown in Figure 5.8. The laser excitation source used was a semiconductor laser diode providing continuous wave (CW) emission at 790nm. A single mode fibre was

again used to provide a well-defined and reproducible point excitation source. The collimated beam produced by microscope objective MO1 was focused onto the sample by microscope objective MO2. The sample was mounted in a closed cycle helium (He) cryostat that provided temperature tuning in the 30K-297K range. The sample position in the He cryostat limited the choice of microscope objective MO2 to those with a working distance greater than ≈15mm. A ×5, 0.12 NA microscope objective was used, producing a ≈15μm diameter spot on the sample surface (measured by imaging onto CCD camera). To produce a smaller excitation spot required for the excitation intensity dependent studies the sample was mounted in a liquid nitrogen cryostat where the sample was positioned immediately behind the cryostat window facilitating the use of a high NA objective lens. Specifically a ×40, 0.5 NA lens was used to produce an excitation spot with a diameter ≈ 2.0μm when the sample was in the liquid nitrogen cryostat.

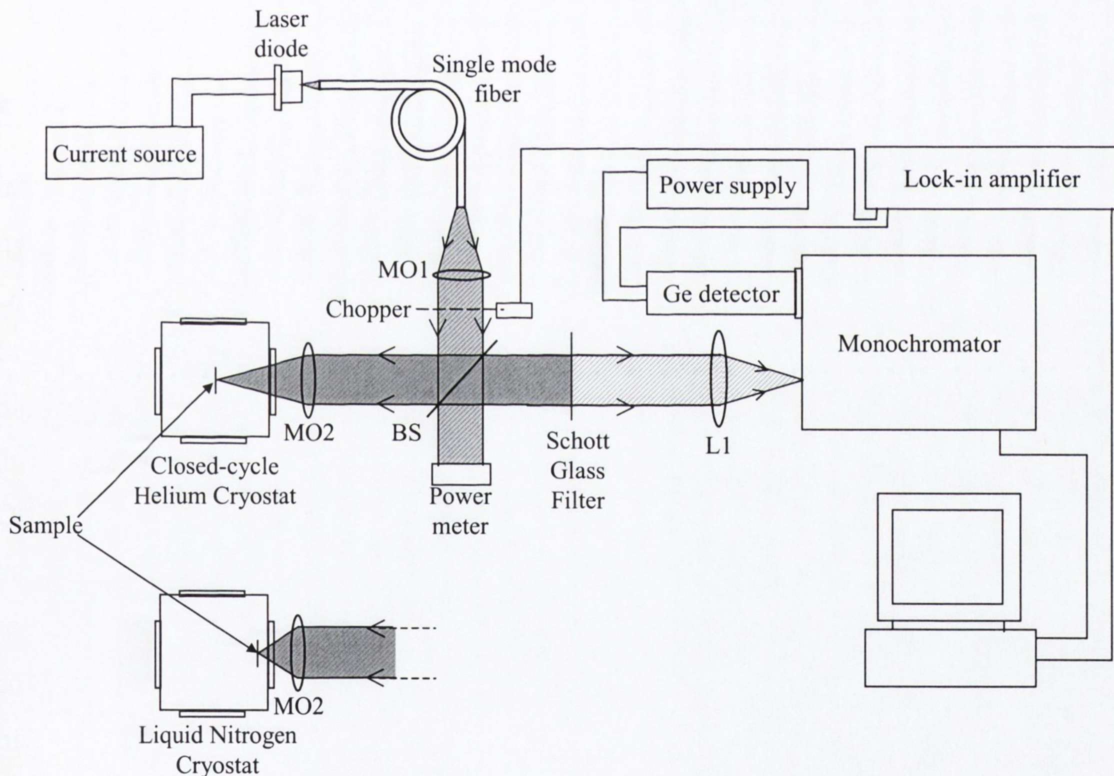

Figure 5.8 *Diagram of experimental setup used to perform photoluminescence measurements on InAs/GaAs QDs and InGaAs/GaAs QWs. MO1 = ×10, 0.25 NA microscope objective, MO2 = ×5, 0.12 NA microscope objective (M02 = ×40, 0.5 NA microscope objective when using the liquid Nitrogen cryostat), L1 = 10 cm focal length spherical lens, and BS = beamsplitter.*

A Schott Glass filter (RG 850), which has a transmission of less than 1×10^{-4} for light with wavelengths < 800nm, was used to remove reflected laser light from the collected beam. The PL signal was dispersed by a monochromator, and measured by a North Coast liquid nitrogen cooled Ge detector attached to the exit slit. The Ge detector is sensitive to near infrared wavelengths between 800nm and 1700nm. The spectral response of the system was calibrated using a white light source of known emission spectrum. The slow time response of the Ge detector ($\approx$10ms) prevented time resolved PL measurements at these wavelengths (the microchannel plate photomultiplier tube used in chapter 4 is only sensitive to wavelengths < $\approx$1000nm). The excitation beam was modulated at 10Hz, and a lock-in amplifier was employed to improve the signal to noise ratio.

5.8 Results and discussion

5.8.1 Temperature dependence of QD and QW PL spectra

In this section the measured PL spectra from our InAs/GaAs QDs and an $In_{0.17}Ga_{0.83}As$/GaAs QW in the temperature range 30K-297K are presented and discussed. Of particular interest in the context of the suitability of these QDs as emitters in etched cavities is the role of thermally activated escape from the dots.

Since the excitation wavelength of 780nm or 1.59eV is above the GaAs bandgap energy the pump beam is predominantly absorbed in the GaAs layers surrounding the thin QD/QW layer, with the created carriers subsequently relaxing into the QDs/QW. These measurements are classified as non-resonant PL since the excitation energy is not resonant with any quantised levels of the QD/QW. The excitation intensity of 50Wcm^{-2}, corresponded to a carrier density of $\approx 6\times10^{9}$cm^{-2} per QD/QW layer, assuming a carrier lifetime of 1ns and accounting for the surface reflection, and absorption length of GaAs, as outlined in section 4.6.1. This carrier density is less than the reported density of similar InAs/GaAs QDs of between 10^{10}cm^{-2} and 10^{11}cm^{-2} [35,36,37,38]. Therefore we create on average less than one electron-hole pair per dot, as confirmed by results in section 5.7.2. The PL spectra obtained from the QD and QW layers under these non-resonant low excitation intensity conditions are shown in Figure 5.9 and Figure 5.10 respectively.

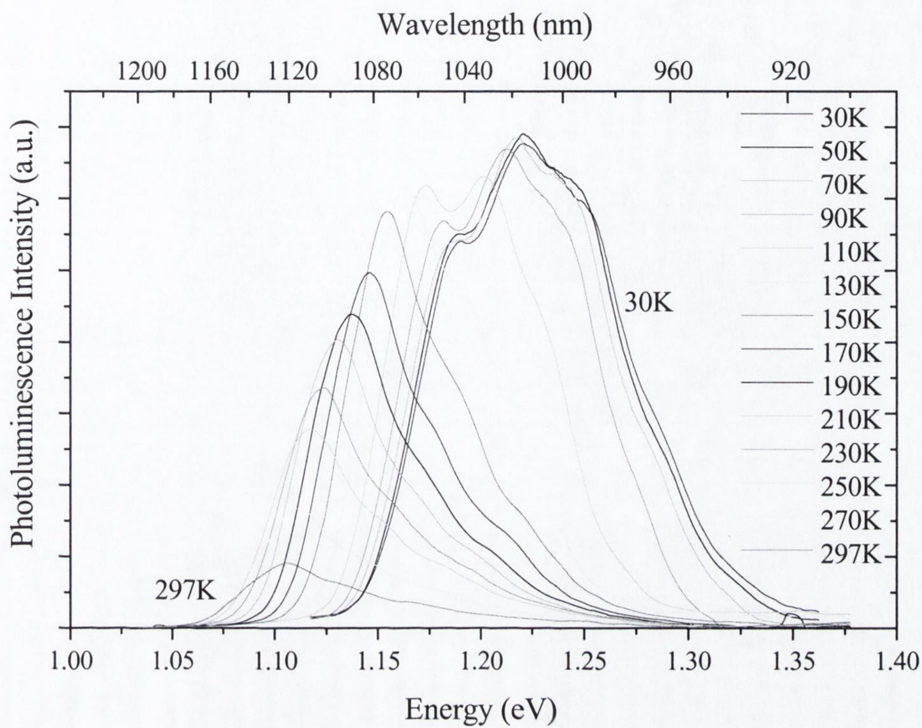

Figure 5.9 *Measured PL spectra of InAs/GaAs QDs in the temperature range 30K-297K.*

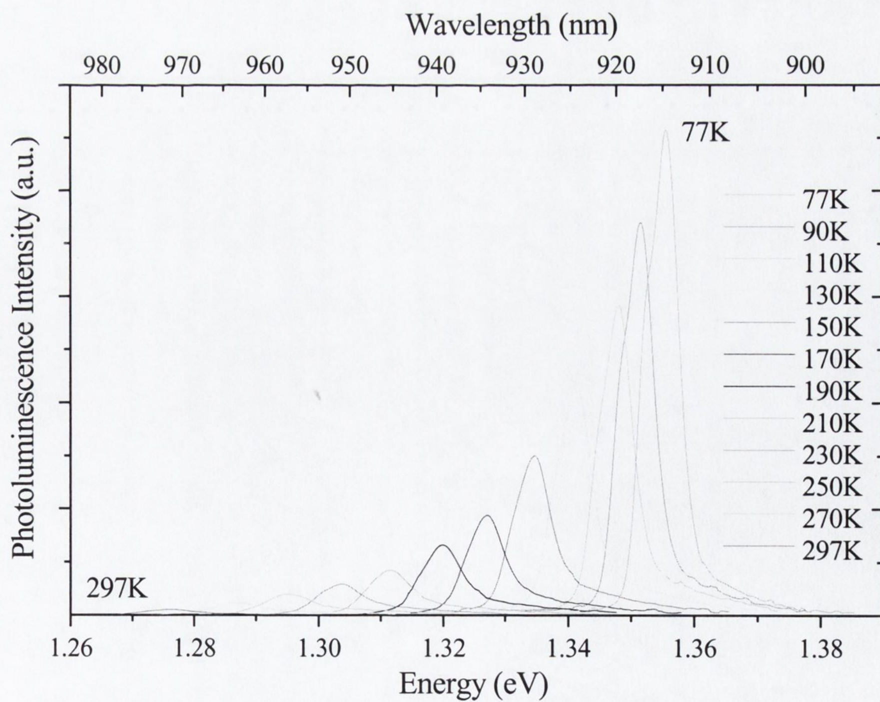

Figure 5.10 *Measured PL spectra of $In_{0.17}Ga_{0.83}As/GaAs$ QW in the temperature range 77K-297K.*

Despite the discrete electron levels in a single quantum dot, no narrow lines were observed in the measured QD PL spectrum at 30K, which has a full width half maximum (FWHM) of approximately 110meV. Assuming a radiative lifetime of 1ns the expected homogeneous broadening of the energy levels in a quantum dot from the uncertainty principle ($\Delta E \geq \hbar / \Delta t$) is only a few μeV, while measured emission linewidths from single InAs/GaAs self-assembled dots of less than 100μeV have been reported [39]. Therefore our QD PL spectrum at low temperatures must be inhomogeneously broadened, with the broadening attributed to the size distribution of the dots. At 30K the thermal energy of the carriers is sufficiently low to prevent carrier escape from even the smallest dots, so carriers recombine in the dot into which they initially relax. Therefore the shape of the PL spectrum at low temperatures corresponds to the distribution of QD sizes, provided the transition energy is approximately linearly dependent on dot size, as theory has predicted (see Figure 5.6). The peak in the PL spectrum at 30K occurs at 1.225eV which matches the predicted ground state transition energy for a quantum dot of ≈10nm base length [40],

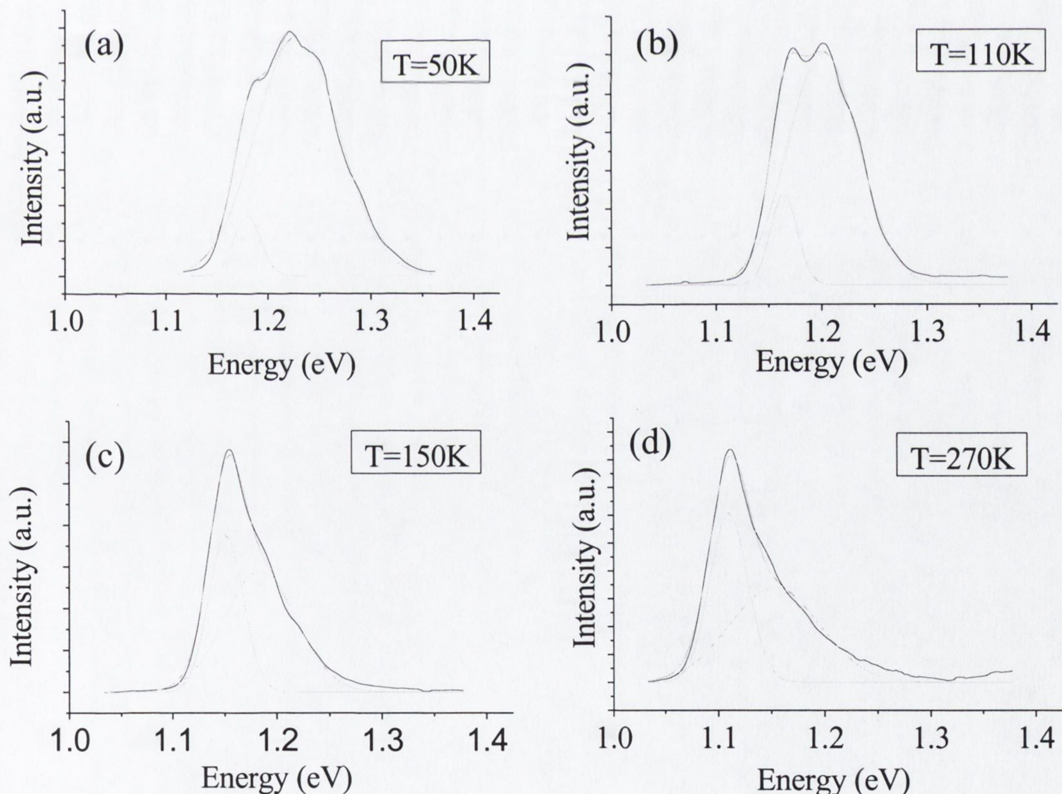

Figure 5.11 *Measured PL spectrum (black line), best fit summation of two Gaussians (red line), and deconvolved individual Gaussian fits (green lines) for four temperatures.*

while the FWHM variation of 10% about the peak in the measured spectrum, suggests a similar variation in dot size.

The QD PL spectrum at 30K appears to contain a small peak superimposed on the low energy side of the main peak, with two separate peaks clearly visible in the 110K spectrum. The low excitation intensity employed and the lower energy of this second smaller peak eliminates the possibility of it being due to excited state transitions. We attribute the two peaks to a bimodal size distribution of QDs, as previously directly observed in atomic force micrographs of similar systems of self-assembled QDs [35,41, 42]. This bimodal distribution of dot sizes has been explained in terms of two distinct thresholds for QD formation, (i) the minimum InAs coverage for dot assembly and (ii) the layer thickness corresponding to the optimal dot size formation [35]. To confirm this

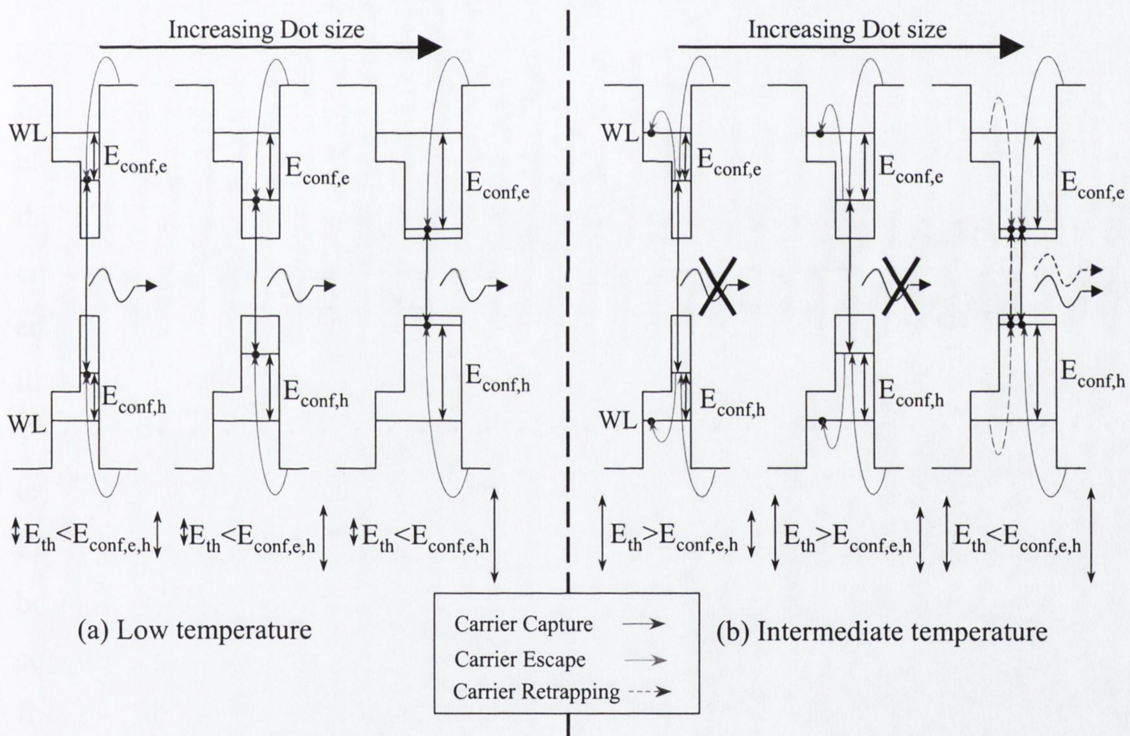

Figure 5.12 *Schematic diagram of carrier dynamics between different sized QDs. (a) at low temperature, the thermal energy of the carriers (E_{th}) is much less than the confinement energy (E_{conf}), carriers are trapped and recombine in all dots (b) at intermediate temperatures, $E_{th}>E_{conf}$ for the smaller dots and $E_{th}<E_{conf}$ for the larger dots, enabling carriers to escape from the small dots into WL states from where they can be recaptured into other dots. The efficient trapping of carriers in the larger dots results in a higher probability of recombination occurring in these dots.*

bimodal size distribution of dots and to identify the roles of both distributions in the observed PL spectra, the measured spectra were fitted by a summation of two Gaussian distributions (when the measured spectra were fitted by a summation of three or more Gaussians the resulting fit was dominated by two of the Gaussian distributions). The results of the two Gaussian fitting procedure applied to PL spectra at four different temperatures are shown in Figure 5.11. The success of the two Gaussian distributions in reproducing the measured PL spectra supports the existence of a bimodal distribution of dot sizes in our sample. The increase in luminescence from the lower energy distribution relative to the higher energy distribution with increasing temperature indicates a redistribution of carriers from the smaller dots to the larger dots at higher temperatures. These carrier dynamics between dots within the layer are essential to understanding the emission characteristics of the QDs. We have seen how the relatively large distribution of QD sizes results in a large inhomogeneous broadening of the PL spectrum, but equally important is the resulting distribution of carrier confinement energies in the QDs. The electron and hole confinement energies (E_{conf}) in a dot are the energy differences between the QD and WL states for the respective carriers. Larger dots have larger confinement energies and hence lower emission energies. The impact of the different confinement energies on carrier trapping and escape for different sized dots and temperatures is illustrated in Figure 5.12.

The spectrally integrated PL for all QDs shown in Figure 5.13 is relatively stable in the temperature range 30-50K and decreases consistently for temperatures higher than 70K. From this dependence we conclude that at temperatures below ≈60K, the carriers exist as bound excitons in the QDs, however, at this temperature the thermal energy becomes comparable to the QD exciton binding energy [43] and the excitons can dissociate into free carriers. These carriers can then be redistributed from the smaller dots to the larger dots by either carrier tunneling between adjacent dots or by carrier percolation through the 2D WL. Carriers can become trapped in material defects during these transport processes where they recombine non-radiatively resulting in a drop in the integrated PL. The redistribution of carriers between QDs is seen by the rapid decrease in the integrated PL from the high energy Gaussian distribution and the rise in the integrated PL from the low energy Gaussian distribution in the 70-150K temperature range. At temperatures

higher than 150K the integrated PL decreases for both Gaussian distributions of dots indicating the thermal energy of the carriers is sufficient to allow escape from even the larger dots.

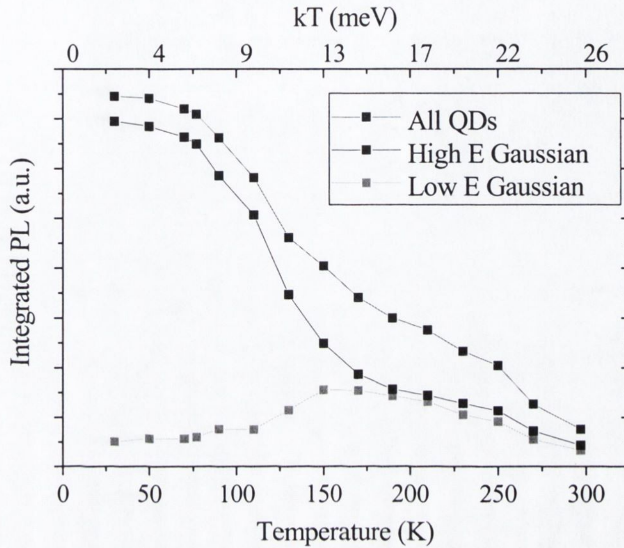

Figure 5.13 *Spectrally integrated PL intensity from all QDs, and separated into emission from both size distributions of dots from fitted Gaussians, as a function of temperature.*

The rate of carrier escape from a given confinement potential is clearly dependent on the thermal energy of the carriers and hence the sample temperature, with this temperature dependence represented by the Arrhenius equation,

$$R = A\exp(-E_a / kT) \tag{5.2}$$

where R is the rate of escape, A is a constant, E_a is the thermal activation energy for the process equal to the confinement energy in this case, and k is Boltzmann's constant. In order to investigate whether the temperature dependence of the integrated PL fits an Arrhenius-type dependence the natural log of the integrated PL is plotted against 1/kT (see Figure 5.14). To obtain a satisfactory fit to the observed behaviour we had to assume two thermally activated nonradiative carrier escape process, with activation energies E_1 and E_2 to compete with radiative recombination, giving [36]

$$I(T) \approx \frac{B_1}{1 + B_2 \cdot \exp(-E_1 / kT) + B_3 \cdot \exp(-E_2 / kT)} \tag{5.3}$$

where I is the spectrally integrated PL and $B_{1,2,3}$ are constants. Since different sized QDs will possess different confinement energies with respect to WL and GaAs states, (5.3) can only provide a simplified approximation to the physical situation. The best fit to the spectrally integrated PL data yielded values of E_1=35±2meV and E_2=370±60meV. The smaller activation energy of 35meV corresponds to the smaller sloped region of Figure 5.14 between 110K and 190K, while the higher activation energy of 370meV corresponds to the higher sloped region between 250K and 300K. However the failure of (5.3) to account for the role of carrier recapture already shown to play an important role in the 110K to 190K temperature range renders any interpretation of the E_1 value as the activation energy for a carrier escape process highly speculative. At higher temperatures the reduced role of carrier retrapping allows the tentative identification of E_2 with the activation energy for a non-radiative carrier escape process. In this respect, the E_2 value of 370±60meV agrees with the predicted combined confinement energy of the electron/hole pair in the QD ground state with respect to the GaAs bandedges (see Figure 5.6).

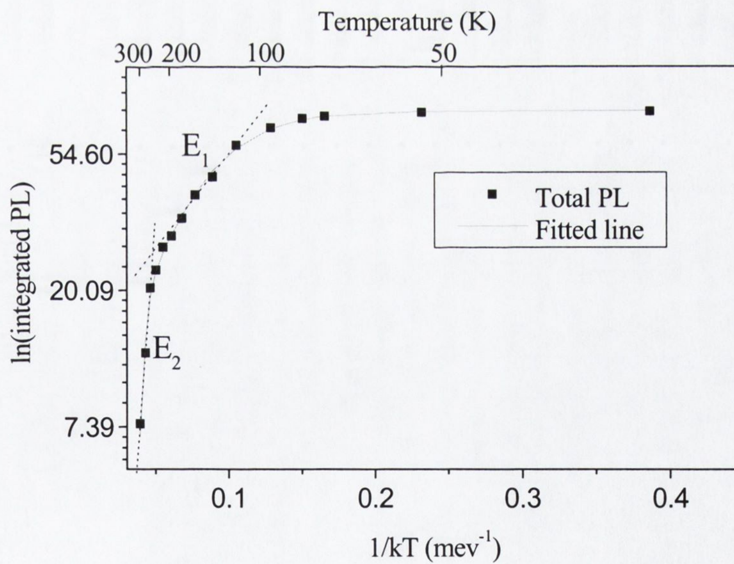

Figure 5.14 *Semi-logarithmic plot of integrated PL intensity against 1/kT, solid line shows fit obtained assuming two thermally activated non-radiative recombination processes. The dotted lines indicate the regions of the fitted line determined by the activation energies E_1 and E_2 individually.*

Therefore we conclude that at temperatures less than 70K, carriers remain trapped in individual QDs, with very little probability of escape. As the temperature increases through the intermediate temperature range of 70K to 200K, carriers possess sufficient thermal energy to escape from increasingly larger QDs, with the largest dots still possessing sufficiently large confinement energies to prevent carrier escape. In this temperature range, we observe an increase in luminescence from the larger dots due to the recapture of carriers from WL states subsequent to their escape from smaller dots, and the tunneling of carriers into between dots. This dynamic exchange of carriers between different dot sizes makes the identification of an activation energy for the dominant carrier loss process using (5.3) impossible. At temperatures greater than 200K, carriers have sufficient thermal energy to escape from even the largest dots, with the dominant carrier loss process at temperatures >250K tentatively identified from an Arrhenius-type dependence as direct carrier excitation from QDs to surrounding GaAs states.

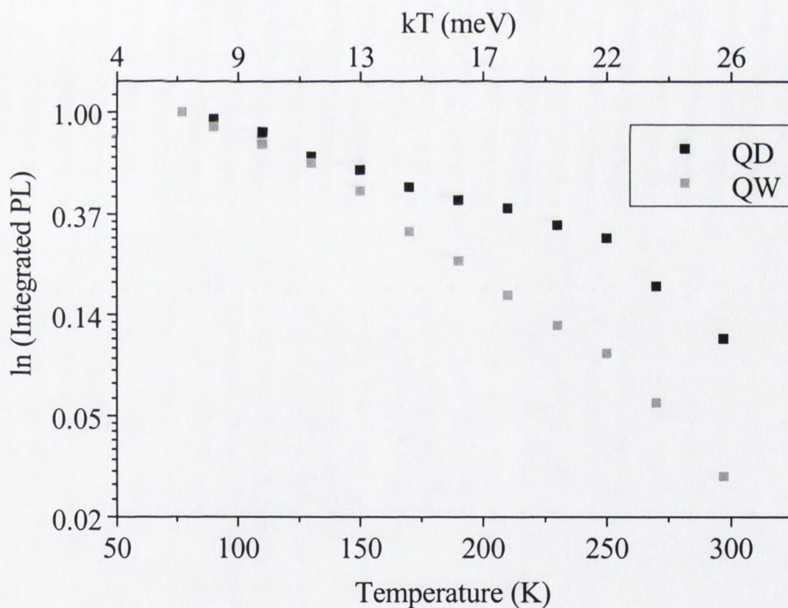

Figure 5.15 *Comparison of spectrally integrated QD and QW PL normalised to their low temperature value, on semi-log plot.*

The temperature dependencies of the spectrally integrated QD and QW PL are compared in Figure 5.15. The more rapid decrease in QW emission relative to the QD emission with increasing temperature in the 77K to 250K range indicates an increased loss of

carriers to nonradiative recombination processes by the QW compared to the QD layer. This can be attributed to both the smaller barrier for carrier escape from the QW compared to the QDs, evidenced by their different emission energies, and the freedom of carriers to move in the plane of the QW and hence interact with defects. At temperatures greater than 250K the rate of decrease of the PL from the QDs is similar to the QW, suggesting the benefits of the increased confinement energy and the potential for carrier localisation in the QDs relative to QWs are less significant at these higher temperatures.
The shift in peak emission energy with temperature of the QW, and two deconvolved Gaussian peaks of the QD spectra are shown in Figure 5.16(a). The temperature dependent energy shift of bulk bandgaps is phenomenologically described by Varshni's formula [44]

$$\Delta E = \frac{AT^2}{T + B} \tag{5.4}$$

where A and B are constants characteristic of a given semiconductor. The energy changes of the bulk InAs and GaAs bandgaps are depicted by the dotted and dashed lines respectively in Figure 5.16(a). The temperature dependence of the emission energy of the QW agrees well with the expected shift in the GaAs bandgap, and agrees with Varshni's equation (5.4) for A = 0.0005 eVK^{-2} and B = 183K. The shift in the peak energy of the low energy Gaussian of the QD distribution is also well described by (5.4) for fitted values of A = 0.00036eVK^{-2} and B = 67K. This temperature dependence of the QD emission energy lies between the expected behaviour of bulk GaAs and InAs. Finally the change in the peak emission energy of the high energy Gaussian of the QD distribution falls outside the boundaries of the GaAs and InAs bandgap shifts, and cannot be fitted to (5.3). This can be explained in terms of the thermal redistribution of carriers between different sized dots in the distribution. As already seen at temperatures above 70K carriers can escape from the smallest dots which emit at the highest energy, and be retrapped in larger dots emitting at lower energies. Therefore the increased shift of the peak emission of the high energy Gaussian distribution of QDs in the 90K to 130K range is attributed to a redistribution of emission towards the lower energy dots within the dot distribution.

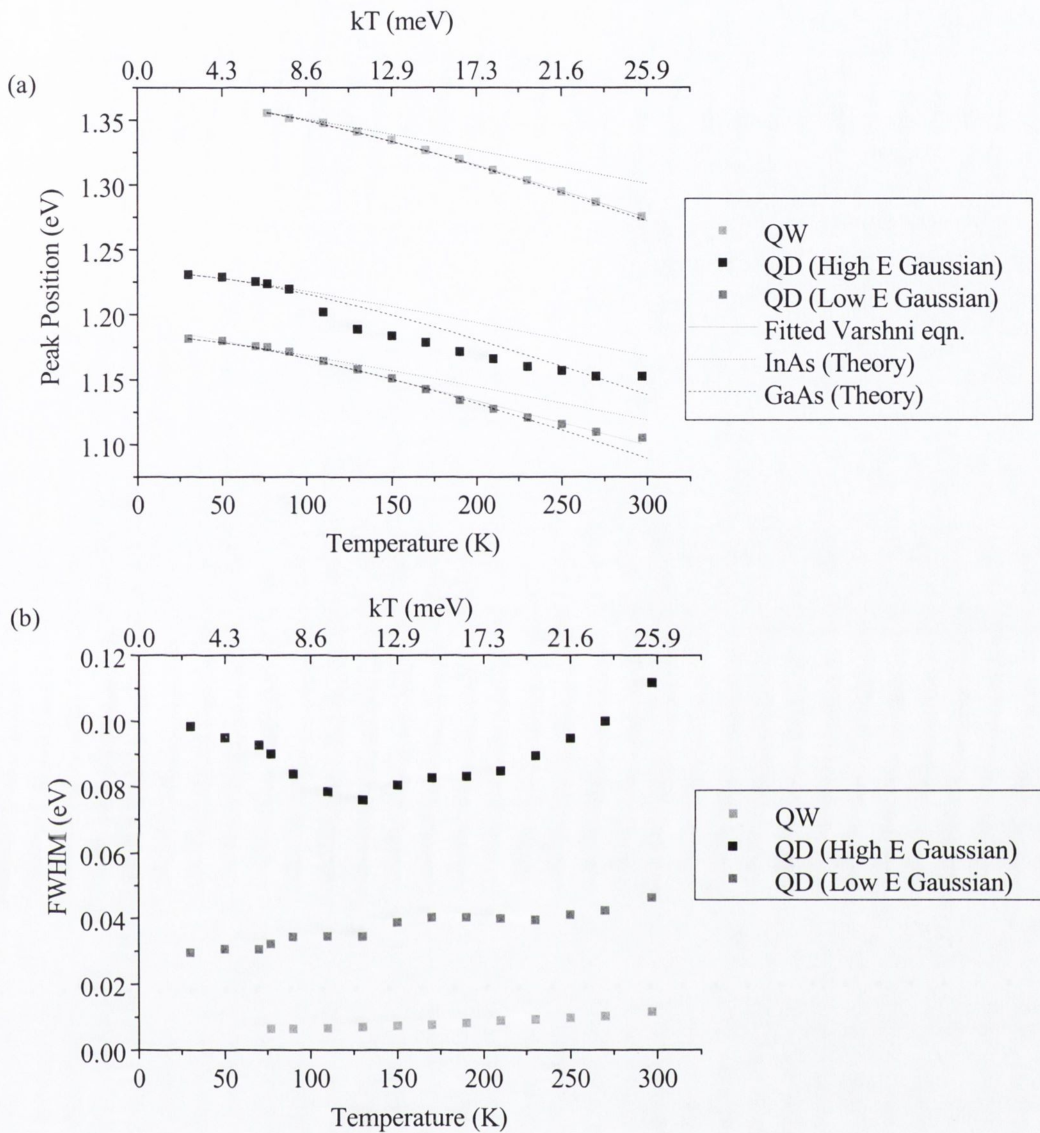

Figure 5.16 *Temperature dependence of (a) peak emission energy (b) FWHM of QW , and deconvolved Gaussian components of QD, PL spectra.*

The large inhomogeneous broadening of the QD spectrum is highlighted in Figure 5.16(b) where the FWHM of either of the deconvolved Gaussian components of the QD spectrum is considerably larger than the FWHM of the QW spectrum. The FWHM of both the QW and the low energy Gaussian of the QDs increase steadily with temperature due to increased probability of thermal population of excited states. The reduction in the FWHM of the emission from the high energy Gaussian distribution of QDs in the 70K to

130K range is consistent with the thermally induced redistribution of carriers towards the more strongly confining low recombination energy dots in this temperature range, at higher temperatures the expected increase in emission linewidth as mentioned above is observed.

5.8.2 Excitation Intensity dependence of QD PL spectrum.

There is an increased probability of carrier escape from excited quantum dot states due to their lower confinement energy. Therefore to experience the full benefits accrued from carrier confinement offered by QDs, the carrier density must not saturate the ground state transition. The reduced area coverage of QDs relative to the continuous QW layer results in a reduced overall number of electron states available for occupation. Therefore saturation of the ground state transition of the QD ensemble is expected to occur at a lower carrier density. This saturation carrier density is obviously dependent on the density of QDs, which is highly dependent on growth conditions and layer thickness, with reported values for similar self-assembled InAs/GaAs QD systems between 10^{10} and 10^{11} cm^{-2} [35,36,37,38]. Since the threshold excitation intensity for saturation of the ground state transition of the QDs in our sample is important to the interpretation of results of measurements in Chapter 6, we attempt to extract an estimate for its value from PL spectra measured at a range of pump intensities.

At low temperatures carriers in the ground state do not possess sufficient thermal energy to populate excited states, therefore excited state emission is only observed when carriers initially created in the surrounding GaAs recombine before relaxing into the ground state of the QD. This failure of the carriers to relax into the lowest energy states can occur due to two reasons, firstly if the ground state is already occupied or secondly due to an effect known as the phonon bottleneck. Carriers release excess energy through the emission of phonons, however the discrete electronic structure of QDs requires mediating phonons to have energy exactly equal to the energy spacing between the levels involved in the relaxation. This strict limitation on the permitted energy release processes can create a bottleneck for carrier relaxation, and is called the “phonon bottleneck” [45]. There have been extensive reported experimental results both supporting [46,47,48] and contradicting [37,49,50] the predicted inhibition of carrier relaxation in QDs. It appears

the influence of the phonon bottleneck on carrier dynamics is dependent on the specific properties of the quantum dot system under investigation. Time resolved PL measurements of the ground state emission from our QDs show fast rise times less than the 80ps resolution of the measurement system. This indicates fast carrier relaxation into the QD ground state, and the absence of any significant "phonon bottleneck" effects in our QD system. Therefore we only expect to observe excited state emission from a QD when it is occupied by more than one electron-hole pair. Due to the random selection of the dot into which a carrier relaxes, this can occur at carrier densities less than the areal density of dots [51], however the probability of it occurring significantly increases as the ground states of the QD ensemble approach full occupation.

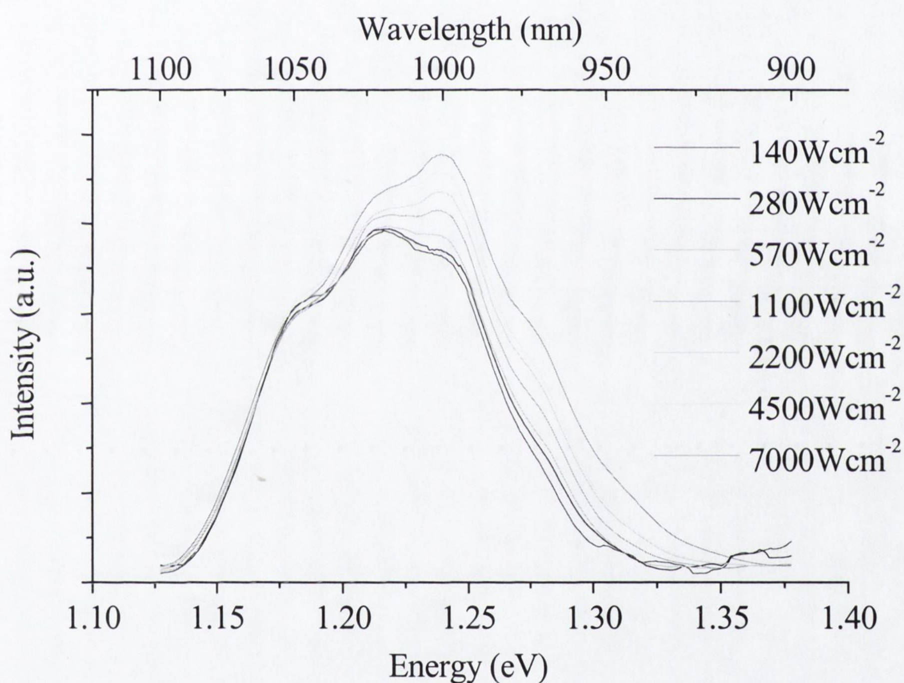

Figure 5.17 *QD PL spectra at 77K at various pump intensities; the spectra are scaled so that the low energy tails of the different spectra match up.*

No distinctly resolved peaks that could be attributed to ground and excited state transitions were observed in the QD PL spectrum even at pump intensities greater than $7kWcm^{-2}$, however there was a relative increase in the high energy component of the spectrum at high pump intensities. To determine whether this was due to the excited state

transitions of the low energy QDs overlapping the ground state transitions of the high energy dots, we show the difference between the spectra recorded at the highest and lowest pump intensities, after matching the low energy tails of the spectra, in Figure 5.18. The shape and FWHM of the difference between the spectra resembles the low pump intensity spectrum but displaced to higher energy. This suggests the existence of an excited state transition at ≈ 63meV above the ground state transition, and is consistent with the lowest excitation intensity spectrum resulting from ground state transitions.

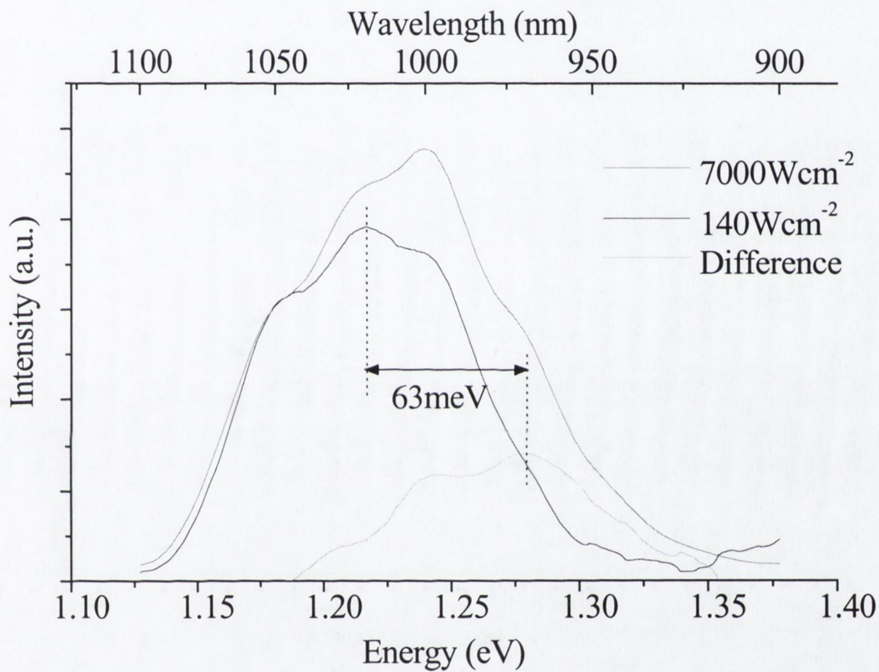

Figure 5.18 *Scaled high and low pump intensity PL spectra from Figure 5.17, and the difference between them. Note the similar shape of the difference and the low pump intensity spectrum.*

The pump intensity dependence of the PL yield from the QDs is summarized in Figure 5.19. The spectrally integrated PL shows an excellent linearity in the excitation intensity range investigated, with the fitted value for the linearity co-efficient a (PL yield = $c \times$ (Excitation Intensity)^{a} [38]) of 0.95 ± .02, where a value of 1 indicates a perfectly linear

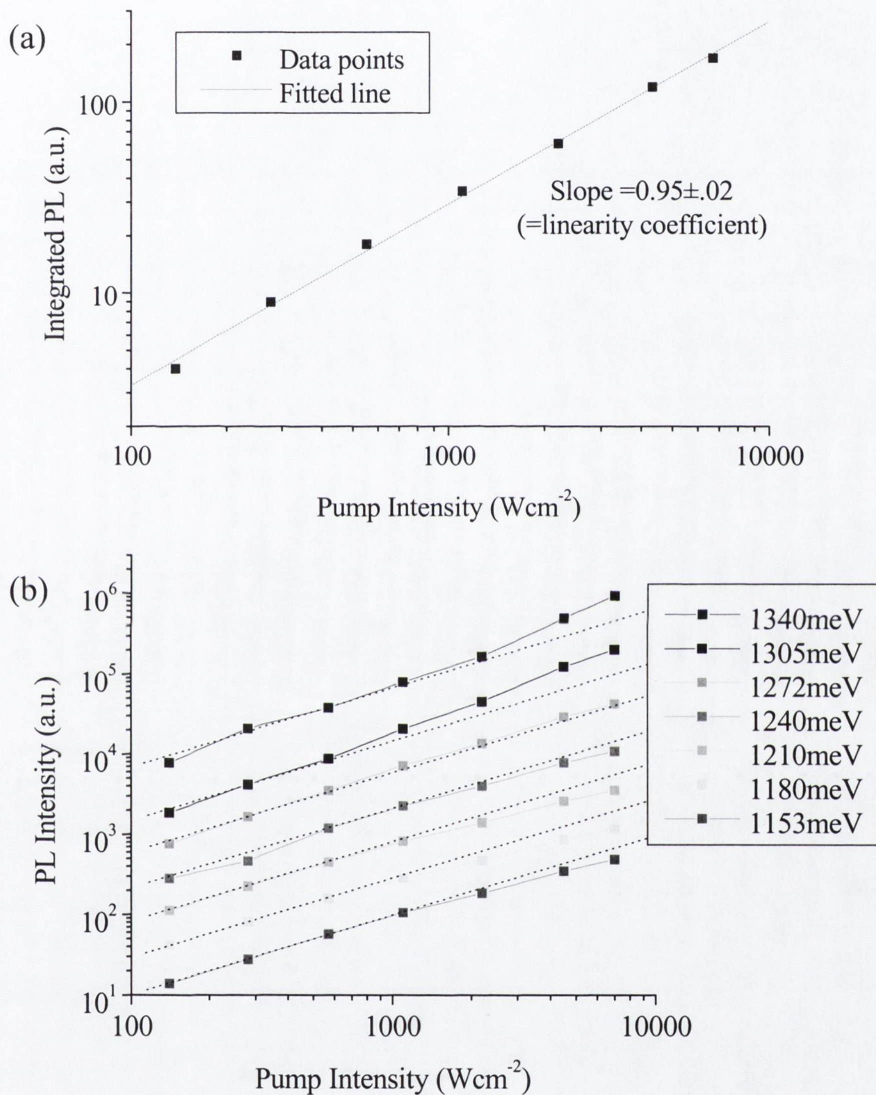

Figure 5.19 *Excitation intensity dependence of PL from QDs at 77K. (a) Spectrally integrated PL yield as a function of excitation intensity, with showing fitted line and corresponding linearity co-efficient. (b) PL intensity as a function of excitation intensity for various emission energies (offset in order of increasing energy for clarity). The dotted lines show a linear dependence on excitation intensity.*

dependence. In order to identify the threshold pump intensity at which the ground state transition saturates, the pump intensity dependence of the PL at a range of emission energies across the spectrum are plotted in Figure 5.19(b). At pump intensities less than $600Wcm^{-2}$, the PL intensity at all emission energies show a linear dependence on pump intensity, however at higher pump intensities only the PL intensity at 1272meV continues to show a linear dependence, with higher emission energies showing a superlinear dependence, and lower emission energies showing a sublinear dependence on pump intensity. The sublinear dependence is due to saturation of the ground state, and the superlinear dependence is due to additional excited state emission. Therefore we identify saturation of the ground state emission occurring at $\approx 600Wcm^{-2}$, for our sample containing three QD layers and our experimental conditions. This pump intensity corresponds to a threshold carrier density of $7.3e10cm^{-2}$ per QD layer, assuming a lifetime of 1ns. This threshold carrier density lies within the bounds of the expected dot densities for our QD system

5.9 Conclusions

The purpose of this chapter has been to characterise the carrier dynamics of the InAs/GaAs quantum dot layers in our sample. The understanding of the electronic properties of the QDs in bulk material is essential to our assessment of their potential advantages as emitters in etched 2D optical microcavities. The range of reported behaviour of similar self-assembled QD systems makes it impossible to extract reliable and consistent predictions for the confinement energies, excitation intensity corresponding to saturation of the ground state transition, and energy separation of ground and excited state transitions for our QDs, from previously published results. Therefore the measurements presented in this chapter provide both a reliable characterisation of the QDs in our microcavity structures and an additional set of results that contribute to the development of a more complete understanding of the recombination and carrier dynamics in InAs/GaAs self-assembled QDs.

A bimodal distribution of quantum dot sizes has been identified, with the temperature dependence of the integrated intensity, peak energy and FWHM of the PL from the QD

layer explained in terms of the dependence of carrier escape, retrapping and tunneling processes on QD size. Three specific temperature ranges were identified, at temperatures below 70K carriers are trapped in all QDs and emission properties are not strongly dependent on temperature, in the 70K to 150K range carriers possess sufficient thermal energy to escape from increasing numbers of QDs with carrier redistribution towards larger dots occurring, finally at temperatures above 150K a decrease in emission from all dots is observed indicating carrier escape from even the largest dots. The excitation intensity dependent measurements showed saturation of the ground state transition at a pump intensity of 600Wcm^{-2}, with increasing emission from excited state transitions at higher pump intensities.

5.10 References

1 "Photoluminescence from InAs quantum dots on GaAs(100)", W. Cheng, X. Xie, Z. Y. Zhong, L. Cai, Q. Huang, and J. Zhou, Thin Solid Films **312** p.287 (1998)

2 "Thermally activated carrier transfer and luminescence line shape in self-organised InAs quantum dots", L. Brusaferri, S. Sanguinetti, E. Grilli, M. Guzzi, A. Bignazzi, F. Bogani, L. Carraresi, M. Colocci, A. Bosacchi, P. Frigeri, and S. Franchi, Appl. Phys. Lett. **69** (22) p. 3354 (1996)

3 "Self-assembled InAs/GaAs quantum dots studied with excitation dependent cathodoluminescence" Y. Tang, D. H. Rich, I. Mukhametzhanov, P. Chen, and A. Mudhukar, J. of Appl. Phys. **84** (6) p. 3342 (1998)

4 "Optical properties of InAs quantum dots: Common trends" M. Grassi Alessi, M. Capizzi, A.S. Bhatti, and A. Frova, Phys Rev B **59** (11) p.7620 (1999)

5 "Overview of fundamentals and applications of electrons, excitons and photons in confined structures" C. Weisbuch, H. Benisty, and R. Houdré, J. of Luminescence **85** p.271 (2000)

6 "Molecular Beam Epitaxy", A.Y. Cho and J. R. Arthur, Prog. Solid State Chem. **10** p.157 (1975)

7 *Quantum well lasers,* edited P. S. Zory Jr. (Academic Press, London, 1993)

8 "Multiple Quantum well reflection modulator", G. D. Boyd, D. A. Miller, D. S. Chemla, S. L. McCall, A. C. Gossard, J. H. English, Appl. Phys. Lett. **50** (17) p.1119 (1987)

9 *Quantum Semiconductor Structures – Fundamentals and Applications*, C. Weisbuch, and B. Vinter, (Academic Press, London, 1991)

10 "Semiconductor quantum dots and related systems: electronic, optical, luminescence and related properties of low dimensional systems" A. D. Yoffe, Advances in Physics, **50** (1) p.1 (2001).

11 "Electronic coupling and structural ordering of quantum dots using InAs quantum dot columns", G. S. Solomon, Journal of Electronic Materials, **28** (5) p.392 (1999)

12 "Quantum dot resonant cavity light emitting diode operating near 1300nm", J. W. Gray, D. Childs, S. Malik, P. Siverns, C. Roberts, P. N. Stavrinou, M. Whitehead, R. Murray and G. Parry. Elect. Lett. **35** (3) p.242 (1998)

13 "Quantum-Dot Heterostructure Lasers" N. N. Ledentsov, M. Grundmann, F. Heinrichsdorff, D. Bimberg, V. M. Ustinov, A. E. Zhukov, M. V. Maximov, Z. I. Alferov, and J. A. Lott, IEEE J. Sel. Top. Quant., **6** (3) p.439 (2000)

14 H. P. Rocksby J. Soc. Glass Techn., 16 p.171 (1932).

15 "Size quantization of the electron energy spectrum in a microscopic semiconductor crystal", A. I. Ekimov and A. A. Onushchenko, JETP Lett. **40** (8) p. 1136 (1984)

16 "Development of IR-emitting colloidal II-VI quantum-dot materials" S. V. Kershaw, Harrison, A. L. Rogach, A. Kornowski, IEEE J. of Sel. Top. Quant. **6** (3) p. 534 (2000)

17 "Fabrication of small laterally patterned multiple quantum wells" A. Scherer and H. G. Craighead, Appl. Phys. Lett. **49** (19) p.1284 (1986)

18 " Fabrication of CdZnSe/ZnSe quantum dots and quantum wires by electron beam lithography and wet chemical etching ", M. Illing, G. Bacher, T. Kummell, A. Forchel, D. Hommel, B. Jobst, and G. Landwehr, Journal of Vacuum Science & Technology B, **13** (6) p.2792 (1995).

19 "10-nm linewidth electron beam lithography on GaAs" H. G. Craighead, R. E. Howard, L. D. Jackel, and P. M. Mankiewich, Appl. Phys. Lett. **42** (1) p.38 (1983).

20 "Enhancement of spin splitting due to spatial confinement in $In_xGa_{1-x}As$ quantum dots", M. Bayer, V. B. Timofeev, T. Gutbrod, A. Forchel, R. Steffen, J. Oshinowo, Phys. Rev. B **52** (16) p. R11623 (1995)

21 *Quantum Dot Heterostructures*, D. Bimberg, M. Grundmann, N. N. Ledentsov (John Wiley & Sons Ltd., Chichester, 1999) page 14.

22 *Properties of lattice-matched and strained Indium Gallium Arsenide*, Edited P. Bhattacharya (INSPEC, London, 1993)

23 I. N. Stranski and L. Krastanov, Sitzungsberichte d. Akad. D. Wissenschaften in Wien, Abt. Iib, band **146**, p.797.

24 Arthur Minnaert, Ph.D. Thesis, Eindhoven University of Technology (2001)

25 "The intrinsic stress of polycrystalline and epitaxial thin metal-films", R. Koch, Journal of Physics – Condensed Matter **6** (45) p.9519 (1994)

26 *Quantum Dot Heterostructures*, D. Bimberg, M. Grundmann, N. N. Ledentsov (John Wiley & Sons Ltd., Chichester, 1999) page 77.

27 *Quantum Dot Heterostructures*, D. Bimberg, M. Grundmann, N. N. Ledentsov (John Wiley & Sons Ltd., Chichester, 1999) page 252.

28 "TEM/HREM Visualisation of nm-scale Coherent InAs Islands (quantum dots) in a GaAs Matrix", S. Ruvimov, and K. Scheerschmidt, Phys. Stat. Sol. (a) **150** p.471 (1995)

29 "Quantum many-body states of excitons in a small quantum dot", A. Barenco and M. A. Dupertuis, Phys. Rev. B **52** (4) p.2766 (1995)

30 "Electronic structure of InAs/GaAs self-assembled quantum dots" M. A. Cusack, P. R. Briddonand and M. Jaros, Phys. Rev. B **54** (4) p.R2300 (1996)

31 "Self-Assembled Semiconductor Structures: Electronic and Optoelectronic Properties", H. Jiang and J Singh, IEEE J. Sel. Top. Quant. **34** (7), p.1188 (1998)

32 "Electronic and Optical properties of strained quantum dots modeled by 8-band k·p theory" O. Stier, M. Grundmann, and D. Bimberg, Phys. Rev. B **59** (8) p.5688-5701 (1999).

33 "Comparison of the electronic structure of InAs/GaAs pyramidal quantum dots with different facet orientations" J. Kim, L.-W. Wang, and A. Zunger, Phys. Rev. B **57** (16) p.R9408 (1998)

34 "Electronic structures of [110]-faceted self-assembled pyramidal InAs/GaAs quantum dots" L.-W. Wang, J. Kim, and A. Zunger, Phys. Rev. B **59** (8) p.5680 (1999)

35 "Size distribution in self-assembled InAs quantum dots on GaAs (001) for intermediate InAs coverage" H. Kissel, U. Muller, C. Walther, W. T. Masselink, Yu. I. Mazur, G. G. Tarasov, and M. P. Lisitsa, Phys. Rev. B **62** (11) p. 7213 (2000)

36 "Temperature Dependent Optical Properties of Self-Organised InAs/GaAs Quantum Dots" R. Heitz, I. Mukhametzhanov, A. Madhukar, A. Hoffmann, and D. Bimberg, J. of Electronic Materials **28** (5) p.520 (1999).

37 "Electronic energy levels and energy relaxation mechanisms in self-organised InAs/GaAs quantum dots", M. J. Steer, D. J. Mowbray, W. R. Tribe, M. S. Skolnick, M. D. Sturge, M. Hopkinson, A. G. Cullis, C. R. Whitehouse, and R. Murray, Phys. Rev. B **54** (24) p.17738 (1996)

38 "Optical Characteristics of Self-Assembled InAs/GaAs Quantum Dots at various Temperatures and Excitations", U. H. Lee, J. S. Yim, D. Lee, H. G. Lee, S. K. Noh, J. Y. Leem, and H. J. Lee, J. of the Korean Phys. Soc. **37** (5) p.593. (2000).

39 "Photoluminescence of Single InAs Quantum Dots Obtained by Self-Organised Growth on GaAs", J.-Y. Marzin, J.-M. Gérard, A. Izrael, and D. Berrier, Phys. Rev. Lett. **73** (5) p.716 (1994)

40 *Quantum Dot Heterostructures*, D. Bimberg, M. Grundmann, N. N. Ledentsov (John Wiley & Sons Ltd., Chichester, 1999) page 126.

41 "Carrier transfer in self-assembled coupled InAs/GaAs quantum dots", G. G. Tarasov, Yu. I. Mazur, Z. Ya. Zhuchenko, A. Maaßdorf, D. Nickel, J. W. Tomm, H. Kissel, C. Walther, and W. T. Masselink, J. of Appl. Phys. **88** (12) p. 7162 (2000)

42 "Photoluminescence study of in situ annealed InAs quantum dots: Double-peak emission associated with bimodal size distribution" H. Lee, R. Lowe-Webb, T. J. Johnson, W. Yang, and P. C. Sercel, Appl. Phys. Lett. **73** (24) p. 3556 (1998)

43 "Exciton localization and temperature stability in self-organised InAs quantum dots", D. I. Lubyshev, P. P. Gonzalez-Borrero, E. Marega, Jr., E. Petitprez, N. La Scala, Jr., and P. Basmaji, Appl. Phys. Lett. **68** (2) p.205 (1996)

44 "Temperature dependence of the energy gap in semiconductors" Y. P. Varshni Physica **34** (1) p.149 (1967).

45 "Intrinsic mechanism for the poor luminescence properties of quantum-box systems", H. Benisty, C. M. Sotomayor Torres, and C. Weisbuch, Phys. Rev. B **44** (19) p.10945 (1991).

46 "Emission from discrete levels in self-formed InGaAs/GaAs quantum dots by electric carrier injection: influenece of phonon bottleneck", K. Mukai, N. Ohtsuka, H. Shoji, and M. Sugawara, Appl. Phys. Lett. **68** (21) p.3013 (1996)

47 "Photoluminescence from a Single GaAs/AlGaAs Quantum Dot", K. Brunner, U. Brockelmann, G. Abstreiter, M. Walther, G Bohm, G. Trankle, and G. Weinmann, Phys. Rev. Lett. **69** (22) p.3216 (1992).

48 "Luminescence from excited states in strain-induced $In_xGa_{1-x}As$ quantum dots", H. Lipsanen, M. Sopanen, and J. Ahopelto, Phys. Rev. B **51** (19) p.13868 (1995)

49 "Energy relaxation by multiphonon processes in InAs/GaAs quantum dots", R. Heitz, M. Veit, N. N. Ledentsov, A. Hoffmann, D. Bimberg, V. M. Ustinov, P. S. Kop'ev, and Zh. I. Alferov, Phys. Rev. B **56** (16) p.10435 (1997)

50 "Rapid carrier relaxation in self-assembled $In_xGa_{1-x}As$/GaAs quantum dots", B. Ohnesorge, M. Albrecht, J. Oshinowo, A. Forchel, Y. Arakawa, Phys. Rev. B **54** (16) p.11532 (1996)

51 "Theory of random population for quantum dots", M. Grundmann and D. Bimberg, Phys. Rev. B, **55** (15) p.9740 (1997)

Chapter 6

Carrier diffusion in InAs/GaAs QD and InGaAs/GaAs QW layers and its impact on the performance of etched microcavity structures.

6.1 Introduction

Having characterised the integrated emission properties of our InAs/GaAs QDs embedded in bulk semiconductor, this chapter focuses on the benefits of such QDs as emitters in etched microcavity structures, such as the microleek structure discussed in chapter 4. A number of emission properties including internal quantum efficiency, emission linewidth and emission wavelength determine the suitability of an active layer for incorporation into any microcavity structure. These emission characteristics have been extensively investigated in both fundamental QD research [1,2,3] and in QD laser research [4,5,6], while the emission linewidth and wavelength of our QDs were discussed in chapter 5. This chapter focuses on another important potential advantage of QDs as emitters in a microcavity that utilizes deeply etched lateral mirrors, namely their ability to reduce the impact of non-radiative recombination at the etched sidewall interfaces. The reduced carrier diffusion in our InAs/GaAs QD layer due to carrier trapping in individual dots is quantified in section 6.4, while the impact of this effect on the emission from an etched microcavity structure is shown in section 6.5.

6.2.Non-radiative surface recombination.

At a semiconductor surface the abrupt termination of the periodic potential of the lattice results in a distribution of allowed energy states within the bandgap. These surface states are predicted to exist even at the boundary of a perfect crystal [7], however in practice the surface states are generally due to the absorption of impurities by dangling bonds on the

surface [8], with electronegative impurities such as oxygen acting as electron acceptors. An extensive review of the effect of impurities absorbed on the surface of a semiconductor is contained in reference [9]. This process results in the creation of surface states of a range of energies in the otherwise forbidden energy gap between conduction and valence bands. A high concentration of deep and shallow trap states in the bandgap, act as non-radiative recombination centres. Therefore we expect that the recombination rate will be enhanced near the surface, resulting in a decreased carrier density at the surface. Carriers will then diffuse from the body of the semiconductor into the surface layer in an attempt to even out carrier differences.

The total number of carriers recombining at the surface per unit area and unit time is given by

$$U_{surface} = Sn \qquad (6.1)$$

where n is the carrier density at the surface and S is the surface recombination velocity, with the dimensions [Length×Time^{-1}], and is defined as

$$S = \sigma v_{th} N_s \qquad (6.2)$$

where σ is the capture cross-section of the recombination centre, v_{th} is the thermal velocity of the carriers, and N_s is the total number of recombination centres per unit area at the surface.

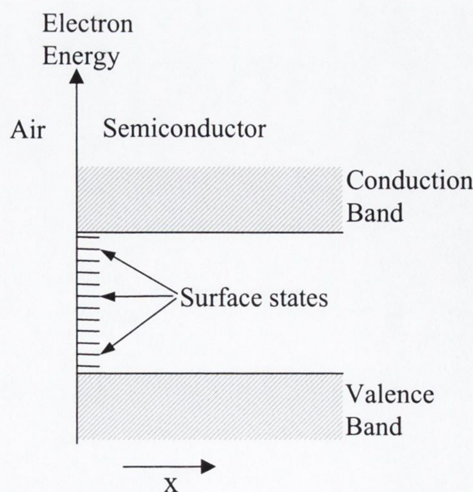

Figure 6.1 *Electron energy levels at crystal surface.*

The magnitude of the surface recombination velocity varies substantially between different materials due in part to the varying stability of surface oxide states [9]. Typical S values are 10^6cms^{-1} for GaAs, 10^3cms^{-1} InP, and 10^1cms^{-1} for Si. Due to the high S value for GaAs we expect to observe strong surface effects at etched interfaces in our GaAs/AlGaAs waveguide samples containing InAs/GaAs QDs or $In_{0.17}Ga_{0.83}As$/GaAs QWs.

6.3 Experimental setup

The experimental setup employed for the both the diffusion and cavity measurements presented in this chapter was similar to that used in chapter 4. The sample was mounted in an open cycle liquid nitrogen cryostat at the focal distance of a long working distance ×40, 0.5 NA microscope objective (MO2) that produced a ≈2μm diameter excitation spot on the sample surface. A laser diode providing CW emission at λ=790nm was used as the excitation source for all measurements except the time-resolved PL measurements for which a mode-locked Ti-Sapph laser was used to provide pulsed excitation. The same optical arrangement and lens (MO1, L2 and L1) were used as previously discussed in section 4.4, which allowed the simultaneous imaging of the sample surface on the CCD camera, and measurement of the emission spectrum. The cooled Ge detector (see section 5.5) was mounted at the exit slit of the monochromator providing spectral sensitivity in the 0.8μm to 1.7μm wavelength range.

The microscope objective MO2 was mounted on a piezoelectric translation stage aligned parallel to the sample surface. Since the collimated input beam to MO2 overfilled the lens aperture, adjusting the position MO2 parallel to the sample surface by up to 50μm (the maximum displacement of the piezo stage) simply shifts the excitation spot position on the sample by the same amount without affecting the spot size or profile. The piezoelectric translation stage was calibrated by imaging the displacement of the laser spot on a calibration grid of known size positioned in the sample plane. While scanning the excitation spot position on a sample the PL intensity was measured by the spectrometer, while a second power meter (PM2 in Figure 6.2) was positioned in front of the CCD camera and measured the intensity of the reflected laser light. The pump beam

was modulated at 10Hz and lock-in amplifiers were employed to remove noise from the detected PL and reflected laser signals. The piezo translation stage, and both lock-in amplifiers were interfaced with a PC using an IEEE GPIB board, and a QBASIC program controlled the synchronised scanning of MO2 and recording of the output signals from the lock-in amplifiers.

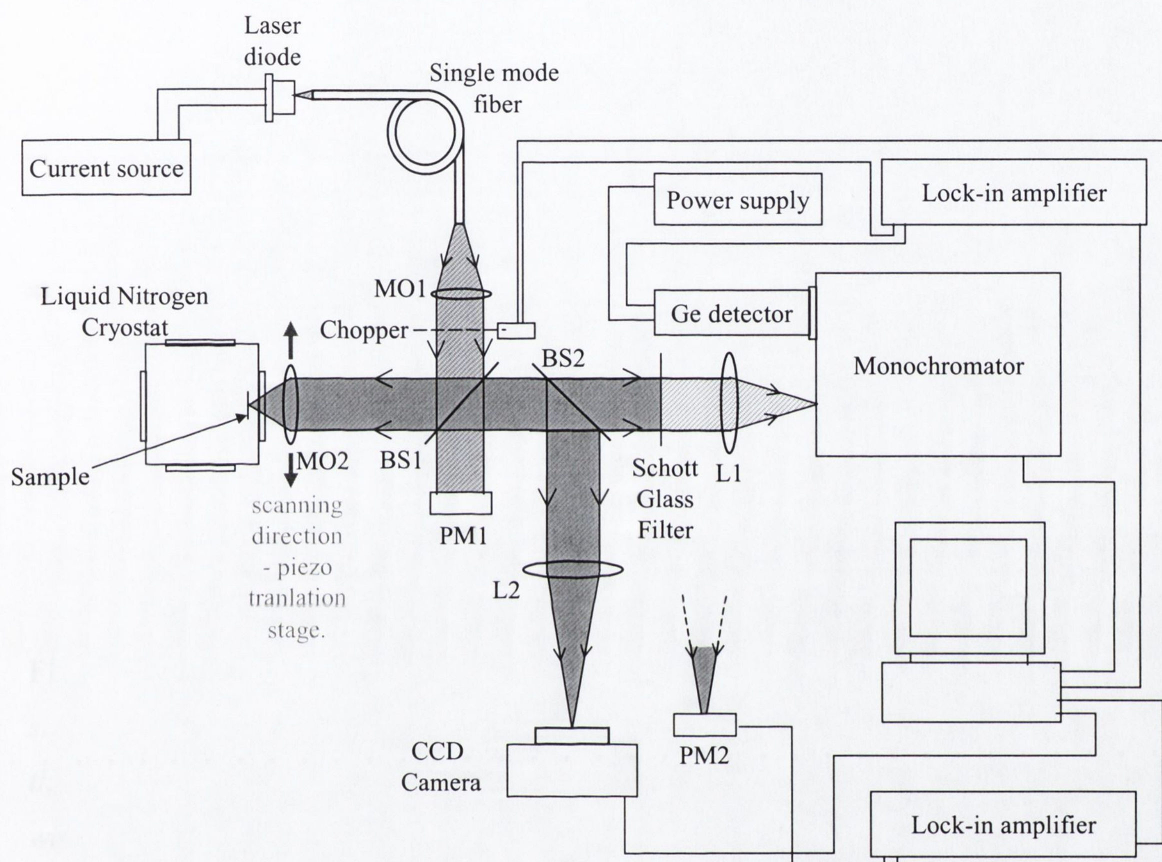

Figure 6.2 *Diagram of experimental setup. MO1 = × 10, 0.25 NA microscope objective, MO2 = ×40, 0.5 NA microscope objective, L1 = 10 cm focal length spherical lens, L2 = 20 cm focal length spherical lens, BS = beam splitter and PM = power meter.*

The stripe excitation used in the PL lifetime measurements shown in Figure 6.9, was created on the sample surface using the optical arrangement shown in Figure 6.3. Two additional lenses, one plano-convex cylindrical and the other spherical of equal focal lengths (= 15cm), were positioned before BS1 in the collimated beam produced by MO1. The two lenses were positioned the sum of their focal lengths apart, resulting in the

formation of a excitation stripe with a FWHM width of 2.4μm, and length 30μm on the sample surface. The PL lifetime measurements were performed using the time resolved single photon counting arrangement discussed in section 4.4, with the microchannel plate photomultiplier replacing the Ge detector at the exit slit of the spectrometer.

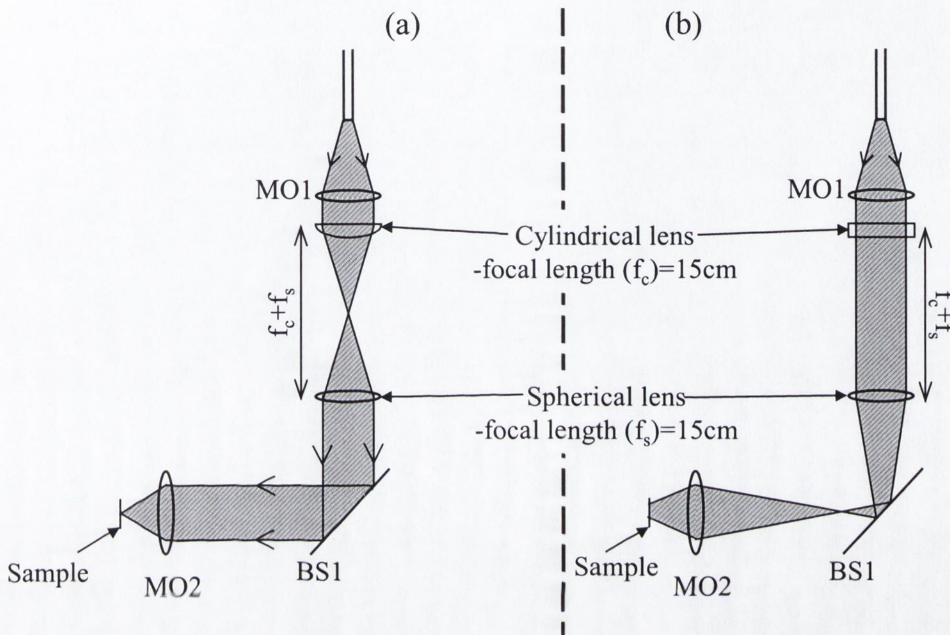

Figure 6.3 *Optical arrangement employed to create the excitation stripe on the sample surface, showing, in two perpendicular planes, the role of the two additional lenses in the formation of the stripe (a) plane in which cylindrical lens focuses light (b) plane in which cylindrical lens has no focusing effect.*

6.4 Diffusion measurements

6.4.1 Introduction

Diffusion is a process in which particles disperse, moving from regions of higher density to regions of lower density. It is an important carrier transport mechanism in semiconductors, and plays a significant role in understanding the operation and design of semiconductor electronic devices. The study of diffusion in semiconductors began with the development of the transistor and the *p-n* junction when it was realised that diffusive

transport under certain conditions could become more important than the drift current in the transition region between the *p* and *n* regions of the *p-n* junction [10,11]. In this work the focus is on lateral carrier diffusion in the active region of an optoelectronic device, a process that provides carriers to the surface traps discussed above. By restricting lateral carrier diffusion in the active layer, the flow of carriers from the centre of devices towards the edges can be controlled. Without the supply of carriers, the trapping sites at the sidewalls are made ineffective, and the quality of the surface is no longer important. Clearly the discrete nature of QDs prevents any carrier transport once the carriers remain trapped within individual QDs. However the thermal redistribution of carriers between different sized QDs in our sample observed in the spectral measurements of chapter 5 indicated the significant probability of carrier escape from our QDs at room temperature. The carriers escape into the continuous wetting layer, in which they are free to diffuse in the two lateral directions before either recombining or being recaptured into another QD. Therefore the ability of our QD active layer to limit carrier diffusion depends on the ratio of time the carriers spend localised in QDs to time spent in the continuous wetting layer or surrounding GaAs.

In this section the ambipolar diffusion of carriers in the intrinsic self-assembled InAs/GaAs QD layer and InGaAs/GaAs QW in our samples are investigated. (We use the term 'QD layer' to refer to both the distribution of QDs and underlying wetting layer). Ambipolar transport refers to the situation where both electrons and holes move together to prevent a large space charge field being established.

Many techniques exist for measuring diffusion in semiconductors including, short circuit photocurrent measurements [12], electron beam induced current [13], cathodoluminescence (CL) [14], time of flight measurements [15], and transient grating techniques. The diffusion length may also be deduced from optical absorption [16] and nonlinear PL [17]. The method we employ exploits the fast non-radiative recombination channel presented by the etched surface. A focused laser beam is used to create carriers in a small spot close to a straight etched edge. The luminescence intensity is then recorded as a function of separation between the excitation spot and etched edge. The PL intensity drops once the excitation spot is close enough to the edge for the created carriers to reach the edge through diffusion. The carrier diffusion is quantified by comparing the measured falloff in PL intensity with separation to the simulated falloff for different diffusion

lengths. While this technique is not the most direct method for measuring carrier diffusion, it has the advantage of providing direct results on the effect of edge recombination as a function of the initial carrier distribution and etched edge separation. Also since etched edges already existed on our sample this technique requires no further sample processing.

Ambipolar diffusion has been extensively investigated in QW layers [14,18,19] however little work has been reported which actually quantifies the reduction in diffusion achieved by utilising QDs, despite many references to the importance of this effect in choosing QDs as emitters in etched microcavity structures [20,21,22]. The reduction in carrier diffusion produced by InGaAs/GaAs self-assembled QDs at room temperature has been measured by CL and its impact on miniature laser performance discussed in references [23] and [24]. Our samples contain InAs/GaAs QD layers and we investigate carrier diffusion in the 77K to 297K temperature range to provide an insight into the role of thermally activated escape from the dots.

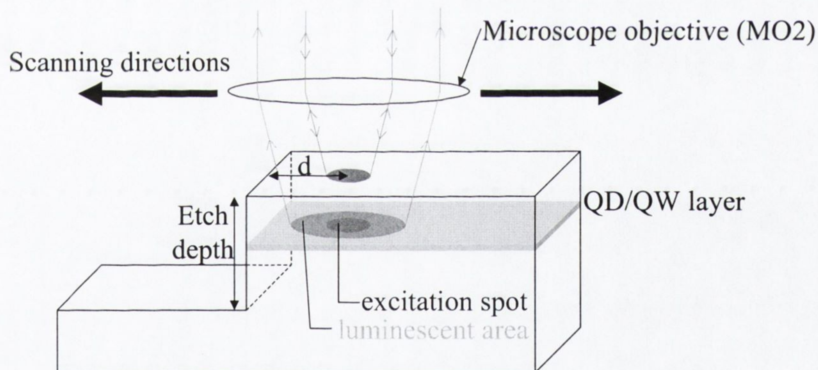

Figure 6.4 *Schematic diagram showing experimental technique employed to quantify carrier diffusion.*

6.4.2 Theory - The Diffusion Equation

In this section the basic equations and terms used to describe carrier diffusion are introduced.

Continuity demands that the rate of change of carrier density in a region of the semiconductor is equal to the number of carriers entering that region plus the creation/annihilation rate in the region, therefore the continuity equation in the two lateral directions takes the form,

$$\frac{\partial N(r,t)}{\partial t} = -\nabla \cdot \mathbf{J}(r,t) + g(r) - \frac{N(r,t)}{\tau} \tag{6.3}$$

$N(r,t)$ is the carrier density as a function of radial coordinate r, and time, t. $\mathbf{J}(r,t)$ is the carrier current density, and $g(r)$ is the rate of carrier generation. The last term in (6.3) accounts for carrier recombination, and assumes an exponential carrier decay characterised by a single lifetime τ. The carrier current density due to diffusion, $\mathbf{J}$, is related to the carrier density, N, by Fick's law,

$$\mathbf{J}(r,t) = -D\nabla N(r,t) \tag{6.4}$$

which although an approximation is known to be true for many systems [25]. D is the diffusion constant and has the dimensions [Length^2 ×Time^{-1}]. Combining (6.3) and (6.4) yields the well known diffusion equation

$$\frac{\partial N(r,t)}{\partial t} = D\nabla^2 N(r,t) + g(r) - \frac{N(r,t)}{\tau} \tag{6.5}$$

As an example of a situation for which a simple analytic solution exists for the diffusion equation, consider carriers being generated at $r = 0$ and $t = 0$ only, and search for a steady state solution ($\partial N/\partial t = 0$). Then for $t > 0$ equation (6.5) reduces to

$$D\nabla^2 N(r,t) - \frac{N(r,t)}{\tau} = \nabla^2 N(r,t) - \frac{N(r,t)}{L^2} = 0 \tag{6.6}$$

where we have defined $L^2 = D\tau$. The parameter L is called the carrier diffusion length. The general steady-state solution to (6.6) is

$$N(r) = Ae^{-r/L} + Be^{r/L} \tag{6.7}$$

where A and B are constants. Assuming the boundary condition $N \to 0$ as $r \to \infty$, forces B = 0. Therefore the solution to the diffusion equation in these conditions is

$$N(r) = N(0)e^{-r/L} \tag{6.8}$$

where $N(0)$ is the value of the carrier concentration at r = 0. The solution shows an exponential decay in the steady state carrier concentration with distance from the source at r = 0, with a decay constant equal to the carrier diffusion length.

This simple example introduces the diffusion length parameter that combines the two material dependent properties, D and τ, in the general diffusion equation (6.5). To simulate our experimental conditions we have to account for the shape of our laser excitation spot, while the presence of a straight etched edge boundary on one side of the spot removes radial symmetry from the problem making it difficult to obtain an analytic solution. Therefore we employ a numerical simulation based on (6.5) to model the diffusion and recombination processes in our experimental system. The details and results of the simulation are contained in section 6.4.4.

6.4.3 Results

Our measurement technique depends on the ability to position our excitation spot at a known separation from a well-defined straight etched edge with sub micron accuracy and stability. To determine whether our experimental setup offered sufficient spatial resolution, the variation in the reflected laser power produced when the excitation spot was scanned across the edge was compared to the profile obtained from the measured CCD image of the laser spot. Assuming a Gaussian shaped excitation spot, fitted values for the laser spot FWHM were extracted from both measurements. A FWHM value of 2.15±0.03μm was obtained from directly fitting the imaged spot, while a FWHM value of 2.1±0.1μm was obtained from fitting the dependence of the reflected laser power on edge

position, assuming constant reflectivity of the incident laser from the sample surface and zero reflectivity beyond the etched edge. Since the value obtained from the scanning edge technique agrees with the value obtained from direct imaging, whose accuracy is only limited by the CCD resolution, this result confirms the presence of a sharply defined edge on the sample, and the ability of the experimental setup to provide spatial stability sufficient to resolve features with dimensions less than the excitation spot size.

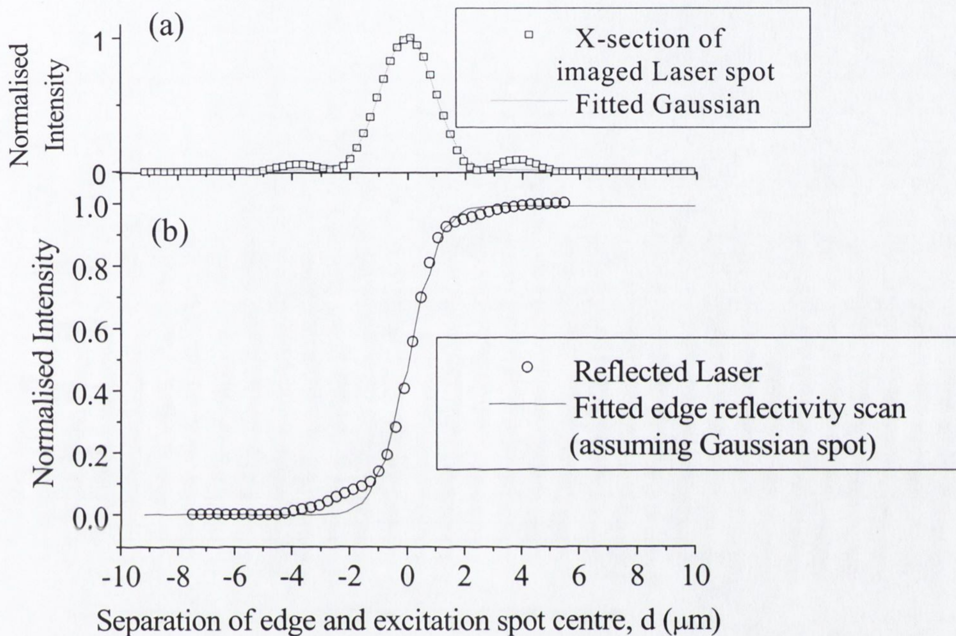

Figure 6.5 *(a) Cross-section through CCD image of laser spot on sample surface, (b) Variation in reflected laser power as function of distance between straight etched edge and centre of laser spot.*

Simultaneous reflected laser and PL edge profiles (reflected/emitted power as functions of edge to centre of spot separation, *d*) for samples containing both QD and QW active layers were measured in the temperature range 77K to 297K. The PL profiles were recorded at the peak of the QD or QW emission spectrum at that temperature. The reflected laser edge profile is used to identify the position of the edge during each scan. In Figures 6.6, 6.7 and 6.8 the laser edge profiles are matched up for the different temperature/pump intensity results, with only one of the laser profiles shown for clarity.

The PL profiles shown in Figures 6.6 and 6.7 were recorded at an excitation intensity of 400Wcm^{-2}, which was sufficiently low to prevent overfilling of the ground state of the

QDs. The excitation intensity dependence of the edge profiles in the $140Wcm^{-2}$ to $7kWcm^{-2}$ range, at 77K is shown in Figure 6.8. The PL spectra at the same range of excitation intensity values and experimental conditions were shown in Figure 5.17.

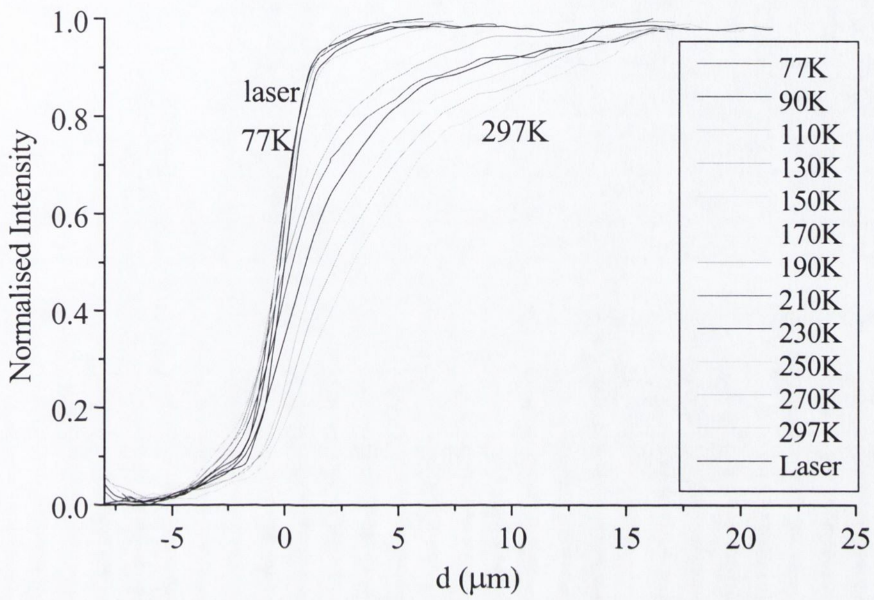

Figure 6.6 *PL edge profiles for sample containing QD active layer.*

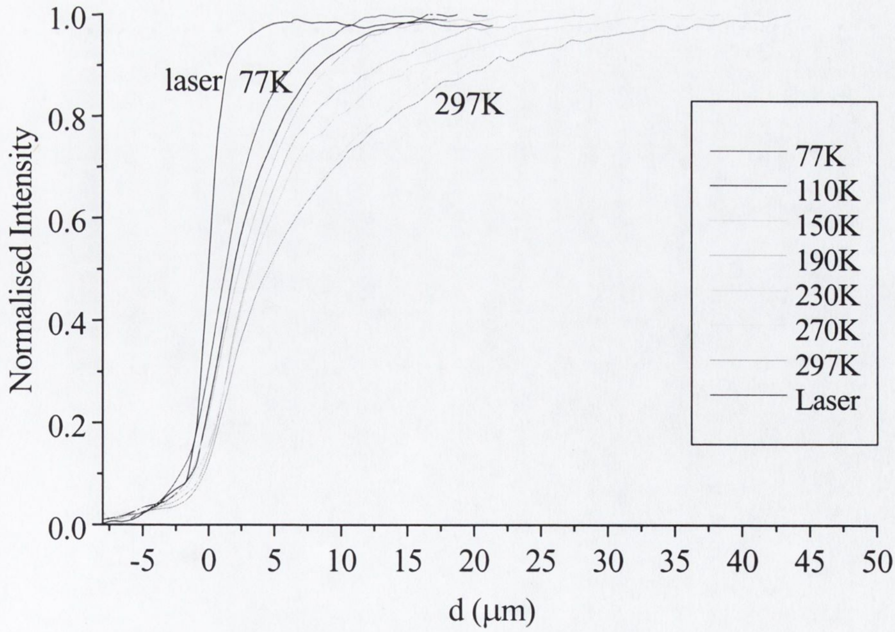

Figure 6.7 *PL edge profiles for sample containing QW active layer.*

The PL edge profile of the QD active layer matches the laser edge profile at temperatures less than 170K. At higher temperatures the PL intensity drops before the laser spot starts to cross the etched edge, with the distance at which the initial drop off in PL is observed occurring at increasing distances from the edge as the temperature increases. The PL edge profiles of the sample containing QW active layers show a similar trend with temperature however the distances at which the falloff in intensity first occurs is greater and even at 77K there is a significant difference between the laser and PL edge profiles.

The PL edge profiles from the QD sample at 77K in Figure 6.8 match the laser profile for excitation intensities less than 1100Wcm^{-2}, at higher pump intensities a drop in emission intensity was observed at greater separation of the excitation spot and edge.

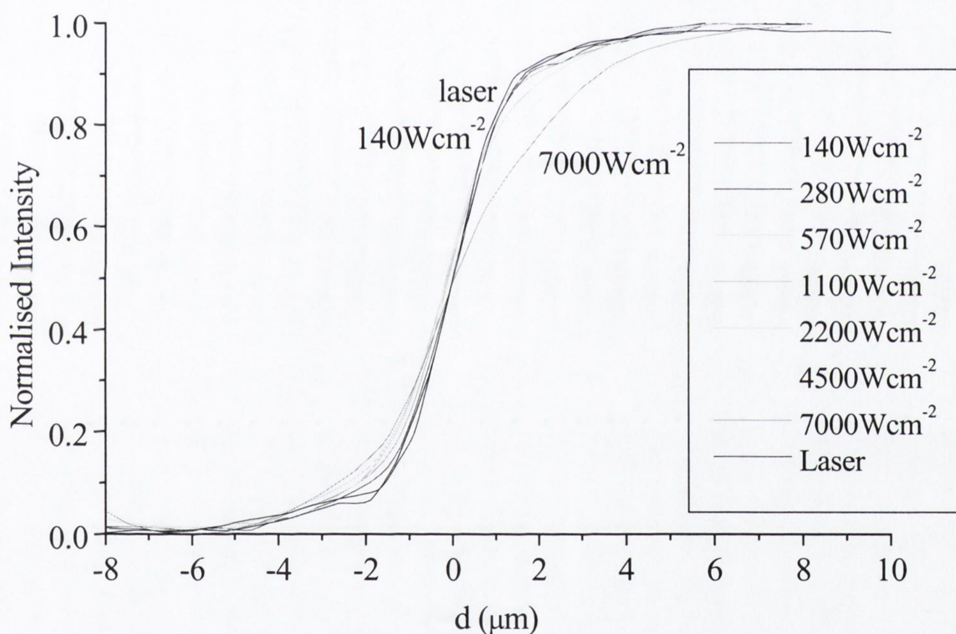

Figure 6.8 *PL edge profiles for sample containing QD active layer at 77K for a range of excitation intensities.*

The fast non-radiative recombination channel presented by the exposed surface produced by the etching process not only reduces the overall PL emission intensity but also reduces the PL emission lifetime if carriers reach the surface. This fast surface recombination was responsible for the reduced PL lifetime from the microleek structure at room temperature. As a second approach to trying to quantify the distance carriers diffuse in the InAs/GaAs

QD layer, the emission lifetime as a function of separation between initial carrier distribution and the etched edge was measured.

However since the responsivity of the microchannel plate PMT detector used to perform time-resolved measurements drops off at wavelengths greater than 850nm, with a maximum detectable wavelength of ≈1μm, the PL lifetimes were recorded at λ= 950nm. The luminescence from the QD sample at this wavelength originates from small QDs in the extreme tail of the QD size distribution. Also the pulsed excitation required for time resolved measurements, results in higher carrier densities than the corresponding average intensity CW excitation. In order to reduce the carrier density while maintaining a measurable PL signal a stripe excitation on the surface of the sample was employed. The stripe was orientated parallel to the etched edge thereby providing a greater excitation area while still maintaining a tightly confined initial distribution of carriers perpendicular to the edge. Figure 6.9 shows a drop in the PL lifetime from the QD sample at room temperature when the stripe excitation is within 7μm of the etched edge. The

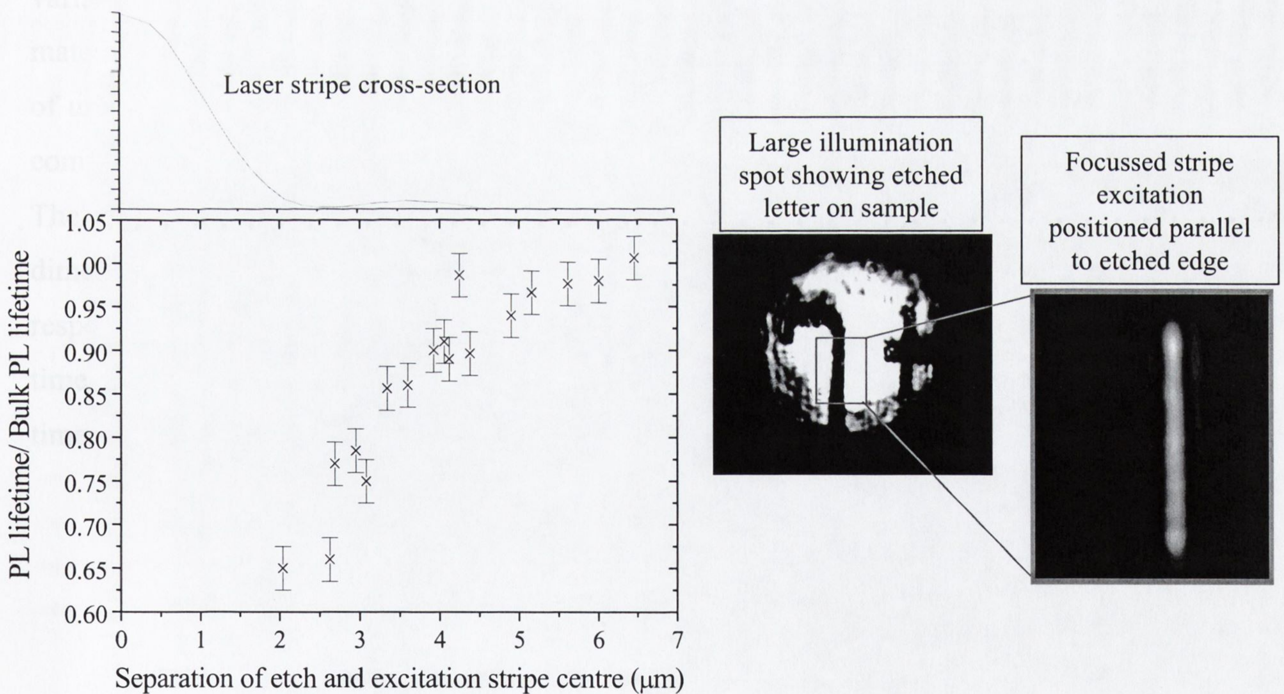

Figure 6.9 *Effect of edge recombination on the PL emission lifetime from QD sample at T = 297K (Excitation intensity = 240Wcm^{-2}, excitation wavelength = 800nm, measurement wavelength = 950nm).*

interpretation of the lifetime results is complicated by the fact that we are only measuring emission from the high-energy tail of the QD spectrum where emission from QD excited states may be present. Also fluctuations and drift in the excitation stripe and edge separation over the long integration period (≈10-20 minutes) of photon arrival times required to measure an emission lifetime, introduces a significant error into the data points. For these reasons we focus on the PL intensity edge profiles to quantify the carrier diffusion in terms of diffusion lengths.

6.4.4 Simulation

A full simulation of the carrier dynamics in a QD layer would account for the different probabilities of carrier capture and escape for the different sized QDs, track the population trapped in different sized dots and free to diffuse in the WL layer at any given time, and allow for recombination occurring in the WL or any of the QDs. Such a simulation would be extremely computationally demanding and would possess too many variables for any fit to the measured data to provide accurate values for the various material parameters. Therefore we simulated the expected edge PL profiles for a system of unconfined carriers assuming different carrier diffusion lengths, which could then be compared to the measured results.

The simulation is based on dividing the surface of the sample (*xy* plane) into a two dimensional rectangular grid, with a grid spacing of *dx* and *dy* in the *x* and *y* directions respectively, and calculating the number of carriers in each cell of the grid $N_{i,j}$ after each time interval *dt*. The change in the number of carriers in a cell in a time interval *dt* at a time *t* is calculated from (6.5) as

$$dN_{i,j}(t) = \left[D\nabla^2 N_{i,j}(t) + g_{i,j} - \frac{N_{i,j}(t)}{\tau_{i,j}} \right] dt \tag{6.9}$$

$\nabla^2 N$ in the lateral directions at each cell in the grid is calculated using a finite difference technique [26], as

$$\nabla^2 N_{i,j} = \frac{\partial^2 N_{i,j}}{\partial x^2} + \frac{\partial^2 N_{i,j}}{\partial y^2} = \frac{1}{dx^2}\left[N_{i+1,j} - 2N_{i,j} + N_{i-1,j}\right] + \frac{1}{dy^2}\left[N_{i,j+1} - 2N_{i,j} + N_{i,j-1}\right] \tag{6.10}$$

The carrier generation term $g_{i,j}$ is calculated assuming a Gaussian shaped excitation spot (FWHM = 2.1μm) a known distance from the edge. The carrier lifetime $\tau_{i,j}$ is determined by the bulk recombination lifetime τb, which is independent of position on sample, and the position dependent non-radiative edge lifetime $\tau edge_{i,j}$.

$$\tau_{i,j} = \frac{\tau b.\tau edge_{i,j}}{\tau b + \tau edge_{i,j}} \tag{6.11}$$

The influence of surface recombination at the etched edge is accounted for by assigning a fast edge recombination lifetime to cells along the etched edge. In order to avoid creating a numerical instability in the finite difference technique used in equation (6.10), the $\tau edge_{i,j}$ term must be made to vary smoothly at the etched edge. This is achieved by using a sigmoidal Richards function [27], with the appropriate parameters to produce a τ value of 10^{-2}ns at the etched edge [28], with a continuous variation of τ between τb and this value occurring over a 100nm region at the edge.

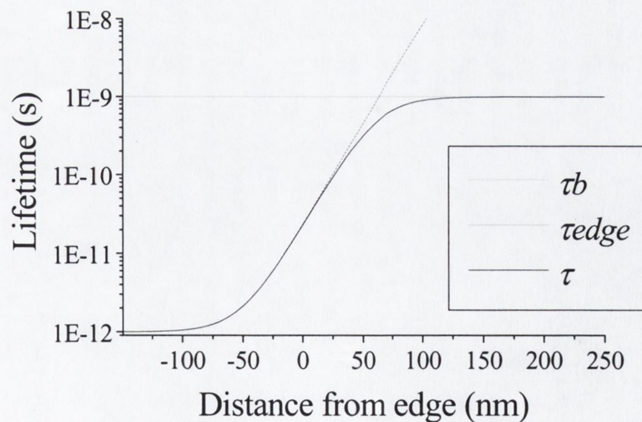

Figure 6.10 *Dependence of bulk, non-radiative edge, and carrier lifetimes on distance from edge as used in simulation.*

To calculate the PL intensity for a given diffusion length, L, and edge to excitation spot separation, d, the carrier distribution is iteratively calculated until a steady state population $N_{i,j}(\infty)$ is established (i.e. $\partial N/\partial t \approx 0$). The PL intensity, I is then calculated as

$$I = A\sum_{i,j}\frac{N_{i,j}(\infty)}{\tau b} \tag{6.12}$$

where A is a constant representing the fraction of the bulk recombination which is radiative.

We simulate the edge profiles for different values of carrier diffusion length, L, from which a bulk carrier diffusion constant D is determined using the bulk recombination lifetime, as $D = L^2/\tau b$. The advantage of performing the simulation for different values of L rather than different values of D is that it removes the dependence of the result on the carrier lifetime and provides a result dependent on only one material parameter. The PL edge profile for a given diffusion length is simulated by determining the PL intensity at a series of values of d. The simulated PL edge profiles for a range of L values are shown in Figure 6.11.

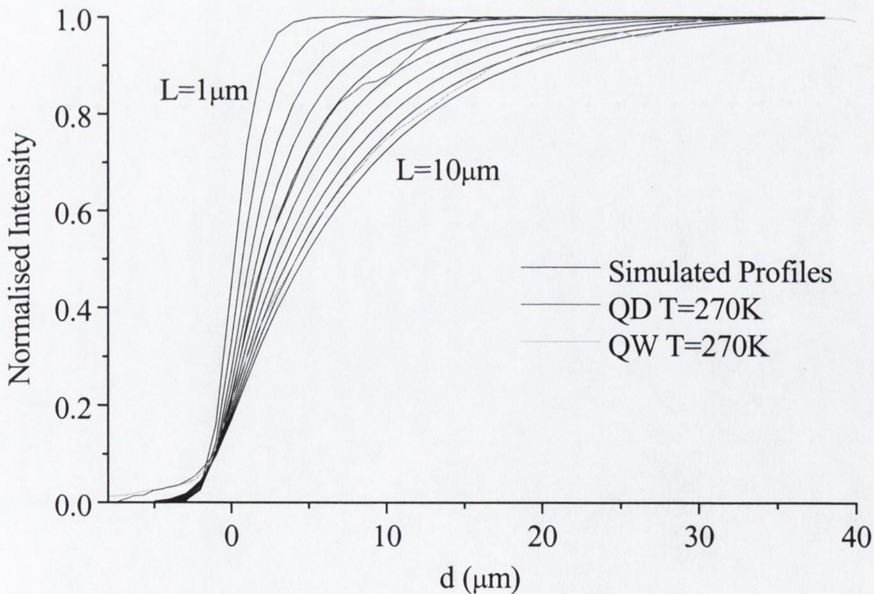

Figure 6.11 *Simulated PL edge profiles for L values between 1 μm and 10μm, with experimental results for the QD and QW sample at T =270K superimposed.*

The shape of the simulated profiles agrees well with the experimental results as can be seen for two typical results in Figure 6.11. However the computational time required to simulate a single edge profile prohibits iteratively adjusting the L value until a best fit between the simulated and measured PL edge profile is achieved. Therefore the d value at which the PL intensity has dropped to 50% of the bulk PL intensity was chosen as a parameter that would allow the fitting of a diffusion length to each measured profile. As a first step the dependence of the d value at which a 50% drop in PL intensity is observed, on the diffusion length has to be determined from the simulated profiles. Figure 6.12 shows the linear relationship between these quantities and the fitted line from which the diffusion lengths corresponding to the experimentally measured 50% PL distances can be determined.

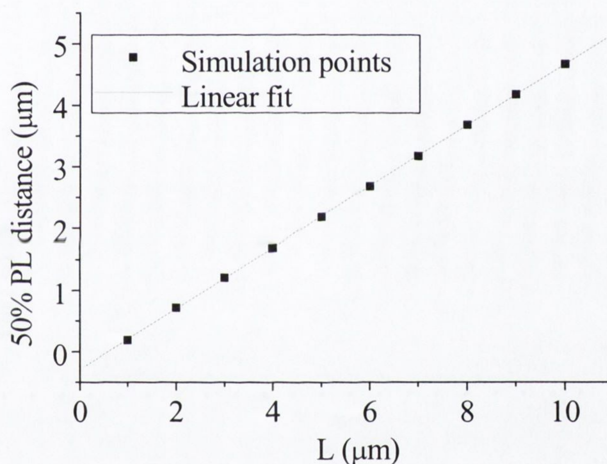

Figure 6.12 *Distance from edge at which simulated PL has dropped by 50%, as a function of diffusion length.*

6.4.5 Discussion

Figure 6.13 shows the distance from the edge at which the measured PL intensity has dropped to 50% of emission intensity from bulk material, and the corresponding diffusion length from the fitted line in Figure 6.12, for both the QD and QW layers as functions of temperature. The carrier diffusion is completely suppressed in the QD layer at temperatures less than 150K, with a small increase in diffusion observed in the 150K to

200K temperature range corresponding to a diffusion length ≈ 0.5μm at 200K. A more rapid increase in carrier diffusion in the QD layer is observed in 200K to 300K range, with carrier spreading at 300K matching that expected for a diffusion length of ≈ 6.5μm. The carrier diffusion length for the QW layers increases consistently with temperature throughout the entire temperature range investigated from ≈3μm at 77K to ≈10μm at 300K.

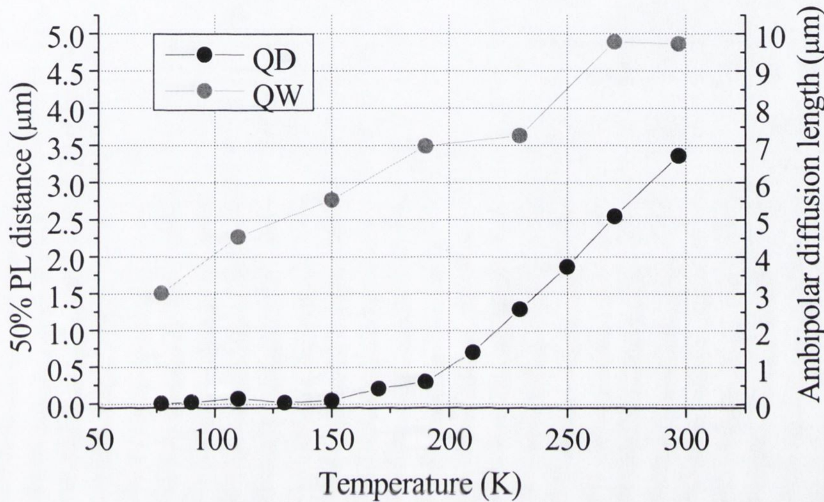

Figure 6.13 *Results of diffusion measurements on QD and QW samples.*

Three possible effects that could have impacted on our experimental technique and that would have led to an overestimation of carrier diffusion, which were considered and subsequently dismissed are discussed below.

(i) The distribution of carriers created in the active layer of the sample not matching the reflected laser spot from the surface of the sample. If the active layer had been positioned several microns below the surface of the sample then the incident laser, focused on the surface of the sample, would have passed through focus when the light reached the active layer resulting in a larger distribution of carrier created in the active layer. However since the active layer was situated < 0.5μm under the surface of the sample which is less than the depth of focus of the microscope objective lens (≈1μm) forming the excitation spot, no appreciable difference would be expected in the laser spot on the surface and at the active

layer. The calculated laser profiles on the surface and at the active layer accounting for the NA of the lens, the excitation wavelength, and the refractive index of the sample agreed to within 100nm [29].

(ii) The existence of a damaged layer of material at the etched surface of the sample. The existence of such a layer has already been discussed in section 5.3, however typical values for the thickness of the damaged surface layer produced by etching methods similar to those employed in the fabrication of these samples is ≈10nm [30], which is less than the resolution to which the sample edge is positioned and therefore lies within our experimental error.

(iii) The re-absorption in the active layer of light originally emitted by the active layer (photon recycling) would result in the creation of carriers away from the initial carrier distribution without any carrier diffusion occurring. The existence of a waveguide in the sample makes this a potentially important effect, since a considerable fraction of the emitted light couples to guided modes that propagate laterally with low scattering losses. However the absorption length of the guided mode by the QD layer was measured as ≈100μm in a very similar structure [31]. Therefore the effect of carrier creation through reabsoption of the guided emission is negligible in the QD sample over the ≈15μm distances investigated. The shorter absorption length expected for the QW sample makes it a potentially more significant effect, however the good agreement between the measured QW PL edge profiles and the modelled profiles assuming a single diffusion length suggests the impact of carrier creation through PL reabsorption is small. Previous results have shown the spatial distribution of PL in the presence of significant reabsorption effects can only be fitted using two diffusion lengths, one to account for carrier diffusion and the other to account for *photon diffusion* [32].

The elimination of these effects combined with the agreement between the reflected laser and QD PL profile at low temperature (implying the expected result of no carrier diffusion), support the accuracy of our measurement technique and of the results shown in Figure 6.13.

The QW diffusion lengths shown in Figure 6.13 are consistent with the 1.5μm and 2.5μm ambipolar diffusion lengths measured for two $In_{0.14}Ga_{0.86}As$/GaAs quantum wells at 85K

by Huang et al. [33], however the 0.9μm ambipolar diffusion length measured by Evoy et al. [34] for $In_{0.1}Ga_{0.9}As/GaAs$ QWs at room temperature is considerably less than our QW diffusion length at room temperature. This difference is attributed to a reduced defect density in our sample, resulting in an increased carrier lifetime and diffusion constant; the variation of the carrier diffusion length with material quality is shown in Huang's results [33]. The ambipolar diffusion length in $GaAs/Al_{0.3}Ga_{0.7}As$ QWs at room temperature is typically ≈1μm [14,24], however an increased diffusion length would be expected for InGaAs/GaAs QWs due to the larger diffusion constant for both electrons and holes in InAs compared to GaAs [35].

In order to obtain some estimation of the trapping efficiency of the QDs, the diffusion length of carriers in the QD layer was divided by the diffusion length in the QW layer at the same temperature and carrier density. If we assume that carrier transport in the QD layer is solely due to carrier diffusion in the continuous InAs wetting layer, that the carrier diffusion constant in the wetting layer is the same as the diffusion constant in the QW, and that the carrier lifetimes are the same for both the QW and QD layer, then the diffusion length in the QD layer divided by the diffusion length in the QW equals the fraction of time carriers in the QD layer spend in the WL. While these assumptions are clearly not completely accurate, Figure 6.14 does provide a broad estimate of the fraction of time carriers in the QD layer are free to diffuse and hence an insight into the efficiency of carrier trapping in the dots as a function of temperature.

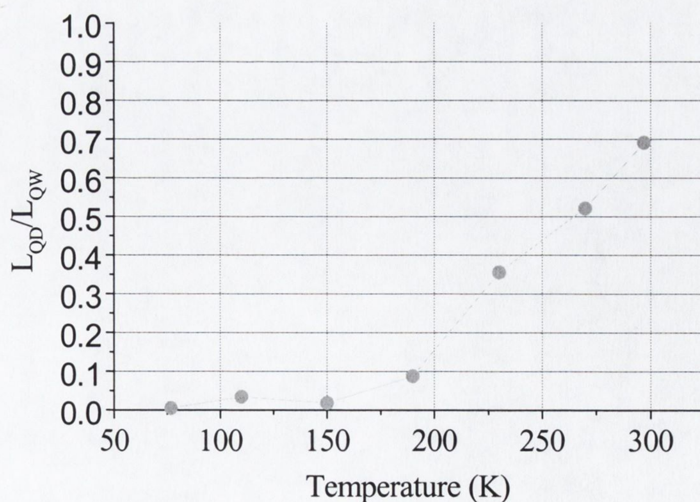

Figure 6.14 QD *carrier diffusion length divided by QW carrier diffusion length.*

Figure 6.8 shows that carrier diffusion in the QD layer at 77K is independent of pump intensity and hence carrier concentration up to 1100Wcm^{-2}. At higher excitation intensities a slight increase in carrier diffusion is evidenced by a reduction in the PL intensity at greater separation of the excitation spot and edge. This increased carrier diffusion is attributed to saturation of the ground states of the QDs, resulting in carrier occupation of less confined QD excited states. The lower confinement energy of excited states introduces an increased probability of carrier escape and hence increased carrier diffusion. The impact of overfilling the ground state is only observed in the PL edge profiles at excitation intensities above ≈ 2000Wcm^{-2} compared to the observation of excited state emission in the PL spectra at excitation intensities > 600Wcm^{-2}. This discrepancy is attributed to the fact that the edge profiles were recorded at the peak wavelength of the low pump intensity PL spectrum (λ = 1022nm), where the contribution of excited state emission to the emission intensity is small relative to ground state emission (see Figure 5.17). Therefore higher pump intensities are required before the impact of excited states becomes significant. Even at the highest pump intensity investigated (7000Wcm^{-2}) the carrier diffusion at 77K in the QD sample is only a fraction of the carrier diffusion measured for the same sample at low pump intensity for temperatures >200K, indicating that the carriers occupying excited states are still strongly confined in the QDs at 77K.

6.5 Cavity measurements

6.5.1 Introduction

This thesis is concerned with investigating the design, advantages and limitations of microcavity LEDs. Key to the success of higher dimensional microcavities is lateral mode control, which requires lateral light confinement to wavelength scales. Smaller device sizes are also of interest in laser diode research where the promise of lower threshold currents and higher modulation speeds has resulted in a continuous miniaturisation of devices. However the increasing surface-to-volume ratio that

accompanies this miniaturisation process increases the potential influence of surface effects, with the magnitude of these effects dependent on the carrier diffusion length.

In this section we return to examining etched microcavity structures, to quantify the impact of non-radiative carrier recombination at etched sidewalls. Our study of the emission properties and carrier diffusion in QD and QW active layers was instigated by the results of emission lifetimes from the microleek structures (see section 4.7.2). The temperature dependence of the emission lifetime from QDs in the microleek structure relative to QDs in bulk material showed the impact of fast non-radiative recombination at etched sidewalls at higher temperatures. However as already mentioned the high carrier densities required for PL lifetime measurements and our inability to measure emission lifetimes at sufficiently long wavelengths to investigate the peak of the QD emission spectrum, makes it difficult to accurately assess the impact of surface recombination from time resolved measurements. In this section the emission intensity from QD and QW active layers in etched cavities are compared to the bulk emission intensities from the same active layers, under CW excitation and using the Ge detector to access the full emission spectrum of the QDs. Cavities containing the same QW and QD active layers as used in the carrier diffusion length measurements were investigated. This allowed an assessment of the dependence of surface recombination effects in etched microcavities on carrier diffusion length.

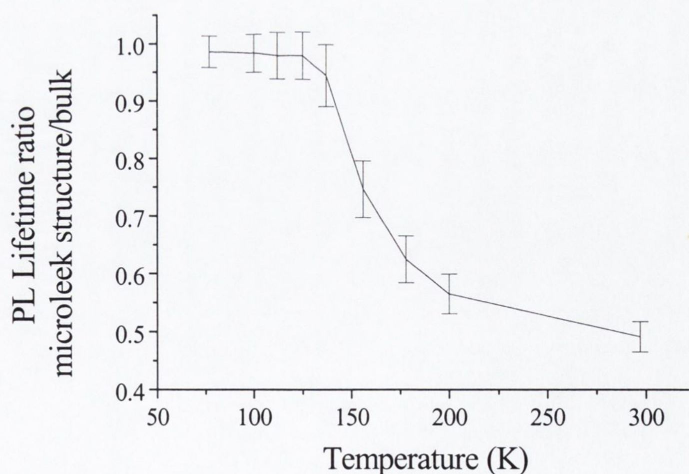

Figure 6.15 *Summary of PL lifetime measurements on microleek structures (see section 4.7.2 for details). The decrease in the PL lifetime from QDs in the microleek relative to the bulk emission lifetime for T >140K is due to the influence of non-radiative edge recombination.*

6.5.2 Cavity structure

The cavities investigated utilised a periodic array of etched air holes that create a two-dimensional photonic bandgap (PBG) to confine the light to hexagonal shaped central cavities. The air holes had a diameter of 150nm and were arranged with a periodic spacing of 240nm. The central cavity was formed by removing 127 holes from the array, leaving a nominal cavity area of $8.4\mu m^2$. The cavities were etched in the same wafers (one containing QDs and one containing QWs) as the microleek cavities, and that the diffusion measurements were performed on. Our measurements did not depend on the optical properties of the cavity, since we measured the intensity of emission from the centre portion of the structure, which consisted of unguided and hence unconfined emission (see chapter 4). These cavity structures were chosen so that our results would provide direct input into the design of similar structures, which are the subject of considerable research due to the potential for omnidirectional light control offered by PBGs [36].

6.5.3 Results and Discussion

In order to measure the emission intensity from the centre of the cavity relative to the bulk emission intensity, the laser excitation spot was scanned across a device. The same experimental setup as was used to measure the edge profiles was employed, providing a simultaneous measurement of both the reflected laser and PL intensities as the excitation spot was scanned. The reflected laser profile was used to ensure that the laser excitation spot was scanned through the centre of the device, while the PL intensities at the beginning and end of the scan, when the excitation spot was far from the device provided the bulk PL intensity. The same excitation intensity of $400Wcm^{-2}$ as in the diffusion measurements was used.

Figure 6.16(b) shows typical reflected laser and PL profiles produced by scanning the laser spot across the cavity. Also shown is a simulated reflectivity scan for the excitation spot passing through the centre of the structure, assuming the same constant reflectivity from the bulk material and the cavity centre, and a 33% drop in this reflectivity value for the etched area. To simplify the simulation the structure was approximated to a circular

shape with an outer radius of 4μm and a central cavity radius of 1.6μm, with both values taken from the SEM image. The magnitude of the drop in reflectivity from the etched regions due to the etched air holes was adjusted to fit the experimental data. The agreement between the shapes of the simulated and measured reflectivity profiles confirms that the laser spot passed through the centre of the structure. The reflected laser profile is independent of sample temperature and was used to ensure that the laser spot passed through the centre of the structure during all scans.

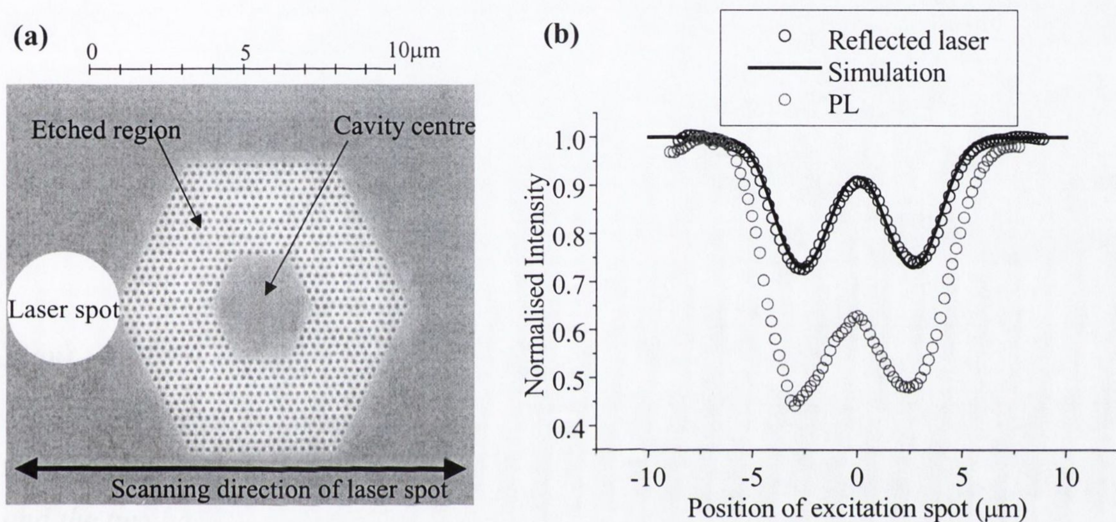

Figure 6.16 *(a) Scanning electron microscope (SEM) image of PBG cavity, with circle representing laser spot superimposed for illustrative purposes. (b) Typical normalised reflected laser and PL profiles produced when the laser excitation spot is scanned across the structure (T = 170K).*

The value of the PL intensity from the centre of the structure normalised to the bulk PL intensity was extracted from the measured PL profiles produced by scanning the laser spot across the structure. Measurements were performed on the sample containing QDs at three different PL emission wavelengths corresponding to the peak intensity and the half maximum intensity on the long and short wavelength side of the peak, while measurements on the structures containing QWs were performed at the peak of the QW emission spectrum. The results of these measurements are shown in Figure 6.17, together with an approximation to the wavelength-integrated result for the QD structure (dashed

line) obtained from the sum of the three individual wavelength results weighted by their spectral intensity.

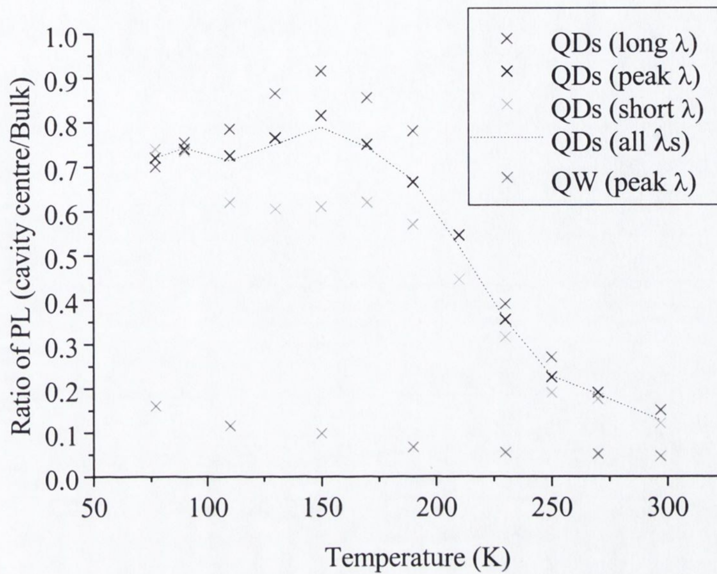

Figure 6.17 *PL intensity when laser spot positioned on centre of structure normalised to PL intensity from bulk material for structures containing QDs and QWs. For the structure containing QDs results for emission wavelengths corresponding to the peak and the two half-maximums in the PL spectrum at that temperature are shown.*

The estimated wavelength-integrated PL intensity from the centre of the etched cavity containing QDs is approximately constant at $0.75 \pm .05$ of the bulk PL intensity, for temperatures less than 150K. At temperatures less than 90K the cavity to bulk PL ratio is independent of QD emission wavelength indicating that carriers are equally trapped in all the different sized dots, emitting at different wavelengths, in the layer. The failure to recover 100% of the bulk PL intensity when the excitation spot was positioned on the centre of the structure even at 77K when efficient trapping of carriers in all dots is expected is due to the edges of the laser spot extending into the etched regions. The fact that the laser spot never fully fitted inside the cavity centre is confirmed by the reduced reflected laser intensity relative to the reflected intensity from bulk material when the

excitation spot is centered on the structure (see Figure 6.16(b)). The removal of semiconductor material to produce the air holes and the damage to remaining material at the etched interfaces reduces the PL intensity from the PBG patterned regions even in the absence of carrier diffusion. At temperatures above 90K the cavity to bulk PL ratio increases for QDs emitting at longer wavelengths and decreases for dots emitting at shorter wavelengths. The differentiation between different emission wavelengths with the spectrally integrated cavity to bulk emission ratio remaining approximately constant (for $T < 150K$) indicates that a redistribution of carriers between dots is occurring with edge recombination having a greater impact on the emission from the smaller dots which have lower confinement energies. However the origin of the increase in the ratio of the cavity to bulk emission intensities is not understood. At temperatures greater than 170K the cavity to bulk emission intensity ratio drops at the three emission wavelengths measured to a value of ≈ 0.15 at room temperature, with the difference between the different wavelengths reducing as the temperature increases. This drop in the cavity to bulk emission ratio is due to increased non-radiative surface recombination as a result of increased carrier diffusion. The observation of this reduction at all wavelengths indicates that carriers have sufficient thermal energy to escape from all the dots. The different confinement energies of the different sized dots is less significant as the thermal energy of the carriers further exceeds the confinement energies of the dots, resulting in the reduced difference between different emission wavelengths.

In comparison the emission intensity from the centre of the QW cavity structure normalised to the bulk emission intensity is only ≈ 0.16 at 77K and drops to ≈ 0.05 at 297K. The inability of the QW to prevent lateral carrier diffusion at any temperature results in increased loss of carriers to non-radiative surface recombination at the etched sidewalls of the structure compared to the QD structure.

6.6 Discussion

Having measured and discussed the carrier diffusion and the impact of edge recombination in etched cavities independently for the same QD and QW layers under the same experimental conditions it remains to compare the two sets of results. The expected

correlation between them is seen in Figure 6.18, with any increase in the carrier diffusion length accompanied by a drop in PL intensity from the centre of the structure.

In the case of the QD layer, the measured carrier diffusion length is effectively zero and the normalised PL intensity from the cavity is constant at 0.75 for temperatures less than 150K, with the carrier diffusion length increasing and the normalised cavity emission intensity decreasing at higher temperatures. From the results of the temperature dependence of the QD PL spectrum in chapter 5 three temperature ranges were identified, corresponding to different carrier confinement regimes. Specifically that carriers are trapped in all QDs at low temperatures (< 70K), with an intermediate temperature range (70K to 150K) existing where carriers possess sufficient thermal energy to escape from increasing numbers of dots resulting in a redistribution of carriers toward the larger dots and finally carrier escape from all dots is possible at temperatures > 150K. Therefore it appears that carrier diffusion is suppressed and hence cavity edge effects minimized even if carriers can escape from the smaller dots so long as the confinement energy of the larger dots in the layer is sufficient to prevent carrier escape. The dependence of the normalised cavity emission intensity from the QD structure on wavelength at

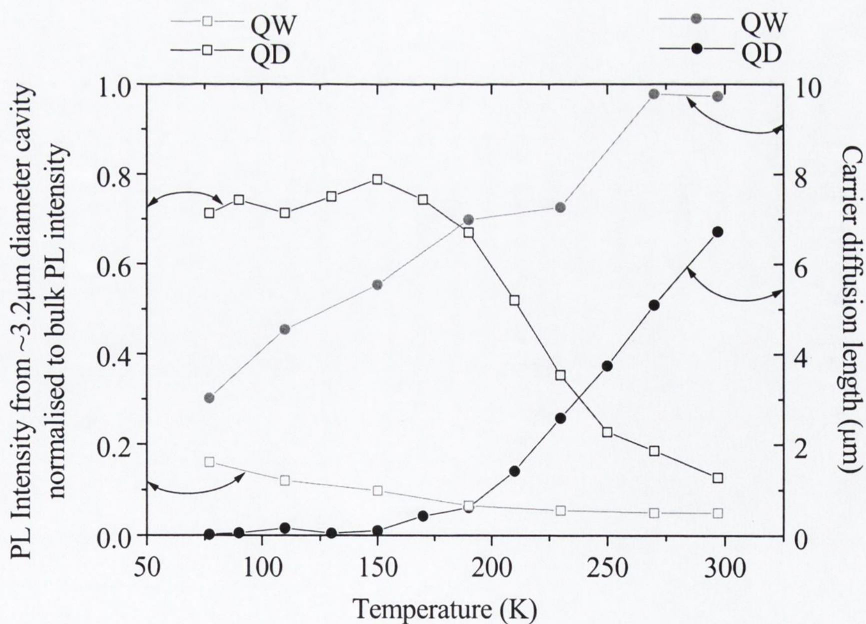

Figure 6.18 *Combined normalised cavity PL intensity and carrier diffusion length results for both QD and QW active layers as function of temperature.*

temperatures > 90K, as shown in Figure 6.17, supports the existence of carrier escape from smaller dots and a redistribution of carriers between dots occurring at temperatures < 150K.

For the QW active layer the continuous increase in the carrier diffusion length with increasing temperature is accompanied by a continuous decrease in the normalised cavity PL intensity over the temperature range investigated (77K –297K). At all temperatures the QW carrier diffusion length is greater and the normalised cavity PL intensity less than for the QD layer.

Finally in order to investigate the relationship between the carrier diffusion length and the impact of surface recombination in the etched microcavity, the normalised PL intensity from the cavity is plotted as a function of the fitted carrier diffusion length in Figure 6.19. Interestingly the relationship between these two quantities differs for the QD and the QW active layers. For the same value of carrier diffusion length the normalised cavity emission intensity is greater from the QD layer than the QW layer. However the carrier diffusion length attributed to the QD layer is only an approximation to the complex carrier dynamics between discrete dots and the wetting layer, and cannot be equated to the diffusion length in the QW layer where all carriers are free to diffuse during their entire lifetime. The cavity containing QDs may lose less carriers to non-radiative edge

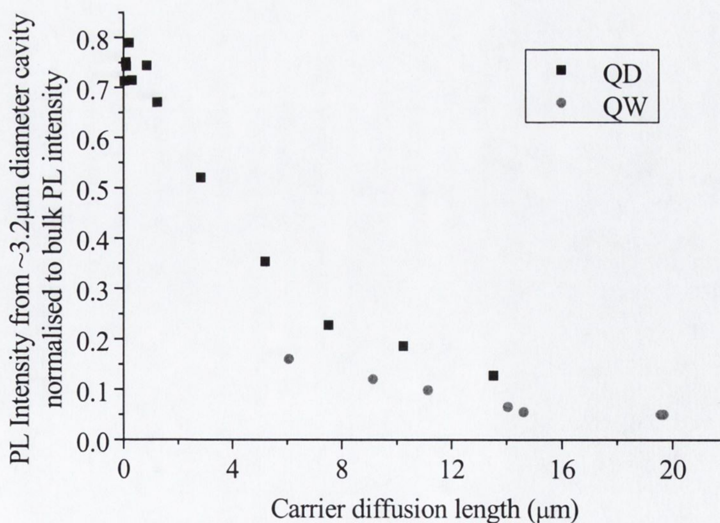

Figure 6.19 *Normalised cavity PL emission intensity as function of carrier diffusion length.*

recombination than the cavity containing QWs despite them having the same average carrier diffusion length because certain carriers in the QD layer may remain trapped in dots and unaffected by surface effects irrespective of the proximity of the surface. Alternatively the different relationship observed for the QD and QW layers may be due to differences in the quality of the etched surfaces in the two samples, with the QW sample possessing an increased surface recombination velocity.

6.7 Conclusion

The ability of QDs to reduce carrier diffusion and hence reduce the impact of surface recombination in etched microcavities relative to QWs has been investigated. The diffusion lengths for carriers in the self-assembled InAs/GaAs QD layer and the InGaAs/GaAs QW at room temperature were measured at 6.5μm and 9.5μm respectively. An increase in the PL emission intensity from a 3.2μm diameter etched cavity at room temperature from 0.05 of the bulk emission intensity for cavities containing QWs to 0.13 of the bulk emission intensity for cavities containing QDs was observed. These results confirm the ability of QDs to reduce carrier diffusion through trapping of carriers in discrete dots, however the thermal energy of carriers at room temperature is sufficient to enable carriers to escape from the dots they initially relax into, thereby preventing the complete suppression of carrier diffusion as observed in the QD layer at low temperatures. Despite the significant reduction in carrier diffusion offered by InAs/GaAs QDs, 87% of the carriers that recombine radiatively in QDs in the absence of etched sidewalls are lost to non-radiative recombination in a 3.2μm diameter etched microcavity at room temperature. Therefore an alternative active layer or an alternative cavity design is required if edge recombination effects are to be eliminated at room temperature in higher dimensional microcavities incorporating deeply etched lateral mirrors.

Since the first signs of edge recombination in the PL edge profiles for the InAs/GaAs QD layer at room temperature were measured when the carriers were created ≈10μm from the edge, any cavity would have to have a diameter >≈20μm and selectively create carriers in the cavity centre if edge effects are to be eliminated while using the same InAs/GaAs QDs and etch depths. However in cavities of this size no microcavity effects would be

present. Likewise if the etch depth was reduced so that the active layers were not etched through then surface recombination would be eliminated, but the optical confinement of the cavity mode would be too weak to observe microcavity effects. Therefore it is difficult to envisage a two or three dimensional cavity design incorporating InAs/GaAs QDs that will produce microcavity effects without losing carriers through surface recombination.

With regard to alternative active layers, QDs with larger confinement energies, for example self-assembled InGaAs/GaAs QDs that emit at ≈1.3μm [37], could reduce the probability of carrier escape from dots at room temperature and thereby reduce carrier diffusion. Importantly our temperature dependent results show that complete trapping of carriers in only the deepest dots of the QD distribution is sufficient to suppress carrier diffusion. An alternative approach to the problem would be to try and reduce the surface recombination velocity by either surface passivation techniques [38] or by changing to a different material such as InP.

While the solution to the problem of surface recombination in microcavities incorporating deeply etched lateral mirrors remains unresolved, our studies have shown that the use of InAs/GaAs QDs as the active layer in the cavity, while offering an improvement over QWs, does not ensure the elimination of undesired edge recombination effects.

6.8 References

1 "Nature of optical transitions in self-organised InAs/GaAs quantum dots", M. Grundmann, N. N. Ledentsov, O. Stier, J. Bohrer, D. Bimberg, V. M. Ustinov, P. S. Kop'ev, and Zh. I. Alferov, Phys. Rev. B **53** (16) p. R10509 (1996)

2 "Optical properties of InAs quantum dots: Common trends" M. Grassi Alessi, M. Capizzi, A.S. Bhatti, and A. Frova, Phys Rev B **59** (11) p.7620 (1999)

3 "High-temperature light emission from InAs quantum dots", A. Patane, A. Polimeni, P. C. Main, M. Henini, and L. Eaves, Appl. Phys. Lett. **75** (6) p.814. (1999)

4 "Threshold Temperature Dependence of Lateral-Cavity Quantum-Dot Lasers", Z. Zou, O. B. Shchekin, G. Park, D. L. Huffaker, and D. G. Deppe, IEEE Photon. Technol. Lett. **10** (12) p.1673 (1998)

5 "Quantum-Dot Heterostructure Lasers", N. N. Ledentsov, M. Grundmann, F. Heinrichsdorff, D. Bimberg, V. M. Ustinov, A. E. Zhukov, M. V. Maximov, Zh. I. Alferov, and J. A. Lott, IEEE J. Sel. Top. Quant. **6** (3) p. 439 (2000)

6 "Continuous-Wave Low-Threshold Performance of 1.3μm InGaAs-GaAs Quantum-Dot Lasers", D. L. Huffaker, G. Park, Z. Zou, O. B. Shchekin, and D. G. Deppe, IEEE J. Sel. Top. Quant. **6** (3) p. 452 (2000)

7 I. Tamm, *Phys. Z. Sowjet* **1**, p. 733 (1932).

8 *Semiconductors*, R. A. Smith, (2nd Ed., Cambridge University Press, Cambridge, 1978)

9 *Surface Physics of Phosphors and Semiconductors*, edited by C. G. Scott and C. E. Reed, (Academic Press, London, 1975)

10 *Electrons and holes in semiconductors*, W. Shockley, (Van Nostrand, 1950)

11 *Semiconductor Physics and Devices: basic principles*, D. A. Neamen, (McGraw-Hill companies Inc., 1997)

12 "Variation of minority-carrier diffusion length with carrier concentration in GaAs liquid-phase epitaxial layers", H. C. Casey Jr., B. I. Miller and E. Pinkas, J. Appl. Phys. **44** (3) p. 1281 (1973)

13 "Use of Schottky-diode collectors for SEM determination of bulk diffusion lengths" C. van Ordorp, R. C. Peters, and M. Klerk, Appl. Phys, Lett. **24** (3) p.125 (1974)

14 "Direct determination of the ambipolar diffusion length in GaAs/AlGaAs heterostructures by cathodoluminescence", H. A. Zarem, P. C. Sercel, J. A. Lebens, L. E. Eng, A. Yariv, and K. J. Vahala, Appl. Phys. Lett. **55** (16) p.1647 (1989)

15 "Optical investigations on the mobility of two-dimensional excitons in GaAs/$Ga_{1-x}Al_xAs$ quantum wells" H. Hillmer, A. Forchel, S. Hansmann, M. Morohashi, E. Lopez, H. P. Meier, and K. Ploog, Phys. Rev. B **39** (15) p.10901 (1989)

16 "Optical properties of n-type GaAs. I. Determination of hole diffusion lengths from optical absorption and photoluminescence measurements", C. J. Hwang, J. Appl. Phys. **40** (9) p. 3731 (1969)

17 "Nonlinear luminescence and time-resolved diffusion profiles of photoexcited carriers in semiconductors" A. Olsson, D. J. Erskine, Z. Y. Xu, A. Schremer, and C. L. Tang, Appl. Phys. Lett. **41** (7) p. 659 (1982)

18 "Direct determination of the ambipolar diffusion length in strained $In_xGa_{1-x}As/InP$ quantum wells by cathodoluminescence", R. B. Lee, K. J. Vahala, C-E. Zah, and R. Bhat, Appl. Phys. Lett. **62** (19) p.2411 (1993)

19 "Optical measurement of the ambipolar diffusion length in a ZnCdSe-ZnSe single quantum well", F. P. Logue, D. T. Fewer, S. J. Hewlett, J. F. Heffernan, C. Jordan, P. Rees, J. F. Donegan, E. M. McCabe, J. Hegarty, S. Tanaguchi, T. Hino, K. Nakano, and A. Ishibashi, J. Appl. Phys. **81** (1) p.536 (1997)

20 "Quantum boxes as active probes for photonic microstructures: The pillar microcavity case" J. M. Gérard, D. Barrier, J. Y. Marzin, R. Kuszelewicz, L. Manin, E. Costard, V. Thierry-Mieg, and T. Rivera, Appl. Phys. Lett. **69** (4) p. 449 (1996)

21 "Optical and Confinement Properties of Two-Dimensional Photonic Crystals" H. Benisty, C. Weisbuch, D. Labilloy, M. Rattier, C. J. M. Smith, T. F. Krauss, R. M. De La Rue, R. Houdré, U. Oesterle, C. Jouanin, and D. Cassagne. Journal of Lightwave Technology, **17** (11), p. 2063, (1999).

22 "Diffraction of cylindrical Bragg reflectors surrounding an in-plane semiconductor microcavity" D. Ochoa, R. Houdré, M. Ilegems, H. Benisty, T. F. Krauss, C. J. M. Smith, Phys. Rev. B **61** (7) p. 4806 (2000)

23 "Lateral Carrier Confinement in miniature Lasers Using Quantum Dots", J. K. Kim, R. L. Naone, and L. A. Coldren, IEEE J. Sel. Top. Quant. **6** (3) p. 504 (2000).

24 "Design parameters for lateral carrier confinement in quantum-dot lasers" J. K. Kim, T. A. Strand, R. L. Naone, and L. A. Coldren, Appl. Phys. Lett. **74** (19) p.2752 (1999)

25 Fred Logue, Ph.D. Thesis, Trinity College Dublin (1996)

26 Advanced Engineering Mathematics, E. Kreyszig, (7th Ed., John Wiley & Sons, Inc., New York, 1993)

27 *Nonlinear regression*, G. A. F. Seber, and C. J. Wild, (John Wiley & Sons, Inc., New York, 1989) p. 332-337.

28 "Time-resolved investigations of sidewall recombination in dry-etched GaAs wires" G. Mayer, B. E. Maile, R. Germann, A. Forchel, P. Grambow, and H. P. Meier, Appl. Phys. Lett. **56** (20) p. 2016 (1990).

29 For details of calculation see Chapter 7 of Ph.D. Thesis, David Fewer, Trinity College Dublin (1997)

30 *Quantum Dot Heterostructures*, D. Bimberg, M. Grundmann, N. N. Ledentsov (John Wiley & Sons Ltd., Chichester, 1999) page 14.

31 "Finely resolved transmission spectra and band structure of two-dimensional photonic crystals using emission from InAs quantum dots", D. Labilloy, H. Benisty, C. Weisbuch, C. J. M. Smith, T. F. Krauss, R. Houdré, U. Oesterle, Phys Rev. B **59** (3) p. 1649 (1999)

32 "Spatial and temperature dependence of carrier recombination in an InGaAs/InP heterostructure", A. F. G. Monte, S. W. da Silva, J. M. R. Cruz, P. C. Morais, and H. M. Cox, J. Appl. Phys. **85** (5) p. 2866 (1999)

33 "Ambipolar diffusion and carrier lifetime measurements in all-binary $(InAs)_2(GaAs)_5$ strained quantum wells grown on GaAs", X. R. Huang, D. S. McCallum, M. D. Dawson, A. L. Smirl, T. F. Boggess, T. C. Hasenberg, and R. L. Tober, J. Appl. Phys. **74** (3) p.1868 (1993)

34 "Cathodoluminescence and photoluminescence analysis of $In_xGa_{1-x}As$/GaAs quantum well structures", S. Evoy, G. F. Redinbo, and H. G. Craighead, Appl. Phys. Lett. **68** (9) p. 1259 (1996)

35 *Modern Semiconductor Device Physics*, S. M. Sze (John Wiley and Sons Inc., New York, 1998)

36 "Directionally dependent confinement in photonic-crystal microcavities" C. J. M. Smith, T. F. Krauss, H. Benisty, M. Rattier, C. Weisbuch, U. Oesterle, R. Houdré, J. Opt. Soc. Am. B **17** (12) p. 2043 (2000)

37 "High characteristic temperature of near-1.3-μm InGaAs/GaAs quantum-dot lasers at room temperature", K. Mukai, Y. Nakata, K. Otsubo, M. Sugawara, N. Yokoyama, and H. Ishikawa, Appl. Phys. Lett. **76** (23) p. 3349 (2000)

38 "Interface Recombination Reduction by $(NH_4)_2S_x$-Passivation in Metalorganic Chemical Vapor Deposition Regrown GaAlAs/GaAs Buried Heterostructure Lasers and

estimation of Threshold currents in Microcavity Surface Emitting Lasers", T. Tamanuki, F. Koyama, and K. Iga, Jpn. J. Appl. Phys. **31** (10) p. 3292 (1992)

Chapter 7

Conclusions

This thesis has been concerned with investigating several aspects of semiconductor microcavity light emitting structures. There has been a progression within the work from planar to higher dimensional microcavities, and finally onto sources for higher dimensional structures. The main conclusions of this work are summarised below.

Our investigations into the emission properties of planar MCLEDs emitting at 650nm for POF applications were presented in Chapter 3. The main focus of this work was to assess the potential for transferring the MCLED technology to this wavelength. Clear microcavity effects were observed in the spectral emission linewidth, angle-resolved spectra and farfield of a MCLED device emitting at 660nm. The low external quantum efficiency (<1.5%) of the device was attributed to a combination of low internal quantum efficiency (≈30%) and a non-optimised cavity design. The poor carrier confinement in the QWs of the device, due to the limited band offsets available in materials required for emission at 650nm, combined with the non-uniform carrier distribution, and device heating contributed to the low internal quantum efficiency. From spectral measurements the occurrence of significant device heating at bias currents >20mA was identified. Therefore the device characterisation results demonstrated the ability to produce microcavity effects in MCLEDs incorporating two DBRs even with the limited DBR refractive index contrast available in the $Al_xGa_{1-x}As$ material system at this wavelength, while also highlighting the difficulty in obtaining high internal quantum efficiency and temperature insensitive performance from active layers emitting at this wavelength.

The optical properties of the characterised MCLED structure were modelled using a dedicated simulation tool capable of the exact calculation of dipole emission in an arbitrary multilayer structure. The extraction efficiency of the characterised device was calculated at 5%, with a factor of two improvement predicted for the correct positioning of the cavity resonance wavelength relative to the QW emission wavelength. Further

optimisation of cavity mirror reflectivities produced modelled extraction efficiencies of 14% into air and 4% into the acceptance angles of a 0.5NA fibre, for a MCLED emitting at 650nm with the same intrinsic QW emission linewidth as deduced from measurements on the characterised MCLED device.

The measured and modelled results on planar MCLEDs emitting at 650nm provided an introduction into the emission properties and design considerations of practical microcavity structures, and as such served as a valuable starting point for our study of novel microcavity designs.

The ultimate limitation on the extraction efficiency of planar MCLEDs was also explored using the model. The presence of leaky and guided modes in structures incorporating a DBR mirror was shown to prevent the realisation of extraction efficiencies in excess of 40% (in the absence of photon recycling effects) for even the best-case scenario of a monochromatic source and a large DBR refractive index contrast. This limitation on planar microcavity device performance is one of the motivations for studying higher dimensional structures, which are the focus of the remainder of this thesis.

The emission properties of a novel higher dimensional microcavity structure (known as a microleek) utilising a circular Bragg reflector to provide lateral confinement and incorporating a waveguide in the vertical direction to produce full three-dimensional photon confinement were investigated in Chapter 4. Lasing was observed from microleek structures containing QWs during photoluminescence measurements at high excitation intensities. The measured emission spectra and nearfields above threshold enabled the identification of cavity modes of known wavelength and azimuthal quantum number. A simple model based on the modes of a disk resonator, adapted to account for penetration of the cavity mode fields into the lateral mirror structure, was shown to successfully reproduce the lasing mode properties. The lasing modes were identified as quasi-radial modes, which are not confined in isolated post structures, thereby confirming the enhanced confinement offered by the microleek structure.

No cavity-induced modification of the spontaneous emission lifetime (Purcell effect) was observed in low temperature time-resolved photoluminescence studies on QDs in microleeks. This was shown to be consistent with theory when correct averaging over the spatial distribution of QDs within the cavity was performed. An increase in the ratio of

the cavity quality factor to cavity mode volume would be required to produce a measurable effect. We estimate that a microleek with a central cavity diameter of $\approx 1.2\mu m$ and a cavity quality factor of ≈ 1200, would be required to produce a factor of 2 enhancement of the spontaneous emission rate.

The impact of fast non-radiative recombination of carriers at the etched sidewalls of the microleek structure was evident in time-resolved PL measurements on the microleek structures containing QDs at room temperature. This failure of the discrete QDs in the active layer to prevent carriers reaching the non-radiative centres at the etched sidewalls of the structure, prompted our investigations into the suitability of QDs as active layers in etched microstructures, and in particular their ability to limit carrier diffusion.

The photoluminescence emission properties of the InAs/GaAs QD and InGaAs/GaAs QW layers in bulk material were investigated as functions of excitation intensity in the 30K to 297K temperature range in chapter 5. The temperature dependence of the emission lineshape, linewidth, integrated intensity, and peak wavelength from the QD layer was explained in terms of thermally activated carrier escape processes, with three distinct temperature ranges identified; (i) temperatures $< 70K$, when carriers are trapped in all QDs and emission properties are not strongly dependent on temperature (ii) temperatures between 70K and 150K, when carriers possess sufficient thermal energy to escape from increasing numbers of QDs starting with the smallest, and a redistribution of carriers towards the larger dots is observed (iii) at temperatures $> 150K$, when carriers can escape from even the largest dots and a decrease in emission from all dot sizes is observed. In contrast the integrated emission from the QW layer decreases consistently with increasing temperature throughout the investigated temperature range. Saturation of the ground state transition in the QD layer at 77K was observed at a carrier density of $7.3e10cm^{-2}$, which is consistent with the expected areal density of dots.

Carrier diffusion and the impact of non-radiative edge recombination on the emission properties of etched microcavity structures were quantified for both QD and QW active layers as functions of temperature in chapter 6. Carrier diffusion in the QD layer was completely suppressed at temperatures $<150K$, suggesting complete carrier trapping in only the largest dots of the layer is sufficient to prevent carrier diffusion, while a continuous increase in the carrier diffusion with increasing temperature above 150K was

observed. The carrier spreading in the QD layer at room temperature was consistent with that expected for an ambipolar diffusion length of 6.5μm. Carrier diffusion in the QW also increased with temperature, from a diffusion length of 1.5μm at 77K to 10μm at 297K. Carrier diffusion in the QD layer was less than in the QW layer at all temperatures, however the ratio between the two decreased with increasing temperature.

The temperature dependencies of the measured ratio of emission intensity from the centre of a 3.2μm diameter etched cavity to the emission intensity from bulk material for both QD and QW active layers were consistent with the carrier diffusion measurements, with any increase in carrier diffusion matched by a drop in the normalised emission intensity from the cavity centre. At room temperature the ratio of cavity centre to bulk emission intensity was 0.13 and 0.05 for QD and QW active layers respectively, indicating the respective loss of 87% and 95% of carriers which combine radiatively in bulk material to edge recombination processes in the etched cavity. Clearly the use of QDs does not eliminate edge recombination effects at room temperature in etched microstructures. The realisation of increased efficiency from higher dimensional microcavities utilising deeply etched lateral mirrors will require either a reduction in the surface recombination velocity or the use of an active layer capable of preventing carrier diffusion at room temperature. A reduced surface recombination velocity could be achieved through either surface passivation techniques or by switching to an alternate material system such as InP. Alternatively QDs with confinement energies greater than carrier thermal energies at room temperature would prevent carrier diffusion and thereby eliminate edge effects in etched structures irrespective surface recombination velocities.

Planar MCLEDs are a mature technology at this stage, with established design rules and performance limitations. Their particular set of emission properties position them favourably for certain fibre optic and interconnect applications where VCSELs are either unavailable or unsuitable.

The realisation of the expected improvements in performance for higher dimensional structures has proved difficult. While lateral mirror structures providing photon confinement to wavelength scale dimensions have been demonstrated, the cavity properties required to produce enhanced spontaneous emission rates or increased

extraction efficiencies are extremely demanding. The enhanced spontaneous emission rates reported from QDs in three-dimensional microcavities at low temperatures highlight the potential of cavity effects for improving LED performance, however the realisation of electrically injected devices operating at room temperature with similar enhanced emission rates remains a distant prospect. Various approaches to achieving increased extraction efficiency from higher dimensional structure are being actively investigated including photon recycling of light from guided to extracted modes and the use of lateral structures to diffract light in the guided modes upwards out of the device. One key consideration in the design and performance of structures incorporating deeply etched lateral features is the role of edge recombination effects. While various schemes have been proposed to reduce the impact of this effect, it still represents a serious limitation on the performance of wavelength scale structures at room temperature. The development of an active layer or processing technique capable of eliminating this effect may well prove a catalyst for major advancements in the performance of etched semiconductor microstructures, a field of research that is sure to remain active for years to come due to its wealth of physics and the exciting potential of as yet unexploited effects.

Appendix A1:

Derivation of Purcell Factor from Fermi's Golden Rule.

(The following derivation is based on the theoretical treatment given in reference [1], which contains a comprehensive discussion of the Purcell factor in terms of both cavity QED and Fermi's Golden Rule)

The spontaneous emission rate for a radiating dipole is given by Fermi's Golden rule as:

$$\frac{1}{\tau} = \frac{2\pi}{\hbar}\rho(\omega_e)\left\langle\left|\vec{d}\cdot\vec{\varepsilon}(\vec{r}_e)\right|^2\right\rangle \tag{A1:1}$$

where τ is the emission lifetime, $\vec{\varepsilon}(\vec{r}_e)$ is the vacuum electric-field at the location $\vec{r}_e$ of the emitter, $\vec{d}$ is the electric dipole and $\rho(\omega_e)$ is the density of photon modes at the emitter's angular frequency ω_e. The averaging of the squared dipolar matrix element is performed over the various modes seen by the emitter.

The insertion of the radiating dipole inside a cavity will change its spontaneous emission rate in three ways: the spectral density of modes, the amplitude of the vacuum field and its orientation with respect to the radiating dipole are all modified. In the following derivation we calculate the change in the spontaneous emission rate for a cavity supporting a single-mode (angular frequency ω_c, linewidth $\Delta\omega_c$, and quality factor $Q=\omega_c/\Delta\omega_c$). In this case, the mode density seen by the emitter is given by a normalised Lorentzian :

$$\rho_{cav}(\omega) = \frac{2}{\pi\Delta\omega_c}\cdot\frac{\Delta\omega_c^{\,2}}{4(\omega-\omega_c)^2+\Delta\omega_c^{\,2}} \tag{A1:2}$$

and

$$\rho_{cav}(\omega_c) = \frac{2}{\pi\Delta\omega_c} = \frac{2Q}{\pi\omega_c} \tag{A1:3}$$

whereas the free-space mode density can be written as:

$$\rho_{free}(\omega) = \frac{\omega^2 V n^3}{\pi^2 c^3} \tag{A1:4}$$

where n is the refractive index, c is the speed of light, and V is the volume.

Field quantisation leads to the following expression for the electric field operator for the cavity mode [2]

$$\hat{\vec{E}}(\vec{r},t) = i\sqrt{\hbar\omega / 2\varepsilon_0 n^2 V_{eff}}\ \vec{f}(\vec{r})\hat{a}(t) + h.c. \tag{A1:5}$$

where h.c. means hermitian conjugate, $\hat{a}$ is the photon creation operator and $\vec{f}$ is the mode spatial function. $\vec{f}$ is a complex vector which describes the local field polarisation and relative field amplitude. V_{eff} is the effective mode volume and is given by

$$V_{eff} = \frac{1}{n^2}\iiint_{\vec{r}} n(\vec{r})^2 \left|\vec{f}(\vec{r})\right| d^3\vec{r} \tag{A1:6}$$

where in this case n is the refractive index at the field maximum.

Using a normalisation volume V, the field operator for each free-space mode is :

$$\hat{\vec{E}}(\vec{r},t) = i\vec{\varepsilon}\sqrt{\hbar\omega / 2\varepsilon_0 n^2 V}\ e^{i\vec{k}\vec{r}}\hat{a}(t) + h.c. \tag{A1:7}$$

where $\vec{\varepsilon}$ is a unit vector describing the polarisation of the mode, and $\vec{k}$ is the mode wavevector.

Using Fermi's Golden Rule to calculate both emission rates, we can compare the spontaneous emission rate of the emitter in the single-mode cavity to the case of a homogeneous surrounding medium:

$$\frac{\tau_{free}}{\tau_{cav}} = \frac{\left(\frac{2\pi}{\hbar}\right)\left(\frac{2}{\pi\Delta\omega_c}\cdot\frac{\Delta\omega_c^{\ 2}}{4(\omega_e-\omega_c)^2+\Delta\omega_c^{\ 2}}\right)\left(\left|\vec{f}(\vec{r}_e)\right|^2 \xi^2 \frac{\hbar\omega}{2\varepsilon_0 n^2 V_{eff}}\right)}{\left(\frac{2\pi}{\hbar}\right)\left(\frac{\omega^2 V n^3}{\pi^2 c^3}\right)\left(\frac{1}{3}\cdot\frac{\hbar\omega}{2\varepsilon_0 n^2 V}\right)} \tag{A1:8}$$

where $\xi = \left|\vec{d}\cdot\vec{f}(\vec{r}_e)\right| / \left|\vec{d}\right|\left|\vec{f}(\vec{r}_e)\right|$ describes the orientation matching of $\vec{d}$ and $\vec{f}(\vec{r}_e)$, and

where 1/3 is the averaging factor accounting for the random polarisation of free-space modes with respect to the dipole. (A1:8) can be rearranged using the substitutions $Q=\omega_c/\Delta\omega_c$ and $\lambda=2\pi c/\omega$ to give

$$\frac{\tau_{free}}{\tau_{cav}} = \frac{3Q(\lambda_c / n)^3}{4\pi V_{eff}} \frac{\Delta\omega_c^{\ 2}}{4(\omega_e - \omega_c)^2 + \Delta\omega_c^{\ 2}} \xi^2 \left|\vec{f}(\vec{r}_e)\right|^2 \qquad \text{(A1:9)}$$

Finally for an emitter in exact resonance with the cavity mode ($\omega_e = \omega_c$), positioned at the maximum of the cavity mode field $\left(\left|\vec{f}(\vec{r}_e)\right| = 1\right)$, and aligned parallel to the cavity mode polarisation ($\xi = 1$), (A1:9) further reduces to

$$\frac{\tau_{free}}{\tau_{cav}} = \frac{3Q(\lambda_c / n)^3}{4\pi V_{eff}} \qquad \text{(A1:10)}$$

The right hand side of (A1:10) is the cavity-induced spontaneous emission enhancement factor first proposed by E. M. Purcell in 1946 [3], and is known as the Purcell factor, F_p. Therefore the Purcell factor can be derived from Fermi's Golden rule for an emitter matched to the frequency, positioned at the antinode, and aligned parallel to the polarisation, of the cavity mode.

---

1 "Semiconductor Microcavities, Quantum Boxes and the Purcell Effect", J. M. Gérard and B. Gayral in *Confined Photon Systems, Fundamentals and Applications*, H. Benisty, J. M. Gérard, R. Houdré, J. Rarirty, and C. Weisbuch (Eds.) (Springer, Verlag, 1999)

2 "Basic of Quantum Optics and Cavity Quantum Electrodynamics", C. Fabre in *Confined Photon Systems, Fundamentals and Applications*, H. Benisty, J. M. Gérard, R. Houdré, J. Rarirty, and C. Weisbuch (Eds.) (Springer, Verlag, 1999)

3 "Spontaneous emission probabilities at radio frequencies", E. M. Purcell, Phys. Rev. **69** p.681 (1946)

Appendix A2:

Model for dipole emission in multilayer structure.

(This appendix contains an outline of the theoretical basis for the model as first developed by Benisty et al [1,2]. The treatment given here is based on, and uses notation consistent with reference [1]. A discussion of alternate methods for modelling dipole emission as well as the historical basis of this model is also contained in reference [1]).

The originality of this model lies in its incorporation of dipole emission within the standard transfer-matrix methods through explicit additive source terms. Our discussion of the model is divided into three sections; the first section introduces source term expressions for various dipole orientations and emission polarisations that are compatible with the transfer matrix formalism. An expression for the emitted power per unit solid angle and unit area in an arbitrary layer of the structure relative to the same quantity at the source is derived in the second section. The final section discusses the implementation of this expression within the transfer matrix framework.

Source Terms

Source terms are introduced as an additive discontinuity of the fields chosen to represent the electromagnetic waves of a given TE or TM polarisation across the dipole layer according to the general form

$$\left(E^{>}\right)-\left(E^{<}\right)=(\text{source terms}) \qquad \text{(A2.1)}$$

where the superscripts > and < denote the +z and –z sides of the dipole layer (z is the common layer axis).

In the plane wave basis, fields depend on layer indices n_j through their complex z-wavevector component, $k_{z,j}$ which obeys the wave equation

$$k_{z,j}{}^{2}+k_{\|}{}^{2}=k_{j}{}^{2}=\frac{\omega^{2}}{c^{2}}n_{j}{}^{2} \qquad \text{(A2.2)}$$

where $k_{||}$ ($=\omega n_j(\sin\theta_j)/c$, with angles θ_j taken between the wavevector and the z-axis) is conserved through all interfaces (Snell's law), and $k_{z,j}$ ($=\omega n_j(\cos\theta_j)/c$) is real for plane

waves and purely imaginary for evanescent waves in a lossless dielectric. The use of $k_{z,j}$ is thus convenient to treat plane and evanescent waves on the same footing, as well as being compatible with the transfer matrix method as seen later. Therefore we want to recast source terms for electric field dipole emission based on k_z's and k's ($\propto n$'s) rather than angles.

We first recall the radiation patterns of an electric dipole in an unbounded medium. The three basic configurations for dipole radiation patterns are depicted in Figure A2.1. The vertical dipole radiates only TM waves with a normalised pattern (power per unit solid angle)

$$\left(\frac{dP}{d\Omega}\right)^{(v,TM)} = \frac{3}{8\pi}\sin^2\theta_1 \qquad \text{(A2.3)}$$

where the subscript 1 refers to the emitters medium, and the total power through 4π steradians is unity. For the horizontal dipole, we assume random orientation in the xy-plane, and take as a basis the two cases depicted in Figure A2.1(b) and (c) for TE and TM polarisations. Normalisation of the total (TE+TM) radiated power per horizontal dipole gives

$$\left(\frac{dP}{d\Omega}\right)^{(h,TE)} = \frac{3}{16\pi} \qquad \text{(A2.4)}$$

$$\left(\frac{dP}{d\Omega}\right)^{(h,TM)} = \frac{3}{16\pi}\cos^2\theta_1 \qquad \text{(A2.5)}$$

The ratio of TE to TM power is 3:1 for the randomly orientated horizontal dipole.

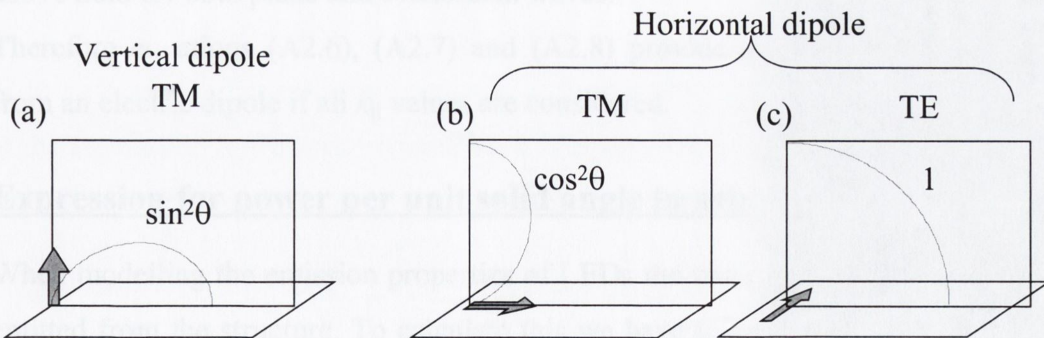

Figure A2.1 *Emission patterns of (a) vertical dipole in TM modes (b) horizontal dipole in TM modes and (c) horizontal dipole in TE modes.*

We first have to express the above source terms as functions of $k_{||}$ and $k_{z,1}$. The field source terms (denoted A) are basically the square root of power per unit solid angle, hence

$$A^{(v,TM)}{}_{\uparrow\downarrow} = \sqrt{\frac{3}{8\pi}}\sin\theta_1 = \sqrt{\frac{3}{8\pi}}\frac{k_{||}}{k_1} \qquad \text{(A2.6)}$$

$$A^{(h,TE)}{}_{\uparrow\downarrow} = \mp\sqrt{\frac{3}{16\pi}} \qquad \text{(A2.7)}$$

$$A^{(h,TM)}{}_{\uparrow\downarrow} = \mp\sqrt{\frac{3}{16\pi}}\cos\theta_1 = \mp\sqrt{\frac{3}{16\pi}}\frac{k_{z,1}}{k_1} \qquad \text{(A2.8)}$$

where ↑ and ↓ denote the +z and –z directions, and we have substituted $k_{||}/k_1$ for $\sin\theta_1$, and $k_{z,1}/k_1$ for $\cos\theta_1$. The origin of the signs of the source terms is discussed in reference [1].

Since dipole radiation is a spherical wave it has arbitrarily large wavevectors in its $k_{||}$ Fourier spectrum, therefore in order to provide a proper generalised source terms, we have to consider $k_{||} = 0$ to ∞ (this corresponds to letting $k_{z,1}$ go from $n_1\omega/c$ at normal incidence to 0 at θ_1=90° all plane waves, and then letting $k_{z,1}$ go from 0 to $+i\infty$ all evanescent waves). Since we are only interested in the farfield emitted power from the structure, we need only consider $k_{||}$ values from 0 to $n_{max}\omega/c$ where n_{max} is the highest refractive index of the multilayers, i.e. we only consider modes which are propagating plane waves in some layer of the structure. The expressions for the source terms given above hold for both plane and evanescent waves.

Therefore equations (A2.6), (A2.7) and (A2.8) provide a full description of emission from an electric dipole if all $k_{||}$ values are considered.

Expression for power per unit solid angle in arbitrary layer of structure

When modelling the emission properties of LEDs the most important result is the power emitted from the structure. To calculate this we have to account for the change in solid angle that is due to refraction. The power per unit solid angle and unit surface area, $\Pi = dP/d\Omega dS$, in some layer is related to the same quantity at the source layer, Π_1, as

$$\frac{\Pi}{\Pi_1} = \frac{dP}{dP_1}\frac{d\Omega_1}{d\Omega} \qquad \text{(A2.9)}$$

In this formula the first factor on the right hand side is the plane-wave power transmission coefficient. It is related to the Poynting vector flux, $\vec{S}$ according to

$$\frac{dP}{dS} = \frac{\vec{S}\cdot\overrightarrow{dS}}{dS} = S\cos\theta = n|E|^2\cos\theta = n|E|^2 k_z/k \qquad \text{(A2.10)}$$

where the direction of $\overrightarrow{dS}$ is normal to the surface element dS. Therefore we obtain

$$\frac{dP}{dP_1} = \frac{|E|^2}{|E_1|^2}\frac{k_z}{k_{z,1}} \qquad \text{(A2.11)}$$

this transfer factor is illustrated in Figure A2.2(a). The second factor in (A2.9), $d\Omega_1/d\Omega$ can be calculated directly from Snell's law as

$$\frac{d\Omega_1}{d\Omega} = \frac{n^2\cos\theta}{n_1{}^2\cos\theta_1} = \frac{nk_z}{n_1 k_{z,1}} \qquad \text{(A2.12)}$$

The expression for the power per unit solid angle and unit area in an arbitrary layer, (including outside structure) can now be rewritten as

$$\begin{aligned}\frac{dP}{d\Omega dS} &= \frac{dP}{dP_1}\frac{d\Omega_1}{d\Omega}\frac{dP_1}{d\Omega_1 dS} \\ &= \frac{|E|^2}{|E_1|^2}\frac{k_z}{k_{z,1}}\times\frac{nk_z}{n_1 k_{z,1}}\times(\text{source terms})\end{aligned} \qquad \text{(A2.13)}$$

In this expression the source terms appear as modulated by the ratio of the squared fields at the source and in the layer of interest. It is equivalent to calculate the fields in the layer of interest $|E_0|^2$ directly from normalised source terms and use the following expression:

$$\begin{aligned}\frac{dP}{d\Omega dS} &= \left[\frac{|E|^2}{|E_1|^2}\times(\text{source terms})\right]\times\frac{nk_z^2}{n_1 k_{z,1}{}^2} \\ &= |E_0|^2\frac{nk_z^2}{n_1 k_{z,1}{}^2}\end{aligned} \qquad \text{(A2.14)}$$

So to calculate the power per unit solid angle and unit area in an arbitrary layer of the structure, we have to calculate the square of the field amplitude in that layer of the structure using the normalised source terms, and then multiply the answer by $\frac{nk_z^2}{n_1 k_{z,1}{}^2}$.

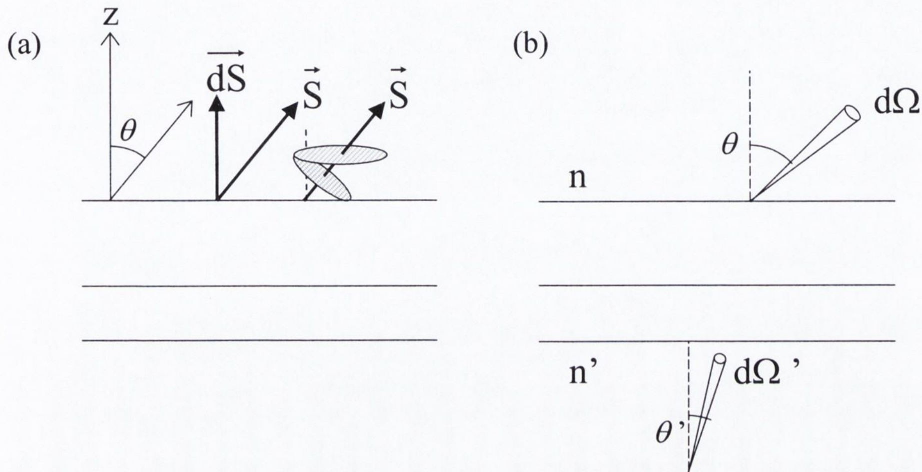

Figure A2.2 *(a) Power flux and Poynting vector crossing a surface: a fixed area normal to $\vec{S}$ (red circle) carries a fixed power, however the projection of this area onto the layer interface (green circle) varies as $1/\cos\theta$. Therefore dP/dS is given by $S\cos\theta$ (b) differential solid angle transfer from one layer to another.*

Implementation of this expression within the transfer matrix framework.

First let us recall that the field in an arbitrary layer j from z_j to z_{j+1} can be represented by a 2×1 vector as a sum of two waves, according to

$$E(z) = E_{j\uparrow}^{(TE,TM)} \exp\left[ik_{z,j}\left(z - z_j\right)\right] + E_{j\downarrow}^{(TE,TM)} \exp\left[-ik_{z,j}\left(z - z_j\right)\right] \equiv \begin{pmatrix} E_{j\uparrow} \\ E_{j\downarrow} \end{pmatrix}_{(TE,TM)} \tag{A2.15}$$

separately for each polarisation, where the $\exp[i(k_x x+k_y y-\omega t)]$ factors have been dropped. The transfer matrix technique is a standard method for the propagation of this wave through a multilayer structure. The technique uses two types of matrices, the first involving $\exp[\pm ik_{z,j}(z_{j+1}-z_j)]$ to account for the propagation of the field through a layer, and the second involving the $k_{||}$ and the refractive indices of the layers at the interface to

account for the Maxwell boundary conditions for tangential fields [3]. Using the product of these matrices (see Figure A2.3) we can calculate the propagation of the field through the structure, accounting fully for all interference effects. A comprehensive discussion of the transfer matrix technique is contained in references [4, 5]

For a structure with internal sources, outside field vectors have a single non-zero term, the outgoing one, i.e. there are no external impinging waves (see Figure A2.3). Then, a 2×2 matrix product (a) depicts propagation from leftmost interface to the source layer, and a matrix (b) depicts propagation from the rightmost interface to the source. Our additive source terms impose the following required relation (equation (A2.1)) between the field vectors on each side of the source layer:

$$\begin{pmatrix} E_{12\uparrow}(\theta_1) \\ E_{12\downarrow}(\theta_1) \end{pmatrix} - \begin{pmatrix} E_{10\uparrow}(\theta_1) \\ E_{10\downarrow}(\theta_1) \end{pmatrix} = \begin{pmatrix} A_{\uparrow}(\theta_1) \\ A_{\downarrow}(\theta_1) \end{pmatrix} \qquad \text{(A2.16)}$$

The fields either side of the source layer can be written in terms of the outside fields by using the matrix relations:

$$\begin{bmatrix} a_{11} & a_{12} \\ a_{21} & a_{22} \end{bmatrix} \begin{pmatrix} 0 \\ E_0(\theta_0) \end{pmatrix} = \begin{pmatrix} E_{10\uparrow}(\theta_1) \\ E_{10\downarrow}(\theta_1) \end{pmatrix}$$

$$\begin{bmatrix} b_{11} & b_{12} \\ b_{21} & b_{22} \end{bmatrix} \begin{pmatrix} E_2(\theta_2) \\ 0 \end{pmatrix} = \begin{pmatrix} E_{12\uparrow}(\theta_1) \\ E_{12\downarrow}(\theta_1) \end{pmatrix} \qquad \text{(A2.17)}$$

Using (A2.16) and (A2.17) one can obtain the following expression for the left outside field E_0

$$E_0 = \frac{b_{21}A_{\uparrow} - b_{11}A_{\downarrow}}{a_{22}b_{11} - b_{21}a_{12}} \equiv \frac{\text{(source terms)}}{\Delta} \qquad \text{(A2.18)}$$

and one can obtain similar expressions for the fields in any layer of the structure from these equations. In all cases we find the same denominator characteristic of the structure, $\Delta = c_{22}$ [where $(c)=(a)(b)^{-1}$ is the structure matrix product], which carries the modal properties of the structure. The numerator takes account of reflection of source terms by the right side of the structure through matrix elements b_{21} and b_{11}.

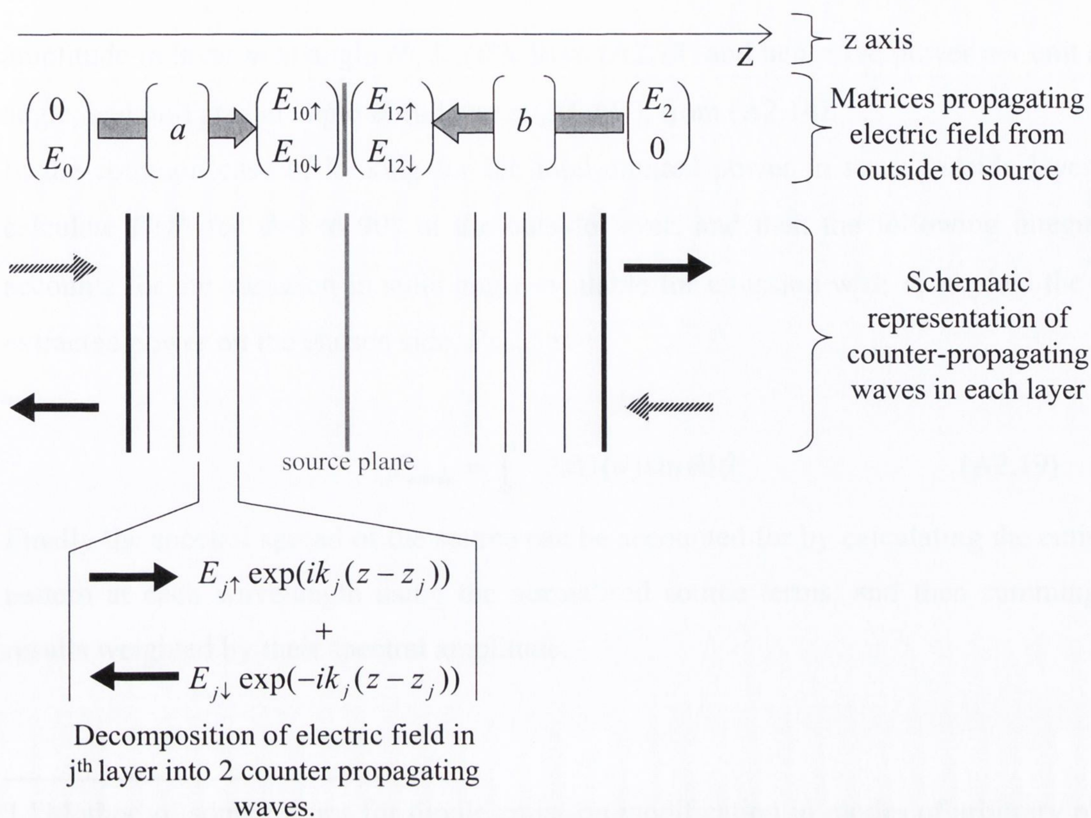

Figure A2.3 *Schematic diagram of layered structure with source plane inside and matrices describing the propagation of electric fields from the outside to the source. Only outgoing fields do not vanish if fields come only from source.*

Therefore to summarise the procedure for calculating the power per unit solid angle, for a given angle θ' in an arbitrary layer of the structure (labelled m): the first step is to calculate $k_{||}$ ($=n_m \sin\theta'$). Then $k_{z,j}$ is calculated in every layer of the structure, according to equation (A2.2). Matrices are then formulated for each layer and interface of the structure for these values of $k_{z,j}$ and the n_j of each layer. From the product of these matrices in suitable order one obtains matrices (a) and (b). The denominator in equation (A2.18), Δ characteristic of the structure can be calculated at this stage. The next step involves the calculation of the source fields ($A_{\downarrow}$ and $A_{\uparrow}$) that couple to the angle θ' in layer m. Since we already have $k_{||}$ and $k_{z,1}$ ($k_{z,j}$ in the source layer) we can directly calculate the correct source amplitude using the relevant equation (A2.6) , (A2.7) or (A2.8) depending on dipole orientation and emission polarisation. We can then calculate the electric field

amplitude in layer m at angle θ', $E_m(\theta')$, from (A2.18) and hence the power per unit solid angle, and unit area at angle θ' in layer m , $\Pi_m(\theta')$, from (A2.14).

In the common case of looking for the total emitted power in some outside layer, we calculate $\Pi(\theta)$ for θ=0 to 90° in the outside layer, and then the following integration accounts for the variation in solid angle available for emission with θ, to yield the total extracted power on the chosen side, P_{extrac} as

$$P_{extrac} = \int_0^{\pi/2} 2\pi\Pi(\theta)\sin\theta d\theta \qquad \text{(A2.19)}$$

Finally the spectral spread of the source can be accounted for by calculating the emission pattern at each wavelength using the normalised source terms, and then summing the results weighted by their spectral amplitude.

---

1 "Method of source terms for dipole emission modification in modes of arbitrary planar structures", H. Benisty, R. Stanley, and M. Mayer, J. Opt. Soc. Am. A **15** (5) p. 1192 (1998)

2 "Impact of planar microcavity effects on light extraction - Part II: Selected exact simulations and role of photon recycling", H. Benisty, H. De Neve, C. Weisbuch, IEEE J Quant. Elect. **34** (9) p. 1632 (1998)

3 *Principles of Optics*, M. Born and E. Wolf (6th Ed., Cambridge University Press, Cambridge, 1980)

4 *Optical waves in layered media*, P. Yeh (Wiley, 1988)

5 *Introduction to Optics*, F. L. Pedrotti, and L. S. Pedrotti, Chapter 19 (Prentice-Hall, New Jersey, 1987)